The survey of Planetary Nebulae in Andromeda (M31): Discrete tracers in the disc and inner halo

Souradeep Bhattacharya

SIGILL·UNIVERSITAT·LUDOVIC·MAXIM

München 2020

The survey of Planetary Nebulae in Andromeda (M31): Discrete tracers in the disc and inner halo

Souradeep Bhattacharya

Dissertation
an der Fakultät für Physik
der Ludwig–Maximilians–Universität
München

vorgelegt von
Souradeep Bhattacharya
aus Agartala, Indien

München, den 28. August 2020

Erstgutachter: Prof. Dr. Ortwin Gerhard
Zweitgutachter: Prof. Dr. Achim Weiss
Tag der mündlichen Prüfung: November 20, 2020

Contents

List of Figures

List of Tables

Acronyms

2D two-dimensional
2dFGRS Two-degree-Field Galaxy Redshift Survey
AD Anderson-Darling
AGB asymptotic giant branch
AGN active galactic nucleus
AVR Age-Velocity dispersion relation
BAO Baryon Acoustic Oscillations
BIC Bayesian Information Criterion
CDM cold dark matter
CEL collisionally-excited line
CFHT Canada-France-Hawaii Telescope
CMB cosmic microwave background
CMD colour-magnitude diagram
CRD Carbon-rich dust
CSPN central star of the planetary nebula
dSph dwarf spheroidal
DM dark matter
ESA European Space Agency
FOV field of view
FWHM full width at half maximum
GC globular cluster
GES Gaia-Enceladus-Sausage
HBB Hot Bottom Burning
HERON Halos and Environments of Nearby Galaxies
HST Hubble Space Telescope
HUDF Hubble Ultra-Deep-Field
ICL intra-cluster light
IFU integral-field unit
INT Issac-Newton Telescope
IR infrared
ISM interstellar medium
KS Kolmogorov-Smirnov
LF luminosity function

LG Local Group
LOS line-of-sight
LOSV line-of-sight velocity
LMC Large Magellanic Clouds
LSB low surface brightness
MATLAS Mass Assembly of early-Type GaLAxies with their fine Structures
MMT Multi-mirror Telescope
MS main sequence
MW Milky Way
NASA National Aeronautics and Space Administration
NEAT Nebular Empirical Analysis Tool
NIR near-infrared
ORD Oxygen-rich dust
PAndAS Pan-Andromeda Archaeological Survey
PHAT Pan-Hubble Andromeda Treasury
PNLF planetary nebula luminosity function
PN planetary nebula
PN.S Planetary Nebula Spectrograph
PSF point-spread function
RGB red giant branch
SB surface brightness
SDSS Sloan Digital Sky Survey
SFH Star Formation History
SMC Small Magellanic Clouds
SPLASH Spectroscopic and Photometric Landscape of Andromeda's Stellar Halo
SSP single stellar population
S/N signal-to-noise ratio
STScI Space Telescope Science Institute
TP-AGB thermally-pulsating asymptotic giant branch
TDU Third Dredge Up
UV ultraviolet
WHT William Herschel Telescope

Zusammenfassung

Andromeda (M 31) ist die unserer Milchstraße (MW) am nächsten gelegene Riesenspiralgalaxie und das massereichste Mitglied unserer Lokalen Gruppe mit einem diffusen Halo von über 100 sq. deg. am Himmel. Aufgrund ihrer Nähe wurde ihre Struktur mit verschiedenen Tracern umfassend untersucht. Die Beobachtungen von Sternen im roten Riesenast in M 31 führten zur Entdeckung einer Vielzahl von Unterstrukturen in ihrem inneren Halo, die ihre turbulente jüngste Formationsgeschichte enthüllten. M 31 steht somit in starkem Kontrast zur MW, welche in den letzten $\sim$ 10 Gyr keine größeren Galaxienfusionen hatte. Um die Struktur und die Evolutionsgeschichte von M31 zu verstehen, sind einheitliche Messungen der Kinematik und der chemischen Häufigkeit über die gesamte Hauptachse der M 31-Scheibe und ihrer inneren Halo-Substrukturen unerlässlich. Solche Messungen, die auf Absorptionsmerkmalen des Sternkontinuumslichts mittels integraler Feldspektroskopie oder Spektren einzelner Sterne beruhen, gehen über das hinaus, was derzeit selbst mit den modernsten Techniken möglich ist. Dies liegt an der sehr großen Winkelgröße von M31, der geringen Oberflächenhelligkeit der äußeren Bereiche und der weiteren Komplikation der Kontamination durch die MW-Halosterne. Daher sind diskrete stellare Indikatoren, die fest im M 31-System verankert sind, erforderlich, um die jüngste Formationsgeschichte aufzudecken. Planetarische Nebel (PNe), helle Emissionsliniennebel der späten Phase der Sternentwicklung, sind ausgezeichnete diskrete stellare Indikatoren für Licht, Chemie und Bewegung in Galaxien.

In dieser Arbeit führen wir mit der MegaCam@CFHT eine vollständige und homogene Durchmusterung des tiefen Schmalbandes [O III] durch, um PNe in M 31 zu identifizieren, das die Scheiben- und inneren Halo-Substrukturen abdeckt. Wir erhalten tiefe PN-Leuchtkraftfunktionen (PNLFs), die unterschiedlichen Substrukturen im inneren Halo und in der Scheibe M 31 entsprechen. Wir beobachten einen Anstieg des schwachen Endes der PNLF, der durch den Anteil älterer Sterne in der stellaren Vorgängerpopulation verursacht wird. Beim Vergleich der PNLFs der verschiedenen Regionen in M 31 stellen wir fest, dass der Große Sternenstrom, sowie die NO und W Substrukturen mit der Bildung aus Trümmern eines einzelnen Satelliten übereinstimmen, während der G1-Klumpen aus der gestörten M 31-Scheibe gebildet wird. Strom-D besteht aus Sternresten eines andern Satelliten.

Das spektroskopische Follow-up einer Teilprobe des PNe in der M 31-Scheibe wurde mit Hectospec@MMT durchgeführt. Die identifizierten PNe wurden in Populations mit hoher und niedriger Extinktion mit einem Durchschnittsalter von ~2.5 Gyr und ~4.5 Gyr getrennt, wobei die dynamisch kälteren dünnen und dynamisch heißeren dicken Scheiben von M 31 jenseits eines galaktozentrischen Radius R_{GC} =14 kpc formen. Es wurde auch festgestellt, dass sich

die beiden Scheiben chemisch in der Argonhäufigkeitsverteilung ihrer PNe unterscheiden und daher unterschiedliche Ursprünge haben. Dies ist die erste Identifizierung der kinematisch und chemisch unterschiedlichen dünnen und dicken Scheiben in M 31, die in der äquivalenten Entfernung der Sonne in M 31 eine Geschwindigkeitsdispersion aufweisen, die jeweils doppelt und dreifach so hoch ist wie die der gleichaltrigen Sterne in der MW. Eine solch steile Alter-Geschwindigkeits-Dispersionsbeziehung in M 31 steht im Einklang mit einer einzelnen größeren Fusion, die vor 2.5 bis 4.5 Gyr mit einem Fusionsmassenverhältnis von ≈1:5 stattfand. Die radialen Häufigkeitsgradienten der dünnen und dicken M 31-Scheibe sind auch viel flacher als von säkularen Prozessen erwartet und unterstützen unabhängig voneinander das massive Akkretionsereignis mit erheblichem Einfluss auf die M 31-Scheibenstruktur.

Abstract

Andromeda (M31) is the nearest giant spiral galaxy to our Milky Way (MW) and the most massive member of our Local Group, with its diffuse halo spanning over 100 sq. deg. on the sky. Given its proximity, its structure has been widely studied with various tracers. The observations of red-giant-branch stars in M31 resulted in the discovery of a plethora of substructures in its inner halo, revealing its tumultuous recent formation history. M31 thus stands in sharp contrast to the MW which has had no major galaxy mergers over the past $\sim$10 Gyr. Uniform measurements of the kinematics and chemical abundances over the entire major axis of the M31 disc and its inner halo substructures is essential to understand the structure and evolutionary history of M31. Such measurements based on absorption features on the stellar continuum light, via integral field spectroscopy or spectra of individual stars, are beyond what is currently possible even with the most advanced facilities. This is because of the very large angular size of M31, the low surface brightness of the outer regions and the further complication of the contamination from the MW halo stars. Thus, discrete tracers firmly in the M31 system are required to unravel its recent formation history. Planetary Nebulae (PNe), bright emission-line nebulae of the late-phase of stellar evolution, are excellent discrete tracers of light, chemistry and motion in galaxies.

In this thesis, we carry out a complete and homogeneous deep narrow band [O III] survey with the MegaCam@CFHT to identify PNe in M31, covering its disc and inner halo substructures. We obtain deep PN luminosity functions (PNLFs) corresponding to distinct substructures in the M31 inner halo and disc. We observe a rise in the faint-end of the PNLF that is driven by the fraction of older stars in the parent stellar population. Comparing the PNLFs of the different regions in M31, we find that the Giant Stream, NE and W Shelves are consistent with having formed from debris of a single satellite while the G1 clump is formed from the perturbed M31 disc. Stream-D is composed of stellar remnants from a distinct satellite.

Spectroscopic follow-up of a subsample of the PNe in the M31 disc was carried out with Hectospec@MMT. The identified PNe were separated into high- and low-extinction samples having average ages of $\sim$2.5 Gyr and $\sim$4.5 Gyr, forming the dynamically colder thin and dynamically hotter thick discs of M31 respectively beyond a galactocentric radius, R_{GC} =14 kpc. The two discs are also found to be chemically distinct from the argon abundance distributions of their PNe and thus have distinct origins. This is the first identification of the kinematically and chemically distinct thin and thick discs in M31, which at the equivalent distance of the Sun in M31 have a velocity dispersion twice and thrice that of the stars of the same age in the MW respectively. Such a steep age-velocity dispersion relation in M31 is consistent with a single major merger that occurred 2.5 – 4.5 Gyr ago with a merger mass ratio $\approx$1:5. The radial abundance gradients of the M31 thin and thick disc are also much flatter than expected from secular processes and independently support the massive accretion event with significant impact on the M31 disc structure.

Chapter 1

Introduction

1.1 Galaxies in the Universe

On 26th April, 1920, the Great Debate took place between the eminent astronomers Harlow Shapley and Heber Curtis at the Smithsonian Museum of Natural History, Washington D.C., USA (for details, see Trimble 1995). They debated on the nature of spiral nebulae and the extent of the universe. Shapley argued that the extent of the Milky Way (MW) was the extent of the universe with spiral nebulae being within the MW. Curtis, on the other hand, championed that the spiral nebulae were in fact "island universes", outside the extent of the MW, which itself was an island universe within a significantly larger universe. The debate was eventually settled by Edwin Hubble who utilised observations of Cepheid variables[1] in the Andromeda (M31) nebula, the Triangulum nebula (M33) and NGC 6822 to find that they lie at much larger distances beyond the extent of the MW and were thus distinct galaxies (for details, see Berendzen & Hoskin 1971) with M31 being the closest giant spiral galaxy to the MW (Hubble 1929). Further observations of such extragalactic nebulae, led to the Hubble classification of galaxies based on their observed morphology (Hubble 1926, 1936).

In the past 100 years since the great debate, galaxies of various morphologies, over large distance scales, and having a wide range of masses have been discovered using a variety of ground and space based telescopes. Figure 1.1 shows the morphological classification of galaxies, the Hubble tuning fork, populated from observations of nearby galaxies ($<$ 30 Mpc) by the *Herschel Space Telescope* and *Spitzer Space Telescope* as part of the Kingfish (Kennicutt et al. 2011) and SINGS surveys (Braun et al. 2007). Elliptical galaxies are to the left of the tuning fork while spirals galaxies are arranged by decreasing spiral arm compactness. The spiral galaxies in the top arm of the tuning fork lack a conspicuous bar while those in the bottom have a prominent bar. Many spiral galaxies have been discovered intermediate between the two. A fraction of galaxies have also been found to be irregular.

As galaxies are observed to larger distances, i.e, at higher redshifts, fewer spiral galaxies and more irregulars appear. The *Hubble Space Telescope* Ultra Deep Field (HUDF; Figure 1.2)

---

[1] Variable star with a linear relationship between luminosity and pulsation period allowing for precise distance determination (Leavitt 1908).

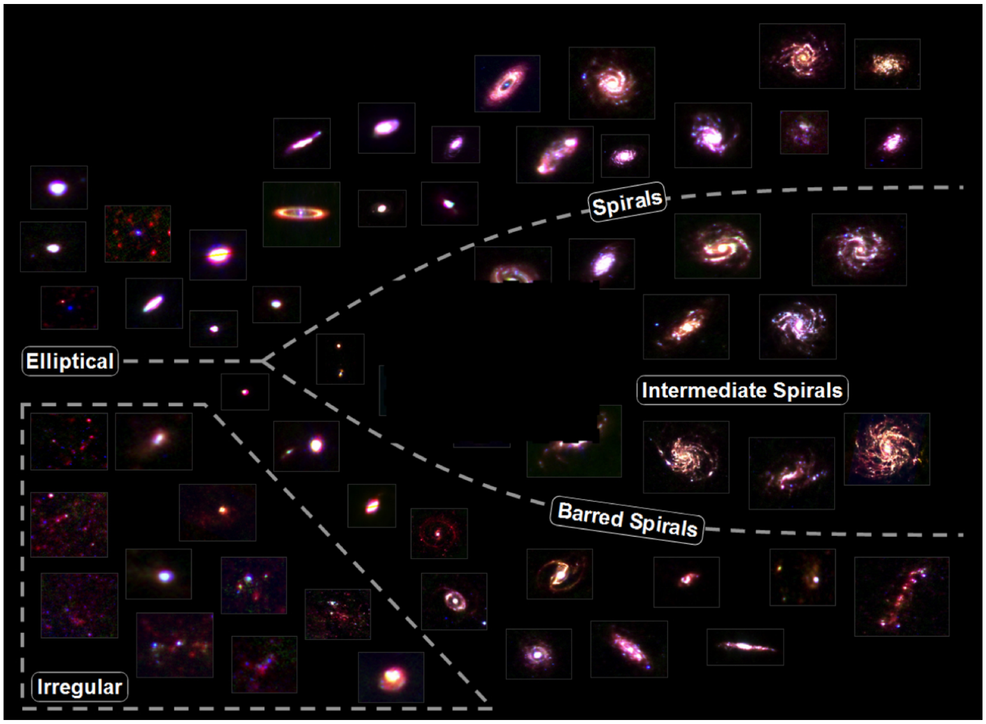

Figure 1.1: The morphological classification of galaxies by Edwin Hubble, popularly known as the Hubble tuning fork. The 61 galaxies shown here have been observed by the *Herschel Space Telescope* and *Spitzer Space Telescope* . Image credit: ESA, C. North, M. Galametz and the Kingfish Team.

shows the menagerie of galaxies observed in the universe, showing galaxies including spirals at low redshifts, $z<1$, to those at large distances, down to redshift $z\sim5$–6 (Beckwith et al. 2006). The lower panel of Figure 1.2 shows five of the high redshift galaxies observed in the HUDF. Along with their irregular morphologies, galaxies number 2–4 also exhibit extended features associated with ongoing merger activity (Straughn et al. 2006). Such morphological evolution of galaxies from the high-redshift to the nearby universe is one of the primary questions tackled by any cosmological model aiming to describe galaxy formation and evolution.

1.1.1 Λ Cold dark matter cosmology

The predominant cosmological model, presently preferred by the scientific community, describing the formation and evolution of the universe is the Λ cold dark matter (ΛCDM) cosmological model. In this paradigm, a cosmological constant (Λ) is associated with dark energy with ordinary matter forming the observed structures of the universe and presence of a postulated cold dark matter (CDM) with the assumption that gravitation on cosmological scales is completely described by general relativity. Λ is associated with negative pressure in vacuum and under general relativity this leads to dark energy in vacuum. Dark energy is invoked to explain the acceleration of the expanding universe forming $68.47\pm0.73\%$ (Planck Collaboration et al. 2018)

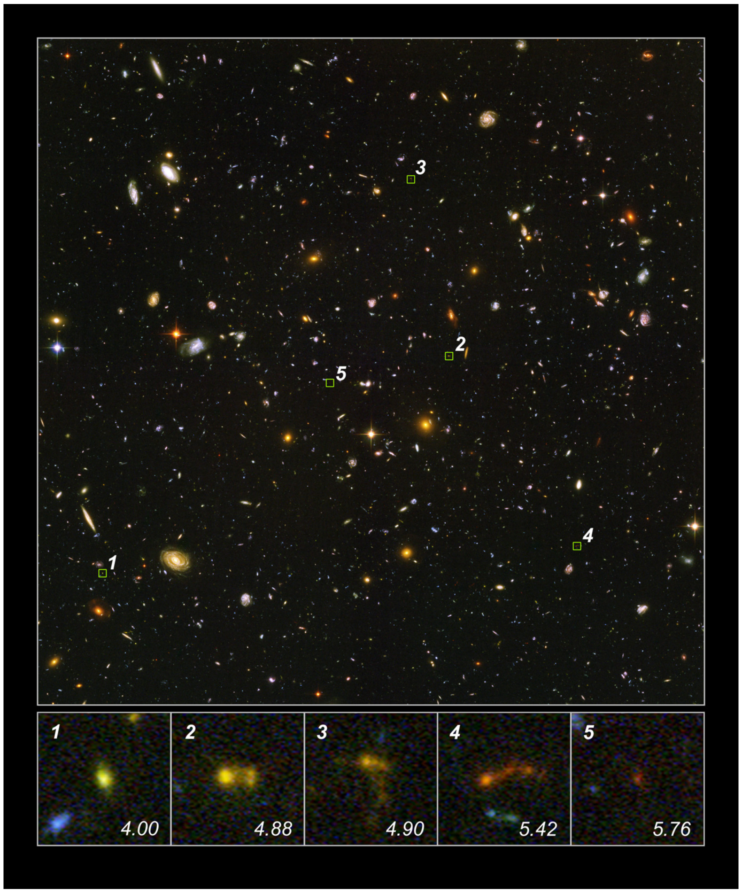

Figure 1.2: [Top] The Hubble Ultra Deep Field (HUDF) showing the menagerie of galaxies in the universe. [Bottom] Five of the high redshift galaxies observed in the HUDF are shown with their redshift values. Image credit: NASA, ESA, STScI (N. Pirzkal).

of the mass-energy density of the universe. A non-baryonic, cold (velocity always far lower than that of the speed of light), dissipationless (no energy lost from radiating photons) and collisionless dark matter, which constitutes about 26.5% (Planck Collaboration et al. 2014) of the mass-energy density of the universe, is postulated to account for gravitational effects observed in very large-scale structures. The remaining 4.9% of the mass-energy density of the universe comprises of all ordinary observed matter.

In ΛCDM, structure is formed hierarchically. Fluctuations, termed baryon acoustic oscillations (BAO), caused by acoustic density waves in the primordial plasma of the early universe were predicted to be present in the density of the visible ordinary matter of the universe (Peebles & Yu 1970; Seo & Eisenstein 2003). The maximum distance the acoustic waves could travel in the primordial plasma before the plasma cooled to become neutral atoms (the epoch of recombination) is the “standard ruler” for length scale in cosmology. This standard ruler, and thereby the signal for BAO, was measured by the 2dFGRS (Cole et al. 2005) and SDSS surveys (Eisenstein et al. 2005). The observation of the BAO signal is one of the most notable successes of the ΛCDM cosmological model. ΛCDM describes well the structure of the cosmic microwave background (CMB Planck Collaboration et al. 2018) with its observed anisotropies postulated to become denser over time till haloes are formed which are the seeds of galaxies. These haloes then grow hierarchially over time with matter accretion and mergers forming large galaxy clusters. Cosmological simulations based on ΛCDM (e.g. Millennium- De Lucia et al. 2006; Illustris- Vogelsberger et al. 2014; Eagle- Schaye et al. 2015; Magneticum- Teklu et al. 2015; Horizon-AGN- Dubois et al. 2016; IllustrisTNG- Pillepich et al. 2018) have been very successful in describing the large-scale properties of the universe., the large-scale structure of galaxies (cosmic web; Bond et al. 1996), clusters of galaxies and gravitational lensing (Walsh et al. 1979). While large scale galaxy properties are well described by ΛCDM cosmological simulations, challenges persist on galaxy and sub-galaxy scales.

1.1.2 Sub-galaxy scale structure of galaxies

As galaxies evolve by matter accretion from their environment and galaxy mergers, structure formation on sub-galaxy scales ensue. The interacting ordinary matter forms the visible luminous sub-galaxy scale structures. The visible matter is initially present as shock-heated gas in the quasistatic hot atmosphere around the galaxy in the cosmic web (e.g. White & Rees 1978). The gas then cools radiatively and falls in a free-fall time to the center of galaxy haloes. The flow of the cooling gas (cooling flow) is the process that determines the baryonic mass of galaxies (Silk 1977). Within the galaxy halo, the gas, originally distributed in mass and angular momentum as the dark matter, cools and collapses until it reaches centrifugal balance in a disc, with an exponential surface density profile thus conserving angular momentum (Firmani & Avila-Reese 2000). The first generation of stars in galaxies are formed from this cold gas (Silk 1977). A stellar halo may be formed from star-formation from cool gas prior to falling into the disc or from stars expelled from the disc after formation. A central bulge (and also bar) may also be formed from secular evolution processes in such a disc. Galaxies then interact in gas-rich mergers that then form subsequent generations of stars, although some star formation also occurs due to secular evolution processes. Thus ΛCDM predicts a two-stage formation of galaxies with their initial secular evolution to form the first generation of stars and then subsequent hierarchical growth of galaxies through mergers and interactions (e.g. Oser et al. 2010).

Merger rate of galaxies is higher in the early universe with large numbers of small haloes merging. For most such galaxies, any sub-galaxy structures formed, mainly its disc, is quickly disrupted by ongoing mergers. Thus, many high-redshift galaxies have irregular structures (Figure 1.2). Some high-redshift galaxies, who have consumed their gas content to form stars, also exhibit elliptical morphologies (e.g. De Lucia et al. 2006). Over time, massive galaxies are formed which continue their hierarchical growth by consuming smaller galaxies but sub-galaxy scale structures, such as bars and spiral arms, become more persistent. These structures may be destroyed in mergers for many galaxies who end up with an elliptical morphology (e.g. De Lucia et al. 2006). They survive in spiral galaxies, either since such spirals didn't have a recent merger or the mergers that took place didn't destroy the observed structures (Hopkins et al. 2009). Disks, bulges and bars may even be formed due to galaxy interactions and mergers (Brooks & Christensen 2016). Large scale cosmological models are typically unable to reproduce the observed

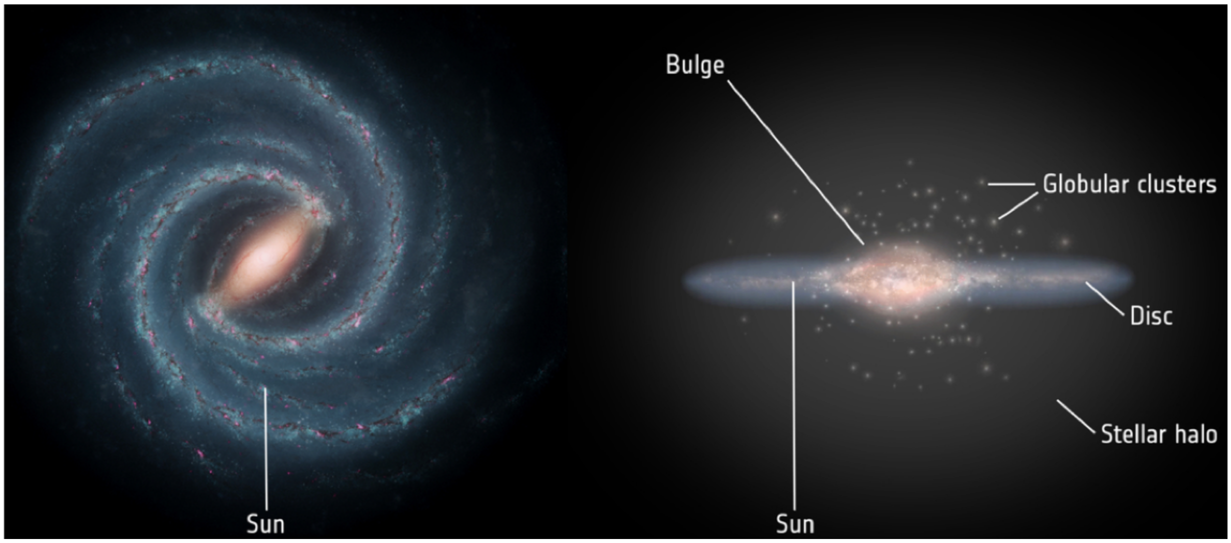

Figure 1.3: The MW as an example of the morphology of a typical spiral galaxy. [Left] An artists impression of the face-on view of the MW showing the spiral structure with central bar. [Right] An artists impression of the edge-on view of the MW showing the central bulge and disc embedded in the stellar halo. Note the thin and thick disc structure of the MW disc. Globular clusters present in the MW halo are marked along with the position of the sun. Credit: Left–NASA/JPL-Caltech; right–ESA

sub-galaxy scale structure of spiral galaxies but predictions are possible from ΛCDM cosmology using simulations of individual or groups of galaxies (e.g. N-body simulations- Ostriker & Peebles 1973; Hydrodynamical simulations- Lindblad et al. 1996). Disc and other sub-galaxy scale structure formation was carefully analysed in the Aquila comparison simulations (Scannapieco et al. 2012) where a spiral galaxy was constructed from multiple simulations with different physical processes. Of particular note are the Auriga simulations (Grand et al. 2017) which are cosmological magnetohydrodynamical zoom simulations of MW-like galaxies which offer detailed insight into sub-galaxy scale structure formation in the ΛCDM cosmological model (e.g. Fragkoudi et al. 2020).

Sub-galaxy scale structure is clearly resolved in nearby galaxies of various morphologies. All these galaxies have the most luminous central body of the galaxy embedded in a faint stellar halo. The most luminous central body is elliptical or irregular for an elliptical or irregular galaxy respectively. For spiral galaxies, as can be seen in Figure 1.3, the spiral arms seen face-on are in a luminous disc with a central bulge. The disc, viewed edge-on, may exhibit a thinner disc structure embedded in a thicker disc structure. The central bulge may also exhibit a bar in case of barred spirals. Note that galaxies at the node of the Hubble tuning fork, termed S0 galaxies, exhibit a disc with no spiral arms.

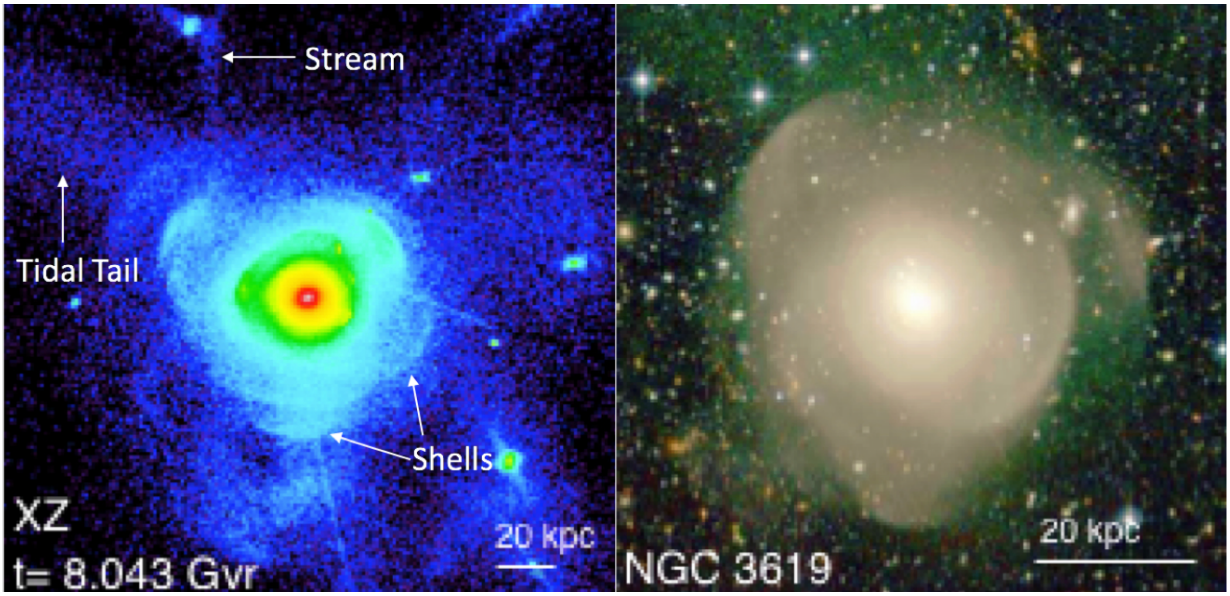

Figure 1.4: [Left] Morphological features associated with galaxy mergers in a simulated galaxy by Mancillas et al. (2019). [Right] The observed low-surface brightness morphological features of an elliptical galaxy from the MATLAS Survey (Bílek et al. 2020).

1.1.3 Imprints of hierarchical formation in galaxies

Independent of the galaxy morphology of visible matter, N-body and hydrodynamical simulations of individual galaxies based on ΛCDM cosmology have predicted observable morphological features in galaxy haloes that are remnants of galaxy interactions and mergers (e.g. Bullock & Johnston 2005; Mancillas et al. 2019). Mass in galaxies is deposited from mergers with fine features present in the halo of galaxies that are generated in such interactions. The features are much fainter than the main luminous body of the galaxy and disperse with time. As can be seen in Figure 1.4 [left], these features can be broadly classified into tidal tails (thick, radially elongated structures connected to the main body of the galaxy), streams (thin, elongated stellar structures) and shells (sharp-edge concentric arc structures). They are typically longer-lived in the galaxy halo at larger distances from the galaxy main luminous body where dynamical times are longer. These structures have long been observed in various galaxies (e.g. Figure 1.4 [right]; see Martínez-Delgado et al. 2010 and references therein) but their detection has now become more common with recent low-surface brightness surveys of the haloes of nearby galaxies (e.g. HERON- Rich et al. 2019; MATLAS- Bílek et al. 2020). While these structures are tell-tale signs of galaxy mergers, they do disperse over time so that majority of the mass brought in by satellites during galaxy merger is either deposited in the halo or the bright main body of the galaxy.

Different galaxy masses are also associated with different metallicities. Chemical processes take place in stellar interiors and over time the material of the galaxy is enriched from supernova explosions, AGB star evolution, AGN evolution etc. (see review by Nomoto et al. 2013). These processes are a function of galaxy mass such that the mass and metallicity of galaxies are found to

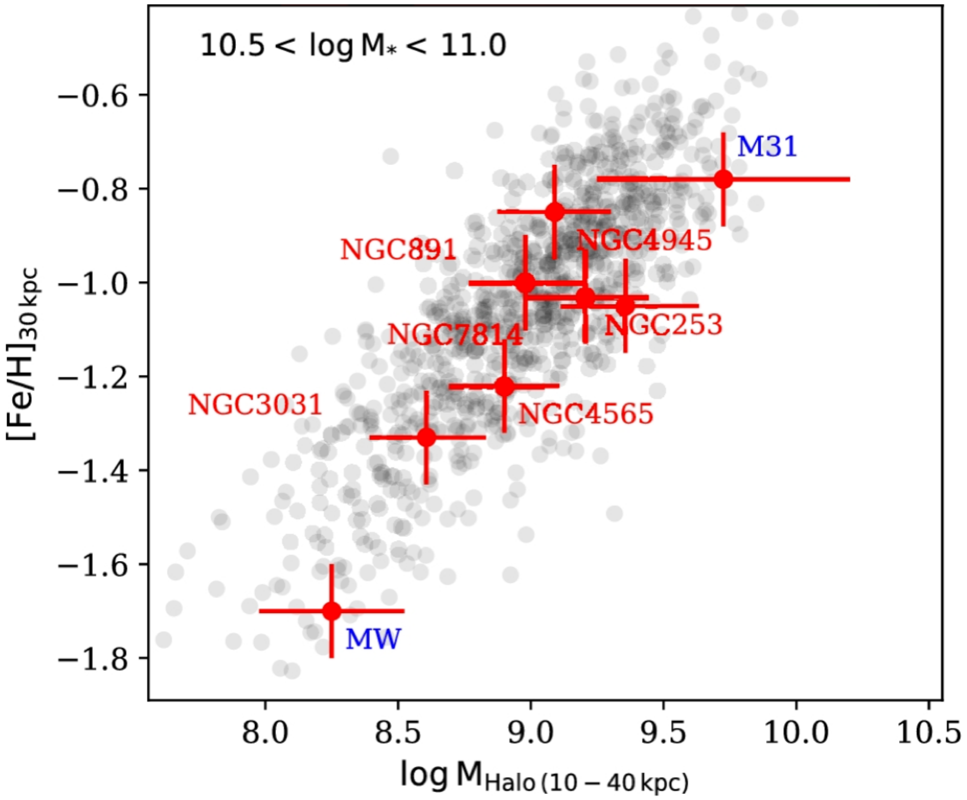

Figure 1.5: The red points show the halo mass vs halo metallicity relation obtained by Harmsen et al. (2017) for near MW-mass spiral galaxies from the GHOSTS survey along with the MW and M31. The grey points show the accreted halo mass vs metallicity relation from similar spiral near MW-mass galaxies from the Illustrus simulation. Credit: D'Souza & Bell (2018b)

be directly related, termed the mass-metallicity relation with more massive galaxies being more metal-rich (see reviews by Pagel & Edmunds 1981 and Sánchez 2020 and references therein). Thus, higher average metallicity of a galaxy halo stellar population would indicate more massive dissolved satellites building-up the halo of a galaxy. Thus the features of hierarchical formation will also reflect the metallicity of their parent satellite galaxy and so will the galaxy halo that is built-up from these satellites.

Using N-body simulations of galaxy mergers with different mass ratios and orbital configurations, Karademir et al. (2019) found that mini-mergers (satellites merging with mass ratio >1:50) typically deposit majority (~75%) of their mass in the halo while satellites merging with mass ratio <1:10 deposit majority(~75%) of their mass in the inner body of the galaxy. D'Souza & Bell (2018b) found, using disc galaxies from the Illustris cosmological simulations, the measured metallicity of the halo of a galaxy increases linearly with accreted halo mass (Figure 1.5). This also agrees with the halo mass and metallicity measured for the MW, M 31 and six spiral galaxies in the GHOSTS survey (Monachesi et al. 2016; Harmsen et al. 2017). The MW and M 31 form the two extremes in this relation with the MW having a less-massive metal-poor halo and M 31 having a more-massive, relatively metal-rich halo. This implies that the MW had a very quiet accretion history while M31 had a very tumultuous one, both extreme cases for spiral galaxies. While the MW was long held as typical example of a spiral galaxy, this result and others like its atypical satellite population (Geha et al. 2017) indicate its properties may not be generalised to all spiral galaxies.

1.1.4 The merger history of our Milky Way

Recent results from Gaia DR2 (Gaia Collaboration et al. 2018) observations have revealed that the most recent major merger in the MW was ~10 Gyr ago (Helmi et al. 2018; Belokurov et al. 2018). While streams associated with the stellar material from this merger are not clearly visible from the morphology of the MW halo, dynamical modelling of Gaia DR2 kinematics and chemical abundance measurements from follow-up spectroscopy have revealed some stream candidates in the velocity phase space (Naidu et al. 2020). The most striking feature for this merger event though is the Gaia-Enceladus-Sausage (GES) feature, remnants of the merged satellite galaxy that overlap in space with the MW bulge and disc stars but stand out in maps of appropriate kinematic properties (Helmi et al. 2018; Belokurov et al. 2018). Thus this merger event deposited satellite material in the MW central luminous body but did not destroy the MW disc. Hydrodynamical simulations have suggested that gas from this merger event led to the formation of the stars presently observed in MW thick disc while the MW proto-disc material was partly ejected, along with some satellite material (Grand et al. 2020), to build up the MW halo while the dynamically cold MW thin disc formed later from subsequent gas accretion from the galaxy surrounding. The chemically distinct thin and thick discs are indeed indicative of separate origins (Bland-Hawthorn & Gerhard 2016).

The Sagittarius dwarf spheroidal (Sgr dSph) galaxy is also currently merging with the MW (Ibata et al. 1994). While it may have induced some kinematic effects on the MW disc (Antoja et al. 2018), having a small mass ($\sim 4 \times 10^8 \mathrm{M}_{\odot}$; Vasiliev & Belokurov 2020) compared to the MW its passage through the disc did not cause substantial dynamical heating with majority of its stellar material being deposited in the MW halo. Other mini mergers that may have occurred in the MW would also have had little impact on dynamical heating of its disc (Karademir et al. 2019). Thus since the GES merger event ~10 Gyr, both the thin and thick disc structures of the MW have largely been affected via secular evolution processes (like influence of spiral structure, interactions with giant molecular clouds and kinematic interactions of the discs with the bar; see Sellwood 2014 for details) affecting both the velocity dispersion and the metallicity distribution within these discs. On the other hand, with a massive relatively metal-rich halo and other observations discussed in the following section, the merger history of M31 is in sharp contrast to that of the MW.

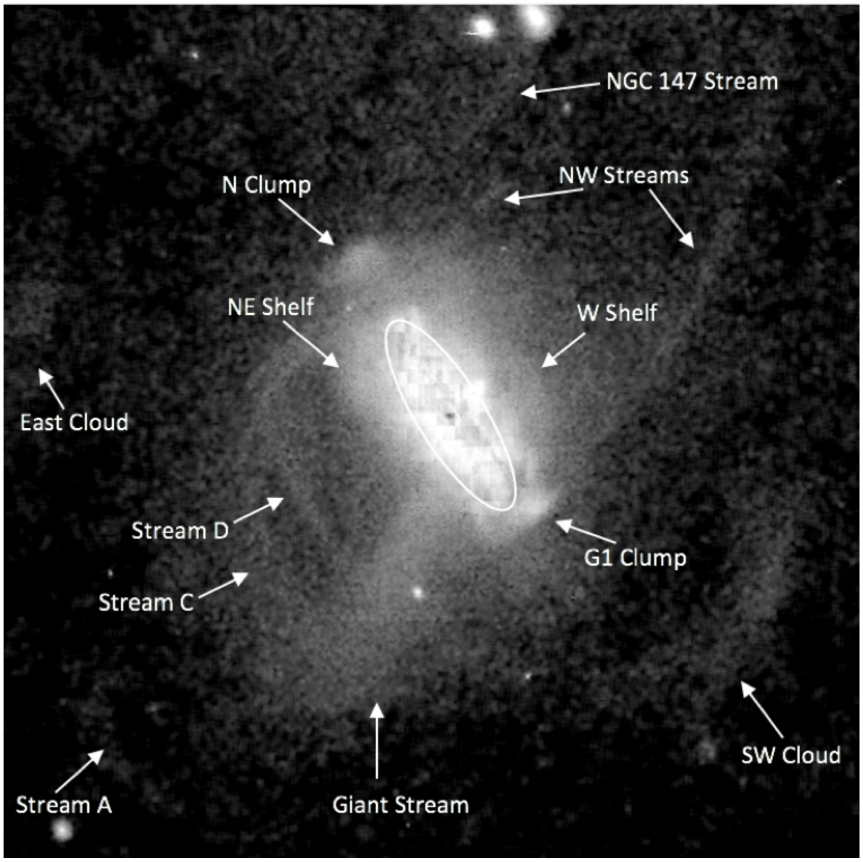

Figure 1.6: The PAndAS map of resolved stars ([M/H]~ -2.5 to -0.7 dex) in the M31 halo and disc. The ellipse shows the M31 disc within ~30 kpc. The PAndAS map is saturated in this region due to crowding. All the major substructures are marked. Smaller substructures closer to the disc are also found by PAndAS but not marked here. Along with the disc, the Giant Stream, NE and W shelves, N and G1 clumps, and Stream-D are the substructures studied in this thesis. Adapted from McConnachie et al. (2018).

1.2 The Andromeda galaxy (M31) as a laboratory of hierarchical formation

M31 is the closest giant spiral galaxy to the MW at a distance of ~ 780 kpc (Conn et al. 2016) with a high inclination to the line-of-sight (i~ 77 deg). It is the largest and most massive galaxy of the Local Group (Yin et al. 2009) with a halo spanning ~100 sq. deg. in the sky. At the distance of M 31, observations of resolved stellar populations is possible with current telescopes and instrumentation. The Pan-Andromeda Archaeological Survey (PAndAS; McConnachie et al. 2009, 2018) obtained the largest map of resolved stellar population, mainly red-giant-branch (RGB) star, in the M31 halo, revealing a wide-array of low-surface brightness substructures (Figure 1.6). The faint fine structures in the M 31 halo are telltale signs of its tumultuous merger history. The presence of these structures along with the massive metal-rich halo of M 31, coupled with the possibility of observing resolved stellar populations, to sufficient depths comparable to the MW, make M 31 the prime laboratory for the study of hierarchical formation of spiral galaxies. Nearly 100 years after its role in the discovery of galaxies, M 31 continues to be a laboratory to aid our understanding of their formation.

1.2.1 Inner halo substructures in M 31 and their posited origins

Since the discovery of the Giant Stream (Ibata et al. 2001) in M 31, its most prominent substructure, the M 31 inner halo has long been a subject of both observational and theoretical studies to understand its formation history. The initial discovery papers for some of these substructures (e.g. Ferguson et al. 2002; Ibata et al. 2005) posited their formation from disruptions of distinct dwarf galaxies having $\sim 10^7$–10^9 $M_\odot$. N-body simulations by Fardal et al. (2006) found that the Giant Stream could be explained as the stellar debris trail of a satellite on its first infall into the M 31 disc while also forming the NE and W shelves in subsequent pericenter passages (Fardal et al. 2007) similar to shells observed in cosmological simulations. The most recent version of this merger model (Fardal et al. 2013) explains the Giant Stream, NE and W shelves as being formed $\sim$ 1 Gyr ago in the minor merger of a $\sim 3.2 \times 10^9 M_\odot$ satellite whose core eventually coalesced with the M 31 disc. This minor merger, however, does not predict the formation of any other substructure marked in Figure 1.6, including the N and G1 clumps.

Deep small pencil-beam photometric observations with the *Hubble Space Telescope* (HST) of some of the M 31 substructures (Figure 1.7) were carried out by Richardson et al. (2008) in order to map the stellar populations in these substructures. They utilised colour-magnitude diagrams (CMDs) to find that the stellar populations in their fields in the W and NE shelves were similar to that of the Giant Stream, hence all termed stream-like fields (square-marked in Figure 1.7), while the stellar populations in their fields in the N and G1 clumps were similar to that of the inner M 31 disc, hence all termed disc-like fields (cross-marked in Figure 1.7). The field in the outer disc (and a few-others) had a stellar population that is a composite between that of the Giant Stream and the inner disc (triangle-marked in Figure 1.7). Bernard et al. (2015) studied the star formation histories (SFHs) of the stellar populations in the HST fields observed by Richardson et al. (2008). They found a ubiquitous burst of star formation ~2 Gyr ago in these fields (Figure 1.7) for each of the substructures and the M 31 disc. The burst was more prominent with a larger percentage of younger stars in the disc-like fields than in the stream-like fields. A higher percentage of stars older than 5 Gyr were present in the stream-like fields in M 31.

However, the properties of the stellar population of a single small field are not necessarily representative of the average stellar population of a substructure (Williams et al. 2017). An example of this is the giant stream which has been found to show a metallicity gradient (Conn et al. 2016) which can not be captured by the small HST pointings utilised by Richardson et al. (2008). The Pan-Hubble Andromeda Treasury (PHAT; Dalcanton et al. 2012) covered about a third of the M 31 disc out to ~20 kpc with HST observations. The SFH of the M 31 inner disc thus obtained showed that there was indeed a ~2 Gyr old burst of star formation in M 31 (Williams et al. 2017), bolstering the ubiquity of the burst of star formation in M 31 found by Bernard et al. (2015). Had the giant-stream formed in a ~1 Gyr old minor merger in M 31, as postulated by Fardal et al. (2013), it would not be associated with the event that triggered the

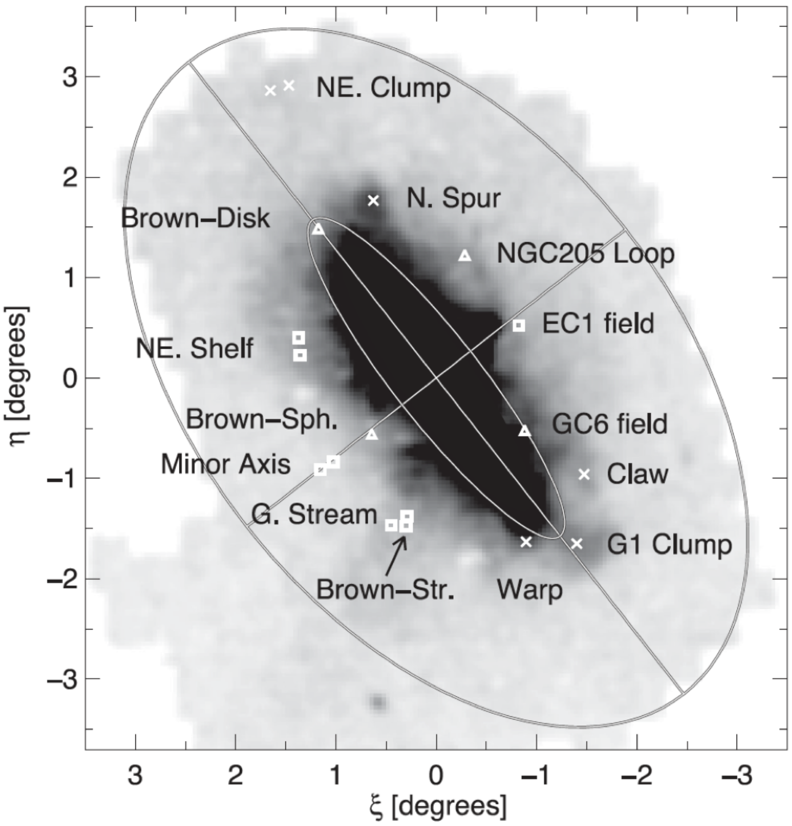

Figure 1.7: The locations of the HST pencil-beam pointings from Richardson et al. (2008), as studied by Bernard et al. (2015). The cross marks are disc-like fields while the square marks are stream-like fields. The triangle marks are composite fields. The pointings are superposed on the map of resolved stars from the INT survey by Irwin et al. (2005). Credit: Bernard et al. (2015)

burst of star-formation ~2 Gyr ago.

Hammer et al. (2018) carried out merger simulations with a massive satellite in M 31 (merger mass ratio = 1:4) in order to simultaneously explain the observed substructures, the high $\sigma_{\rm LOS}$ of the M 31 disc and the ~2 Gyr old burst of star formation. In these simulations, a massive satellite in-falls along the giant stream to the M 31 disc with orbital configurations similar to that of the minor-merger models by (Fardal et al. 2013). However, this satellite is gas-rich and massive which upon encountering the M 31 pre-merger disc, deposits much of its cold gas onto M 31. The pre-merger disc is perturbed by this satellite in multiple pericenter passages forming the M 31 thick disc. The Giant Stream, NE-Shelf and W-shelf are formed, as in the minor merger scenario, from the satellite debris but the N and G1 clumps are also formed from the perturbed disc. They predict that the cold gas deposited by the satellite is responsible for a burst of star-formation in the M 31 disc, leading to the inside-out formation of a distinct thin disc (yet to be observed) in M 31. The satellite eventually coalesces with the M 31 bulge. D’Souza & Bell (2018a) also support the major merger scenario in M 31 from comparison with similar galaxies in the Illustris simulations. However, they associate the nearby dwarf elliptical galaxy, M 32, as the possible remnant of the massive merged satellite.

The proposed merger scenarios in M 31 make distinct quantifiable predictions on the kinematics of the stellar population in the substructures and disc of M 31. The major merger scenario (Hammer et al. 2018) predicts the distinct thin and thick discs in M 31 while the minor merger would have no impact on the disc (Fardal et al. 2013). The predictions from the two scenarios are also different for the overdensities in the M 31 inner halo regions with most substructures formed in the same accretion event in the case of a major merger while only the Giant Stream, NE and W shelves are formed in the minor merger with other substructures formed in separate mini merger events. Their global stellar population properties will be different depending on their origin from either a massive satellite, perturbed disc debris or a small satellite. The line-of-sight velocities (LOSV) of the stars in the substructures will also be tell-tale signs of their originating event by constraining the orbital parameters of in-falling satellites.

However, this is an observational challenge also in the M 31 halo because it is spread over ~100 sq. deg. on the sky, with MW stars overlapping in space, velocity and colors with those of M31. The SPLASH survey (Guhathakurta et al. 2005) acquired sparse, pencil-beam spectra of RGB stars in 50 fields scattered across the entire M31 halo (out to 130 kpc) but covered only a small fraction (3×10^{-3}) of the entire halo area and required tackling contamination (from MW halo stars of similar colour and velocities) and completeness issues. The difficulty is further enhanced by the significant time required to obtain LOSVs for RGB stars through absorption spectra at the distance of M 31 (> 200 nights for the SPLASH survey).

1.2.2 The structure of the M 31 disc

Concurrently, being the nearest giant spiral galaxy, M 31 has also long been a subject of study in order to understand the properties of the discs of spiral galaxies. While the MW discs can be studied in great detail with many tracers, our vantage point in the MW disc implies that only a section of the MW may be observed accurately and precise distance measurements are difficult to obtain. In external galaxies all stars can be presumed to be in approximately the same distance and also allowing for mapping of radial variation in properties. This is especially true for M 31 whose properties have long been observed with different stellar tracers due to its proximity. Competing theories of formation of thin and thick disc evolution in spiral galaxies persist with some (e.g. Bovy et al. 2012) implying thick discs simply evolve from thin discs with dynamical heating from secular evolution while others (e.g. Comerón et al. 2019) argue that thin and thick discs may be separately formed in distinct events. M 31 is an essential laboratory to test for presence of thin and thick discs in spiral galaxies as such discs have only been studied in detail in the MW (Bland-Hawthorn & Gerhard 2016) and distant edge-on galaxies (Yoachim & Dalcanton 2006; Comerón et al. 2019) with limited potential for detailed observations.

While long considered to harbour a typical galaxy disc (e.g. Wyse & Mayall 1942; Arp 1964; Rubin & Ford 1970), deep observations of the HI gas in the M 31 disc showed peculiar warps in the disc structure (Chemin et al. 2009). To possibly understand the origin of these warps and relate it to the accretion events that formed the substructures, line-of-sight velocity measurements of the resolved stellar population were attempted by (Dorman et al. 2015) as part of SPLASH survey (Guhathakurta et al. 2005). They found that the M 31 disc, with a velocity dispersion, $\sigma_{\mathrm{LOS}} \sim 90$ km s^{-1}, for ~4 Gyr old RGB stars, is significantly dynamically hotter than even the thick disc of the MW with $\sigma_{\mathrm{U}} \sim 35$ km s^{-1} (comparable measurement value to the $\sigma_{\mathrm{LOS,M31}}$; Nordström et al. 2004). Its disc velocity dispersion thus stands in contrast to that of the MW, but presence of distinct thin and thick discs in M 31, as in the MW, have not been observed. The LOSV measurements from Dorman et al. (2015) using resolved stars relies on candidates selected photometrically from the CMD of PHAT stars (Dalcanton et al. 2012). The age of these candidates are assigned from their position in the CMD which can be greatly affected by reddening. Hence, the age-velocity dispersion relation they obtain is from stars whose classification in different age bins suffered from ambiguity. Furthermore, their observations were also limited to the PHAT survey footprint, covering only about a quarter of the M31 disc along its major axis out to $\mathrm{R_{GC}} \sim 18$ kpc.

The chemical abundance measurements for these resolved stars also needs to be carried out through absorption-line spectroscopy requiring ~6 hours for even a small pencil-beam field ($16' \times 4'$ for Deimos@Keck; Escala et al. 2020) and is not scalable to the entire M 31 disc with current instrumentation. Hence no distinct thin disc is detected from observations of resolved stars. Saglia et al. (2018) used Integral Field Unit (IFU) spectroscopy to observe the central ~5 kpc in M 31, with the bulge and bar, and some fields in the disc out to ~ 15 kpc. They measured simultaneously the kinematics and chemistry of the central region in M 31, successfully measuring the distinct stellar populations in the M 31 bar and bulge. However, just covering these central regions required 221 fields with ~ 90 hours of total observation time using the VIRUS-W spectrograph at the McDonald Observatory. However, measurement of the LOSV of the tracers in the M31 disc is required to assess the presence of discrete discs in M 31.

1.2.3 Discrete tracers in M 31

Thus, the measurement of LOSVs of the stellar population in the disc and substructures of M 31 is timely to set constraints on the structure of the M 31 disc, to assess the presence of thin and thick discs, and possibly rule out models on the basis of their predictions. Discrete tracers that firmly represent the M 31 stellar population, whose LOSVs can be measured with reasonable time, are thus feasible candidates to obtain the LOSV map of the M 31 disc, halo and substructures. Globular clusters (GCs) are one such candidate discrete tracers. GCs are compact, mostly old, bright stellar clusters that are formed during the early evolution of galaxies. However, the GCs do not necessarily represent the complete kinematic characteristics of the underlying stellar population and cosmological models including GCs and their relation to the hosting galaxy are still under development (E-Mosaics models- Pfeffer et al. 2018). In M 31, the GCs in fact do not trace many of the brightest substructures (e.g. Giant Stream; Huxor et al. 2014; Veljanoski et al. 2014a) and thus do not provide sufficient observable constraints to completely understand the recent formation history of M 31. Planetary Nebulae (PNe), on the other hand, are known to be one of the brightest and ubiquitous discrete tracers of light, kinematics and chemistry of stellar populations in nearby galaxies.

PNe are emission-line nebulae in the late phase of stellar evolution. At any give time, a fraction of the stars with initial masses between ~ 0.7 and 8 $\mathrm{M}_{\odot}$in a galaxy are going through the

Figure 1.8: [Left] Abell 39 is a PN in the MW having a spherical morphology. It consists of an expanding spherical shell of shock-heated material ionised by the hot central star of the PN which eventually cools to form the white dwarf. Only ~3% of MW PN have such a spherical morphology. [Right three panes] Three MW PN with varied non-spherical morphologies which consist of a more complexly shaped expanding shell but are still ionised by a central star. Credit: Wenger et al. (2012), H. Bond (STScI), B. Balick (Univ. Washington) and NASA

PN phase. PN properties may thus be linked to that of their parent stellar population PNe with PN kinematics and chemical abundances in particular being the discrete sampling of the kinematics and chemistry of their parent stellar population. PN properties have been successfully utilised to measure a number of properties of their parent galaxy like distances (e.g. Ciardullo et al. 1989), chemical abundance gradients (e.g. Magrini et al. 2009), kinematics (e.g. Pulsoni et al. 2018) and fraction of intra-cluster light (ICL; e.g. Longobardi et al. 2015). In the subsequent section, we describe PNe and their suitability as discrete tracers in M 31.

1.3 Planetary Nebulae as discrete tracers of galaxy stellar populations

1.3.1 The structure and evolution of planetary nebulae

PNe are stars in the late stages of stellar evolution that have recently left the asymptotic giant branch (AGB) and are evolving towards the white dwarf stage. They have a bright envelope of gas and dust ejected in the AGB phase that is ionised by the central hot white dwarf (Figure 1.8). PNe are traditionally considered to evolve from single stars with masses between ~ 0.7 and 8 $M_\odot$, but have been shown to exhibit a wide variety of striking morphologies (Figure 1.8) having a complex system of dusty gas and shells possibly pointing towards a common envelope binary evolution in many systems (Jones & Boffin 2017).

Modelling efforts of PN typically focus on the evolution of the central star in the AGB phase and the expansion of a spherical nebular shell (Vassiliadis & Wood 1994; Miller Bertolami 2016, e.g.). Figure 1.9 shows the evolution of a single star with initial mass of 2 $M_\odot$ from the AGB to a white dwarf, via the PN stage. AGB stars have a degenerate carbon-oxygen core surrounded by helium-fusion shell, in turn surrounded by a thinner hydrogen-fusion shell and a convective hydrogen-rich envelope. Following an early helium burning stage, the AGB star enter a

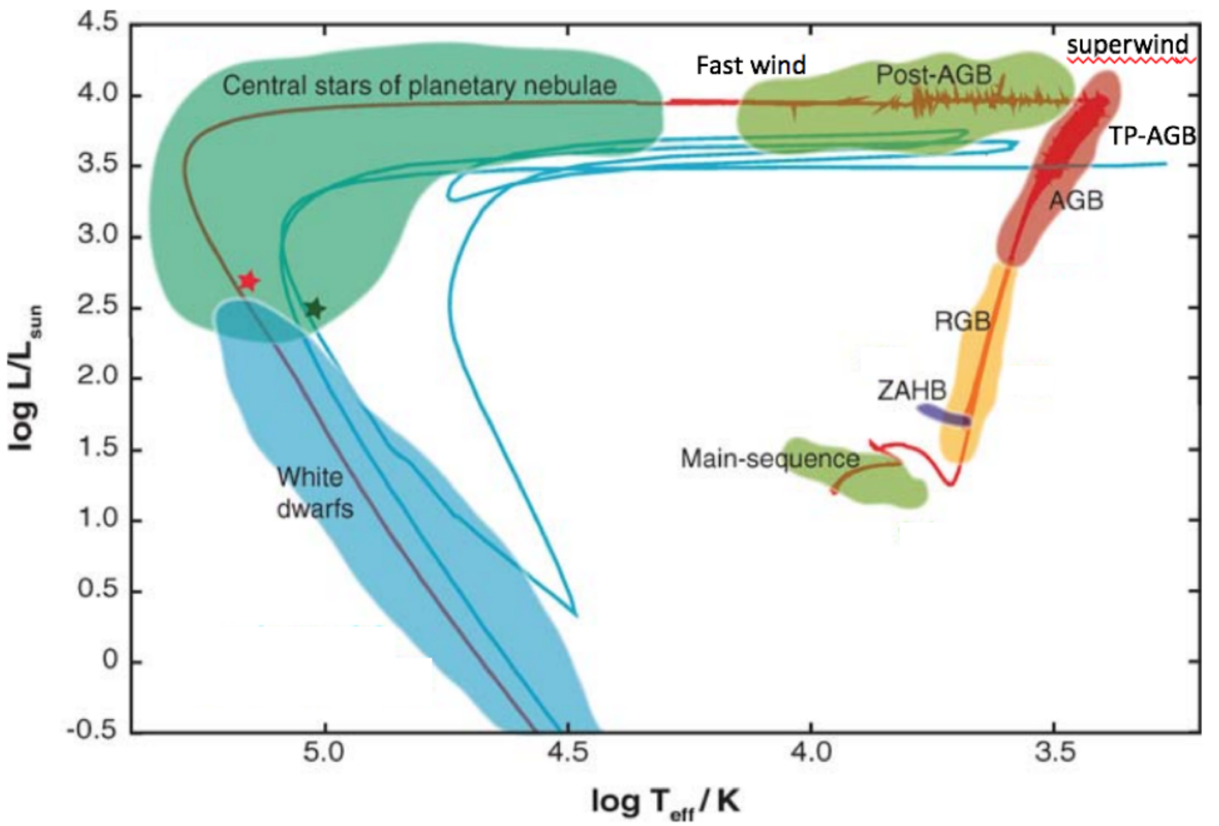

Figure 1.9: The Hertzsprung-Russel (HR) diagram showing the evolution of intermediate-mass stars from the main-sequence to the white-dwarf stage through the RGB, AGB, post-AGB and PN stages. This figure and details of the process are provided by Herwig (2005).

thermally-pulsating (TP-AGB) phase, where mass-loss occurs with the luminosity of the star changing periodically due to consecutive He and H shell burnings.

Towards the end of the AGB phase, a high density superwind (10–20 km s^{-1}) is released, expanding slowly and ejecting mass in the stellar H envelope. In this post-AGB phase, the mass in the stellar H envelope eventually decreases to the extent that a fully developed convection zone can no longer be sustained and the envelope shrinks, eventually becoming radiative. The star's luminosity, determined by the ongoing shell fusion around the degenerate stellar core, remains nearly constant. The temperature of the central star increases to ~30000 K while the radius of the circumstellar envelope decreases to ~3 R$_{\odot}$. A fast (~1000 km s^{-1}) stellar wind is developed in this stage from the central star which produces a shock-heated shell from the AGB-star ejecta.

This shell is then photo-ionised from the ultraviolet radiation (UV) of the central star, producing a spectra (Figure 1.10) with characteristic collisionally-excited lines (CELs), [OIII] 5007 Å being the strongest line, and some recombination lines. Eventually, the PN shell expands and the ionising white dwarf become cooler, such that the PN becomes less luminous till the extent where the PN shell has been lost. This visibility lifetime of a typical PN can vary between 1000 and 30000 years (Buzzoni et al. 2006). See review by Herwig (2005) for details of AGB and

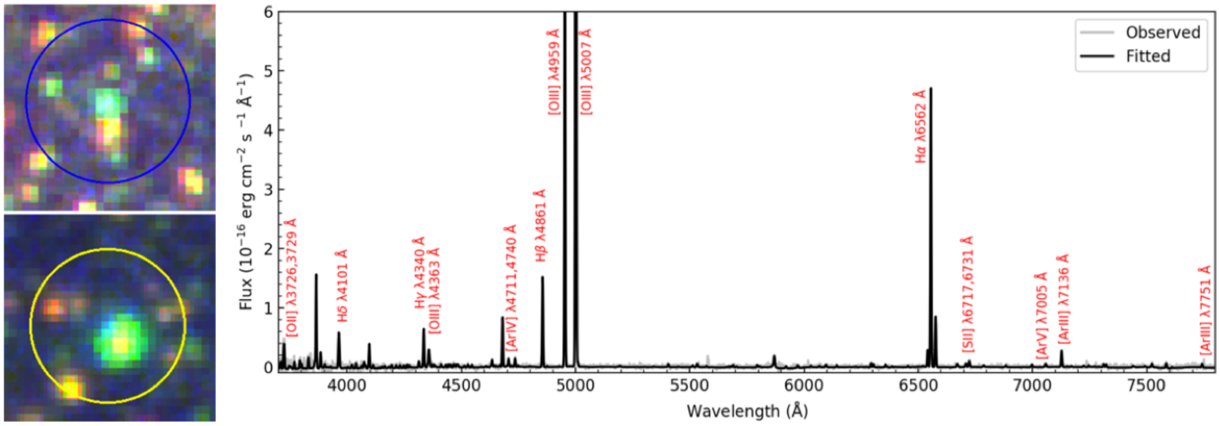

Figure 1.10: [Left] Point-like PNe observed in M 31 from HST observations. The circles represent 0.5 arcmin. [Right] Spectra of a PN observed in M 31, showing the brightest lines.

post-AGB evolution. The timescales of these processes and their effect on surface chemistry has been modelled by Miller Bertolami (2016).

1.3.2 Extragalactic planetary nebulae

The spatial diameter of any PNe observed in the MW is well below 1 pc, being on average ~ 0.3 pc in the MW bulge (e.g. Acker et al. 1992; Frew et al. 2013). Thus at extragalactic distances, PNe appear as point-sources (Figure 1.10), specifically in M 31 a 0.3 pc PN would span $0.08''$ on sky, much lower than the angular resolution of current instrumentation. While their morphology can not be resolved, the spectra of extragalactic PN show the same brightest lines as those in the MW PNe, including the bright [OIII] 5007 Å line. PNe are detected in photometric observations of galaxies with narrow-band filters (on-filter) centred on the [OIII] 5007 Å line but not detected with broad-band filters (off-filter) owing to their absence of continuum emission. An automatic selection procedure to detect PNe using this on-off technique was developed and validated in Arnaboldi et al. (2002, 2003), further optimised for large imaging surveys by Longobardi et al. (2013) and Hartke et al. (2017).

At any time in a galaxy a fraction of the stars in the ~ 0.7 and 8 $M_\odot$ initial mass range are going through the PN phase. Thus, PN population properties can be connected to the properties of the parent stellar population, except for the youngest most massive stars with initial mass more than $8M_\odot$. This covers the entire stellar population of a galaxy with ages between $\sim$100 Myr to $\sim$11 Gyr. PN population properties and their connection to their parent stellar population are described in the following subsections.

PN luminosity function (PNLF)

The characteristic [O III] 5007Å (M_{5007}) PN luminosity function (PNLF, see Figure 1.11) was first described by Ciardullo et al. (1989). Their analytical formula is as follows:

$$N(M) \propto e^{0.307M}(1 - e^{3(M^{*}-M)}) \tag{1.1}$$

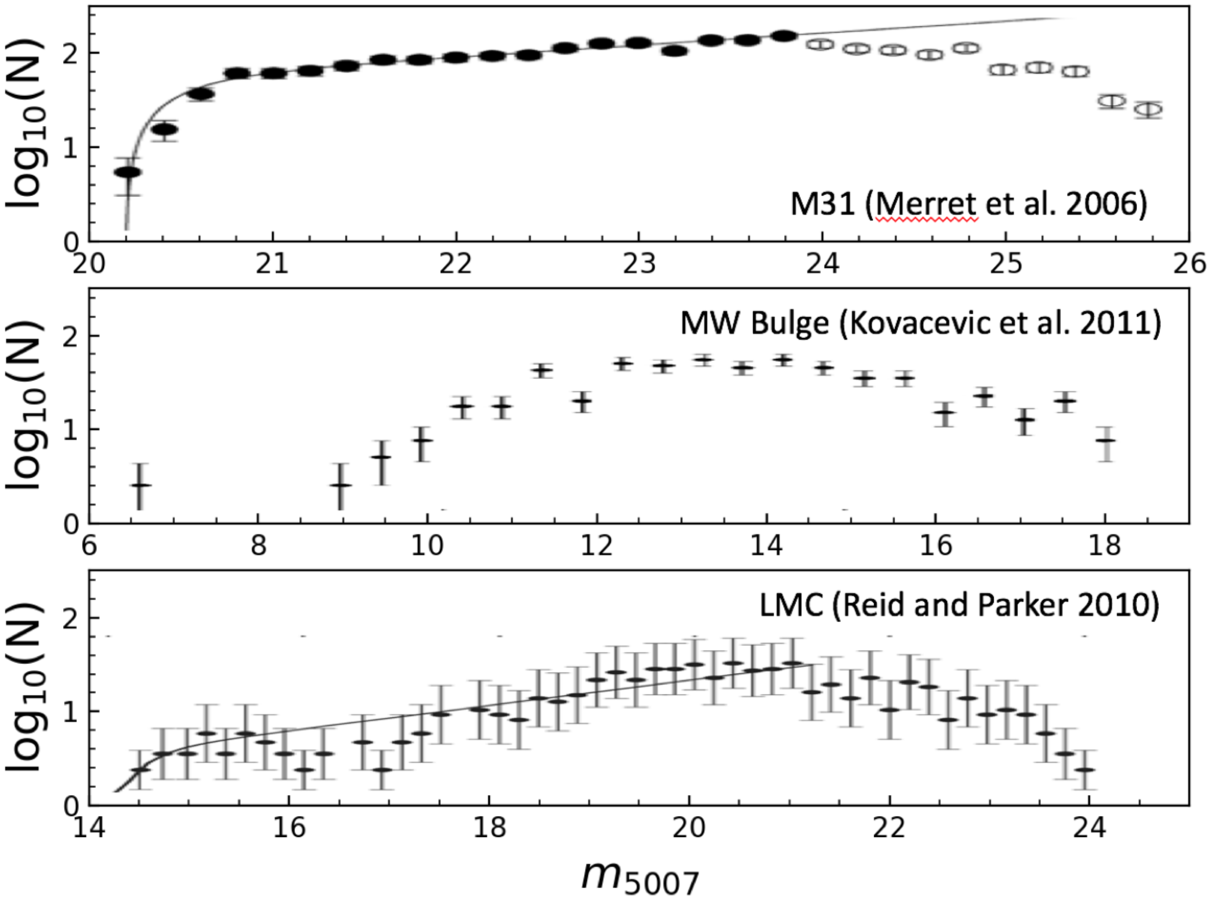

Figure 1.11: [Top] The PNLF of the M31 disc and bulge from Merrett et al. (2006). [Middle] The PNLF of the MW bulge PNe at an assumed distance of 8 kpc (Kovacevic et al. 2011). [Bottom] The PNLF of the LMC (Reid & Parker 2010). Note the apparent magnitude scales of each panel is different. The analytical PNLF function by Ciardullo et al. (1989) is fitted to the M31 and LMC PNLFs.

The PNLF is theoretically expected to follow an exponential function (Jacoby 1980) describing the slow evolution of the PN central star embedded in rapidly expanding, optically thin nebula (Henize & Westerlund 1963). A PN evolving from a SSP is expected to be at the absolute bright cut-off, M^*, at the start of its evolution and its nebula would fade till ~8 mag before dissipating completely (Buzzoni et al. 2006). By virtue of its observed invariant absolute bright cut-off currently measured at $M^* = -4.54 \pm 0.05$ at near-solar metallicities (see Ciardullo et al. 2013, and references therein), the PNLF is a reliable secondary distance indicator for determining galactic distances out to ~20 Mpc. While M^* gets fainter in low metallicity populations (e.g. Ciardullo & Jacoby 1992; Ciardullo et al. 2002; Hernández-Martínez & Peña 2009) according to theoretical predictions by Dopita et al. (1992), it seems to be invariant with both the age of the stellar population or galaxy morphological type (Ciardullo et al. 2013).

The invariant nature of the absolute bright cut-off of the PNLF has been a subject of various theoretical studies (e.g. Marigo et al. 2004; Gesicki et al. 2018) but the reason for the invariance is not yet confirmed. While Gesicki et al. (2018) find that the latest post-AGB evolution models by Miller Bertolami (2016) do show that M^* varies negligibly with age for stellar populations younger than 6 Gyr, Davis et al. (2018) have shown that the age of the stellar population in the bulge of M 31 is greatly underpredicted by these models. Close binary stars having undergone common envelope evolution while evolving as blue-straggler stars have been suggested as a possible candidate for the PNe at the bright cut-off of the PNLF (Ciardullo et al. 2005). In such a scenario, a companion star transfers its mass to the pre-PN star, either completely fusing or remaining in a close-binary system. The pre-PN star, now with increased accreted mass and appearing as a blue straggler in the HR diagram, then goes through the PN evolution mimicking the properties of a star with higher initial mass. This scenario in fact explains the varied morphologies of PNe observed in the MW (Jones & Boffin 2017) but predicts large numbers of PNe in globular clusters, where large numbers of blue stragglers are found (Ciardullo et al. 2005). Such high numbers of PNe have not been found in globular clusters of the MW (Jacoby et al. 2017) and M31 (Jacoby et al. 2013) where 4 and 3 PN have been respectively identified, commensurate with the expected numbers of PNe from stellar population models with single stellar evolution. Thus, tension still persists in the nature of the PNe at the bright cut-off of galaxies.

The relation of the faint end of the PNLF with its parent stellar population remains even more elusive with theoretical studies requiring more observational constraints to the faint end of the PNLF (Gesicki et al. 2018). While initial studies attributed a constant slope to the PNLF (Ciardullo et al. 1989), later studies have found it to vary especially for elliptical galaxies with older stellar populations. To account for this, the generalised analytical formula for the PNLF was introduced by Longobardi et al. (2013) as follows:

$$N(M) = c_1 e^{c_2 M}(1 - e^{3(M^* - M)}) \tag{1.2}$$

where c_1 is a normalisation constant and c_2 is the slope at the faint end. The aforementioned Ciardullo et al. (1989) analytical LF is then a specific case of the generalised analytical formula with $c_2 = 0.307$ that reproduces their best fit to the PNLF of the M31 bulge. Observations suggest that the slope described by the parameter c_2 is correlated with the star formation history(SFH) of the parent stellar population (Ciardullo et al. 2004; Ciardullo 2010; Rodríguez-González et al. 2015).

Both the nature of the bright cut-off of the PNLF and its faint-end may simply be understood from observation of the MW PNLF. This has however not been possible since the absolute magnitude of most MW PNe are elusive as the distance to MW PNe are difficult to measure. When distances may be approximated, such as for the MW bulge at $\sim$ 8 kpc, the PNLF obtained is still rife with incompleteness issues such that the MW PNLF shape (Figure 1.11) has little resemblance with that of other galaxies (Kovacevic et al. 2011). Thus, the shape of the PNLF is best constrained from observations of Local Group galaxies where the PNe can be detected to magnitudes well below the bright-cutoff in reasonable time.

Reid & Parker (2010) detect PNe down to $\sim$10 mag below M^* in the Large Magellanic Clouds (LMC) with 90% completeness at $\sim$ 6 mag below M^* (Figure 1.11). While the PNLF follows the analytical function described by (Ciardullo et al. 1989), it shows a characteristic dip at ~2.5 mag below M^* after which it shows a steeper rise. Even more pronounced dips have been observed in other local group galaxies like the Small Magellanic Clouds (SMC; Jacoby & De Marco 2002) and NGC 6822 (Hernández-Martínez & Peña 2009). However, there is further theoretical tension regarding the age of the PNe that occupy different magnitude ranges of the PNLF and exhibit such shapes. In the post-AGB stellar evolution models by Marigo et al. (2004), the faint-end of the PNLF is populated by PNe evolving from older stellar populations and powered by less-massive central stars (see their Figures 18 & 25 and associated text). This is in contrast to the predictions by Méndez et al. (2008) where the faint-end of the PNLF is populated by PNe from massive progenitor stars from young stellar populations which have faded rapidly while losing their envelope. Further observational constraints are required to understand the nature of the PNLF and its relation to the post-AGB evolution of its parent stellar population.

PN luminosity-specific frequency (α-parameter)

The PN luminosity-specific frequency (α-parameter; Jacoby 1980) provides the number of PNe expected per unit bolometric light. It is the ratio of the total number of PNe, $N_{\rm PN}$, to the total bolometric luminosity of the parent stellar population, $L_{\rm bol}$, given by

$$\alpha = \frac{N_{\rm PN}}{L_{\rm bol}} = B\tau_{\rm PN} \tag{1.3}$$

where B is the specific evolutionary flux (stars yrs^{-1} L$_\odot^{-1}$), which is defined as the rate of stars in a single-stellar population (SSP) leaving the main-sequence towards the post-main-sequence evolutionary stages normalised by the unit of light, and $\tau_{\rm PN}$ is the PN visibility lifetime (Buzzoni et al. 2006). In practice, the PN population observed in a galaxy is magnitude-limited such that within a given magnitude range δm below the PNLF bright cut-off, the $\alpha_{\delta \rm m}$ is measured. This is then converted to α following conversion factors calculated by Buzzoni et al. (2006) using synthetic PN population models from SSP. It is to be noted that if multiple stellar populations are present in the same overlapping spatial region, they would have distinct α-parameter values. An example of this is seen by Longobardi et al. (2013) who found that the α-parameter for the M87 stellar population is about a third of that of the intra-cluster light (ICL) in the Virgo cluster.

PNe as kinematic tracers

The strong [OIII] emission from PNe allows for reliable LOSV measurements from spectroscopic observations with much lower exposure times compared to that of RGB stars at the same distance. This makes PNe as valuable kinematic tracers which provide a discrete sampling of the velocity phase space of a galaxy's entire stellar population. PNe have been used successfully to trace the kinematics of different galaxy types including surveys of elliptical galaxies (e.g. Hui et al. 1995; Arnaboldi et al. 1996, 1998; Coccato et al. 2009; Pulsoni et al. 2018), and many spiral galaxies (e.g. Ciardullo et al. 2004; Herrmann et al. 2008; Aniyan et al. 2018). PN kinematics have been shown to be in good agreement with kinematic measurements from absorption-line studies and IFU measurements in the region of overlap (e.g. Coccato et al. 2009; Aniyan et al. 2018). PN kinematics can also distinguish overlapping stellar populations like those of a substructure on the main luminous body of a galaxy (e.g. M87 and its crown substructure-Longobardi et al. 2015), the dissolving stellar population of a dwarf galaxy and the larger host

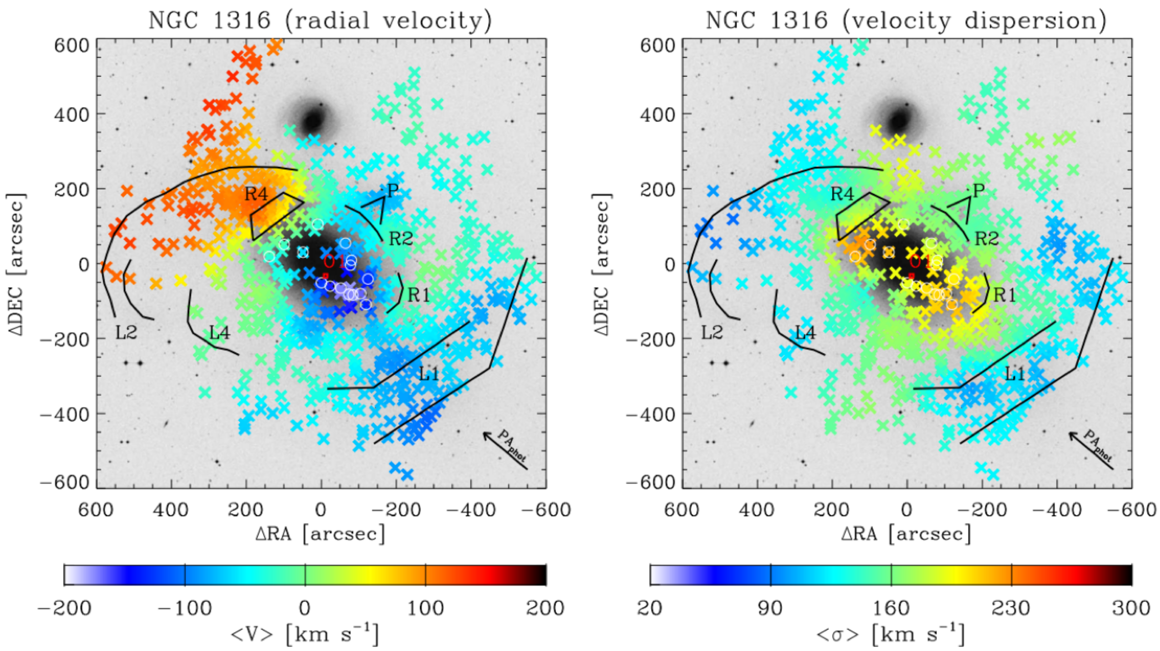

Figure 1.12: Smoothed velocity field [Left] and velocity dispersion field [Right] from PNe as kinematic tracers in NGC 1316 shown on the DSS image. The circles highlight the PNe belonging to a structure identified in the phase space, co-spatial with the bright luminous body of the galaxy. The black contours trace substructure identified from low-surface brightness imaging. Credit: Pulsoni et al. (2018)

elliptical (e.g. M49 and its dwarf- Hartke et al. 2018), and the dynamically hot and cold discs of a face-on spiral galaxy (e.g. NGC628- Aniyan et al. 2018). Figure 1.12 shows the smoothed velocity and velocity dispersion field of NGC 1316, an elliptical galaxy, whose substructures are identified from PNe kinematics by Pulsoni et al. (2018).

PNe as tracers of chemistry

As stars are formed in galaxies, they reflect the metallicity of the gas in the inter-stellar medium (ISM) from which they were formed. Direct determination of the present-day (< 0.5 Gyr) ISM condition is possible from spectroscopic observations of HII regions[2], which are emission line-objects and the abundances of certain elements, typically oxygen, can be measured from their spectra. To understand the processes dictating chemical evolution of galaxies, it is important to obtain the metallicity of stars of different ages which reflect the ISM conditions at the time of birth. Determination of stellar metallicity is indirectly possible from isochrone fitting of CMDs but requires assumptions on the age and [α/Fe] content of galaxy populations in the fitted isochrone models (e.g Bernard et al. 2015; Williams et al. 2017). Indirect measurements of metallicity are also possible from IFU measurements but even here the age-metallicity degener-

---

[2] A gas-cloud partially ionized by OB stars where recent star formation has occurred. Typical H II regions have sizes larger than 50 pc but can be even larger than a kpc.

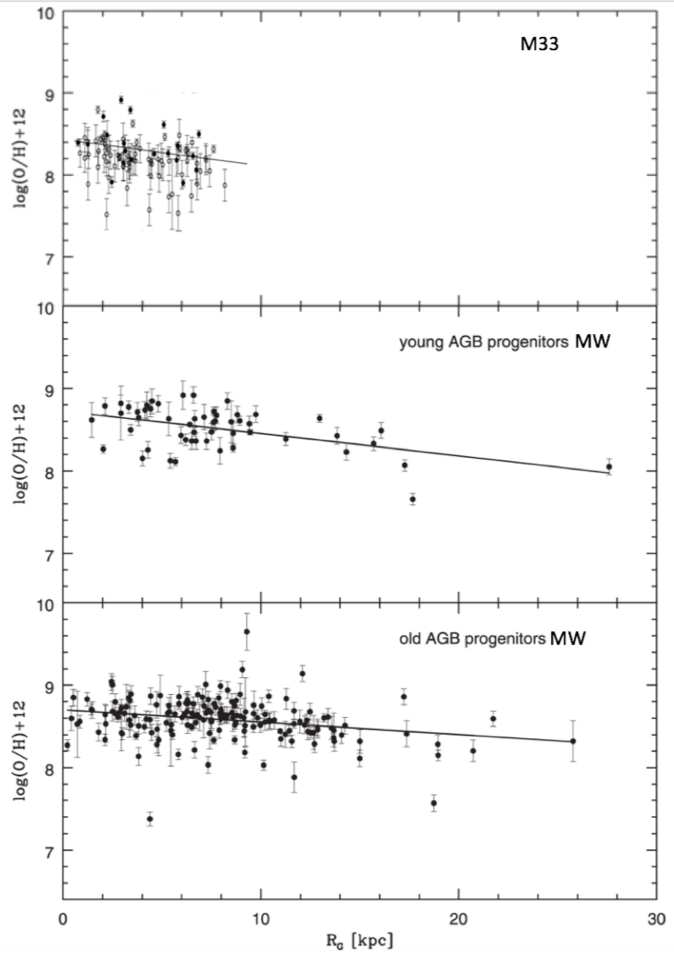

Figure 1.13: Oxygen abundances, 12+(O/H), are plotted against galactocentric radius for [Top] all PNe in M33 (Magrini et al. 2009), [Middle] PNe with progenitors younger than 7 Gyr in the MW thin disc and [Bottom] PNe with progenitors older than 7 Gyr in the MW thick disc (Stanghellini & Haywood 2018). The black lines show their fitted radial abundance gradients.

acy needs to be overcome and thus requires the fitting of SSP models (e.g. Wilkinson et al. 2015). Direct abundance measurements of various elements are possible from spectroscopy of individual stars in any galaxy. However, such observations are very time-intensive for large distances beyond the MW, even more so than that for determining LOSV from spectra.

The abundances of certain elements measured from the spectroscopy of PNe reflect the ISM metallicity conditions at the time of birth of the PNe progenitor (Osterbrock & Ferland 2006). Elements like oxygen[3], argon, chlorine, etc. are minimally affected by the AGB evolution and thus consistent with initial ISM conditions (Stanghellini & Haywood 2018). Hence, PNe of different ages allow for the direct measurements of the chemical evolution of galaxies (e.g. Magrini et al.

---

[3] Some evidence of oxygen enhancement and depletion has been found in marginal amounts in MW PNe (Delgado-Inglada et al. 2015)

2016). Deep spectral observations allow for determination of abundances of multiple elements in MW PNe but such deep spectra become very time intensive for PNe in other galaxies. For extragalactic PNe, the elemental abundances are typically limited by observations of the temperature sensitive [OIII] 4363 Å line, the brightest temperature sensitive line, and extinction corrections from the ratio of the Hβ and Hα lines with electron densities typically determined from the [OII] or [SII] doublets (Osterbrock & Ferland 2006).

PN abundances have been measured in the MW, Local Group galaxies like M33 (Magrini et al. 2009), M31 (Sanders et al. 2012), other Local Group dwarf galaxies (see Gonçalves 2019, and references therein), and outside the local group only in the spiral galaxy M 81 at ~3.5 Mpc from the MW (Stanghellini et al. 2014). In NGC 6822 (Hernández-Martínez et al. 2011), M33 (Magrini et al. 2009) and M81 (Stanghellini et al. 2014), PNe oxygen abundances have been compared to that for HII regions to provide evidence for the chemical evolution of galaxies. For disc galaxies, this is possible through the comparison of radial metallicity gradient values (Aller 1942) obtained from PNe (Figure 1.13) and HII regions (Magrini et al. 2016). In an inside-out build-up scenario of a galaxy disc, negative radial metallicity gradients are expected (e.g. Sánchez-Menguiano et al. 2018). Hydrodynamical simulations have shown that the radial metallicity gradient in galaxies is modified both in case of secular evolution (e.g. Gibson et al. 2013) and also in the case of galaxy mergers (e.g. Zinchenko et al. 2015; Tissera et al. 2019). In the MW, the radial metallicity gradient for both thin and thick disc PN formed at different epochs (Figure 1.13) have been obtained separately allowing for significant constraints on its chemical evolution (Stanghellini & Haywood 2018). However, for other galaxies, distinct radial metallicity gradient measurements from spatially overlapping PN populations formed at different epochs have so far had little success (e.g. Peña & Flores-Durán 2019).

1.3.3 Planetary Nebulae in M 31

M31 has a long history of PN observations which have simultaneously provided insight on PN population properties and the formation history of M 31. The PNLF was first calibrated by Ciardullo et al. (1989) with observations of a PN sample in the bulge of M 31. The current largest survey of M 31 PNe was carried out by Merrett et al. (2006) finding 2615 PNe covering its bulge and disc out to a galactocentric radius, $R_{GC} \sim 25$ kpc. They had simultaneously obtained photometry and LOSV for these PNe using the purpose-built Planetary Nebula Spectrograph (PN.S Douglas et al. 2002) at the William Herschel Telescope (WHT). They corroborated the PNLF shape down to ~3.5–4 mag below the bright cut-off (Figure 1.11). They also found an extension of the Giant Stream on the M31 disc from PN kinematics (Merrett et al. 2003), finding constraints on the infall path of a possible merging satellite, later matched in simulations by Fardal et al. (2006). Spectroscopic follow-up of some of the PNe identified by Merrett et al. (2006) were carried out by Sanders et al. (2012) who obtained the oxygen abundance measurements of 51 PNe, thereby finding the radial metallicity gradient of the M31 disc with PNe. They found a characteristically flat radial metallicity gradient, later supported by other studies (Kwitter et al. 2012; Fang et al. 2018; Peña & Flores-Durán 2019). A steepening of the radial metallicity gradient over time from older PNe to younger HII regions was found by Sanders et al. (2012) but was attributed to radial migration rather than secular chemical evolution by Magrini et al. (2016).

Finally, from fitting observed spectral lines of a small sample of PNe with synthetic models of photoionised nebulae with CLOUDY (Ferland et al. 1998), Ciardullo & Jacoby (1999) suggested a linear relation between PNe circumstellar extinction and their core masses. This was corroborated later by Kwitter et al. (2012) but also from observations of a small sample of PNe in M 31. While such a relation may be theoretically explained from the dust production of AGB stars being linear with initial mass in the 1–2.5 $M_\odot$ range (Ventura et al. 2014), it has not been observed for PNe in other galaxies nor corroborated with other methods.

1.4 This thesis

The aim of this thesis is to carry out a survey of PNe in the disc and inner halo of M 31. Pne are bonafide tracers of the stellar populations in M31 because the apparent bright cut-off of the M 31 PNLF is fainter than the faintest PNe in the MW (Figure 1.11). Thus there is no contamination from MW PNe in the area covered by M31 on the sky. Another source of contamination in detecting PNe are Lyman-α galaxies at redshift ~3.14 which masquerade as PNe in [OIII] filters. However, they only appear at $m_{5007} \sim 26.5$ mag (Longobardi et al. 2013), ~6.5 mag below the bright cut-off for M 31. Thus any PNe candidates detected in M 31 down to ~6.5 mag below the bright cut-off would be discrete tracers firmly in the M 31 system.

The PNLF in M 31 can be detected down to considerable depth allowing for improved understanding of its faint-end and its relation to post-AGB evolution of its parent stellar population. With the large number of PNe expected for the luminous M 31, additional PN population properties may be uncovered with good number statistics, which was previously possible only for MW PNe. The PNLF in the different substructures and disc in M 31 reflects their stellar population properties like age and metallicity and thus can be utilised to measure differences between these substructures.

As found by Merrett et al. (2006), PNe are discrete tracers of disc kinematics in M 31 which with a large sample may be utilised to assess the structure of the disc. Furthermore, they can be used to identify kinematically distinct substructures even when streams are overlapping with the more luminous disc. Additionally, since PNe are also chemical tracers, their abundance measurements can provide insight on to the chemical evolution of M 31, both through radial metallicity gradient measurements of the disc and also through identification of chemically distinct substructure.

PNe thus provide insight on the stellar population properties like age and metallicity, exact measurements of LOSV and chemical abundances, with a large uniform coverage with the same tracer. Thus, any radial trends analysed in M 31 may be linked to its stellar population properties rather than to any selection biases in the tracers. These measurements are only feasible with PNe with current instrumentation.

The aims of the chapters in this thesis are as follows:

- Chapter 2: We carry out the survey of PNe in the central 16. sq. deg. of M 31 with the Megacam instrument at the Canada-France-Hawaii Telescope (CFHT). PNe are identified in the disc and some of the inner halo substructures in M 31 from narrow-band [OIII] and broad g-band images. The aim is to identify a firm sample of PNe, with minimal contamination from MW stars and background galaxies, down to ~6 mag below the M 31 PNLF bright cut-off. This will be the deepest PNLF in M 31 till date with uniform coverage allowing for studies of the faint-end of the PNLF.

- Chapter 3: Through a spectroscopic follow-up of a subsample of the PNe in the M 31 disc with the MMT, measurements of their LOSV and extinction are obtained. These are combined with the archival sample from Sanders et al. (2012). The aim is to identify distinct PN samples whose approximate ages can be determined through comparison of PN properties with stellar evolution tracks. The goal is to obtain the rotational velocities and corresponding velocity dispersion profiles from different PN samples and assess the presence of thin and thick discs in M 31. This will allow us to construct the age-velocity dispersion relation for the M31 disc which can provide insight into its formation history.
- Chapter 4: The photometric survey of PNe is extended to cover 54 sq. deg. in M 31 with PNe identified in six major inner-halo substructures – the Giant Stream, North East Shelf, G1-Clump, Northern Clump, Western Shelf and Stream D. The goal of this chapter is to characterise the average stellar populations in these large substructures by linking their stellar population properties with that of their PNLF properties.
- Chapter 5: The spectroscopic subsample of disc PNe is increased and the elemental abundances (oxygen and argon) of the PNe are measured. The goal of this chapter is to assess whether the thin and thick disk in M31 have different chemical properties and measure their abundance gradients.
- Chapter 6: The results of this work are discussed and conclusions are drawn on the formation history of M 31 and PN population properties. Future prospects are also discussed.

Chapter 2

Imaging the disc and halo with MegaCam at the CFHT

The contents of this chapter have been published in Bhattacharya et al. (2019a, Astronomy & Astrophysics, 624, A132)

2.1 Introduction

The Andromeda galaxy, M31, is the closest giant spiral disc to our Milky Way (MW). It lies at a distance of ∼ 780 kpc with a high inclination to the line of sight (i∼ 77 deg) making it ideally suited for studies of its halo regions. Since galaxies are believed to be formed by hierarchical mass assembly, their outskirts with long dynamical timescales are expected to have coherent debris from past accretion events for the greatest longevity (Ferguson & Mackey 2016). Through the Pan-Andromeda Archaeological Survey (PAndAS; McConnachie et al. 2009) map of the resolved stellar population number counts, we now know about the substructures present in the M31 halo (Giant Stellar Stream, G1 and NE clump, NE and W shelves; McConnachie et al. 2018) and that the stellar halo extends out to 165 kpc.

Because of the faint surface brightness of the M31 halo, $\mu_v > 25$ outside the main disc (∼ 15 kpc major-axis distance), the use of discrete stellar tracers is superior to integrated absorption-line spectroscopy in providing a global mapping of the halo kinematics. Globular clusters (GCs) have been shown to efficiently trace the outer halo (outside 50 kpc) substructures of M31 (Mackey et al. 2010; Veljanoski et al. 2014b) bolstering the idea that these clusters and the substructures they trace have been accreted in various merger events. However, the inner halo substructures (within 50 kpc) are not well traced by the GCs. Some of these substructures, especially the Giant Stream, may have resulted from a single merger event ∼ 2 Gyr ago (Bernard et al. 2015; Hammer et al. 2018) perhaps between M31 and the large ($M_{M32P} \sim 2.5 \times 10^{10}$ $M_{\odot}$) progenitor of M32 (D'Souza & Bell 2018a).

We can gain information on the motions of the stars in the low surface brightness regions of M31 by studying planetary nebulae (PNe) that act as discrete tracers of stars in the halo. PNe are the glowing shells of gas and dust observed around stars that have recently left the asymptotic giant branch (AGB) and are evolving towards the white dwarf stage. They are traditionally considered the late phases of stars with masses between ~ 0.7 and 8 $M_{\odot}$, but have been shown to exhibit a wide variety of striking morphologies pointing towards a binary evolution in many systems (Jones & Boffin 2017). Since the timescales between the AGB and PN phases are short, the distribution and kinematics of PNe are expected to be identical to their parent population, having the same angular momentum distribution as the stellar population (e.g. Hui et al. 1995; Arnaboldi et al. 1996, 1998; Méndez et al. 2001). Studying PNe as a population provides insight into galactic structure and evolution. Because of their relatively strong [O III] 5007Å emission, PNe can be readily identified. They have been shown to be efficient tracers of stellar light in different galaxies like M87 (Longobardi et al. 2013), M49 (Hartke et al. 2017), and many other early-type galaxies (Coccato et al. 2009; Cortesi et al. 2013; Pulsoni et al. 2018). The luminosity-specific PN number (α-parameter) varies slightly with B-V colour of galaxies with higher values for late-type galaxies and lower values for early-type galaxies (Buzzoni et al. 2006). Different α-parameter values point to differences in stellar populations even within the same galaxy (e.g. M49; Hartke et al. 2017).

The characteristic [O III] 5007Å PN luminosity function (PNLF) has proven itself to be a reliable secondary distance indicator for determining galactic distances out to ~20 Mpc by virtue of its invariant absolute bright cut-off, M*. The faint end of the PNLF was shown by Jacoby (1980) to follow an exponential function expected from slowly evolving central stars embedded in rapidly expanding, optically thin nebulae (Henize & Westerlund 1963). The PNLF was first described by Ciardullo et al. (1989) estimated empirically from the brightest PN they found in the centre of M31 as

$$N(M) \propto e^{0.307M}(1 - e^{3(M^{*}-M)}) \tag{2.1}$$

The bright end exponential cut-off, supported with accurate measures of foreground extinction, is currently measured at $M^{*} = -4.54 \pm 0.05$ mag (Ciardullo et al. 2013). Apart from M* reducing in low metallicity populations (e.g. Ciardullo & Jacoby 1992; Ciardullo et al. 2002; Hernández-Martínez & Peña 2009), the PNLF cut-off has proved to be largely invariant with metallicity and age of the parent stellar population, and galaxy type.

The faint end of the PNLF has been shown to vary considerably, depending on the details of the stellar population. It is seen to be correlated with the star formation history of the parent stellar population, with steeper slopes associated with older stellar populations and conversely flatter slopes with younger populations (Ciardullo et al. 2004; Ciardullo 2010; Longobardi et al. 2013; Hartke et al. 2017). The changes in the PNLF slope can result from the superposition of multiple stellar populations, which can then be disentangled using the PNe kinematics (Longobardi et al. 2015; Hartke et al. 2018). The PNLF has also been shown to display a dip for some galaxies. The dip is seen ~ 3.5 mag below the bright cut-off in the Small Magellanic Cloud (SMC; Jacoby & De Marco 2002), ~ 2.5 mag below the bright cut-off for NGC 6822 (Hernández-Martínez & Peña 2009) and also slightly in the Large Magellanic Clouds (Reid & Parker 2010), and ~ 1 mag below the bright cut-off in M87 (Longobardi et al. 2015). This dip is thought to be related to the opacity of the PN and may be characterised by accounting for circumstellar extinction in the PNe. Circumstellar extinction correction indeed modifies the PNLF (Reid & Parker 2010; Davis et al. 2018), but it is difficult to estimate for the faint end of the PNLF (beyond ~ 2.5 mag below the bright cut-off) to test for changes in opacity of the PN. Additionally, PNe mimics like H II regions and symbiotic stars (SySts) may be misidentified as PNe thereby affecting the PNLF.

Since the first empirical study of the PNLF by Ciardullo et al. (1989) using 104 objects in the M31 bulge, the number of PNe known in M31 has increased by leaps and bounds. Most notably, Merrett et al. (2006, hereafter M06) utilised the custom-built Planetary Nebula Spectrograph (PNS; Douglas et al. 2002) at the William Herschel Telescope (WHT) to identify 2615 PNe in the disc and bulge of M31, and to simultaneously obtain their [O III] 5007Å magnitude and line-of-sight velocity (LOSV). M06 corroborated the PNLF found by Ciardullo et al. (1989) and increased the photometric depth to $\sim$ 3.5 - 4 mag below the bright cut-off along with the increased uniform coverage. Since then, Martin et al. (2018) and Li et al. (2018) have identified more PNe in the central regions and circumnuclear region of M31, respectively, adding to the large number of PNe already known in M31.

While some of the PNe identified by M06 have been shown to be H II regions (Sanders et al. 2012; Veyette et al. 2014), the M06 PNe sample remains the largest uniform sample of PNe in any galaxy. The LOSV of the M06 PNe predicted links between the NE shelf and the giant stream substructures of M31 which have been further explored in deep spectroscopic chemical tagging studies by Fang et al. (2015, 2018) to further establish these links. However, while some identified PNe have been associated with the halo, a uniform survey of PNe in much of the metal-poor halo of M31 and the inner-halo substructures is necessary not only to unambiguously trace them, but also to probe the variation in the PNLF further out from the disc to corroborate the invariant nature of its bright cut-off and observe the evolutionary effects on its faint end.

In this paper, we survey the inner 16 square degrees of M31 (corresponding to 20-30 kpc from the centre), covering the disc, parts of the inner halo, and some of the inner halo substructures. We detect PNe using the on-off-band technique to a depth further than M06. We describe the observations and data reduction in Section 2.2, and the identification of PNe in Section 2.3. In Section 2.4 we describe the identification of the PNe counterparts in a subsample of *Hubble Space Telescope* (HST) data. We obtain the α-parameter in Section 2.5 and analyse the PNLF in Section 4.3. We present the discussions of the results in Section 3.4.2, and we summarise and conclude in Section 6.2.

2.2 CFHT MegaCam M31 PNe survey

2.2.1 Imaging and observations

The observations were carried out with the MegaCam wide-field imager (Boulade et al. 2003) mounted on the 3.6-meter Canada-France-Hawaii Telescope (CFHT), located near the summit of the Mauna Kea mountain on Hawaii's Big Island at an altitude of 4204 meters. MegaCam is comprised of a mosaic of 40 individual 2048 × 4612 CCDs, resulting in a contiguous field of view of 0.96 × 0.94 degrees with a pixel scale of $0.187''$/pixel. The inner 20-30 kpc radius of the M31 halo were observed through 16 pointings of the MegaCam imager. The fields are shown in Figure 2.1. The observations were carried out, under photometric conditions, during two runs: October 9-11 and November 6-7, 2016. Over the course of the observations, seeing

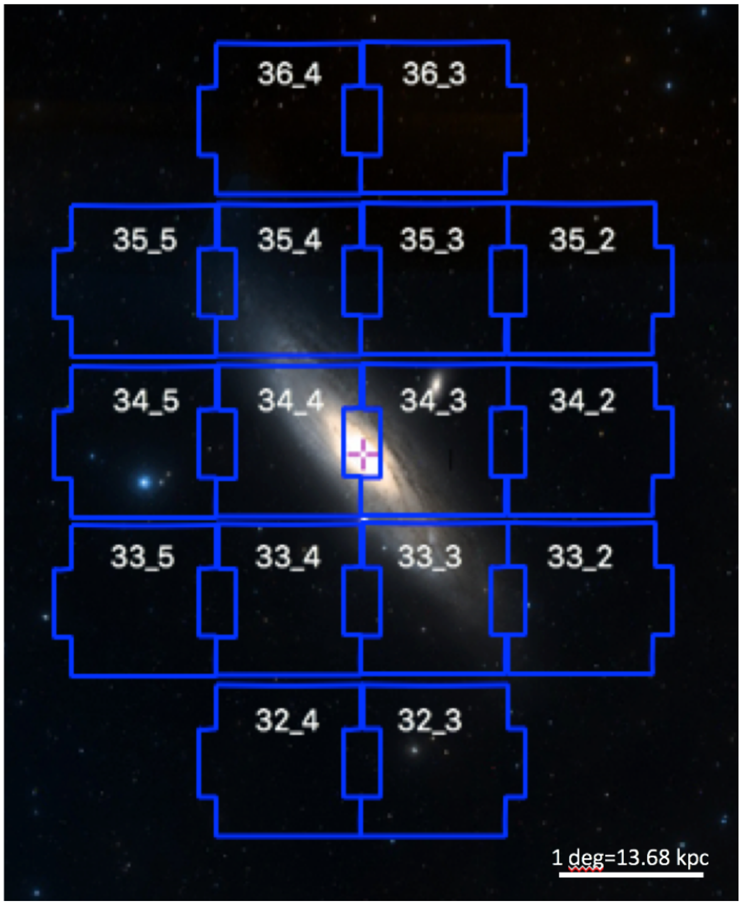

Figure 2.1: Fields observed with CFHT MegaCam (in blue, labelled with their observation ID). North is up, east is left. The background image is from SDSS obtained using the Aladin Sky Atlas (Bonnarel et al. (2000)).

varied between 0.5″ and 1.1″, while the airmass varied between 1.03 and 1.48.

M31 is observed through a narrow-band [O III] filter (λ_c = 5007 Å, $\Delta\lambda$ = 102 Å, on-band) and a broad-band g-filter (λ_c = 4750 Å, $\Delta\lambda$ = 1540 Å, off-band). The photometry is calibrated with observations of spectrophotometric standard stars. Each on-band image generally consists of four dithered exposures with a total exposure time of 1044 s, and each off-band image of three dithered exposures with a total exposure time of 300 s. For some fields there are more dithered images for both on-band and off-band, leading to higher exposure times. A summary of the field positions and exposure times for the on-band and off-band exposures is presented in Table 2.1. The exposure time was chosen such that PNe with an apparent narrow-band magnitude of 6 mag from the bright cut-off m_{5007} = 20.2 mag, in the m_{5007} system described by Jacoby (1989), can still be detected.

Table 2.1: Summary of the field positions, exposure times, and seeing for the narrow-band (on-band) and broad-band (off-band) images. Limiting magnitudes ($m_{5007,\mathrm{lim}}$; described in Sect 2.3.2) for each field are also provided.

Field	α (J2000) (h:m:s)	δ (J2000) ($\circ$:′:″)	$\mathrm{Exp}_{[\mathrm{O\,III}]}$ (s)	$\mathrm{Exp}_{\mathrm{g}}$ (s)	$\mathrm{S}_{\mathrm{FWHM}}$ (″)	$m_{5007,\mathrm{lim}}$ (mag)
36_4	00:45:51.9	43:24:20.5	4 × 261	3 × 100	0.97	26.08
36_3	00:40:14.7	43:24:23.7	4 × 261	3 × 100	0.95	26.26
35_5	00:51:18.0	42:21:48.2	4 × 261	4 × 100	0.85	26.30
35_4	00:45:48.0	43:23:02.4	8 × 261	5 × 100	0.64	26.40
35_3	00:40:17.2	42:23:05.6	4 × 261	6 × 100	0.66	26.17
35_2	00:34:45.9	42:21:57.6	4 × 261	3 × 100	0.68	26.12
34_5	00:51:09.5	41:20:18.6	4 × 261	3 × 100	0.90	26.26
34_4	00:45:44.1	41:21:18.7	5 × 261	3 × 100	0.85	26.16
34_3	00:40:18.7	41:21:21.6	4 × 261	3 × 100	0.92	25.93
34_2	00:34:53.3	41:20:27.6	6 × 261	9 × 100	0.47	26.02
33_5	00:51:02.7	40:18:41.6	4 × 261	3 × 100	0.77	25.94
33_4	00:45:41.3	40:19:48.0	4 × 261	3 × 100	0.76	25.64
33_3	00:40:20.9	40:19:50.8	4 × 261	3 × 100	0.84	25.89
33_2	00:35:00.6	40:18:57.6	4 × 261	3 × 100	0.54	25.90
32_4	00:45:39.0	39:18:16.9	4 × 261	3 × 100	0.60	26.13
32_3	00:40:25.1	39:18:26.8	4 × 261	3 × 100	0.59	26.10

2.2.2 Data reduction

The data are pre-processed using the Elixir[1] pipeline (Magnier & Cuillandre 2004), which accomplishes the bias, flat, and fringe corrections and also determines the photometric zero point of the observations. The zero points for the [O III] and g-band frames in AB magnitudes, normalised to a 1 s exposure, are $Z_{[\mathrm{O\,III}]} = 23.434$ and $Z_g = 26.5$. For every observed field, a weight map is computed corresponding to each exposure using WeightWatcher[2] (Marmo & Bertin 2008). This is used to assign higher weights to pixels that are more reliable compared to their local backgrounds. For each field, the exposures corresponding to the on-band image and those corresponding to the off-band image are then combined using SWARP[3] (Bertin et al. 2002) to produce the respective on-band and off-band images. The exposures are combined using median-type combination in conjunction with their respective weight maps, while a background subtraction is carried out with a background mesh size of 25 pixels. The images thus obtained are used for source extraction.

---

[1] http://www.cfht.hawaii.edu/Instruments/Elixir/home.html

[2] http://www.astromatic.net/software/weightwatcher

[3] http://www.astromatic.net/software/swarp

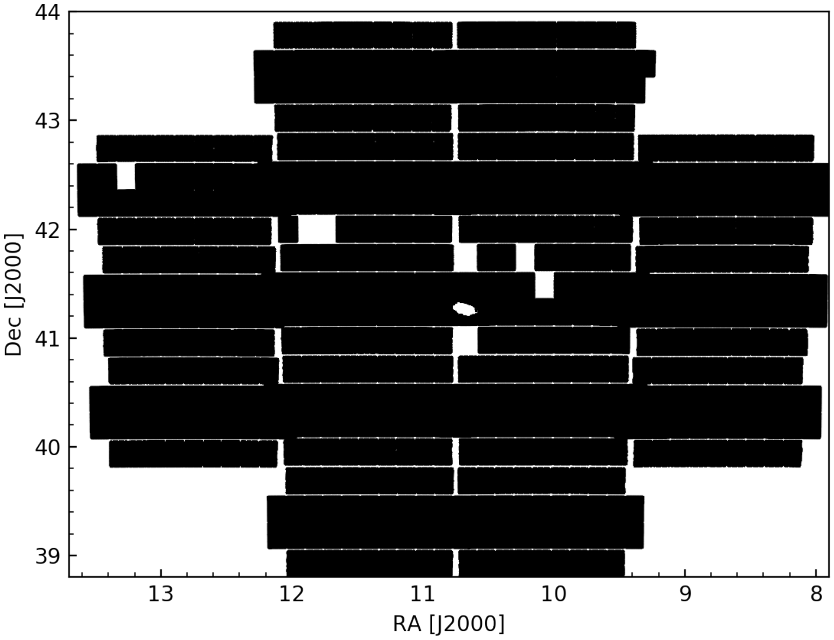

Figure 2.2: The effective survey area is shown in black. CCD edges and noisy or saturated regions have been masked.

2.3 Selection of PNe candidates and catalogue extraction

Having a bright [O III] 5007 Å and no continuum emission, extragalactic PNe can be identified as detected objects in the on-band [O III] image that are not detected in the off-band continuum images or that have an excess [O III] - g colour. Additionally, PNe are typically unresolved at extragalactic distances from ground-based observations and so we only considered point-like objects for analysis. We used the automatic selection procedure developed and validated in Arnaboldi et al. (2002, 2003), which has been optimised for large imaging surveys by Longobardi et al. (2013) and Hartke et al. (2017).

2.3.1 Source extraction

We used SExtractor (Bertin & Arnouts 1996), a source detection algorithm that detects and measures flux from point-like and extended sources, to detect and carry out photometry of the sources on the images. For each field, we measure the narrow-band and broad-band magnitudes, m_n and m_b, in dual-image mode for sources detected on the narrow-band image. The broad-band magnitudes were extracted using the same apertures as the narrow-band image. Sources were detected in the narrow-band image requiring that 25 adjacent pixels or more have flux values 1.2 $\times$ σ rms above the background. Local backgrounds were calculated for the detected sources on

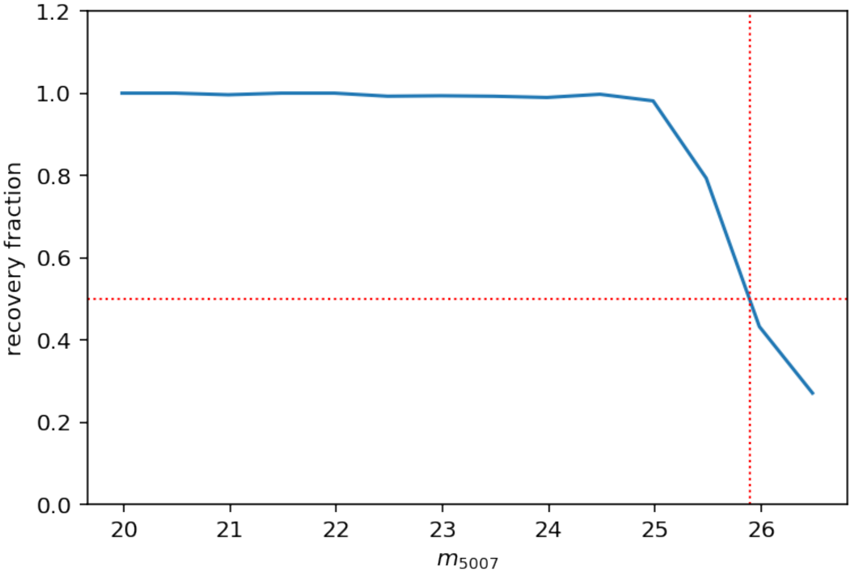

Figure 2.3: Recovery fraction of simulated sources for a single field to illustrate the limiting magnitude at the 50% completeness limit.

apertures having a width of 25 pixels. and magnitudes were measured with different apertures having widths of 15, 17, 19, and 21 pixels. Magnitudes were also measured with an aperture having a width of 5 pixels corresponding to the core of the sources $\mathrm{m_{core}}$. Sources for which a broad-band magnitude could not be detected at the position of the [O III] detection were assigned a $\mathrm{m_b}$ corresponding to $1 \times \sigma$ rms above the background in the broad-band image, similar to Arnaboldi et al. (2002). The narrow-band magnitude, $\mathrm{m_n}$, in the AB system was converted to the $\mathrm{m_{5007}}$ system as $m_{5007} = m_\mathrm{n} + 2.27$ (see Appendix A.1.1 for details). The central part of our survey covering part of the bulge of M31 are mostly saturated. In some observed fields, a few CCDs were noisy. Such noisy regions and CCD edges, affected by dithering and saturation, were masked as detailed in Appendix A.1.3. The effective survey area is shown in Figure 2.2.

2.3.2 Limiting magnitude

In order to determine the limiting magnitude of our sample for each field, we simulated a synthetic point-like population onto the on-band image (with its corresponding exposure time and zero-point) using the Image Reduction and Analysis Facility (IRAF[4]) task *mkobjects*. The synthetic population follows a PNLF as detailed in Ciardullo et al. (1989) and the sources have a Moffat PSF profile as detailed in Appendix A.1.2. The sources are then extracted. The magnitude aperture most suited to recovering the simulated sources is found to be 15 pixels as detailed in Appendix A.1.4. The limiting magnitude is defined as the magnitude at which the recovery

---

[4] http://iraf.noao.edu/

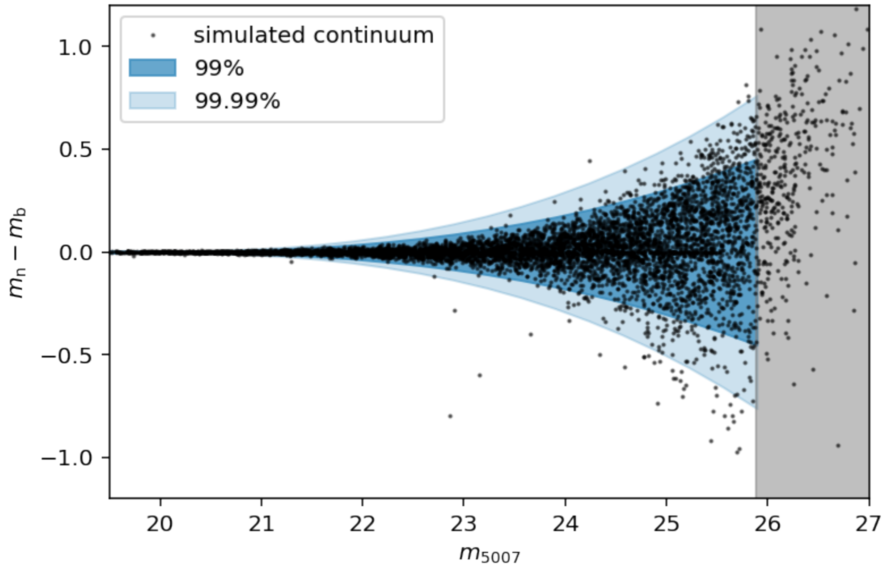

Figure 2.4: Colour-magnitude diagram showing the synthetic continuum sources and the 99% and 99.99% limits on their positions for a single field. The region beyond the limiting magnitude of this field is shown in grey.

fraction of the simulated sources drops below 50% (Figure 2.3). This limiting magnitude varies between $m_{5007} = 25.64$ for the shallowest observed field, Field# 33_4, and $m_{5007} = 26.4$ for the deepest observed field, Field# 35_4. The limiting magnitude is provided for each field in Table 2.1.

2.3.3 Colour selection

We selected PNe candidates based on their position on the m_{5007} versus $m_n - m_b$ colour-magnitude diagram (CMD). These are sources with a colour excess $m_n - m_b < -1$ that are brighter than the limiting magnitude. The colour excess corresponds to an equivalent width $EW_{obs} = 110$ Å (Teplitz et al. 2000) and was chosen in order to limit contamination from background galaxies.

Sources that do not have an excess in $m_n - m_b$ are classified as continuum sources. However, some colour excess may be seen for some of these sources during the source extraction from the images, especially for those with fainter magnitudes. We thus simulated the same synthetic point-like population onto the off-band image and checked their position on the extracted m_{5007} versus $m_n - m_b$ CMD (Figure 2.4). We calculate the 99% and 99.99% limits on their positions in the CMD, below which the probability of detecting continuum sources was reduced to the 1% and 0.01% level respectively. Sources with colour excess within the 99.99% limit are also discarded as possible PNe.

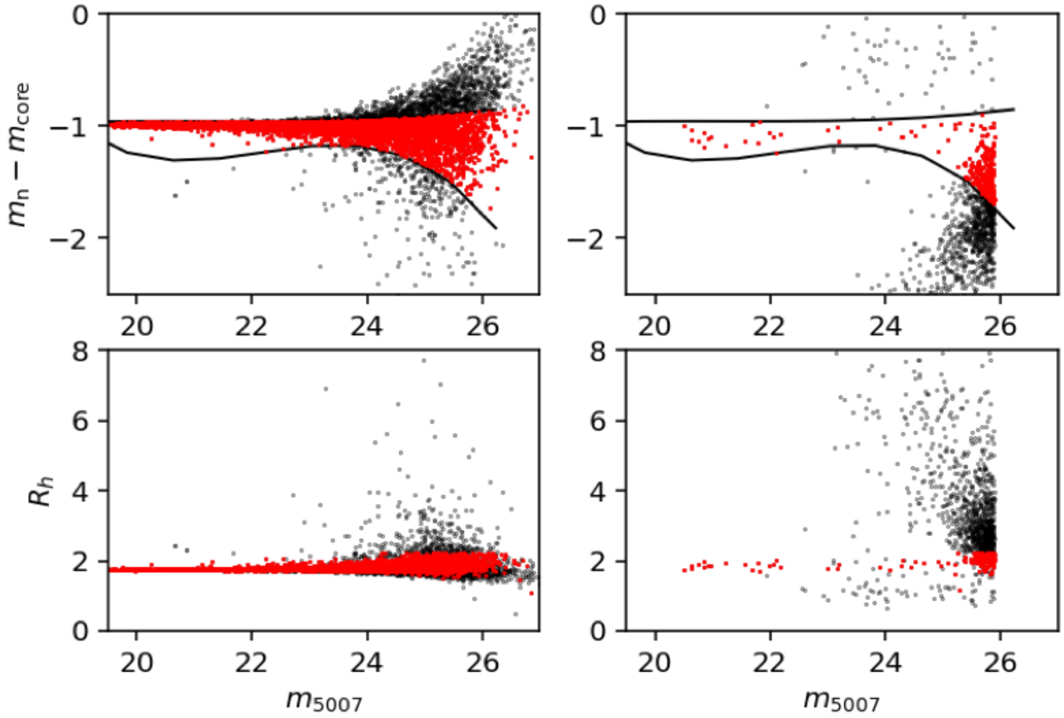

Figure 2.5: [Top] Difference between m_n and m_{core} for all sources in black and those within the 95% limits of the simulated population in red for the simulated population (left) and as applied to the real sources (right) for a single field. [Bottom] Same as the top panel, but for half-light radius, R_h.

2.3.4 Point-like selection

Planetary nebulae are typically unresolved point-like objects at extragalactic distances, and to differentiate them from extended ones (e.g. background galaxies or other extended objects with strong [O III] emission), we analyse the light distribution of the simulated sources, as described in Section 2.3.2, on the on-band image. For each field, we use the half-light radius (R_h) of the simulated sources, which is the radius within which half of the object's total flux is contained, to determine its upper limit (R_{hmax}) corresponding to 95% of the simulated population. We considered sources as point-like if they satisfied the following two criteria: (i) they have a half-light radius such that $1 < R_h < R_{hmax}$, and (ii) they fall in the region where the difference between m_n and m_{core}, magnitude of the source for flux within an aperture of 5 pixels, is within the 95% limit of the simulated population. The point-like selection criteria are shown in Figure 2.5, as applied to the colour-selected simulated population and to the real sources.

In order to estimate the number of continuum sources that may be misidentified as PNe in any field, we count the number of point-like continuum sources (excluded as PNe by the colour selection criteria) and multiply by 0.01%. We estimate that in each field, our identified PNe

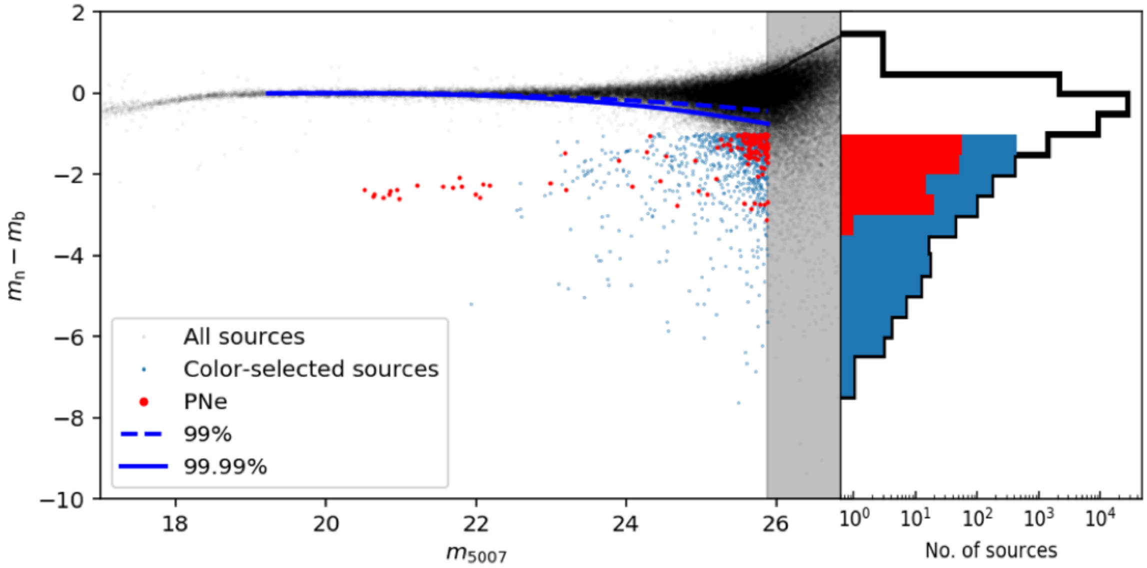

Figure 2.6: Colour-magnitude diagram for a single field showing all the detected sources (brighter than the limiting magnitude) in black, the colour-selected sources in blue, and identified PNe in red. The 99% and 99.99% limits for the continuum sources are shown in blue, while the region beyond the 50% completeness limit is shown in grey. The histogram (in logarithmic scale) shows clearly the number of PNe recovered as a function of colour with all the detected sources (brighter than the limiting magnitude) in black, the colour-selected sources in blue, and identified PNe in red.

sample may be contaminated by 2-4 continuum sources that lie in the faint magnitudes > 25.

2.3.5 PNe catalogue

For each field, the [O III] sources that are brighter than the limiting magnitude and fulfil both the point-like and colour selection criteria are considered as PNe candidates. They are shown in the CMD in Figure 2.6 for a single field. Since the bandwidth of the broad-band filter also covers that of the narrow-band filter, the bright PNe are expected to show some remnant flux in the broad band as well. This remnant broad-band flux is in the ratio of the filter widths and leads to nearly a constant colour excess, $m_n - m_b = 2.5\log(\frac{\Delta\lambda_{[O\,III]}}{\Delta\lambda_g}) = -2.95$, for the bright PNe. The observed constant colour excess is slightly less negative due to the flux contributed to the broad band from the [O III] 4959 Å line which is expected to be ∼ 1/3 of the brightness of the [O III] 5007 Å line in PNe, as seen in Figure 2.6. The final catalogue of confirmed PNe is then checked for spurious sources by eye. Regions of spurious sources, typically caused by saturated stars, are masked and the final catalogue of confirmed PNe is obtained for each field. Counting the PNe identified in the overlapping regions of adjacent fields only once, we identify an unprecedented 4289 PNe in M31 in our survey. Their spatial distribution, overlaid on a map

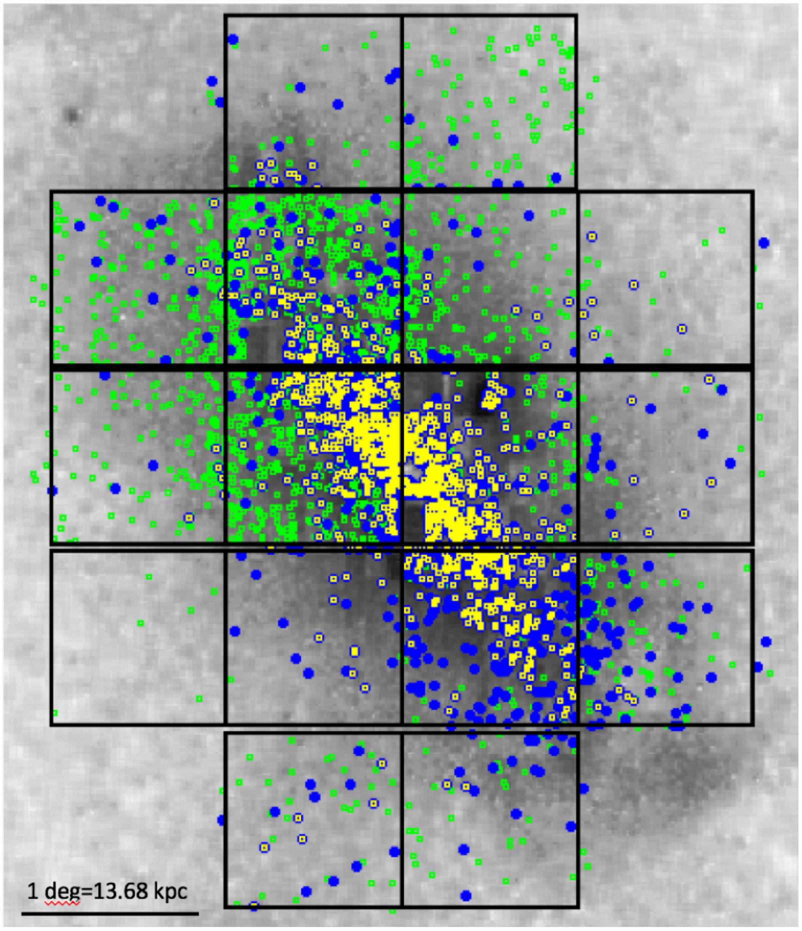

Figure 2.7: Planetary nebulae identified by the survey. (blue - PNe brighter than m_{5007} = 25.64 which is the 50% completeness limit of the shallowest field (Field# 33_4), green - PNe with fainter than m_{5007} = 25.64 with photometric depth varying with field) are overlaid on the map of RGB stars identified by the PAndAS survey. The M06 PNe re-identified by our survey are shown in yellow. North is up, east is left.

of RGB stars identified by the PAndAS survey, is shown in Figure 2.7. Our survey is uniformly complete (in the effective survey area) down to m_{5007} = 25.64 which is the 50% completeness limit of the shallowest field (Field# 33_4). However photometric depth varies with fields and we find PNe down to m_{5007} = 26.4 for the deepest field (Field# 35_4).

2.3.6 Completeness correction

Our colour and point-like selection criteria would exclude a number of PNe that are affected by photometric errors, especially in the fields covering the bright M31 disc. Thus, in order to determine the selection completeness of our extracted sample, we follow the procedure outlined in Longobardi et al. (2013) and Hartke et al. (2017). We simulated a population of 10^4 point-like

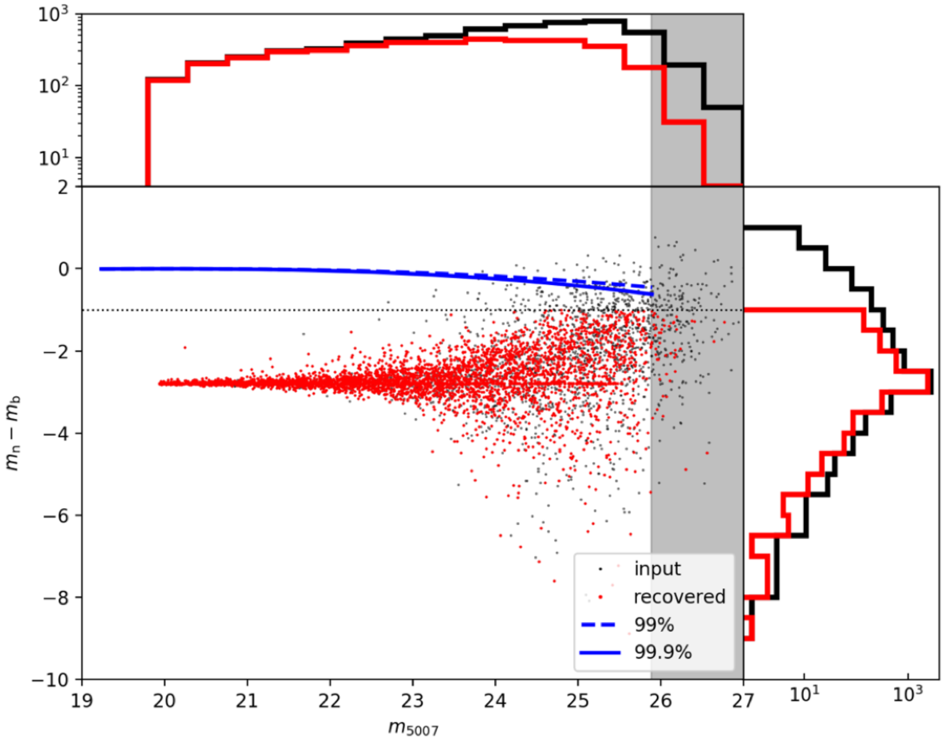

Figure 2.8: Colour-magnitude diagram for a single field showing all the simulated sources in black and those recovered as PNe in red (See Section 2.3.6). The 99% and 99.99% limits for the continuum sources are shown in blue, while the region beyond the limiting magnitude is shown in grey. The dotted black line shows the colour selection adopted to limit contamination from background galaxies. The histograms (in logarithmic scale) show the number of PNe recovered as a function of colour (right) and magnitude (top) with the simulated sources in black and those recovered as PNe in red.

sources (Sect. 2.3.2) on the narrow-band image. On the broad-band image, we also simulate sources at the same positions with their fluxes scaled down by the ratio of the filter widths[5]. We then use SExtractor in dual-mode to simultaneously extract m_n and m_b of these simulated sources. Figure 2.8 shows the CMD of the simulated population for a single field. The colour excess remains nearly constant for the bright simulated sources, as expected from the ratio of their filter widths, but many are missed at fainter magnitudes. We can thus determine the selection completeness of the simulated population at different magnitude ranges for each field. To a single candidate extracted in a given field, we assign the value of the selection completeness at that magnitude as a probability of being detected after the selection effects. We also compute the detection completeness of the simulated population at different magnitude ranges from the recovery fraction and similarly assign a detection probability to each PN candidate extracted in each field. The completeness correction is thus obtained from both the selection and the detection

---

[5] We neglect the contribution from the [O III] 4959 Å line in the broad-band image.

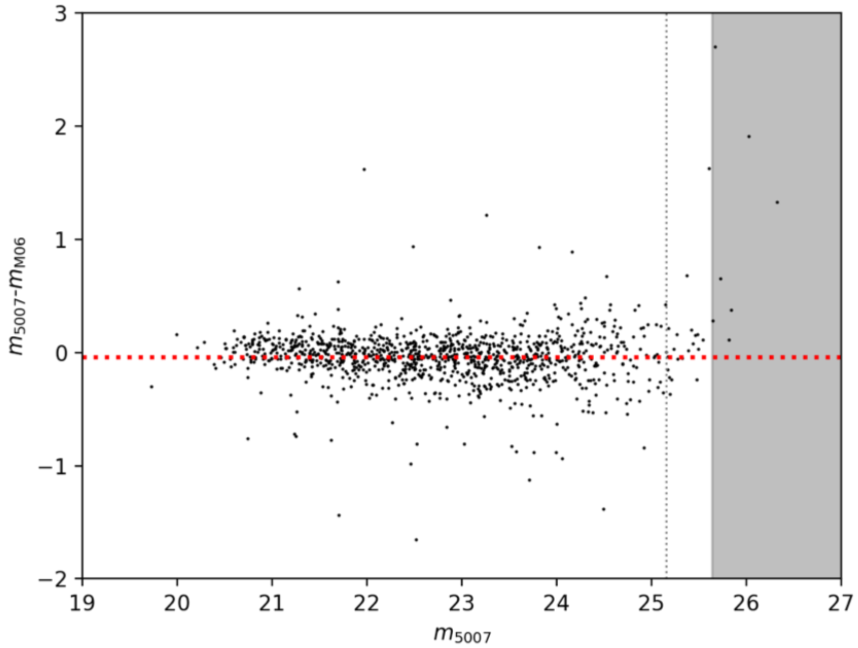

Figure 2.9: Difference between the narrow-band magnitudes of this work and M06 obtained for the matched sources, plotted against m_{5007}. The red dashed line corresponds to the mean offset. The region beyond the limiting magnitude of the shallowest field (Field# 33_4) is shown in grey. The grey dotted line shows the 90% completeness limit of the shallowest field.

probability (see further details in Sect. A.1.5).

2.3.7 Comparison with the Merrett et al. (2006) PNe catalogue

We identify those sources in our PNe catalogue that have a counterpart in the catalogue of PNe identified by M06 by matching them spatially within a 3″ aperture (Figure 2.9). The astrometry of the M06 sample is reliable up to 3″ (Veyette et al. 2014). We match 1099 such sources (in yellow in Figure 2.7). The narrow-band magnitudes of the matched PNe in our survey are 0.045 mag brighter than the corresponding value in M06, well within the photometric uncertainty of the M06 sample. We thus validate the [O III] 5007 Å photometry of our PNe with the sample of M06. The photometry of the M06 PN sample is not very accurate for fainter sources because the PN.S instrument used by M06 has not been optimised for photometry measurements, but rather for the measurement of radial velocities.

While we find most of the PNe found by M06 in the observed fields, we miss quite a few in the regions that we masked, mainly in the crowded bulge and the CCD edges. In our survey area, we recover 82.22% of the M06 PNe. Up to 25% of the M06 PNe candidates were actually H II regions in the M31 disc (Veyette et al. 2014). The spatial resolution of MegaCam bolstered

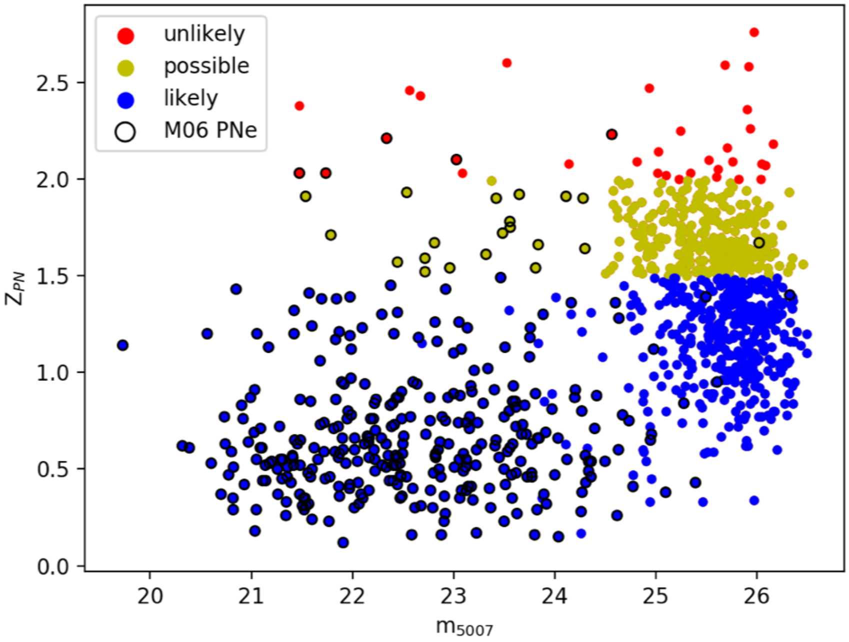

Figure 2.10: Merit function, Z_{PN}, of the PHAT-matched PNe plotted against m_{5007}. The 'likely', 'possible', and 'unlikely' PNe are shown in blue, yellow, and red, respectively. The PNe previously found by M06 are ringed in black.

by the favourable seeing allows us to improve the image quality and obtain an accurate PSF to identify PNe in M31. The H ɪɪ regions would appear as extended objects and discarded as PNe by our point-like selection. We investigate the contamination of our PNe catalogue by H ɪɪ regions in the next section and further discuss it in Section 2.7.1. Thus, the 82.22% recovery fraction of the M06 PNe is driven by the tighter morphological constraints on the light distribution of the detected [O ɪɪɪ] sources in our survey. Since the limiting magnitude of our survey is 1.5-2 mag fainter than that of M06, we find a much larger number of new PN candidates in the overlapping area.

2.4 Counterparts in HST imaging

To test the image quality of our PNe survey, and to estimate the possible contamination from H ɪɪ regions and other sources, we identified PNe counterparts in the HST data available from the Panchromatic Hubble Andromeda Treasury (PHAT) (Dalcanton et al. 2012) covering a portion of the M31 disc.

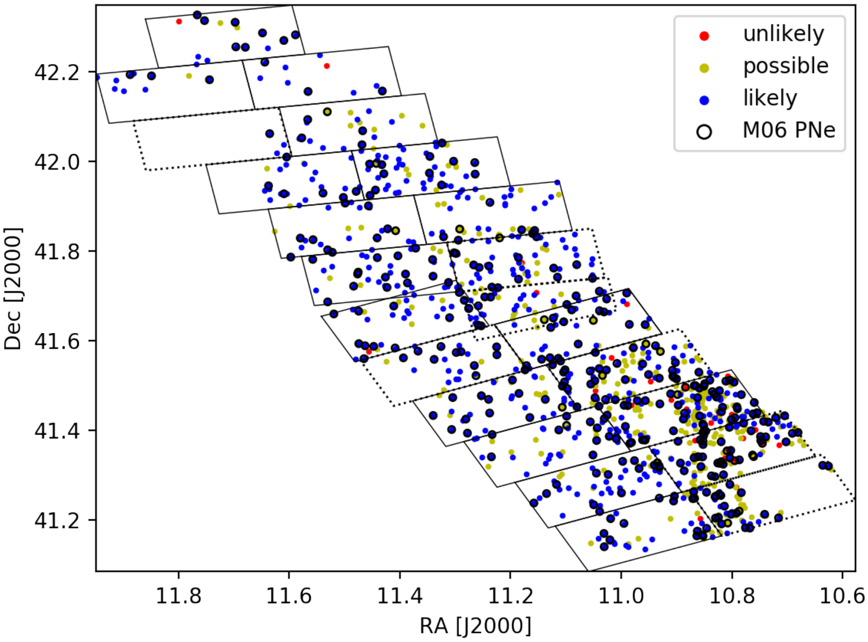

Figure 2.11: Spatial distribution of the PHAT-matched PNe in the PHAT footprint. The solid bricks are those previously analysed by Veyette et al. (2014), while the dashed ones have been analysed here for the first time. The 'likely', 'possible', and 'unlikely' PNe are shown in blue, yellow, and red, respectively. The PNe previously found by M06 are ringed in black.

2.4.1 The Panchromatic Hubble Andromeda Treasury

The PHAT[6] survey covers ~ 1/3 of the star-forming disc of M31 in six bands from the near-UV to the near-IR using the HST imaging cameras (WFC3/IR, WFC3/UVIS, and ACS/WFC cameras). It combines the wide-field coverage typical of ground-based surveys with the precision of HST observations. The overall survey strategy, initial photometry, and data quality (DQ) assessments are described in detail in Dalcanton et al. (2012). We utilise the second generation of photometric measurements of the resolved stars in the PHAT imaging (Williams et al. 2014), which takes advantage of all available information by carrying out photometry simultaneously in all six filters, resulting in a significant increase in the depth and accuracy the photometry over that presented in Dalcanton et al. (2012).

2.4.2 Finding PNe counterparts in PHAT

Veyette et al. (2014) conducted a search for M06 PNe counterparts in 16 of the 23 bricks in the PHAT footprint. They find that ~ 25% of the PNe identified by M06 in the M31 disc are either

---

[6] https://archive.stsci.edu/prepds/phat

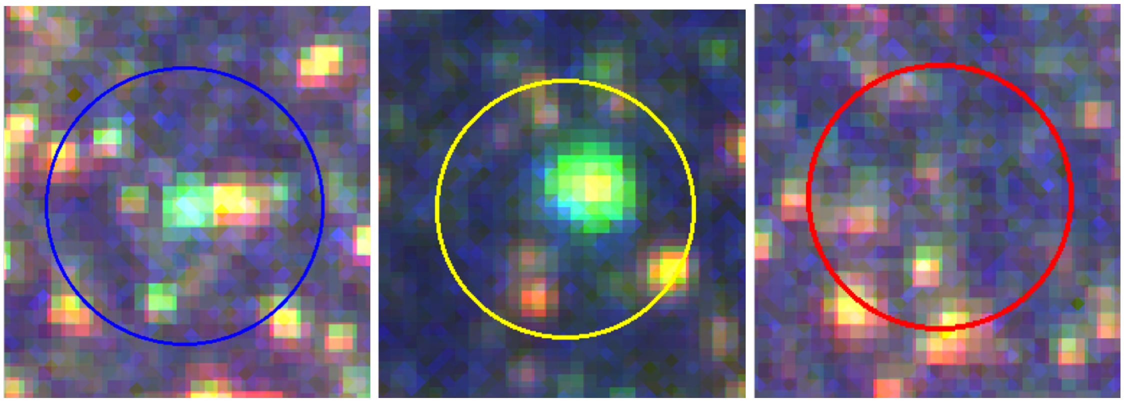

Figure 2.12: True colour images of PHAT-matched PNe. F814W, F475W, and F336W were used for the red, green, and blue images, respectively. One ‘likely’ (left), ‘possible’ (centre), and ‘unlikely’ (right) PN is shown. The circle denotes 0.5″ around the PN position.

H ɪɪ regions resolved in HST or stellar contaminants. They utilised the photometry presented in Dalcanton et al. (2012). They found a linear relation between the M06 m_{5007} magnitude and the PHAT F475W magnitude given by

$$F475W = -0.2240 + 1.0187 \times \mathrm{m}_{5007} \tag{2.2}$$

We adopt a similar method for identifying PHAT counterparts to our PNe in the entire PHAT footprint. However, we search for our counterparts in the updated PHAT photometry from Williams et al. (2014). We only consider those sources from the v2 star files whose square of the sharpness parameter in the F475W filter is below 0.2, to avoid cosmic rays and extended objects. The selection is made on the basis of the following parameters: 1. difference between F475W mag and the F475W mag expected from the m_{5007} using the relation described by Veyette et al. (2014); 2. the F475W − F814W colour; 3. the positional separation between the PNe and the PHAT counterpart; and 4. the roundness of the PSF. To automatically select candidates on the basis of these parameters, we construct an initial training set with the PNe in common with Veyette et al. (2014). We calculated the average value ($\bar{X}_{\mathrm{PN}}$) and 1σ spread (σ_{PN}) of each identification parameter. We found that the separation is within 0.7″. For every PNe, the differences between the training set ($\bar{X}_{\mathrm{PN}}$) and the source (X_{s}) parameter values were normalised by the σ_{PN} of the parameter values for each source in PHAT within 1″ of our PNe location. These normalised parameters are of the form

$$Z_{\mathrm{x}} = \frac{|X_{\mathrm{s}} - \bar{X}_{\mathrm{PN}}|}{\sigma_{\mathrm{PN}}} \tag{2.3}$$

We obtain the sum of these normalised parameters, with half the weight given to roundness, as the merit function Z_{PN}:

$$Z_{\mathrm{PN}} = \frac{Z_{\mathrm{F475W}} + Z_{\mathrm{colour}} + Z_{\mathrm{sep}} + 0.5 \times Z_{\mathrm{round}}}{3.5} \tag{2.4}$$

For each PNe, the PHAT source with the lowest value of Z_{PN} is considered as the counterpart. The distribution of the assigned Z_{PN} with the m_{5007} of the PHAT-matched PNe is shown in Figure 2.10. Thresholds in Z_{PN} are used to classify the PNe based on the Z_{PN} assigned to those PHAT sources

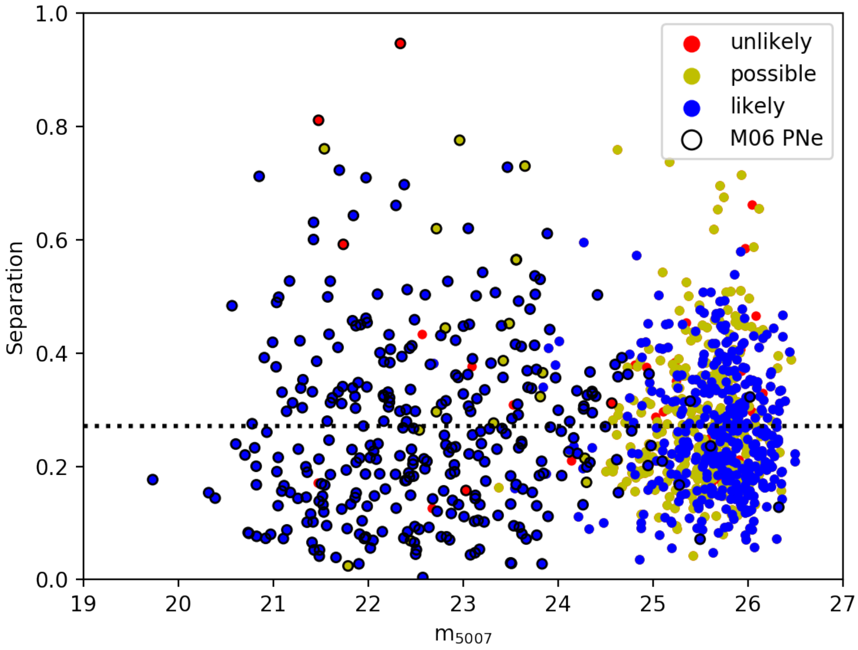

Figure 2.13: Positional separation between the PNe and their PHAT counterparts plotted against m_{5007}. The dashed line shows the mean positional separation. The 'likely', 'possible', and 'unlikely' PNe are shown in blue, yellow, and red respectively. The PNe previously found by M06 are ringed in black.

which were not PNe counterparts. PNe with $Z_{PN} < 1.5$ are classified as 'likely', those with $1.5 < Z_{PN} < 2$ are classified as 'possible' and those with $Z_{PN} > 2$ are classified as 'unlikely'. The likely PHAT sources have a significantly lower Z_{PN} than that of other PHAT sources in the search region, but those that are possible do not stand out quite so much. Those classified as unlikely may not be PNe at all as stellar PHAT sources can have $Z_{PN} \sim 2$, even though most of them have $Z_{PN} > 4$. The spatial distribution of PHAT PNe counterparts is presented in Figure 2.11.

2.4.3 Characteristics of the PHAT-matched PNe

Of the 1023 PNe in the PHAT footprint, 700 are classified as likely, 292 as possible and 31 as unlikely. True colour images of three PNe, one for each classification, is shown in Figure 2.12. None of the PHAT PNe are resolved as H ii regions. The 31 unlikely PNe (~3% of the PHAT PNe) may be stellar contaminants. Of the H ii regions spectroscopically identified by Sanders et al. (2012), 81 are present in the PHAT footprint. Many of these were misidentified by M06 as PNe. We misidentify only three of these H ii regions (probably compact H ii regions) as PNe, which is a testament to the photometric quality and improved spatial resolution of our survey.

The mean positional separation of our PNe and their PHAT counterparts is 0.27″ which is

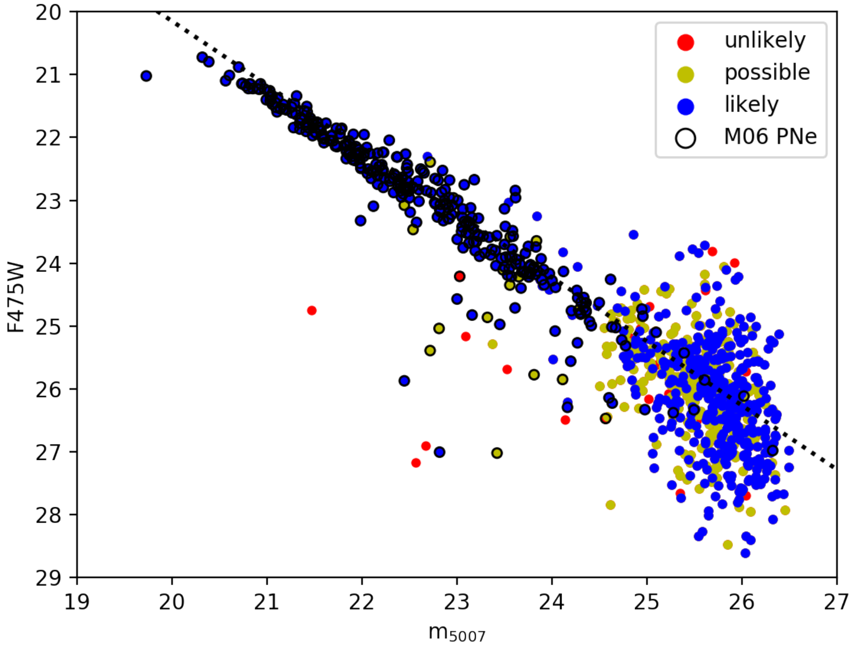

Figure 2.14: F475W mag of the PHAT-matched PNe plotted against m_{5007}. The dashed line shows their relation described by Veyette et al. (2014). The 'likely', 'possible', and 'unlikely' PNe are shown in blue, yellow, and red respectively. The PNe previously found by M06 are ringed in black.

a testament to the accurate astrometry of the image and the Elixir pipeline greatly benefiting our survey. Figure 2.13 shows the variation in separation with m_{5007}. The separation remains largely uniform throughout the range of m_{5007}. The correlation between m_{5007} and the PHAT F475W mag is also seen for our PNe (Figure 2.14), although there is larger dispersion at the faint end. Similarly the variation in the the PHAT F475W mag with the F475W – F814W colour (Figure 2.15) shows that most of the faint sources that are classified as possible and unlikely have a higher F475W – F814W colour. The dispersion in F475W mag and the higher colour for some of the faint sources may be due to the [O III] 5007 Å line not being as prominent as the continuum flux in F475W for the fainter PNe.

2.5 Planetary nebula luminosity-specific frequency

The PNe population follows the sampled (bolometric) luminosity of its parent stellar population. The PN luminosity-specific frequency (α-parameter; Jacoby 1980) is the ratio of the total number of PNe, $N_{\rm PN}$, to the total bolometric luminosity of the parent stellar population, $L_{\rm bol}$, given by

$$\alpha = \frac{N_{\rm PN}}{L_{\rm bol}} = B\tau_{\rm PN}, \tag{2.5}$$

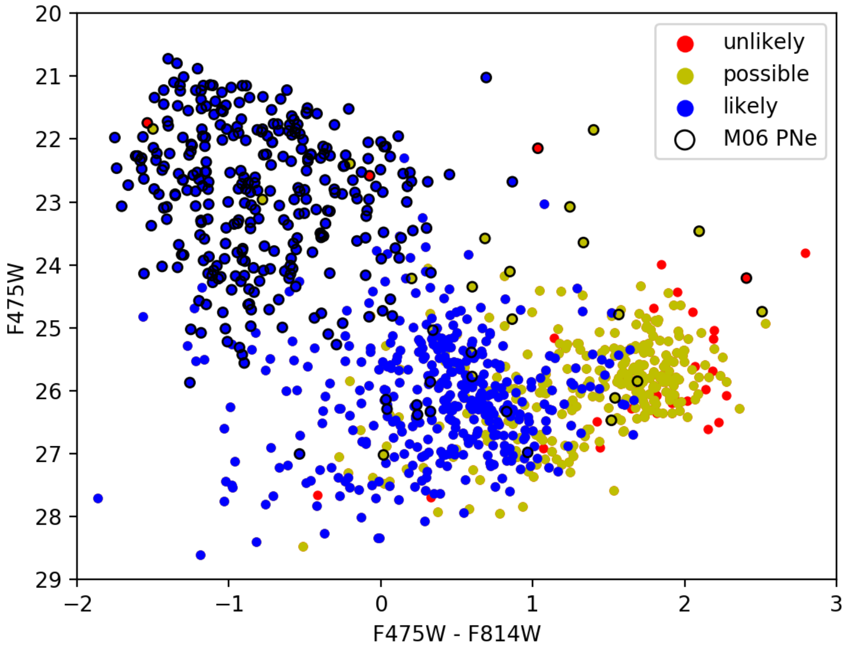

Figure 2.15: F475W mag of the PHAT-matched PNe plotted against its F475W − F814W colour. The 'likely', 'possible', and 'unlikely' PNe are shown in blue, yellow, and red respectively. The PNe previously found by M06 are ringed in black.

where B is the specific evolutionary flux (stars yrs^{-1} L$_{\odot}^{-1}$) and $\tau_{\rm PN}$ is the PN visibility lifetime (Buzzoni et al. 2006). The α-parameter value provides the number of PNe expected per unit bolometric light. We determine the radial PN number density profile and by comparison with the stellar surface brightness profile of M31, derived from broad-band photometric studies, we compute the α-parameter value, similarly to the procedure followed for M87 (Longobardi et al. 2013) and M49 (Hartke et al. 2017).

2.5.1 Radial PN number density profile

Figure 2.16 shows the distribution of PNe on the sky together with 15 elliptical bins aligned using the known position angle, PA = 38° of M31 and its ellipticity = 0.73 (Walterbos & Kennicutt 1988). The binning was chosen such that each bin contains the same number of PNe brighter than m$_{5007}$ = 25.64, which is the 50% completeness limit of the shallowest field (Field# 33_4). These bins correspond to 0.65-26.13 kpc radial distances projected on the minor axis of M31, R$_{min}$. The PN logarithmic number density profile is defined as

$$\mu_{\rm PN}(r) = -2.5\log_{10}\Sigma_{\rm PN}(r) + \mu_0, \tag{2.6}$$

where μ_0 is a constant in order to match the PN number density profile with the stellar surface brightness profile, and $\Sigma_{\rm PN}$ is the completeness-corrected PN number density which is in turn

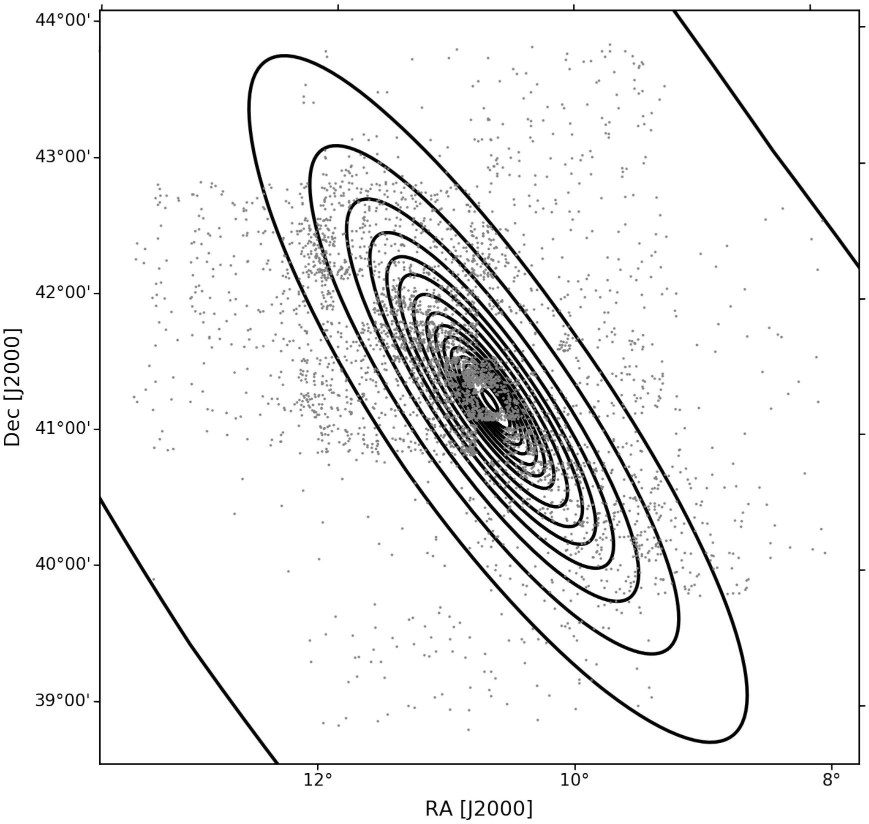

Figure 2.16: Planetary nebulae are shown spatially divided into elliptical bins containing an equal number of PNe brighter than the 50% completeness limit of the shallowest field (Field# 33_4).

given by

$$\Sigma_{\rm PN}(r) = \frac{N_{\rm PN,corr}(r)}{A(r)} \tag{2.7}$$

and $N_{\rm PN,corr}$ is the completeness-corrected PN number in any elliptical bin. The completeness correction accounts for both detection and colour incompleteness, detailed in Sect A.1.5. The parameter $A(r)$ is the observed area in any elliptical bin. We obtain the density profile using only the PNe within 2.5 mag of the bright cut-off ($m_{5007} < 22.56$). The resulting PN density profile in each elliptical bin is matched to the V-band surface brightness profile, obtained by Irwin et al. (2005) using photometry and number counts along the minor axis of M31. It is shown in Figure 2.17. We compute $\mu_0 = 11.085 \pm 0.004$. Courteau et al. (2011) decomposed the M31 luminosity profile into the bulge, disc, and halo components finding that the halo component becomes significant from $R_{min} \sim 8$ kpc and it dominates the luminosity profile over the disc from $R_{min} \sim 11$ kpc. The PN density profile follows the surface brightness profile from $R_{min} \sim 2 - 8$ kpc, where the disc dominates the luminosity profile. The M31 B-V colour, available out to

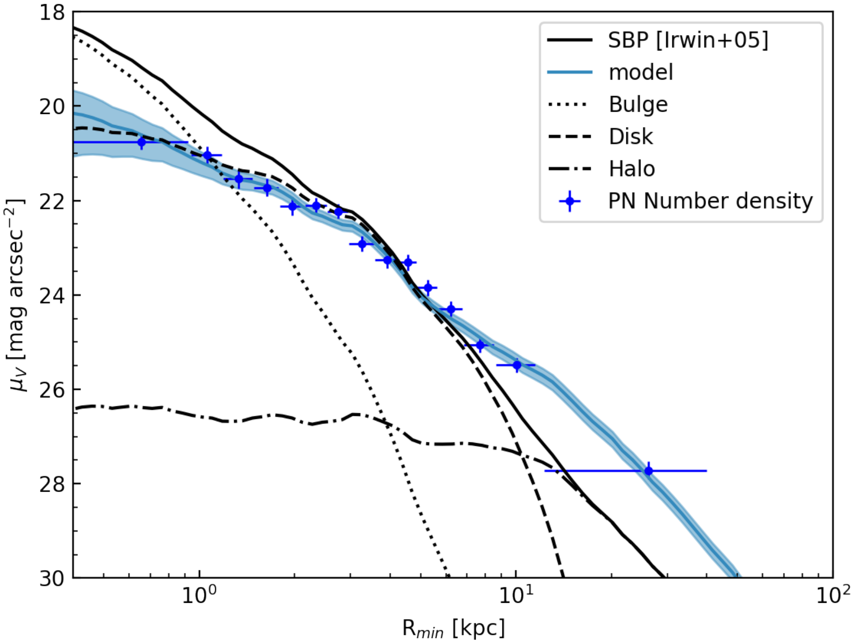

Figure 2.17: Radial surface brightness profile of M31 (Irwin et al. 2005) (in black) and the PN density using only the PNe within 2.5 mag of the bright cut-off, obtained at different elliptical bins (in blue). The Courteau et al. (2011) decomposition of the M31 luminosity profile into the bulge, and disc and halo components scaled to the V-band surface brightness profile are also shown. The three-component photometric model for the predicted PN surface density is shown in blue.

R$_{min}$ ∼ 10 kpc, shows a gradient towards bluer colours at larger radii (Walterbos & Kennicutt 1988; Tempel et al. 2010). We find a flattening of $\mu_{\rm PN}$ with respect to the observed surface brightness profile at larger radial distances. This correlates with the B-V colour gradient and the increasing dominance of the halo component in the light-profile. Additionally, the light from the inner-halo substructures is underestimated by the surface brightness profile obtained along the minor axis of M31 at larger radii. This may also lead to a flattening of $\mu_{\rm PN}$.

2.5.2 PN luminosity-specific number: the α-parameter

We can compute the value of α for the observed M31 PNe from μ_0 using the relation

$$\alpha = \frac{1}{s^2} 10^{0.4(\mu_0 - K - (BC_\odot - BC_V))}, \tag{2.8}$$

where the $K = 26.4$ mag arcsec^{-2} is the V-band conversion factor to physical units L$_\odot$pc^{-2}, $BC_\odot = -0.07$ is the solar bolometric correction, and $s = D/206265$ is a scale factor related to the galaxy distance D. A fixed value of $BC_V = 0.85$ can be assumed with 10% accuracy based on the

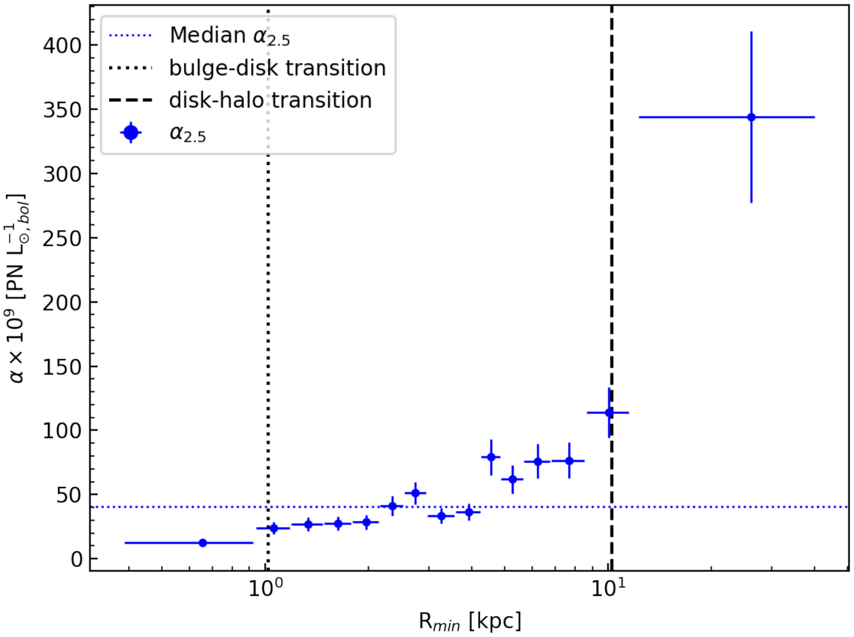

Figure 2.18: Values of $\alpha_{2.5}$ obtained at different elliptical bins (in blue). The dotted black line and the dashed black line show the bulge-disc transition and the disc-halo transition, respectively, from the Courteau et al. (2011) decomposition of the M31 luminosity profile.

study of stellar population models for different galaxy types (irregular to elliptical; see Buzzoni et al. 2006).

For the PNe within 2.5 mag of the bright cut-off, we obtain $\alpha_{2.5} = (40.55 \pm 3.74) \times 10^{-9}$ PN $L^{-1}_{\odot,\mathrm{bol}}$. For a PN population following the PNLF described by Ciardullo et al. (1989), this corresponds to a $\log\alpha = \log(\alpha_{2.5}/0.1) = -6.39 \pm 0.04$ and $\tau_{\mathrm{PN}} = (22527.78 \pm 207.78)$ yr (based on relations described in Buzzoni et al. 2006). M06 obtained $\alpha_{2.5} = (15 \pm 2) \times 10^{-9}$ PN $L^{-1}_{\odot,\mathrm{bol}}$, but only within 1.8 kpc of the minor-axis radius. Scaling our PN number density profile to the surface brightness profile only within this interval, we find $\mu_0 = 10.33 \pm 0.01$ corresponding to $\alpha_{2.5} = (20.16 \pm 1.87) \times 10^{-9}$ PN $L^{-1}_{\odot,\mathrm{bol}}$, which is closer to the value obtained by M06. This may be due to the bulge, disc, and halo components of M31 having differing α-parameter values.

2.5.3 Three-component photometric model for M31

Longobardi et al. (2013) and Hartke et al. (2017) also saw differences in the α-parameter values associated with different components of the surface brightness profile, although they looked at halo and intra-group light components. As in their procedure, we describe a photometric model for the predicted PN surface density as

$$\widetilde{\Sigma}_{\mathrm{PN}}(r) = (\alpha_{2.5,\mathrm{bulge}} I_{\mathrm{bulge}}(r) + \alpha_{2.5,\mathrm{disk}} I_{\mathrm{disk}}(r) + \alpha_{2.5,\mathrm{halo}} I_{\mathrm{halo}}(r)) s^2, \tag{2.9}$$

where $\alpha_{2.5,\mathrm{bulge}}$, $\alpha_{2.5,\mathrm{disk}}$, and $\alpha_{2.5,\mathrm{halo}}$ are the $\alpha_{2.5}$ values associated with the bulge, disc, and halo components of M31, respectively; I_{bulge}, I_{disk}, and I_{halo} are the surface brightness profiles of the bulge, disc, and halo components of M31, respectively, as per the Courteau et al. (2011) decomposition of the M31 luminosity profile into the bulge, disc, and halo components, scaled to the V-band surface brightness profile observations by Irwin et al. (2005).

We simultaneously fit the different α-parameter values of the photometric model to the observed PN surface density to obtain $\alpha_{2.5,\mathrm{bulge}} = (5.28 \pm 6.25) \times 10^{-9}$ PN $L^{-1}_{\odot,\mathrm{bol}}$, $\alpha_{2.5,\mathrm{disk}} = (39.16 \pm 3.33) \times 10^{-9}$ PN $L^{-1}_{\odot,\mathrm{bol}}$ and $\alpha_{2.5,\mathrm{halo}} = (273.89 \pm 41.31) \times 10^{-9}$ PN $L^{-1}_{\odot,\mathrm{bol}}$. The model is also shown in Figure 2.17. While the $\alpha_{2.5,\mathrm{bulge}}$ is not very well constrained, we find the $\alpha_{2.5,\mathrm{disk}}$ is quite close to the $\alpha_{2.5}$ obtained for the whole PN sample, which is expected since the surface brightness profile of M31 is dominated by the disc component in our survey. We also find that $\alpha_{2.5,\mathrm{halo}} \sim 7\alpha_{2.5,\mathrm{disk}}$. The observed variation in α-parameter values in different galaxies that spans almost two orders of magnitude was studied by Buzzoni et al. (2006), who show that late-type spiral and irregular galaxies with bluer B-V colours are expected to have larger α-parameter values than the redder early-type galaxies. Their analysis is based on population synthesis models of galaxies with different ages, metallicities, and morphological types. The different stellar populations in these galaxies thus exhibit very different α-parameter values. Hartke et al. (2017) also found that α-parameter values for the intra-group light of M49 is three times larger than that of its halo. Hartke et al. (2018) later confirmed that the halo PNe and intra-group light PNe were kinematically different, and correspond to two separate parent stellar populations. We can thus infer that the larger α-parameter value of the bluer halo of M31 may indicate that the stellar population of the inner halo is different from that of the disc. While the bluer halo is thus expected to have a higher $\alpha_{2.5}$ than the disc, its absolute value measured for the M31 halo is the highest observed in any galaxy.

We also obtain the radial variation of the α-parameter values (Figure 2.18) by scaling the PN number density individually in each elliptical bin, which shows an increase at larger radii. The increasing trend in the α-parameter values is a direct consequence of the flattening of μ_{PN}, given the B-V colour gradient of M31. The radial variation of the α-parameter values found by M06 also showed an slight increasing trend within the errors at larger radii. However, for the furthest radial bin in Figure 2.18, the minor-axis surface brightness profile may be underestimating the light from the known inner halo substructures of M31 primarily found along the disc major axis. This may also be contributing to the large $\alpha_{2.5,\mathrm{halo}}$ value. More accurate surface brightness profile measurements need to be performed in order to quantify the contribution of substructures to the minor-axis surface brightness profile of M31.

2.6 Planetary nebula luminosity function

For different galaxies, the generalised analytical formula for the PNLF introduced by Longobardi et al. (2013) is

$$N(M) = c_1 e^{c_2 M}(1 - e^{3(M^* - M)}), \tag{2.10}$$

where c_1 is a normalisation constant, c_2 is the slope at the faint end, and M^* is the absolute magnitude of the LF bright cut-off. The Ciardullo et al. (1989) analytical LF is then a specific

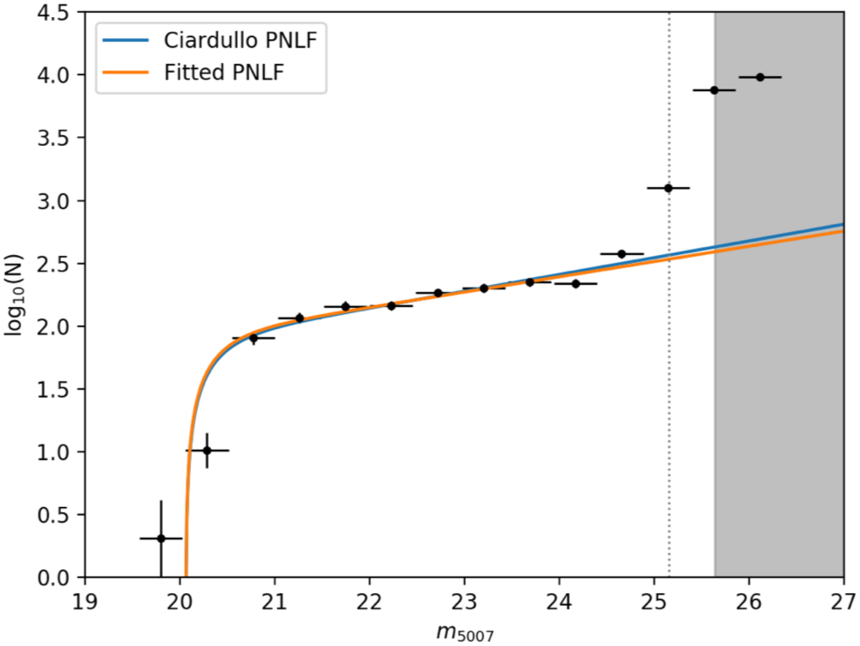

Figure 2.19: Completeness-corrected PNLF for the whole catalogue of M31 PNe is shown fitted by both the generalised analytical formula (in orange) and the Ciardullo et al. (1989) analytical LF (in blue). The region beyond the limiting magnitude of the shallowest field (Field# 33_4) is shown in grey. The grey dotted line shows the 90% completeness limit of the shallowest field.

case of the generalised analytical formula with $c_2 = 0.307$ that reproduces their best fit to the PNLF of M31. Observations suggest that the slope described by the parameter c_2 is correlated with the star formation history of the parent stellar population (Ciardullo et al. 2004; Ciardullo 2010; Longobardi et al. 2013; Hartke et al. 2017). In order to ascertain the robustness of the morphology of the PNLF at magnitude ranges not reached before, we investigate the M31 PNLF from our survey with different independent methods.

2.6.1 PNLF of M31

The PNLF is corrected for detection completeness and also for selection completeness due to the colour and point-like selection, detailed in Sect. 2.3.6. Figure 2.19 shows the PNLF of M31 for all the PNe identified by our survey, fitted by the generalised analytical formula with $c_2 = 0.279 \pm 0.024$, which agrees well with that previously found by Ciardullo et al. (1989). Only the data corresponding to $m_{5007} < 24$ are considered for the fit. The bright cut-off remains consistent with the known value of M*. The faint end of the PNLF shows a rise with respect to the fitted function. This rise is seen at $m_{5007} > 24.5$ in all the fields of the survey. This rise was not seen by M06 whose sample was photometrically complete to a brighter magnitude

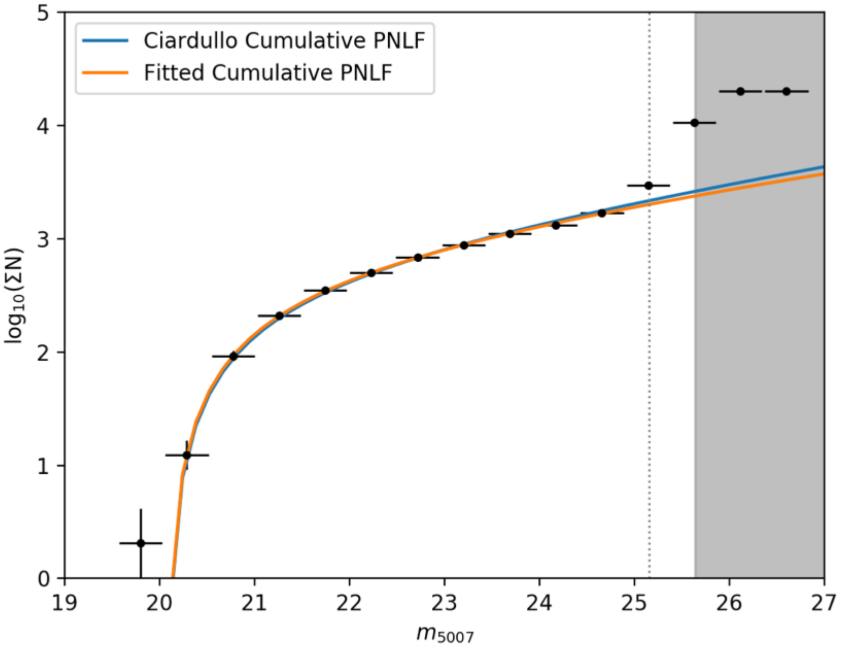

Figure 2.20: Completeness-corrected cumulative PNLF (binned for visual clarity) for the whole catalogue of M31 PNe is shown fitted by both the generalised analytical formula for the cumulative PNLF (in orange) and the cumulative PNLF corresponding to the Ciardullo et al. (1989) analytical formula (in blue). The region beyond the limiting magnitude of the shallowest field (Field# 33_4) is shown in grey. The grey dotted line shows the 90% completeness limit of the shallowest field.

(m_{5007} = 23.5).

2.6.2 Cumulative PNLF

The M31 PNe can be fitted to a cumulative luminosity function (e.g. Peña et al. 2007, for NGC 3109) to avoid potential histogram binning considerations such as the bin size, limits, or the position of the first bin. However, some important features of the canonical PNLF (such as the dip) could be lost. Rodríguez-González et al. (2015) presented the Cumulative PNLF corresponding to the analytical PNLF described by Ciardullo et al. (1989). The Cumulative PNLF for the generalised PNLF is presented as follows:

$$I(M) = c_1 e^{c_2 M}[\tfrac{1}{c_2} e^{c_2 M} + \tfrac{1}{3-c_2} e^{3(M^*+\mu)-(3-c_2)M} - (\tfrac{1}{c_2} + \tfrac{1}{3-c_2}) e^{c_2(M^*+\mu)}] \tag{2.11}$$

Figure 2.20 shows the cumulative PNLF of M31 for all the PNe identified by our survey, fitted by the generalised analytical formula with $c_2 = 0.257 \pm 0.011$, which agrees well with that found from the canonical PNLF, thereby corroborating that the effect histogram binning considerations

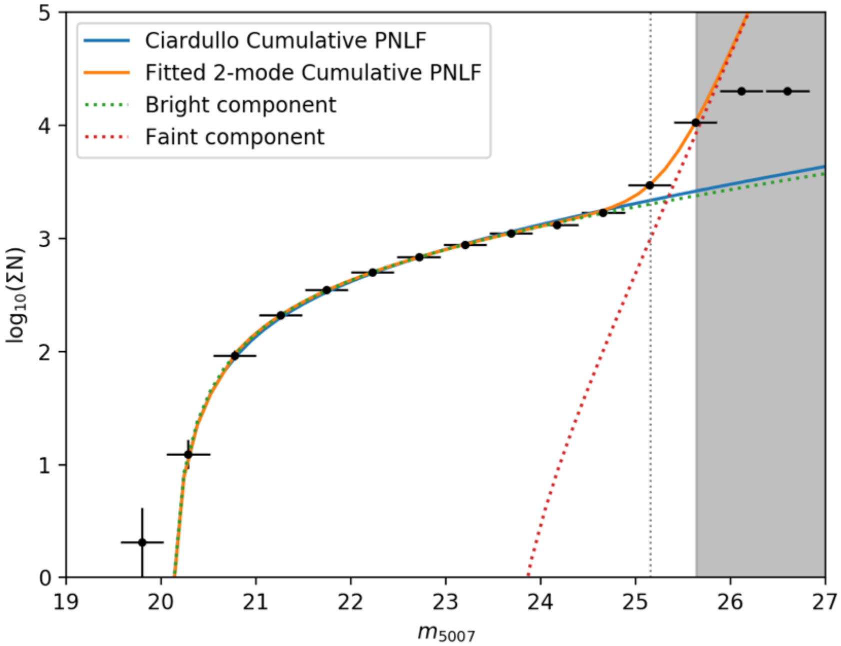

Figure 2.21: Completeness-corrected cumulative PNLF (binned for visual clarity) for the whole catalogue of M31 PNe. It is fitted with two modes of the generalised analytical formula for the cumulative PNLF (in orange) with one component dominating the brighter end (in green) and another dominating the faint end (in red). The cumulative PNLF corresponding to the Ciardullo et al. (1989) analytical formula (in blue) is also shown. The region beyond the limiting magnitude of the shallowest field (Field# 33_4) is shown in grey. The grey dotted line shows the 90% completeness limit of the shallowest field.

on the canonical PNLF is negligible. Only the data corresponding to $m_{5007} < 24$ are considered for the fit. The faint end of the cumulative PNLF also shows the rise with respect to the fitted function.

2.6.3 Two-mode PNLF

The rise at the faint end of the PNLF may be an indication that there are two PN populations, one dominating the brighter end and a second one at the fainter end. Thus, we fit the observed cumulative PNLF with two modes similar to Rodríguez-González et al. (2015). The two-mode PNLF is defined as $I_{2m}(M) = I_b(M) + I_f(M)$, where $I_b(M)$ is the cumulative function for the generalised PNLF set to parameters found in the previous section, which accurately represents the observed PNLF before the rise at the faint end, and $I_f(M)$ is a cumulative function for the generalised PNLF considered with free parameters, c_{f1}, c_{f2}, and M^*_f, which are the normalisation constant, slope, and bright cut-off of a possible second faint PNe population. Rodríguez-González

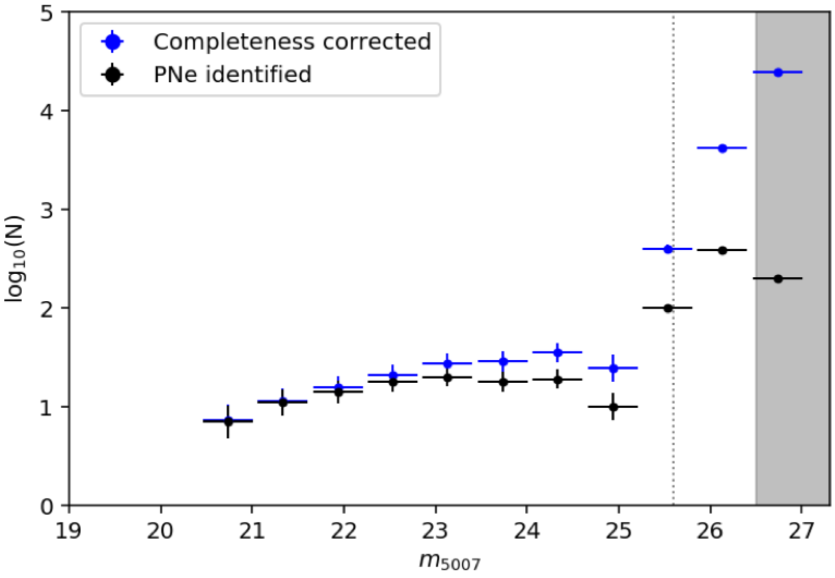

Figure 2.22: For the deepest field (Field# 35_4), the observed number of PNe in each magnitude bin (in black) and the completeness corrected number (in blue). The region beyond the limiting magnitude of this field is shown in grey. The grey dotted line indicates the 90% completeness limit of this field.

et al. (2015) had included an additional magnitude cut-off in their definition of the two-mode PNLF where the contribution of the brighter mode was set to zero at this magnitude and only the faint-end contribution was present. We do not include this magnitude cut-off because any PN population, such as the one dominating in the brighter end, should have a contribution down to ∼ 8 mag below the bright cut-off (Buzzoni et al. 2006). The two-mode fit of the observed PNLF is shown in Figure 2.21. For the second possible PNe population, we find $c_{f2} = 4.4 \pm 0.1$ and $M^*_f = -1 \pm 0.3$. Thus, the observed cumulative PNLF may have a second PN population with a much steeper slope and very different bright cut-off.

2.6.4 PNLF of the deepest field

The deepest field in our survey is Field# 35_4, which has a limiting magnitude at $m_{5007} = 26.4$ and is 90% complete at $m_{5007} = 25.6$. The PNLF for the PNe observed in this field is shown in Figure 2.22 both before and after completeness correction. We note that the rise in the PNLF at $m_{5007} > 25$ is present in the observed PNLF within the 90% completeness limit. Thus, the rise of the PNLF is a physical property of the observed PN sample.

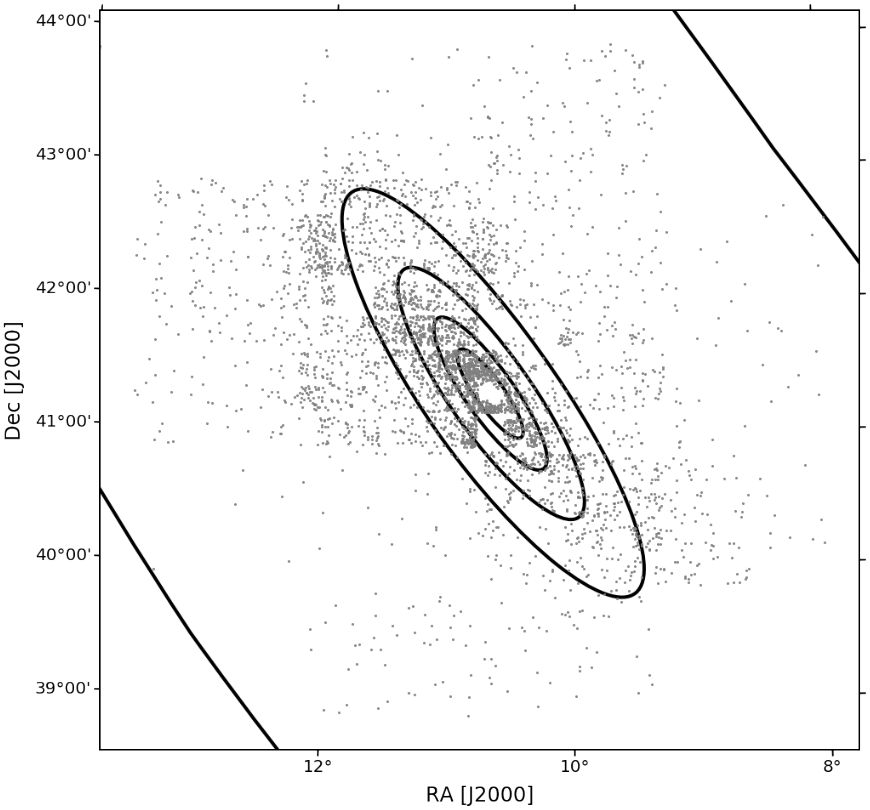

Figure 2.23: Same as Figure 2.16, but with five elliptical bins.

2.6.5 Radial variation of PNLF

We divide the PNe spatially into five elliptical bins (Figure 2.23) similar to Figure 2.16. The PNLF corresponding to each bin is shown in Figure 2.24. Only the data corresponding to $m_{5007} < 24$ are considered to fit each PNLF. We observe that the rise in the PNLF remains invariant as we go radially outwards indicating that the rise is ubiquitous throughout the surveyed area, and is not a function of photometry in crowded areas. Pastorello et al. (2013) identified PNe in the high metallicity nuclear region within 80 pc of the centre of M31 with HST and SAURON data. They found a PNLF with a paucity of bright PNe within $\sim$ 1 mag of the bright cut-off. We find that the bright cut-off remains invariant as we go radially outwards, but this is expected because the median metallicity of the disc and inner halo stars is largely uniform as the metal-poor inner halo is colligated with stars associated with the more metal-rich substructures (Ibata et al. 2014). We note that the PNLF corresponding to the innermost bin, covering part of the bulge of M31 which is mostly saturated in our survey, has a steeper fitted slope as expected from PNe corresponding

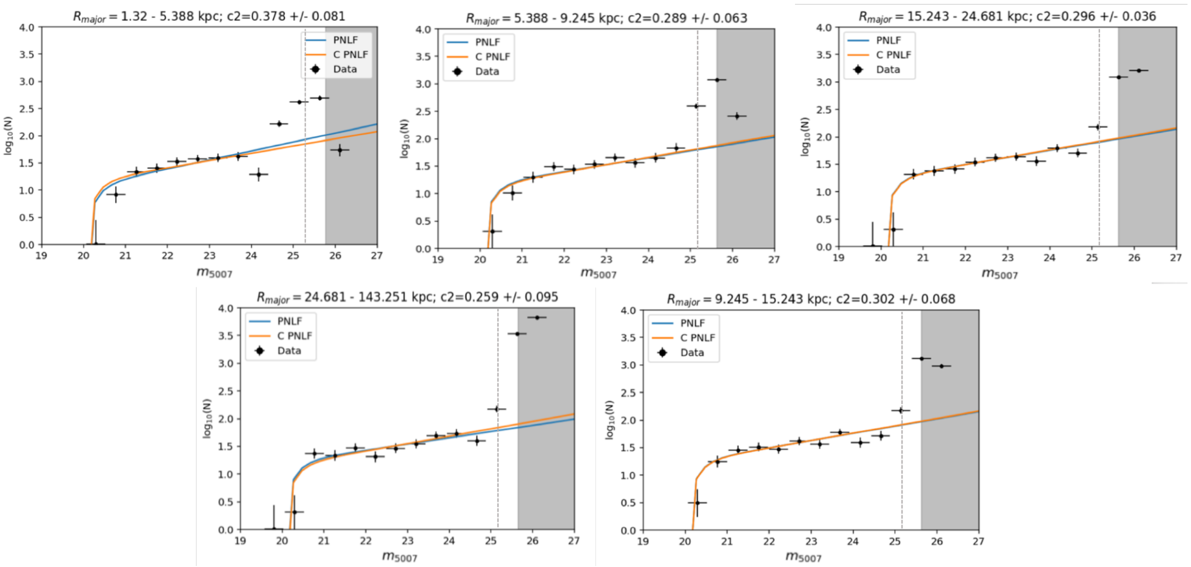

Figure 2.24: Completeness-corrected PNLF for each elliptical bin fitted by both the generalised analytical formula (in blue) and the Ciardullo et al. (1989) analytical LF (in orange). The projected major-axis elliptical radii covered by each bin is indicated along with the fitted slope of the PNLF. The region beyond the limiting magnitude of the shallowest field (Field# 33_4) is shown in grey. The grey dotted line shows the 90% completeness limit of the shallowest field.

to an older parent stellar population (Longobardi et al. 2013).

2.6.6 PNLF of PHAT-matched PNe

Figure 2.25 shows the PNLF of the PHAT-matched PNe. The faint end of the PNLF still shows a rise even for the conservatively selected ‘likely’ PNe. This indicates that the colour and magnitude of faint PNe are consistent with those of the bright PNe.

2.6.7 Comparison with other deep PN surveys in Local Group galaxies

We compare the shape of the M31 PNLF with that of other surveys in different galaxies that sample similar magnitude intervals from the bright cut-off. A catalogue of PNe with m_{5007} down to ~ 10 mag below the bright cut-off of the PNLF is available for the Large Magellanic Cloud (LMC) from Reid & Parker (2010). This catalogue is not completeness corrected as the m_{5007} magnitudes are estimated from spectroscopy but is expected to be largely complete to ~ 6 mag below the bright cut-off, i.e. the magnitude interval covered by our survey of PNe in M31. Another catalogue of PNe is available for the Small Magellanic Cloud (SMC) from Jacoby & De Marco (2002) with m_{5007} down to ~ 8 mag below the bright cut-off. It is also not corrected for completeness, but has significantly fewer PNe than the LMC and may suffer from significant completeness issues ~ 6 mag below the bright cut-off. A catalogue of PNe identified in the MW bulge is also available (Kovacevic et al. 2011), and assuming that all their PNe are at a constant

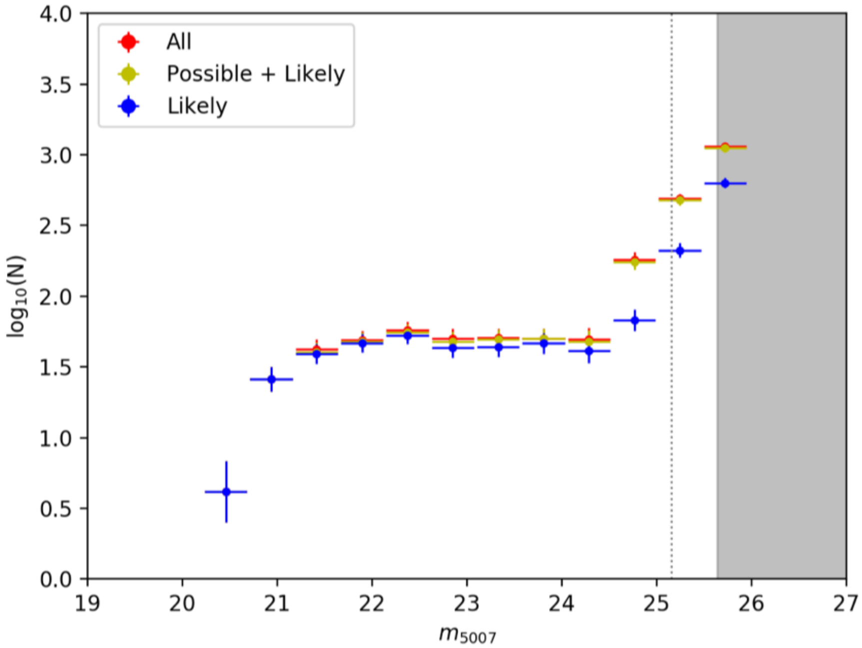

Figure 2.25: Completeness-corrected PNLF for PHAT-matched PNe is shown for the 'likely' (blue), 'possible + likely' (yellow) and 'possible + likely +unlikely' (red) cases. The region beyond the limiting magnitude of the shallowest field (Field# 33_4) is shown in grey. The grey dotted line shows the 90% completeness limit of the shallowest field.

8 kpc distance (Majaess 2010), i.e. the average distance to the MW bulge, a PNLF may be constructed. The distance approximation may be inaccurate, and completeness information is also unavailable.

Considering the LMC, SMC, and MW bulge PNe at the distance of M31 normalised for the number of PNe in M31, we can compare the shape of their PNLF with that of M31 (Figure 2.26). We note that the difference in the bright cut-off is expected from the difference in metallicity between the three galaxies. The dip in the PNLF seen for both the LMC and the SMC, albeit at different magnitudes, is not seen for M31. The MW bulge PNe seem to show a different slope, but no rise is evident. However, we cannot disregard the possibility that a dip or a rise at the faint end of the PNLF may be seen pending accurate distance determination. The rise at the faint end of the PNLF of M31 is much steeper than any of the others.

2.7 Discussion

2.7.1 Possible sources of contamination

As discussed in Section 2.3.4, up to 50 continuum sources may contaminate our PNe catalogue,

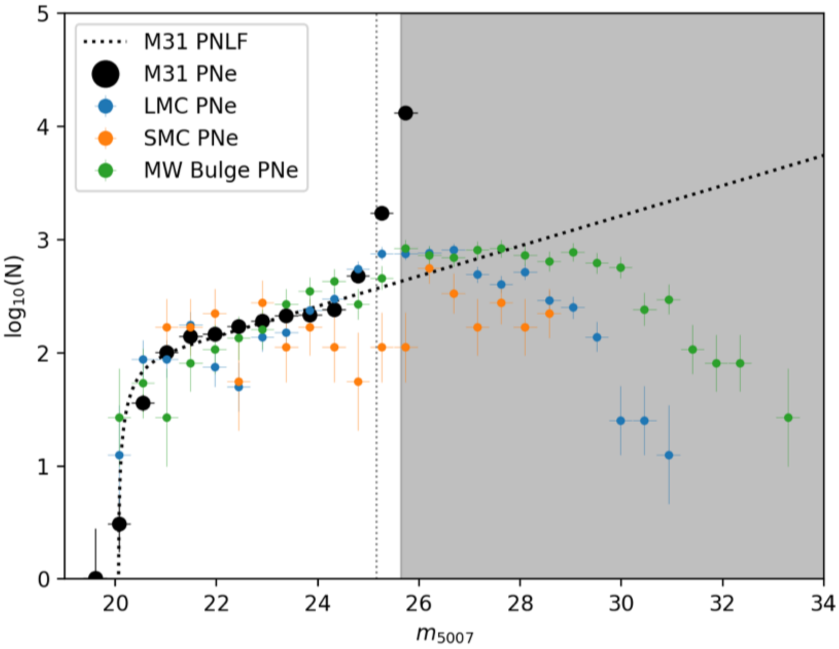

Figure 2.26: Completeness-corrected PNLF for the whole catalogue of M31 PNe (black points) is shown fitted by the Ciardullo et al. (1989) analytical LF (black dotted line). The LMC (Reid & Parker 2010), SMC (Jacoby & De Marco 2002), and MW Bulge PNe (Kovacevic et al. 2011) shifted to the distance of M31 are shown in blue, orange, and green, respectively. The region beyond the limiting magnitude of the shallowest field (Field# 33_4) is shown in grey. The grey dotted line shows the 90% completeness limit of the shallowest field.

most of which should be fainter than $m_{5007} = 25$. This is also corroborated for the PHAT counterparts where ~3% of the matched PNe may actually be stellar contaminants. The contamination from Milky Way (MW) halo and disc PNe is negligible as there are no MW halo PNe at $m_{5007} >$ 20.5 (Kovacevic et al. 2011). Background galaxies at redshift z = 0.345 that are [OII]3727 Å emitters can be another source of contamination, but they are not known to have $EW_{obs} > 95$ Å (Colless et al. 1990; Hammer et al. 1997; Hogg et al. 1998). Our colour selection thus renders their contamination negligible.

H II regions are also bright in the [O III] 5007 Å line and are present in the same region of the CMD as PNe. However, H II regions appear extended at the distance of M31 and with the photometric quality of our survey, we are able to significantly limit their contamination as seen in Section 2.4. Some compact H II regions, especially in the disc of M31, may still contaminate our survey. Of the 253 H II regions identified by Sanders et al. (2012) later from spectroscopy, M06 had classified 101 of them as PNe. We find only 15 of these in our survey as PNe, thereby corroborating the excellent photometric quality of our survey. Other [O III] 5007 Å sources like SySts may also mimic PNe and contaminate our survey. We investigate in the following whether

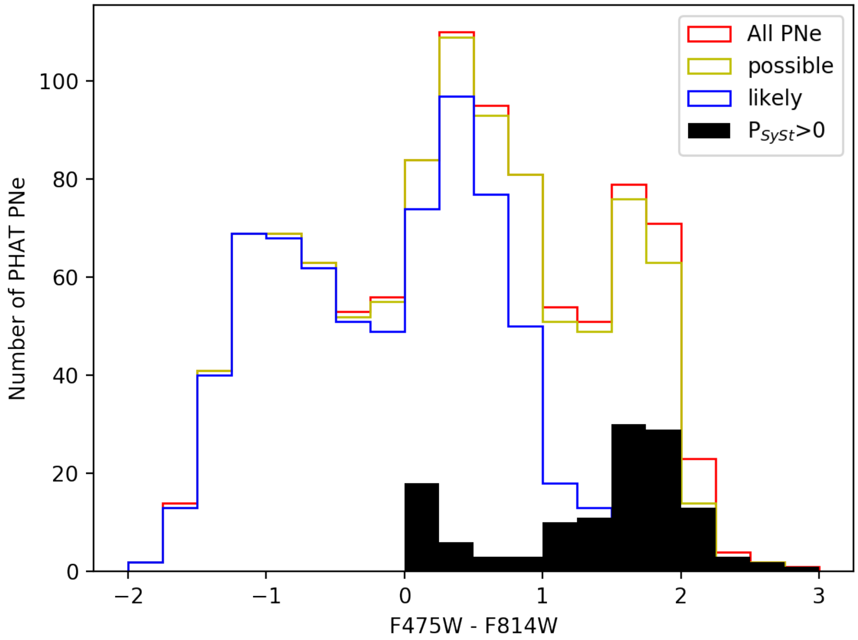

Figure 2.27: Histogram for PHAT-matched PNe is shown for the 'likely' (blue), 'possible + likely' (yellow) and 'possible + likely + unlikely' (red) cases. The histogram of possible SySts are shown in black.

the contribution from SySts is responsible for the two-mode PNLF investigated in Section 2.6.3.

2.7.2 Symbiotic star contribution to PNLF

SySts are among the longest orbital period interacting binaries, consisting of an evolved cool giant and an accreting, hot, luminous companion (usually a white dwarf) surrounded by a dense ionised nebula. Depending on the nature of the cool giant, there are two main classes of SySts: the S-types (stellar), which are normal M giants with orbital periods of the order of a few years, and the D-types (dusty), which contain Mira variable primaries surrounded by warm dust with orbital periods of a decade or longer. Mikołajewska et al. (2014) found 31 confirmed Systs in M31, 10 of which had unambiguous PHAT counterparts. Of these, 9 were S-types and their spectra show that the continuum emission is high in the F814W filter. Mikołajewska et al. (2014) utilised this to identify the PHAT counterpart of their SySt as the PHAT source that had the brightest F814W mag in their 0.75″ search radius. It is also seen that the F475W − F814W colour of these SySt generally have a high positive value which can be used to distinguish them from PNe.

We estimate the probability that each of our PHAT-matched PN is a SySt by checking how close it was in F814W mag ($F814W_{\mathrm{PN}}$) to the brightest F814W mag source ($F814W_{\mathrm{high}}$) in our

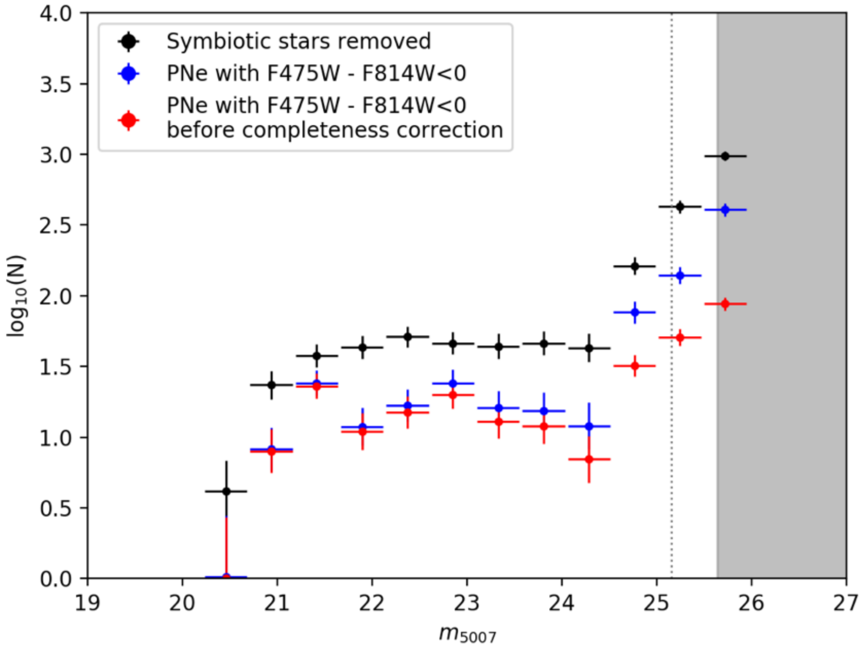

Figure 2.28: Completeness-corrected PNLF for PHAT-matched PNe with the contribution from SySts removed is shown in black. The completeness-corrected PNLF for only those PNe with $F475W - F814W < 0$ is shown in blue. The PNLF for the observed PHAT-matched PNe with $F475W - F814W < 0$ is shown in red. The region beyond the limiting magnitude of the shallowest field (Field# 33_4) is shown in grey. The grey dotted line shows the 90% completeness limit of the shallowest field.

search radius, and also if it had a colour excess in F814W with respect to F475W. The probability, P_{SySt}, is given by the following formula:

$$P_{\mathrm{SySt}} = \frac{\mathrm{F814W_{PN}} - \overline{\mathrm{F814W}}}{\mathrm{F814W_{high}} - \overline{\mathrm{F814W}}} \times \mathrm{P_{col}} \tag{2.12}$$

Here $\overline{F814W}$ is the mean F814W mag of all sources in the search radius and P_{col} is the colour excess check, which equals 1 if $F475W - F814W > 1$ (most of the Mikołajewska et al. 2014 SySt have this), 1/2 if $0 < F475W - F814W < 1$ (some of the confirmed PNe have this), and 0 otherwise. PHAT-matched PN with F814W below the $F8\bar{1}4W$ are set to have a $P_{\mathrm{SySt}} = 0$. We find that there is a systematic overestimation of P_{SySt} since PHAT-matched PNe just above their $\overline{F814W}$ would still be assigned a small value of P_{SySt}. We thus update the P_{SySt} by subtracting the mean of the probability, $\overline{P_{\mathrm{SySt}}}$, from each source and setting those with negative values to zero. We find that most PHAT-matched PNe with a probability of being a SySt are clustered around a high $F475W - F814W$ colour (Figure 2.27). Removing the contribution of SySts from the PNLF (Figure 2.28), it is evident that the rise at the faint end of the PNLF cannot be explained by SySts. Figure 2.28 also shows the PNLF for only those PHAT-matched PNe with $F475W - F814W < 0$

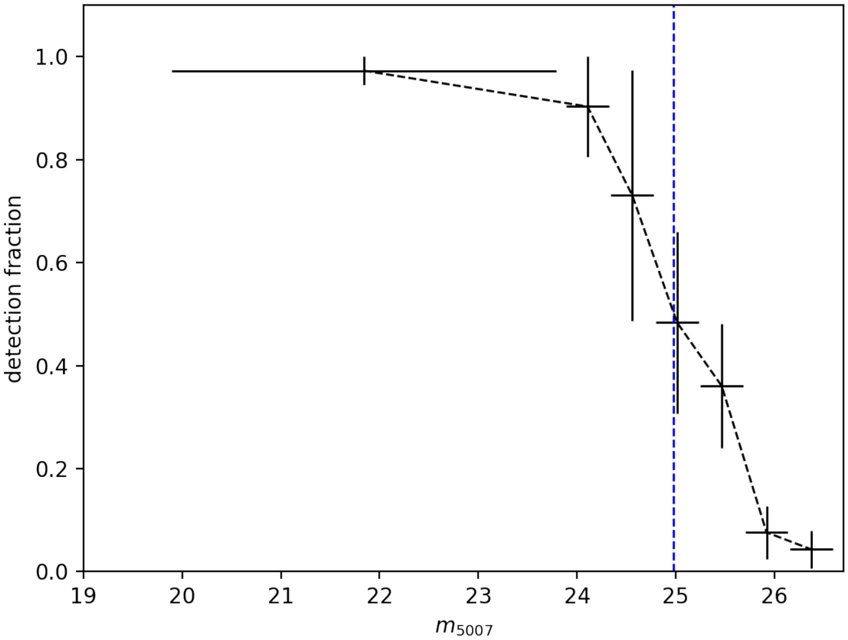

Figure 2.29: Fraction of PNe targeted with spectroscopic observations where a narrow [O III] 5007 Å emission line was detected. The uncertainty in detection fraction is the binomial proportion confidence-interval of observed PNe in any magnitude bin obtained using the Wilson score interval method (Wilson 1927). The blue dashed line shows the 50% detection limit of the spectroscopic follow-up.

to show that the rise in the PNLF is not dependent on the $F475W - F814W$ colour. Continuum stars are unlikely to have $F475W - F814W < 0$ and considering that we limit contamination from H II regions, the sources with $F475W - F814W < 0$ are most likely genuine PNe. The rise in the observed PNLF is indeed visible, even prior to completeness correction.

D-type SySts do not show an excess in the F814W filter. Thus, in our analysis a D-type SySt cannot be distinguished from a PNe. Even so, their numbers are expected to be far lower than that of a S-type SySt and so there should not be any significant number of D-type SySts plaguing our data. Mikołajewska et al. (2014) had one D-type SySt in the PHAT footprint, which we indeed misidentify as a PNe in our study.

2.7.3 Spectroscopically confirmed PNe and the faint end of the PNLF

A spectroscopic follow-up of a complete subsample of the M31 PNe was carried out with the Hectospec multifibre positioner and spectrograph on the Multiple Mirror Telescope (MMT) (Fabricant et al. 2005). Observations were made on September 15, 2018, and October 10, 2018, with an exposure time of 9000 seconds each, and also on December 4, 2018, with an exposure time

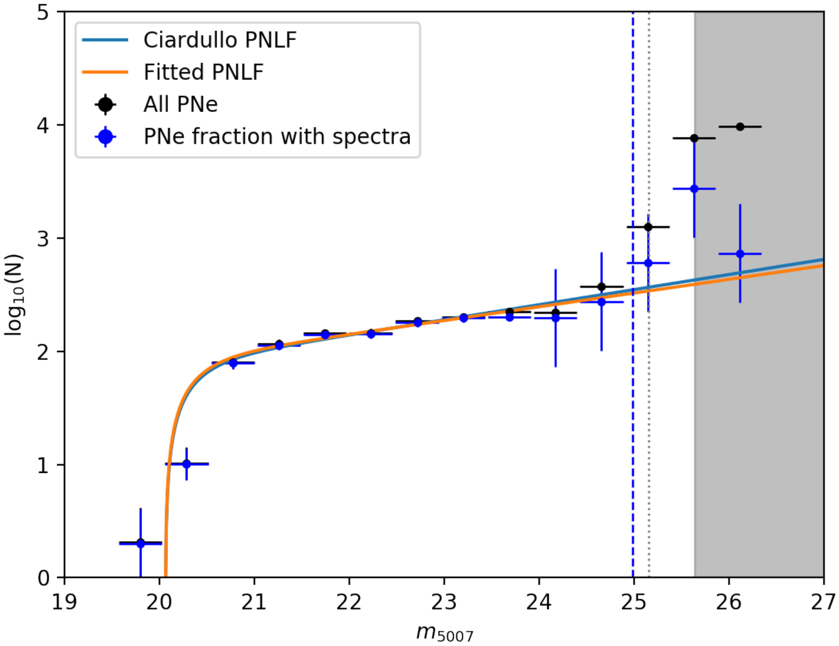

Figure 2.30: Completeness-corrected PNLF for all PNe (in black) fitted by both the generalised analytical formula for the cumulative PNLF (in orange) and the cumulative PNLF corresponding to the Ciardullo et al. (1989) analytical formula (in blue). The completeness-corrected PNLF accounting for the detection fraction from spectroscopy is shown in blue. The region beyond the limiting magnitude of the shallowest field (Field# 33_4) is shown in grey. The grey dotted line shows the 90% completeness limit of the shallowest field. The blue dashed line shows the 50% detection limit of the spectroscopic follow-up.

of 3600 seconds. The Hectospec 270 gpm grating was used and provided spectral coverage from 3650 to 9200 Å at a resolution of ∼ 5 Å. Each Hectospec fibre subtends 1.5″ on the sky. The fibres were placed on PNe candidates to maximise the observation of bright PNe, obtain their LOSV, and determine their chemical abundances. Of the 343 PNe candidates observed in M31, 129 had confirmed detection of the [O III] 4959/5007 Å emission lines. The [O III] 5007 Å emission line was detected in all cases with a signal-to-noise ratio higher than 8. All of them also had the Hα line present. Since our original PNe sample is largely devoid of H II regions, these observed sources are expected to be PNe. Details of the spectroscopy confirming them as PNe, along with their LOSV distribution and chemical abundances will be presented in a forthcoming paper (Bhattacharya et al. in preparation). The fraction of PNe detected as a function of magnitude is shown in Figure 2.29.

The spectroscopic follow-up shows that all the PNe candidates observed were confirmed as PNe, from the presence of [O III] 4959/5007 Å and Hα emission lines, down to 24.5 magnitude, but only a fraction of the targeted PNe candidates at fainter magnitudes could be confirmed.

While the required emission lines may not have been detected due to a low signal-to-noise ratio in the spectra for the faint targeted PNe candidates, it is also possible that those faint sources are continuum contaminants or background galaxies instead. Making the conservative assumption that all such sources are not PNe, we can modify the PNLF to account for this behavior. Since the rise in the PNLF is seen at different radii at about the same extent, we can compute the expected PNLF for the fraction of PNe that are conservatively confirmed spectroscopically, as shown in Figure 2.30. The PNLF is still consistent with the rise at the faint end of the PNLF although the uncertainty in the fraction with spectral confirmation is large.

2.7.4 Summary of the observational evidence for the rise at the faint end of the PNLF

Our investigation of the morphology of the PNLF is carried out at different positions and radial distances, and considering the effects of possible contaminants. The rise at the faint end of the PNLF is observed not only in the PNLF for the whole survey but also in individual fields, including the deepest field discussed in Section 2.6.4. In this field, it is already visible for the observed PNe even before completeness correction.

The rise at the faint end of the PNLF occurs from $m_{5007} \sim 24.5 - 25$ and is present at varying radial distances from the centre of M31 (Section 2.6.5). If the rise at the faint end of the PNLF was due to compact H II regions, it would be largely present only in the disc of M31 and not in all radial elliptical bins. In the survey region in common with *HST* data from PHAT, we also see the rise in the PNLF for those PNe with reliable PHAT counterparts (Section 2.6.6). The rise is especially evident when looking at the PNLF from PHAT-matched PNe with $F475W - F814W < 0$, a region in colour occupied almost exclusively by PNe, even prior to completeness correction (Figure 2.28). The spectroscopic follow-up also shows that the rise at the faint end of the PNLF is seen in confirmed PNe, albeit with large errors.

This observational evidence means that it is reasonable to believe that the rise in the PNLF is indeed physical and associated with the PN population and their parent stars. Rodríguez-González et al. (2015) fitted the two-mode PNLF for NGC 6822 (an irregular galaxy in the local group) and from its star formation history they show that the two modes of the PNLF may correspond to PNe associated with the two episodes of star formation, with the older parent stellar population corresponding to the fainter PNe. It is possible that the second PN population in M31 is associated with an older stellar population. With data from the PHAT survey, Williams et al. (2017) found that there was a burst of star formation $\sim 2 - 4$ Gyr ago throughout the M31 stellar disc. Bernard et al. (2015) studied individual HST fields associated with the disc and inner halo substructures of M31 to find that all the fields show a burst of star formation ~ 2 Gyr ago even though most of the stars in the M31 outer disc formed > 8 Gyr ago. Since the slope of the PNLF associated with PNe belonging to an older stellar population is seen to be steeper (Section 2.6.3), it is possible that the steep rise at the faint end of the PNLF is caused by PNe associated with the older population while the PNe associated with the ~ 2 Gyr old burst of star formation populate the brighter magnitudes of the PNLF.

Another possible reason for the rise in the faint end of the PNLF could be a change in opacity of the nebula of the PNe. The PNe occupying the bright end of the PNLF could be more opaque, with the nebula more efficiently reprocessing the ionising flux of the central star into [O III] 5007 Å, while the faint end may be populated by the more transparent PNe. The significant dependence of the PNLF on the considerations of the nebular transparency is also evident in the models by Gesicki et al. (2018). This scenario has previously been invoked to describe the dip in the PNLF seen in the SMC (Jacoby & De Marco 2002).

2.8 Conclusions

We present a 16 square degree survey in the disc and inner halo of M31 with the MegaCam at the CFHT using the narrow-band [O III] 5007 Å filter and the broad-band *g* filter. We identify point-lke PNe from the colour excess between the narrow-band and broad-band images down to a limiting magnitude between m_{5007} = 25.64 for the shallowest observed field to m_{5007} = 26.4 for the deepest observed field. We obtain 4289 PNe, the largest sample outside the MW, of which 1099 were previously observed by M06. Using a simulated PN population, we are able to account for incompleteness. We find counterparts in PHAT for 1023 of our identified PNe in the PHAT footprint. We find no resolved H II regions and a very small fraction (~3%) of PNe that could be stellar contamination. The α-parameter value obtained shows an increasing trend as we go further away from the centre of M31, but reasonably matches the value obtained by M06 for the central regions. The high value of the obtained $\alpha_{2.5,\mathrm{halo}}$ may be attributed to the bluer halo of M31 indicating that the stellar population in the halo, at radii larger than ~ 10 kpc, may be different from that of the inner disc.

The PNLF of the whole sample is complete down to ~5.5 mag fainter than the bright cut-off and shows a significant rise at the faint end. The generalised analytical formula fitted to the completeness corrected PNLF, for magnitudes brighter than $m_{5007} < 24$, returns parameters that are in agreement with those previously determined by Ciardullo et al. (1989). The rise at the faint end is seen at different elliptical radial distances from the centre and also in the PHAT-matched PNe implying that this rise is not associated with crowding. The rise is steeper than that seen in the LMC and the SMC. It is also not caused by contaminating sources like symbiotic stars, and seems to be a property of the parent population of the PNe, evident from the comparison with PHAT. Early findings from the spectroscopic follow-up also show that the rise in the number of PNe at faint magnitudes is physical, albeit with large uncertainty. It is possible that the PNe in M31 associated with the population created from the burst of star formation ~ 2 Gyr ago populate the brighter magnitudes of the PNLF, while those at the faint end are associated with the older population. It is also possible that the faint end is populated by PNe with more transparent nebulae, while those with opaque nebulae populate the bright end.

Chapter 3

Age-velocity dispersion relation in the disc from planetary nebulae

The contents of this chapter have been published as Bhattacharya et al. (2019b, Astronomy & Astrophysics, 631, A56)

3.1 Introduction

Discs in late-type galaxies contain two distinct dynamical populations: the 'cold' thin disc and the 'hot' thick disc, as found in the Milky Way (MW; e.g. Gilmore & Reid 1983) and nearby edge-on galaxies (Yoachim & Dalcanton 2006; Comerón et al. 2019). The thin-disc stars are younger with rotational velocities close to that of the collisional gas (Roberts 1966). The thick-disc stars are older and through dynamical heating, via secular evolution of the disc (Sellwood 2014) or mergers with satellite galaxies (Quinn & Goodman 1986), their rotational velocity decreases and velocity dispersion increases. In the solar neighbourhood, velocity dispersion appears to increase monotonically with age (Delhaye 1965; Casagrande et al. 2011), but it is not known if that is representative of the entire MW disc. A major part of the MW thick disc is also found to be chemically distinct from its dominant thin disc (see review by Bland-Hawthorn & Gerhard 2016). While mergers of satellite galaxies can dynamically heat galactic discs, the cold MW disc does not seem to have undergone any major merger event in the last 10 Gyr.

The Andromeda (M31) galaxy is the closest giant spiral galaxy to the MW. A number of substructures have been observed in the inner halo of M31 (McConnachie et al. 2018) that may have resulted from a recent merger (Fardal et al. 2013; Hammer et al. 2018). This may also be linked to an observed burst of star formation $\sim$ 2 Gyr ago (Bernard et al. 2015; Williams et al. 2017). It is well known that the velocity dispersion of a disc stellar population increases with age (Strömberg 1925; Wielen 1977). Dorman et al. (2015, hereafter D15) estimated the age–velocity dispersion relation (AVR) for the M31 disc with kinematics of stars from the SPLASH spectroscopic survey (Guhathakurta et al. 2005, 2006). D15 assigned ages to stars based on their position on the colour-magnitude diagram (CMD; see their Figure 6) from the PHAT survey (Dalcanton et al. 2012). While their main sequence (MS) stars are well separated in this CMD, the red giant branch (RGB) and asymptotic giant branch (AGB) loci overlap, resulting in a more ambiguous age separation. D15 construct the line-of-sight (LOS) velocity dispersion ($\sigma_{\rm LOS}$) versus radius profiles for the different populations. Their Fig. 16 shows a general trend of increasing $\sigma_{\rm LOS}$ with age, although with significant overlap of these profiles among populations and radii. On the basis of this trend, D15 state that the RGB population in M31 has a velocity dispersion that is nearly three times that of the MW.

Planetary nebulae (PNe) are discrete tracers of stellar populations and their kinematics have been measured in galaxies of different morphological types (e.g. Coccato et al. 2009; Cortesi et al. 2013; Pulsoni et al. 2018; Aniyan et al. 2018). Planetary nebulae in M31 have negligible contamination from MW PNe or background galaxies (Bhattacharya et al. 2019a). A number of PN properties are related to the mass, luminosity, and age of their progenitor stars. For example, from the central star properties derived from modelling nebular emission lines of PNe in the Magellanic clouds and M31, Ciardullo & Jacoby (1999) find a correlation between PN circumstellar extinction and the mass of their central star. Dust production of stars in the AGB phase scales exponentially with their initial progenitor masses for the $1 \sim 2.5 M_\odot$ range after which it remains roughly constant (Ventura et al. 2014). Additionally, PNe with dusty high-mass progenitors evolve faster (Miller Bertolami 2016) and so their circumstellar matter has little time to disperse, while PNe with lower central star masses evolve sufficiently slowly that a larger fraction of dust is dissipated from their envelopes (Ciardullo & Jacoby 1999). Kinematics of young and old stellar populations are well-traced by high- and low-mass giant stars, respectively, in the MW through their rotational velocity and velocity dispersion (e.g. Aniyan et al. 2016). In the M31 disc, different kinematics of younger and older stellar populations are expected to correlate with high- and low-extinction PNe, respectively.

In this paper, we identify PNe populations based on their extinction for the first time, allowing us to obtain two distinct age populations for the M31 disc. The data used in this work are described in Section 3.2. In Section 3.3, we first discuss classification of PNe based on their extinction values. We then obtain the rotational velocity curve and rotational velocity dispersion for the M31 disc high- and low-extinction PNe. We assign ages to the two PNe populations by comparing modelled central star properties in Kwitter et al. (2012, hereafter Kw+12) to the Miller Bertolami (2016) stellar evolution tracks. We then obtain the AVR for the M31 disc in Section 3.4 and compare it with previous determinations in M31 and the MW. From the comparison with simulated galaxies, we estimate the mass ratio of a possible merger event in the M31 disc. We summarise our results and conclude in Section 3.5.

3.2 Data description

Bhattacharya et al. (2019a) identified PN candidates in a 16 sq. deg. imaging survey of M31 with MegaCam at the CFHT, covering the disc and inner halo. Spectroscopic observations of a complete subsample of these PN candidates were carried out with the Hectospec multifibre positioner and spectrograph on the Multiple Mirror Telescope (MMT; Fabricant et al. 2005). The Hectospec 270 gpm grating was used and provided spectral coverage from 3650 to 9200 Å at a resolution of ~ 5 Å. Each Hectospec fibre subtends $1.5''$ on the sky and was positioned on

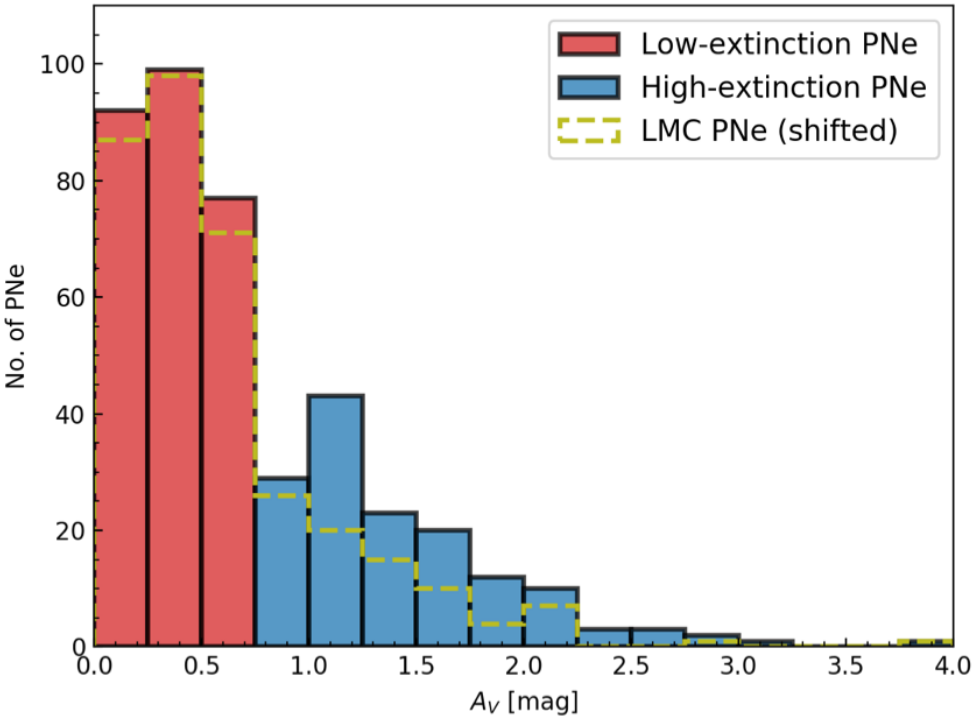

Figure 3.1: Histogram showing the distribution of extinction values for the San+12 and Bh+19b PNe. The high- and low-extinction PNe lie in the blue and red shaded regions, respectively. The distribution of extinction values of the LMC PNe observed by Reid & Parker (2010), shifted such that its peak corresponds to that of the M31, is shown in yellow.

the PN candidates in each field. On September 15, 2018, and October 10, 2018, with an exposure time of 9000 seconds each, two fields in the southwest region of the M31 disc were observed, while on December 4, 2018, with an exposure time of 3600 seconds, one field covering the northern part of the M31 disc and the Northern Spur substructure was observed. Of the 343 observed PNe candidates, 129 had confirmed detection of the [O III] 4959/5007 Å emission lines. Of these observed PNe, 92 showed the Hβ line and their extinctions (A_V) could be determined from the Balmer decrement. Details of the spectroscopic observations of the PNe along with the extinction determination and chemical abundances will be presented in a forthcoming paper (Bhattacharya et al. 2019b in preparation, hereafter Bh+19b).

Sanders et al. (2012, hereafter San+12) also studied PNe and H II regions in the M31 disc and outer bulge using Hectospec on the MMT. These latter authors observed 407 PNe; 321 of them with the Hβ line detected and subsequent reliable extinction measurements. The combined sample of PNe with extinction measurements in M31 from San+12 and Bh+19b therefore consists of 413 PNe.

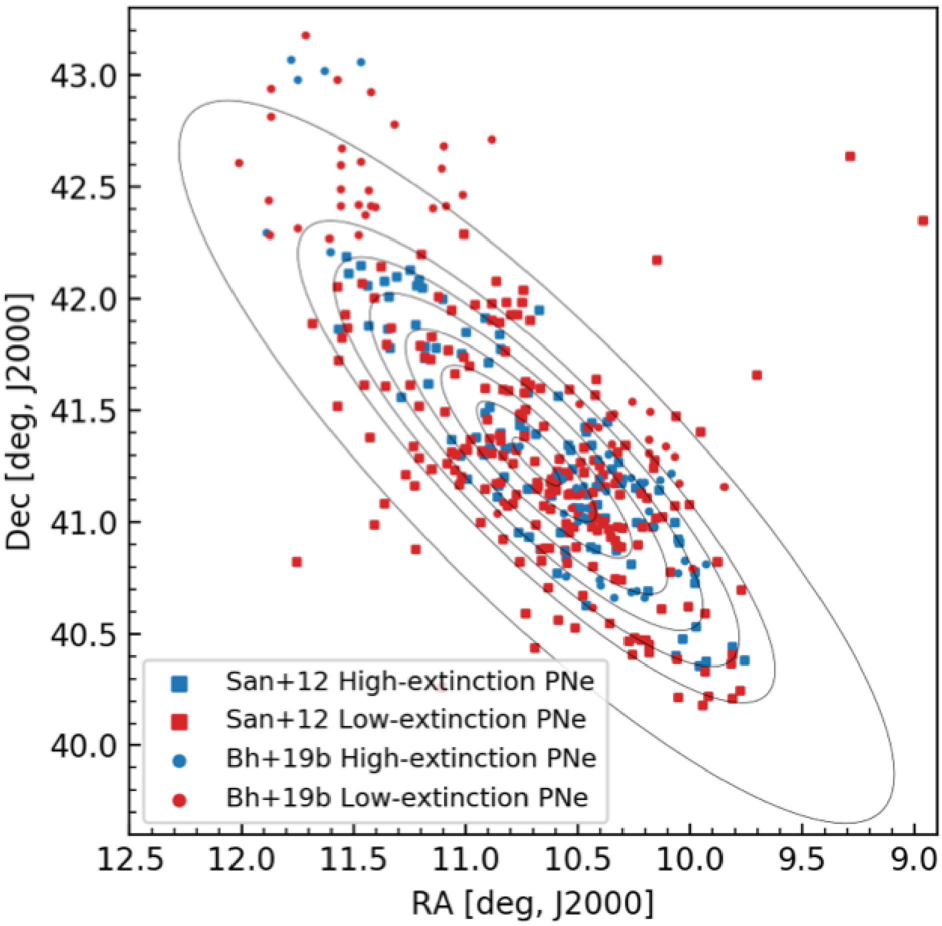

Figure 3.2: Position on sky of San+12 PNe (squares) and Bh+19b PNe (circles). The high-extinction PNe are shown in blue while the low-extinction PNe are shown in red. The PNe are divided into elliptical bins to obtain rotation curves.

3.3 Analysis

3.3.1 Classification of planetary nebulae based on extinction measurements

The distribution of the M31 PNe extinction values (see Figure 3.1) exhibits a sharp drop at A_V = 0.75 mag, increases again at A_V =1–1.25 mag, and drops off gradually at larger values of A_V. Figure 3.1 also shows the distribution of the LMC PNe extinction values (Reid & Parker 2010), shifted such that their peak (originally in the A_V = 0.75–1 mag bin) is coincident with the distribution of the M31 PNe extinction values (A_V = 0.25–0.5 mag bin). The shifted distribution of the LMC PNe extinction values also shows a sharp drop at A_V = 0.75 mag and gradually falls off while that of the M31 disc PNe shows a secondary peak at A_V =1–1.25 mag. The distribution of M31 PNe extinction values around the first higher peak possibly results from an older parent stellar population (numerically more prevalent), spawning PNe having lower

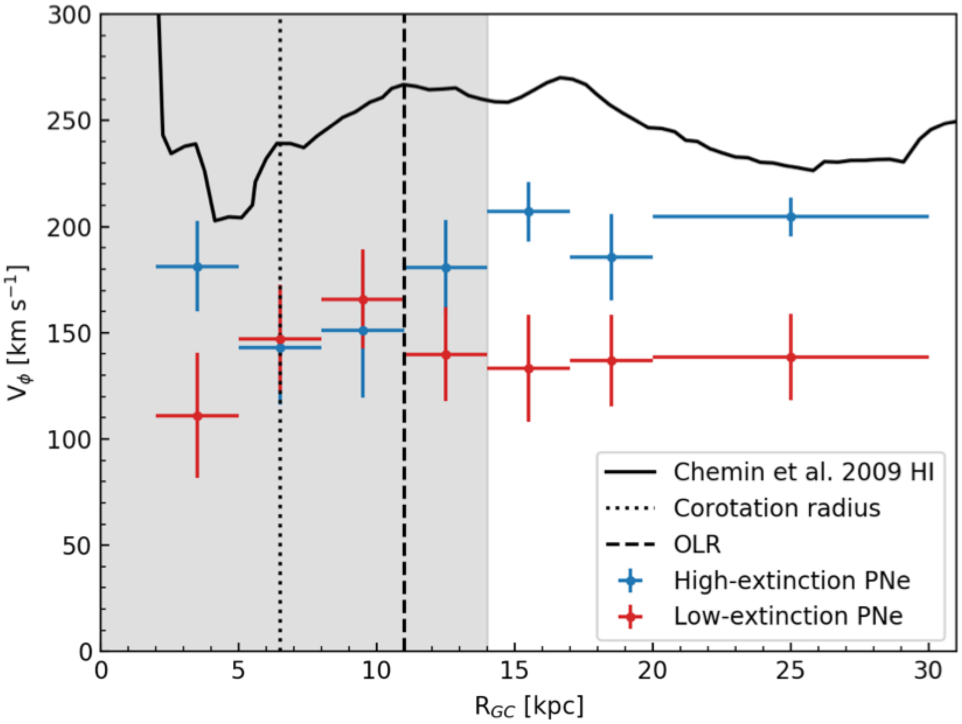

Figure 3.3: Rotational velocities for the high- and low-extinction PNe are shown in blue and red, respectively. The black line shows the H I rotation velocity from Chemin et al. (2009). The corotation radius (black dotted line) and outer Lindblad resonance (OLR; black dashed line) of the M31 bar are as found by the models of Blaña et al. (2018). The grey shaded region is possibly influenced by different dynamical heating events and is not discussed here.

circumstellar extinction values (further discussions in Section 3.3.3), while the secondary peak at higher circumstellar extinction values would indicate the presence of a younger parent stellar population.

We therefore classify M31 PNe with extinction values higher and lower than $A_V = 0.75$ mag as high- and low-extinction PNe, respectively. Our PNe sample is then divided into 145 high- and 268 low-extinction PNe, which are expected to be associated with younger and older parent stellar populations, respectively. We note that using a different extinction value within the $A_V = 0.65 - 0.85$ mag range for the classification of the two PN populations has negligible effect on the rotation curves obtained in Section 3.3.2. The high-extinction PNe classification is not biased by the LOS dust attenuation in M31 according to our investigation in Appendix B.1. Figure 5.1 shows the spatial distribution of the PNe in the M31 disc.

3.3.2 Rotation curves

For both San+12 and Bh+19b PNe, the LOS velocities (LOSVs) are obtained from full spectral fitting, resulting in an uncertainty of 3 km s^{-1}. The PNe are de-projected on to the galaxy plane

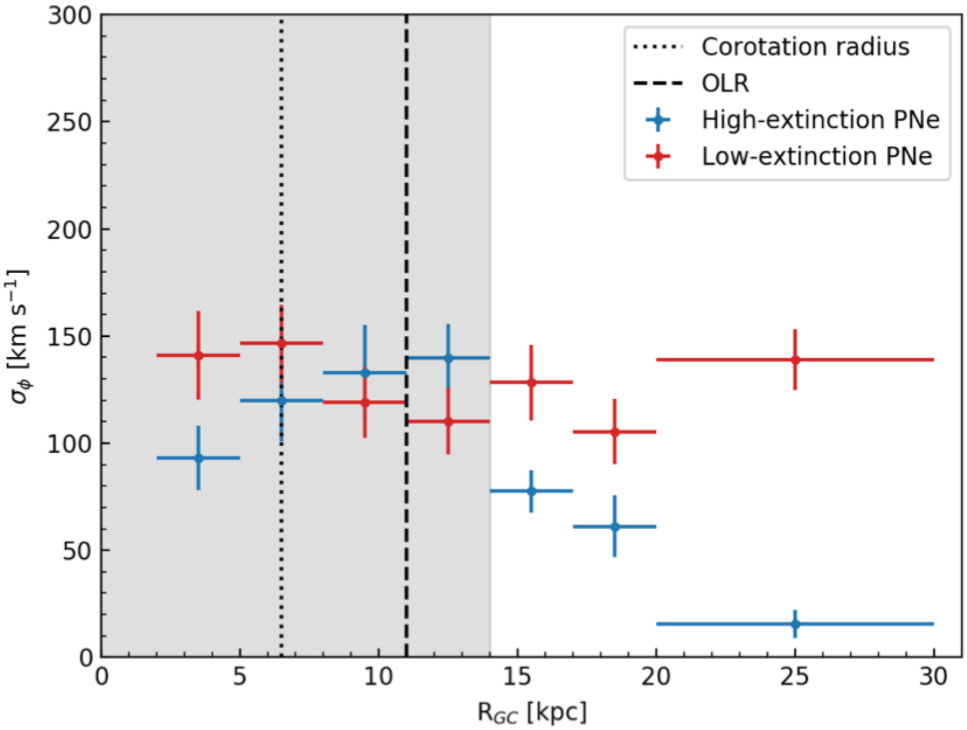

Figure 3.4: Rotational velocity dispersion for the high- and low-extinction PNe are shown in blue and red, respectively. The black lines and grey shaded region are the same as in Figure 3.3.

based on the position angle (PA = 38°) and inclination (i = 77°) of M31 in the planer disc approximation. They are then binned into seven elliptical bins (Figure 5.1) with the first six bins covering 3 kpc each starting at a deprojected major axis radius $\mathrm{R_{GC}}$ = 2 kpc from the centre of M31 and the final bin covering $\mathrm{R_{GC}}$ = 20–30 kpc. Planetary nebulae observed outside $\mathrm{R_{GC}}$ = 30 kpc probably belong to the inner halo substructures, possibly the Northern Spur, and are hence not included in the analysis. The position of the PNe in each bin can be described using cylindrical coordinates, with the $z = 0$ kpc plane as the local plane of the galaxy, $r = 0$ kpc as the galactic centre, and ϕ measured counterclockwise from the position angle of M31. The LOSV for the PNe, V_{LOS}, in each bin is then fitted by the following equation:

$$\mathrm{V_{LOS}} = \mathrm{V_{sys}} + \mathrm{V}_\phi \cos(\phi) \sin(\mathrm{i}) + \mathrm{V_R} \sin(\phi) \sin(\mathrm{i}) + \mathrm{V_{err}}, \tag{3.1}$$

where V_{sys} is the systemic velocity of M31, assumed to be −309 km s^{-1} (Merrett et al. 2006); V_ϕ is the rotational velocity in the plane of the galaxy; V_{R} is the radial streaming motion that can be inwards or outwards; i is the inclination of M31 mentioned previously; and V_{err} = 3 km s^{-1} is the uncertainty in measurement. LOSVs for the high- and low-extinction PNe are fitted separately in each elliptical bin using LMFIT (Newville et al. 2014) to obtain V_ϕ, V_{R}, and ϕ as the parameters describing the mean motion of the PNe populations in each bin. We note that V_{Z}, the off-plane motion in the z direction, is considered to be zero as no net off-plane motion is expected for PNe in the disc.

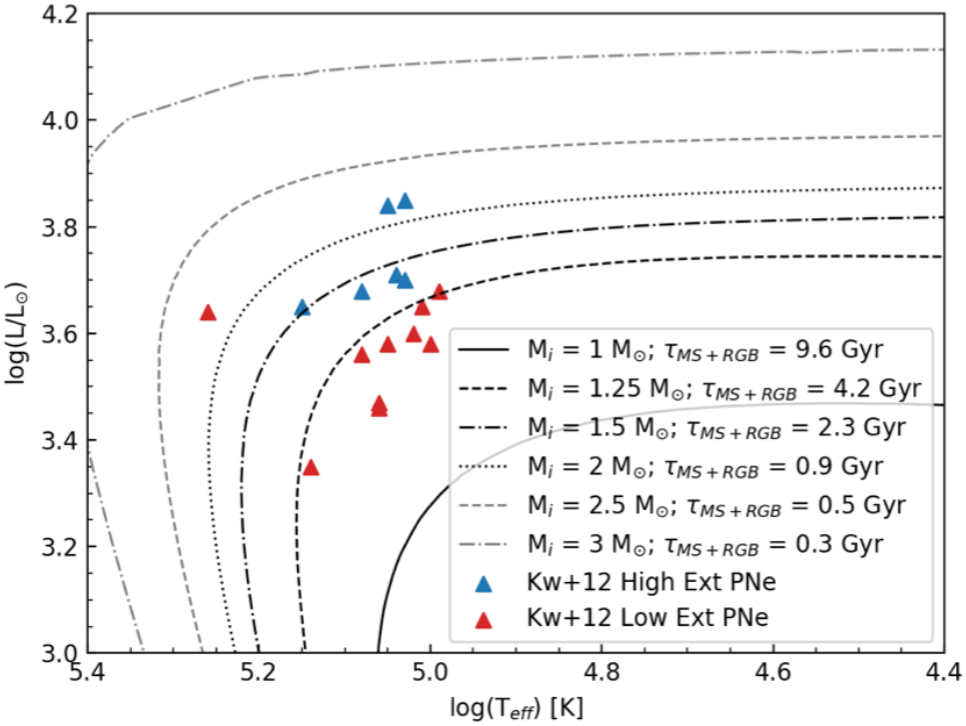

Figure 3.5: High- and low-extinction PNe observed by Kw+12 are shown in blue and red, respectively in the log(L/L$_\odot$) vs. log(T$_\text{eff}$) plot. The stellar evolution tracks from Miller Bertolami (2016) corresponding to metallicity, $Z_0 = 0.01$, are shown in black. The initial stellar mass and $\tau_\text{MS+AGB}$ are also labelled.

The obtained V_ϕ rotation velocity curves for the high- and low-extinction PNe are shown in blue and red, respectively, in Figure 3.3. The uncertainty in the fitted V_R is relatively high and their values are close to zero in each bin. Thus, no clear evidence of radial streaming motion is found in either PN population. Setting $V_\text{R} = 0$ km s^{-1} also has a negligible effect on the rotation curves. The difference in rotational velocities between the gas and the stellar population in a disc is a measure of the asymmetric drift and is higher for older stellar populations that have more non-circular orbits as a result of dynamical heating (Strömberg 1946). Outside $\text{R}_\text{GC} = 14$ kpc, the high-extinction PNe have a rotational velocity closer to that of the H I gas derived by Chemin et al. (2009), indicative of a dynamically young population, while that of the low-extinction PNe is much further away from that of the H I gas, indicative of a dynamically older population (Strömberg 1946).

We estimate the rotational velocity dispersion, σ_ϕ, as the standard deviation with respect to the fitted V_ϕ in each bin. The σ_ϕ profiles for the high- and low-extinction PNe are shown in Figure 3.4. Outside $\text{R}_\text{GC} = 14$ kpc, σ_ϕ is lower for the high-extinction PNe – as expected for a dynamically young population – than that measured for low-extinction PNe, a dynamically older population. In the outermost bin, σ_ϕ increases sharply for the low-extinction PNe population. This may be due to the presence of PNe associated with the M31 inner halo substructures like the Northern Spur or the NGC 205 loop at this distance from the M31 centre. Within 14 kpc, both the high- and low-extinction PNe samples show an overall reversal in the V_ϕ rotation curves and in σ_ϕ, but both populations are dynamically hot. While this might be linked to the interaction of the disc with the bar in M31 as modelled by Blaña et al. (2018) for the inner two bins, other sources of dynamical heating may be at play for $R_{GC} = 8 - 14$ kpc, either stemming simply from the secular evolution of the disc and/or through a merger event. This will be investigated in a forthcoming paper (Bhattacharya et al. 2019b in preparation). Given the large values of $\sigma_\phi \approx 130$ km s^{-1} for the low-extinction PNe, their parent stellar population may be distributed as a flattened spheroid, rather than a planer disc. Given the inclination of the M31 disc, deprojecting these PNe as a planer disc may result in an overestimate of their R_{GC} values, leading to a bias in the estimated σ_ϕ. We investigate the effect of disc thickness in Appendix B.2. We find that the scale height of the low-extinction PNe is $H_{\mathrm{Low\ ext}} \approx 0.86$ kpc. Within our 3 kpc bin sizes, only $\sim 10\%$ of the low-extinction PNe may be included in a different bin. The effect on the estimated σ_ϕ values of these $\sim 10\%$ PNe in different bins is within the measurement uncertainties.

3.3.3 Ages of the M31 disc planetary nebulae

Kw+12 observed sixteen PNe in the outer disc of M31 to measure various emission lines and determine chemical abundances. They used the CLOUDY photoionization codes (Ferland et al. 1998) to estimate the bolometric luminosity ($L/L_\odot$) and effective temperature (T_{eff}) of the central stars of these PNe. Figure 3.5 shows their estimated $\log(L/L_\odot)$ versus $\log(T_{\mathrm{eff}})$, coloured by their extinction classification (high-extinction: blue; low-extinction: red). The post-AGB stellar evolution tracks from Miller Bertolami (2016) for a metallicity $Z_0 = 0.01$ are also plotted in Figure 3.5. It is clear that the high-extinction PNe in this subsample lie either around the tracks corresponding to an initial progenitor mass of 1.5 $M_\odot$ and age ($\tau_{\mathrm{MS+AGB}}$; lifetime in main-sequence and AGB phases) of 2.3 Gyr or are even younger with higher initial progenitor masses. The low-extinction PNe in this sub-sample, barring one, are older than 4.2 Gyr with initial progenitor mass lower than 1.25 $M_\odot$. We note that these ages could be uncertain up to $\sim$ 1 Gyr based on the estimations by Kw+12. We may therefore assign the mean ages corresponding to the Kw+12 high- ($\sim$ 2.5 Gyr) and low- ($\sim$ 4.5 Gyr) extinction PNe to those with the corresponding extinction values in the San+12 and Bh+19b PNe populations.

3.4 Age–velocity dispersion relation

3.4.1 The observed age-velocity dispersion relation in M31

We obtain the AVR in M31 for two elliptical bins with R_{GC} = 14–17 and 17–20 kpc. These are presented in Figure 3.6, clearly showing the increase in the velocity dispersion with age. In Figure 3.6, we also present the age–velocity dispersion value for the MS ($\sim$ 30 Myr age), $\sigma_{\phi,\,\mathrm{MS}} = 30 \pm 10$ km s^{-1}, obtained by D15 in the R_{GC} = 14–17 kpc bin.

Based on models fitting the star formation rate, gas profiles, and metallicity distributions of the M31 and MW discs, Yin et al. (2009) find that R_{GC}=19 kpc in the M31 disc is the equivalent

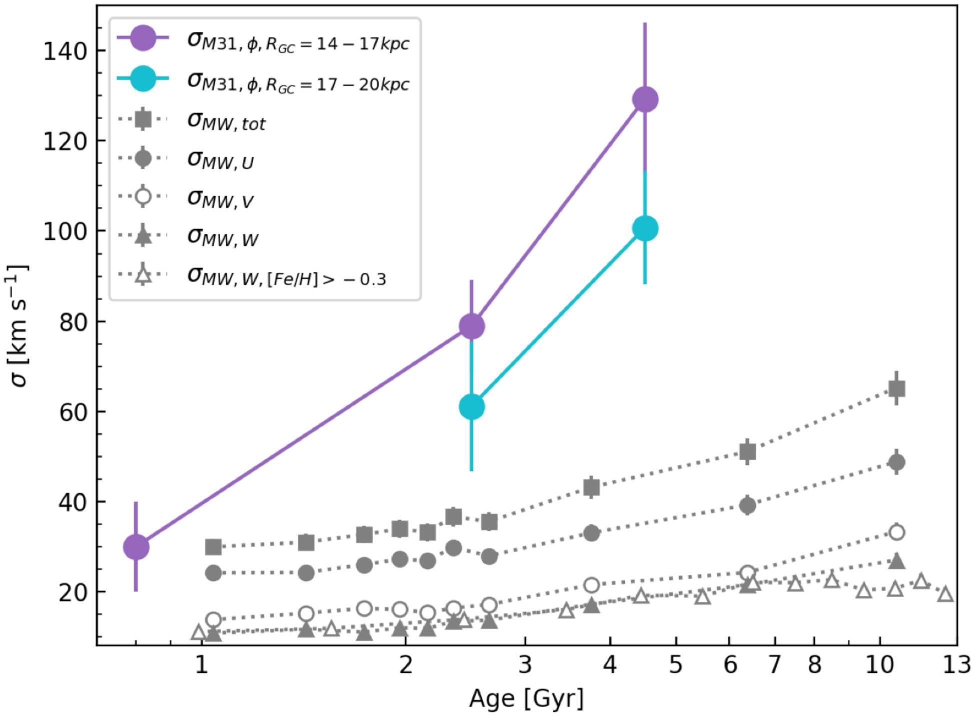

Figure 3.6: Age–velocity dispersion relation for PNe in the M31 disc at R_{GC} = 14–17 and 17–20 kpc is shown in magenta and cyan, respectively. The assigned age is shown in log scale with the MS (~ 30 Myr age; D15) in the R_{GC} = 14–17 kpc bin shown at 0.8 Gyr for visual clarity. The AVR obtained in the solar neighbourhood in the MW (Nordström et al. 2004) is shown in grey for comparison. Their total velocity dispersion is shown with squares while the velocity dispersion in the space velocity components (*U, V, W*) is shown with filled circles, open circles, and filled triangles, respectively. We also present, with open triangles, the velocity dispersion in the W component from Aniyan et al. (2018) for only those MW stars with [Fe/H]< −0.3, showing a flattening in the MW AVR at older ages.

distance, in disc scale lengths, of the Sun ($R_\odot$=8 kpc) in the MW disc. We therefore compare the velocity dispersion of the MW disc obtained in the solar neighbourhood by Nordström et al. (2004) to our σ_ϕ in the R_{GC}=17–20 kpc bin, where $\sigma_{\phi,\,2.5\,\mathrm{Gyr}} = \sigma_{\phi,\,\mathrm{High\ ext}} = 61 \pm 14$ km s^{-1} and $\sigma_{\phi,\,4.5\,\mathrm{Gyr}} = \sigma_{\phi,\,\mathrm{Low\ ext}} = 101 \pm 13$ km s^{-1}. Nordström et al. (2004) describe the MW velocity dispersion in space-velocity components (*U, V, W*), defined in a right-handed Galactic system with *U* pointing towards the Galactic centre, *V* in the direction of rotation, and *W* towards the north Galactic pole (Figure 3.6). The equivalent in the MW disc for the σ_ϕ in the M31 disc would be some combination of $\sigma_{\mathrm{MW,U}}$ and $\sigma_{\mathrm{MW,V}}$ with a value intermediate between the two (D15). We compare our obtained σ_ϕ of the M31 disc with the $\sigma_{\mathrm{MW,U}}$, which is ~ 29 km s^{-1} and ~ 35 km s^{-1} for 2.5 Gyr and 4.5 Gyr old populations, respectively. In the R_{GC}=17–20 kpc bin, the σ_ϕ of the 2.5 Gyr and 4.5 Gyr old populations in M31 are about twice and three times that of the $\sigma_{\mathrm{MW,U}}$ of the 2.5 Gyr and 4.5 Gyr old MW thin disc populations, respectively.

3.4.2 Comparison with previously measured and simulated age–velocity dispersion relations

The AVR in M31 was previously estimated by D15 from the σ_{LOS} of stars whose classification in different age bins suffered from ambiguity. Their observations were also limited to the PHAT survey footprint, covering about a quarter of the M31 disc along its major axis out to $\mathrm{R_{GC}} \sim 18$ kpc. Our observed PNe sample covers the entire M31 disc out to $\mathrm{R_{GC}} = 30$ kpc, and the high- and low-extinction PNe are well separated in age (Figure 3.5). The σ_ϕ values for the high- and low-extinction PNe agree within errors with that obtained by D15 for older AGB (~ 2 Gyr old) and RGB (~ 4 Gyr old) stars, respectively. Quirk et al. (2019) fitted the rotation curves for stellar populations identified by D15. In the $\mathrm{R_{GC}} = 14 - 17$ kpc bin, V_ϕ for the high-extinction PNe is in good agreement with that obtained by Quirk et al. (2019) for older AGB stars, but for the low-extinction PNe it is lower than that of RGB stars by $\sim$ 30 km s^{-1}. This is possibly due to their RGB population being contaminated by younger AGB stars, resulting in a V_ϕ value that is closer to that of the HI gas.

The AVR for the M31 disc shows a steep slope in the 0–2.5 Gyr age range and an even steeper slope in the 2.5–4.5 Gyr age range than those for the MW disc in similar age bins. The AVR of the MW disc is considered to be driven by secular evolution channels (see review by Sellwood 2014). An AVR with velocity dispersion increasing gradually with age is also measured in simulated disc galaxies with similarly quiescent merger histories (from zoom-in cosmological simulations by House et al. 2011; Martig et al. 2014). However, simulated disc galaxies undergoing a single merger show a significant increase in velocity dispersion for stellar populations older than the end of the merger (Martig et al. 2014, see their Figure 2), with larger velocity dispersion for higher merger mass ratios. After the end of the merger, it takes $\sim$ 2 Gyr for stellar populations to form with velocity dispersion values similar to those for quiescent discs. The high $\sigma_{\phi,\,4.5\ \mathrm{Gyr}}$ values in the M31 disc are reminiscent of those seen in populations older than the merger event in simulated galaxies. The lower $\sigma_{\phi,\,2.5\ \mathrm{Gyr}}$ values in the M31 disc are reminiscent of the lower values predicted by simulations some time after the end of the merger. Finally, the velocity dispersion for the MS in M31 is akin to that for quiescent discs, also observed at least $\sim$ 2 Gyr after the merger event in the simulated galaxies. Therefore, we may deduce from the observed AVR in the M31 disc that a single merger event took place 2.5 – 4.5 Gyr ago.

3.4.3 Estimation of the merger mass ratio

In the framework of a single merger in the M31 disc, we estimate the merger mass ratio and satellite mass required to produce the dynamically hot 4.5 Gyr-old population with disc scale height $\mathrm{H_{4.5\ Gyr}} = \mathrm{H_{Low\ ext}} \approx 0.86$ kpc (Appendix B.2). We use the relation between disc scale height (H) and satellite-to-disc-mass ratio ($\mathrm{M_{sat}/M_{disc}}$) described by Hopkins et al. (2008) for a satellite galaxy (assumed to be a rigid body) that merged with a disc galaxy (assumed to be a thin disc) on an in-plane prograde radial orbit. The relation in the case of a satellite merging with a Mestel (1963) disc galaxy, having constant circular velocity $V_{c,disc}$, is as follows:

$$\frac{\Delta \mathrm{H}}{\mathrm{R_{e,disc}}} = \alpha_{\mathrm{H}}\,(1 - \mathrm{f_{gas}})\,\frac{\mathrm{M_{sat}}}{\mathrm{M_{disc}}}\,\tilde{\mathrm{h}}(\mathrm{R/R_{e,disc}}), \tag{3.2}$$

where ΔH gives the increase in scale height in the disc galaxy following the merger; $\alpha_{\rm H} = 1.6\tilde{\rm v}$ is a derived constant with $\tilde{\rm v} = ({\rm V}_{\rm c,disc}/{\rm V}_{\rm h})^2$, V_h being the halo circular velocity; $f_{\rm gas}$ is the gas fraction in both the disc galaxy and satellite (assumed to be equal) before the merger; R is the galactocentric radius of the population with scale height H; and $R_{\rm e,disc}$ is the disc effective radius.

We assume that the M31 disc evolved by secular evolution prior to the merger event. Therefore, we adopt the scale height of the old thin disc of the MW as measured in the solar neighbourhood, $H_{MW} \approx 300$ pc (see Bland-Hawthorn & Gerhard 2016, and references therein), as the pre-merger scale height $H_{\rm pre-merger}$ for the M31 disc. Thus, $H_{\rm pre-merger} \approx H_{\rm MW} \approx 0.3$ kpc and $\Delta H = H_{4.5\ \rm Gyr} - H_{\rm pre-merger} \approx 0.56$ kpc. R = 18.5 is the median of the $R_{\rm GC}$=17–20 kpc bin, which is the equivalent disc scale length in M31 to the solar neighbourhood. From Blaña et al. (2018), we adopt $V_{c,disc} = 250$ km s^{-1}, $R_{\rm e,disc} = 9.88$, and $V_h = 182$ km s^{-1}. The present-day gas fraction in M31 is ∼ 9% (Yin et al. 2009) but M31 is observed to have undergone a burst of star formation ∼ 2 Gyr ago which produced ∼ 10% of its mass (Williams et al. 2017). Assuming that the stellar mass formed in this burst was present as gas mass before the merger, we adopt $f_{\rm gas} = 0.19$. Plugging these values into Equation 3.2, we obtain $M_{\rm sat}/M_{\rm disc} \approx 0.21$ or $M_{\rm sat} : M_{\rm disc} \approx 1 : 5$. Given that the total mass of the M31 disc is 7×10^{10} $M_\odot$ (Yin et al. 2009), a 1.4×10^{10} $M_\odot$ satellite is required to dynamically heat the M31 disc.

3.5 Summary and conclusion

We classify the observed sample of PNe based on their measured extinction values into high- and low-extinction PNe which are associated with 2.5 Gyr and 4.5 Gyr parent populations, respectively. By fitting rotation curves to the two PNe populations in de-projected elliptical bins, we find that the high- and low-extinction PNe are dynamically colder and hotter, respectively, especially at $R_{\rm GC} = 14 - 20$ kpc (Figures 3.3, 3.4). We thus obtain the AVR at these radii and find that σ_ϕ increases with age in the M31 disc, which is dynamically much hotter than the stars in the MW disc of corresponding ages.

There is an interesting timescale coincidence between the age of the high-extinction PNe and the ∼ 2 Gyr old burst of star formation observed both in the stellar disc and inner halo of M31 (Bernard et al. 2015; Williams et al. 2017). We speculate that most of the high-extinction PNe, causing the secondary peak in the extinction distribution (Figure 3.1), are those whose progenitors formed during the ∼ 2 Gyr old star formation burst, while the low-extinction PNe were likely formed earlier. The high-extinction PNe are kinematically tracing the younger thin disc of M31 outside $R_{\rm GC} = 14$ kpc from the centre and are clearly separated, both in V_ϕ and σ_ϕ, from the dynamically hotter low-extinction PNe which may be associated with the thicker disc. Some low-extinction PNe may also be associated with the old thin disc and inner halo of M31.

Using hydrodynamical simulations, Hammer et al. (2018) argue that a single major merger 2 – 3 Gyr ago, where the satellite eventually coalesced to build up the M31 bulge after multiple passages, can explain the dynamical heating of the M31 disc. These latter authors also predict a merger with a mass ratio of at least 1:4.5 from their simulations, and also a decreasing trend in the velocity dispersion with radius, as observed, albeit within errors, in Figure 3.4. Such a merger could also explain the burst of star formation ∼ 2 Gyr ago and the presence of the M31 inner halo substructures. Fardal et al. (2013) also use hydrodynamical simulations to predict the formation of the giant stream from a merger $\sim$ 1 Gyr ago with a $\sim 3.2 \times 10^9 M_\odot$ satellite. The AVR measured in the M31 disc using PNe is indicative of a single merger occurring 2.5 – 4.5 Gyr ago with a merger mass ratio $\approx$ 1:5, with a 1.4×10^{10} $M_\odot$ satellite galaxy. Such a galaxy would have been the third largest member of the local group, more massive than M33 (Kam et al. 2017). This is consistent with the prediction from Hammer et al. (2018). In conclusion, the kinematics of the M31 disc PNe have been able to shed light on the recent dynamical evolution of M31. Our next step is to use PNe to further investigate the interface of the disc and inner halo of M31.

Chapter 4

Constraints from deep planetary nebula luminosity functions on the origin of the inner halo substructures in M 31

The contents of this chapter have been submitted as a paper for publication to Astronomy & Astrophysics

4.1 Introduction

Within the Lambda cold dark matter (ΛCDM) cosmological model, galaxies evolve by hierarchical mass accretion (White & Rees 1978; Bullock & Johnston 2005). Fossil records of these processes are observed in the outskirts of massive galaxies in the form of shells, streams, tidal tails and other substructures (e.g. Mihos et al. 2005; Martínez-Delgado et al. 2010; Crnojević et al. 2016). The masses and chemical properties of the accreted satellites may be uncovered from the kinematics and chemical abundances of surviving substructures (Johnston et al. 2008). Andromeda (M 31) is the nearest giant spiral galaxy to the Milky Way (MW) at a distance of $\sim$ 773 kpc (Conn et al. 2016). The Pan-Andromeda Archaeological Survey (PAndAS; McConnachie et al. 2009, 2018) produced a map of resolved red giant branch (RGB) star counts that revealed multiple substructures (Figure 4.1) out to a projected radii of $\sim$ 150 kpc around M 31. These features unveiled the tumultuous merger history of M 31. With faint structures detected down to unprecedented surface brightness levels ($\mu_V \sim 33$mag arcsec^{-2}), M 31 provides the best current laboratory for studying the signatures of extended galaxy assembly.

The Giant Stream is the most prominent substructure in the M 31 halo. It was first discovered by Ibata et al. (2001) who linked its origin to that of an infalling satellite. The subsequent discoveries of other substructures, particularly those near the disc-halo interface, namely – North East Shelf (NE-Shelf), G1-Clump, Northern Clump (N-Clump), Western Shelf (W-Shelf) and Stream D, led to intense speculations on their origin. Fardal et al. (2013) showed that N-body simulations of a satellite of $\sim 3.2 \times 10^9 \mathrm{M}_\odot$ infalling along the Giant Stream $\sim$ 1 Gyr ago can reproduce the structure and kinematics of the Giant Stream and also of the NE and W shelves.

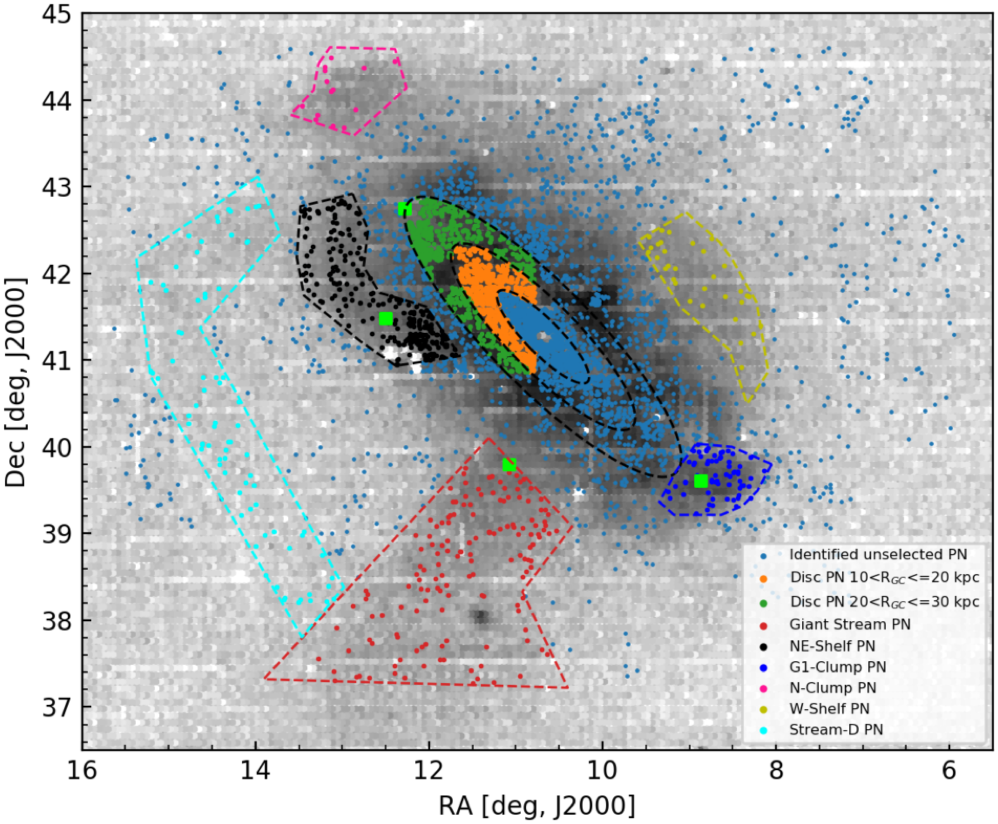

Figure 4.1: Position on sky of PNe (all marked points) identified by Paper I and Bhattacharya et al. (2020b, in prep.). They are overlaid on the number density map of RGB stars from PAndAS (McConnachie et al. 2018), binned for visual clarity and shown in grey. The PNe selected for the PNLF analysis in the two disc regions and six substructure regions are marked with different colours. North is up, east is left. The HST fields observed by Bernard et al. (2015) to obtain the SFH of four of the M 31 regions have been marked with green squares.

The N and G1-Clump, though, do not arise naturally in models of the dissolution of the Giant Stream progenitors from minor mergers, and they were linked to distinct accretion events of dwarf galaxies (Ferguson & Mackey 2016). Most recently, using hydrodynamical simulations, Hammer et al. (2018) argued that a single merger of a more massive satellite with total mass $1.4 \times 10^{10} M_{\odot}$, occurring 2 – 3 Gyr ago, is able to perturb the pre-existing M31 disc leading to the origin of the substructures along its major axis, as well as that of the Giant stream and the associated NE and W shelves.

Not only the morphology of the low surface brightness substructures, but also the 2 Gyr old burst of star formation, observed in the M 31 disc and in some inner halo *Hubble* Space Telescope (HST) pointings (Bernard et al. 2015; Williams et al. 2017), and the dynamical heating of the disc (Dorman et al. 2015; Bhattacharya et al. 2019b, hereafter Paper II) are consistent with the predictions from the fairly major merger in M 31 (Hammer et al. 2018). However, further investigation is required to link the origin of any of the observed substructures with either the pre-existing disc or the satellite remnant.

Indeed, the HST observations by Richardson et al. (2008) and subsequent star formation histories (SFHs) computed by Bernard et al. (2015) for 14 pencil beam pointings, some of which are aligned with the M 31 overdensities, have stellar populations similar to that of the Giant Stream, while others are more similar to the M 31 disc. An intrinsic limit of this approach though is the tiny area coverage of each single HST field within a significantly more extended subregion in the M 31 inner halo (Williams et al. 2017). Therefore the properties sampled in such tiny area may not provide a robust measurement of the average stellar population parameters, if there is a significant variance/gradient in the stellar population of any subregion, for example the metallicity gradient observed within the Giant Stream (Conn et al. 2016). However, a robust assessment of the average stellar population properties within an entire substructure is feasible by the accurate measurements of the deep luminosity function of their associated Planetary Nebulae (PNe) populations.

PNe are identified from their relatively strong [O III] 5007Å emission and negligible continuum. The characteristic [O III] 5007Å (M_{5007}) PN luminosity function (PNLF) was first described by Ciardullo et al. (1989). The analytical formula

$$N(M) \propto e^{0.307M}(1 - e^{3(M^{*}-M)}) \tag{4.1}$$

was fitted to the bright PNe detected in the centre of M 31 (Ciardullo et al. 1989). The PNLF is a reliable secondary distance indicator for determining galactic distances out to ~20 Mpc by virtue of its invariant absolute bright cut-off, M*, currently measured at $M^{*} = -4.54 \pm 0.05$ at near-solar metallicities (Ciardullo et al. 2013). While M^{*} gets fainter in low metallicity populations (e.g. Ciardullo & Jacoby 1992; Ciardullo et al. 2002; Hernández-Martínez & Peña 2009), according to theoretical predictions by Dopita et al. (1992), it seems to be invariant on either the age of the population or galaxy morphological type. The faint end of the PNLF is theoretically expected to follow an exponential function (Jacoby 1980) describing the slow evolution of the central star (CSPN) embedded in a rapidly expanding, optically thin nebula (Henize & Westerlund 1963).

The slope of the PNLF measured at a few magnitudes fainter than its bright cut-off is observed to vary depending on the SFH of the parent stellar population. In galaxies where the PNLF has been observed to ~3 mag below M*, steeper PNLF slopes were observed for elliptical galaxies with older stellar populations (e.g. Longobardi et al. 2013; Hartke et al. 2017) and conversely flatter slopes for younger populations (e.g. M33; Ciardullo et al. 2004). In surveys deeper than ~3 mag below M*, the shape of the PNLF may exhibit further changes in slope, as seen in the Large Magellanic Cloud (LMC; Reid & Parker 2010) or dips, e.g. that in the Small Magellanic Cloud (SMC; Jacoby & De Marco 2002) and NGC 6822 (a Local Group dwarf irregular galaxy; Hernández-Martínez & Peña 2009). Rodríguez-González et al. (2015) describe a two-mode PNLF for NGC 6822 and show that these modes of the PNLF may be associated with the two episodes of star formation, with the younger and older parent stellar population dominating the brighter and fainter PNe respectively. Indeed Valenzuela et al. (2019) showed theoretically that the shape of the PNLF at the faint-end is quite sensitive to the distribution of masses of the PN central stars, which is a product of the SFH in any galaxy. In Bhattacharya et al. (2019a,

Table 4.1: No. of PNe in each studied region in our M 31 survey. N_{PN}– Total number of PNe identified in each M 31 region; N'_{PN}– Number of PNe identified within the magnitude range $m_{5007} \leq 26.16$ mag in each M 31 region.

Region	N_{PN}	N'_{PN}
Disc ($10 < R_{GC} \leq 20$ kpc)	705	624
Disc ($20 < R_{GC} \leq 30$ kpc)	507	321
Giant Stream	151	113
NE-Shelf	250	106
G1-Clump	65	48
N-Clump	14	8
W-Shelf	32	31
Stream-D	78	36

hereafter Paper I), we observed a rise in the faint-end of the PNLF in the central 16 sq. deg. of M 31 conceivably linked to the SFH of M 31.

With our extended data-set it is possible, for the first time in any galaxy, to link the global PNLFs of sub-regions in M 31 to the metallicities and SFHs of their parent stellar populations. In Section 4.2, we describe our PN survey of M 31 and set the geometrical boundaries around any regions with RGB overdensities where the PNLFs are measured. In Section 4.3, we obtain the PNLFs, compute the parameters that best describe them and carry out the quantitative comparisons via statistical methods. In Section 4.4, we use stellar population parameters to interpret the difference among PNLFs as differences in old star fraction or metallicity. In Section 4.5, we discuss the implications of our results on the origin of the M31 inner halo substructures. We draw our conclusions in Section 4.6.

4.2 Substructures in M 31 and their PN samples

In Paper I, we identified PNe candidates in a 16 sq. deg. imaging survey of the disc and disc-halo interface of M 31 using the MegaCam wide-field imager (Boulade et al. 2003) mounted on the 3.6-meter Canada-France-Hawaii Telescope (CFHT). M 31 was observed through a narrow-band [O III] filter (λ_c = 5007 Å, $\Delta\lambda$ = 102 Å, on-band) and a broad-band *g*-filter (λ_c = 4750 Å, $\Delta\lambda$ = 1540 Å, off-band). The photometry has been calibrated with observations of spectrophotometric standard stars. Additional 38 sq. deg. were obtained in late-2019, covering the inner halo of M 31 and its substructures. Details of these observations will be presented in Bhattacharya et al. (2020b, in preparation). The PN identification in each of these pointings was also carried out in the same way as described in Paper I using the on-off band technique developed and validated in Arnaboldi et al. (2002, 2003), later optimised for large imaging surveys by Longobardi et al. (2013). The PNe are identified as point-like sources having an excess [O III] - *g* colour. The complete imaging survey led to the identification of 5265 PNe in M 31, the largest PN sample in any galaxy (Paper I, Bhattacharya et al. 2020b, in preparation). Of these, 4085 are newly discovered, down to $m_{5007} \leq 26.7$ mag in the deepest pointing. In Paper I, we verified that the

Table 4.2: Cumulative PNLF fit parameters and corresponding region properties. The cumulative PNLF fit parameters in the different regions are shown in Columns 2–6. The faint-end exponential could not be constrained for the N-Clump and W-Shelf. Column 8 lists the [M/H] measurement corresponding to each region which, along with the relevant literature references, are discussed in Section 4.4.1.

Region	M^*	c_1	c_2	c_{f1}	c_{f2}	[M/H]
LMC	-4.44 ± 0.00	40.49 ± 3.10	0.22 ± 0.03	43.95 ± 9.38	0.56 ± 0.31	-0.61 ± 0.05
Disc (10-20 kpc)	-4.55 ± 0.03	78.73 ± 5.49	0.27 ± 0.03	0.31 ± 0.38	5.88 ± 0.94	0
Disc (20-30 kpc)	-4.25 ± 0.05	29.96 ± 2.05	0.23 ± 0.03	0.23 ± 0.03	8.00 ± 1.68	-0.45 ± 0.18
Giant Stream	-3.60 ± 0.17	8.33 ± 1.26	0.32 ± 0.10	0.03 ± 0.06	6.67 ± 1.40	-0.52 ± 0.17
NE-Shelf	-4.59 ± 0.11	3.38 ± 0.29	0.00 ± 0.04	0.01 ± 0.01	7.56 ± 0.40	-0.4
G1-Clump	-4.83 ± 0.25	2.80 ± 0.57	0.04 ± 0.10	0.49 ± 0.23	4.01 ± 0.39	-0.37
N-Clump	-5.92 ± 0.39	0.83 ± 0.08	0.00 ± 0.00	N.A.	N.A.	N.A.
W-Shelf	-3.40 ± 0.12	3.89 ± 0.79	0.01 ± 0.13	0.01 ± 0.01	9.96 ± 7.59	-0.52
Stream-D	-2.69 ± 0.18	1.83 ± 0.21	0.00 ± 0.05	0.03 ± 0.11	4.82 ± 1.58	-1.10 ± 0.25

identified PNe have counterparts in the HST data from the Panchromatic *Hubble* Andromeda Treasury (PHAT; Dalcanton et al. 2012) in the regions of overlap, with at most ~ 3% possible contamination.

In Figure 4.1 we show all the PNe (all coloured points) identified by the narrow band imaging survey. They are overlaid on the map of RGB stars from PAndAS (McConnachie et al. 2018). The prominent substructures appear as overdensities in this map of RGB stars. Akin to McConnachie et al. (2018), we define the spatial boundaries of these substructures with polygons around the regions of higher spatial density. The identified overdensities, as marked with dashed lines in Figure 4.1, are the Giant Stream (red), North-East Shelf (NE-Shelf; black), G1 Clump (dark blue), Northern Clump (N-Clump; pink), Western Shelf (W-Shelf; yellow) and Stream D (cyan). The PNe included within a given region are considered to belong to that substructure and used for subsequent analysis. Figure 4.1 also shows elliptical projections of circular annuli in the disc (black dashed) at galactocentric distances of R_{GC}= 10, 20 and 30 kpc, covering the disc of M 31. As found in Paper II, the PNe in the $10<R_{GC} \leq 20$ kpc disc region of M 31 belong both to the (heated) thin and thicker disc, while the PNe in the $20<R_{GC} \leq 30$ kpc disc region are dominated by PNe belonging to the thicker disc of M 31. In what follows, we only consider PNe in the disc regions which were selected from the fields with limiting magnitude of $m_{5007} \geq 26.16$ mag[1]. Figure 4.1 shows the PNe in the defined $10<R_{GC} \leq 20$ and $20<R_{GC} \leq 30$ kpc disc regions in orange and green respectively. Table 4.1 lists the different regions studied in this work along with the number of PNe identified in those regions, N_{PN}, and those within the magnitude range $m_{5007} \leq 26.16$ mag utilized in the subsequent analysis, N'_{PN}.

---

[1] The fields in the south-east of the M 31 disc have a brighter limiting magnitude (50% detection completeness limit computed from injection of artificial sources) of m_{5007} ~25.89 mag. We thus confine the analysis of the PNLFs in the disc to the fields for the north-west corner of the M 31 disc with sensitivity as deep as that reached in the substructures' fields. See Paper I for details of limiting magnitudes of different fields.

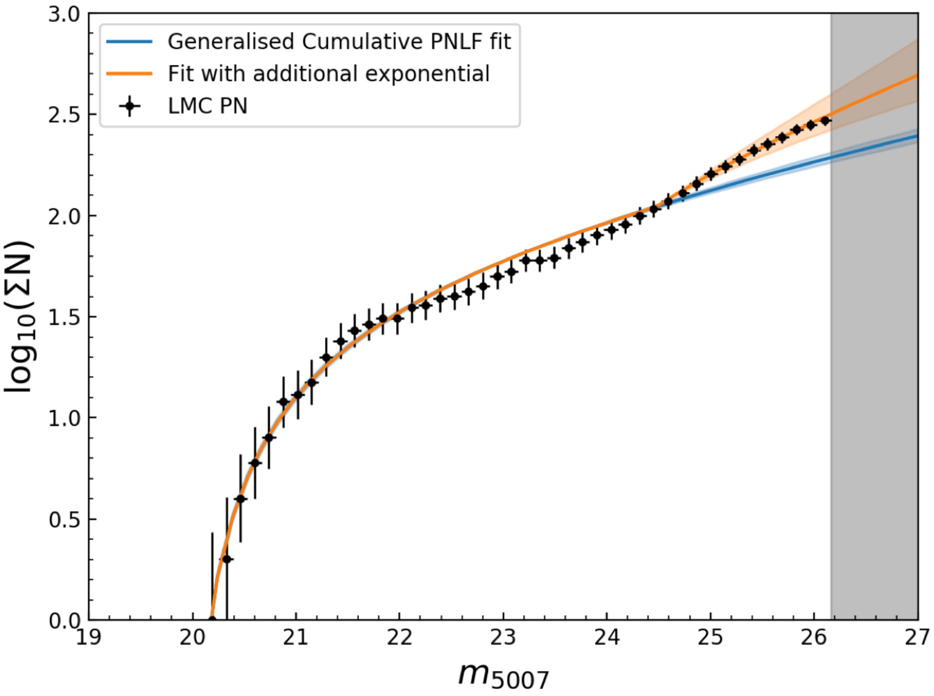

Figure 4.2: Cumulative PNLF for the LMC PN sample from Reid & Parker (2010) shifted to the apparent bright cut-off of the M 31 disc region at $10<R_{GC}\leq 20$ kpc. The cumulative PNLF are fitted by the generalised cumulative function (in blue) for $m_{5007}\leq 24.5$ mag and a function which additionally includes an exponential at the faint-end (in orange). The uncertainty in the fits are shaded. The region fainter than the limiting magnitude of the shallowest field ($m_{5007}>26.16$ mag) in our M 31 survey is shown in grey.

4.3 The Planetary Nebula Luminosity Function

4.3.1 Fitting the Cumulative PNLF

A quantitative analysis of the luminosity function of the PN subsamples selected in any M 31 region can be performed on the cumulative luminosity function to avoid potential histogram binning issues such as the bin size or position of the first magnitude bin (e.g. Peña et al. 2007, for NGC 3109). For an observed PN population (as in Sections 4.3.2 & 4.3.3), the cumulative PNLF is constructed by taking into account the detection and selection completeness. The detection completeness correction accounts for the non-detection of PNe due to noise. Colour or point-like selection criteria which would exclude those PNe affected by photometric errors is accounted for with the selection completeness correction. See Paper I for further detailed information.

The PNLFs for PN populations in different galaxies are described by the generalised analytical formula introduced by Longobardi et al. (2013), which is given hereafter:

$$N(M) = c_1 e^{c_2 M}(1 - e^{3(M^{*}-M)}) \tag{4.2}$$

where c_1 is a normalisation constant, c_2 is the slope in the intermediate magnitude range. The Ciardullo et al. (1989) LF is then a specific case of the generalised formula with $c_2 = 0.307$. The cumulative PNLF corresponding to the generalised analytical PNLF (Paper I) is:

$$\mathrm{I(M)} = \mathrm{c_1 e^{c_2 M}}[\frac{1}{\mathrm{c_2}}\mathrm{e^{c_2 M}} + \frac{1}{3-\mathrm{c_2}}\mathrm{e^{3(M^*+\mu)-(3-c_2)M}} - (\frac{1}{\mathrm{c_2}} + \frac{1}{3-\mathrm{c_2}})\mathrm{e^{c_2(M^*+\mu)}}] \qquad (4.3)$$

Its free parameters are c_1, c_2 and M^*. M^* is theoretically expected to become fainter with decreasing metallicity (Dopita et al. 1992).

In Paper I, we found an additional ubiquitous rise in the faint-end of the M 31 PNLF, with at apparent $\mathrm{m_{5007}}$ magnitudes fainter than $\mathrm{m_{5007}}$ =25 mag. We describe such rise with an additional exponential function in the cumulative PNLF which has the following form:

$$\mathrm{I_f(M)} = \frac{\mathrm{c_{f1}}}{\mathrm{c_{f2}}}(\mathrm{e^{c_{f2}M}} - 1) \qquad (4.4)$$

where c_{f1} is a normalization constant and c_{f2} is the slope of this exponential function. Thus the cumulative PNLF can be described over the entire magnitude range by:

$$\mathrm{I_{tot}(M) = I(M) + I_f(M)} \qquad (4.5)$$

For a given PN population, the free parameters in Equation 4.3 are fitted to the PN brighter than $\mathrm{m_{5007}}$ = 25 mag[2]. Once these are determined, they are kept fixed, and the additional parameters, c_{f1} and c_{f2}, for $I_f(M)$ in Equation 4.5 are determined from the PNe with $\mathrm{m_{5007}} \leq 26.04$ mag.

4.3.2 Independent calibration to a large PN sample- Cumulative PNLF of the LMC

Reid & Parker (2010) measured the PNLF in the LMC reaching ∼ 8 mag fainter than the bright cut-off. This is one of the deepest survey of PNe in any galaxy, making it a suitable independent data-set to apply our fitting procedure. By keeping the absolute bright cut-off of the more metal-poor LMC PNLF constant, $M^* = -4.44$ (Reid & Parker 2010), we obtain the cumulative PNLF of the LMC (Figure 4.2) shifted to the distance and average foreground extinction (0.19 mag; Schlegel et al. 1998) of M 31. It is fitted as previously described to derive the parameter values noted in Table 4.2. The LMC PNLF is also well described by the $I_{\mathrm{tot}}(M)$ function; the faint-end of the LMC cumulative PNLF indeed requires the additional exponential component to reproduce the rise at the faint magnitudes.

4.3.3 Cumulative PNLFs of the M 31 regions

We obtain the cumulative PNLF in each identified region of M 31. Each magnitude limited sample reaches $\mathrm{m_{5007}} \leq 26.16$ mag, ∼ 6 magnitudes below the bright cut-off for M 31. Figure 4.3 shows the completeness-corrected cumulative PNLFs for the PNe identified in the two

---

[2] The free parameters in in Equation 4.3 are fitted to the PN brighter than $\mathrm{m_{5007}} \leq 24.5$ mag for the LMC described in Section 4.3.2 beyond which the LMC PNLF shows the rise at the faint-end.

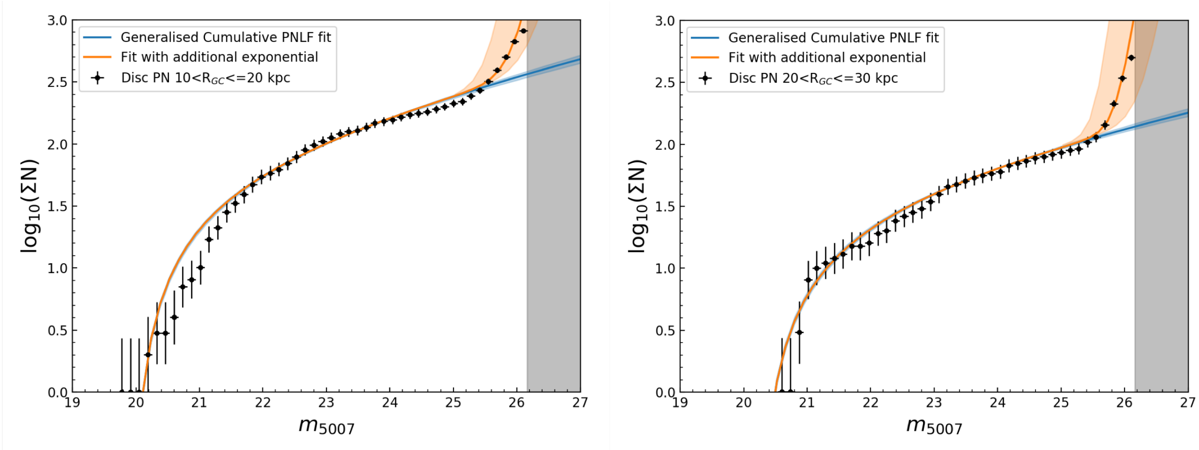

Figure 4.3: Completeness-corrected cumulative PNLF for the disc regions with 10<R_{GC} ≤20 kpc (left) and 20<R_{GC} ≤30 kpc (right). The cumulative PNLF are fitted by the generalised cumulative function (in blue) for m_{5007} ≤25 mag and a function which additionally includes an exponential at the faint-end (in orange). The uncertainty in the fits are shaded. The region fainter than the limiting magnitude of the shallowest field (m_{5007} >26.16 mag) is shown in grey.

disc regions of M 31. Figure 4.4 shows those computed for the six RGB overdensity regions. The different surface brightness and SFH of each substructure is reflected in the different total number of PNe observed in each region and in turn in the normalization parameter, c_1, of the cumulative PNLF, with brighter regions showing a larger c_1 value than the fainter ones. The PNLF in each M 31 region is fitted by the generalised cumulative PNLF (in blue), and with $I_{\mathrm{tot}}(M)$ which includes the faint-end exponential (in orange). The fitted parameter values for all regions are tabulated in Table 4.2. For the N-Clump, the exponential function was unconstrained and hence its c_{f1} and c_{f2} values are not listed.

We note that while $I_{\mathrm{tot}}(M)$ describes the cumulative PNLF of all the M 31 regions well, the fit to the cumulative PNLF of the 10<R_{GC} ≤20 kpc disc region is less optimal in the m_{5007} ∼ 20.5–21.5 mag interval. This region has the largest number of PNe, N'_{PN} = 624, amongst all the regions studied here. Given the large number statistics, small differences in the SFH likely leave an imprint on the PNLF. Thus it is possible that minor features in the cumulative PNLF, like for the brighter magnitudes (m_{5007} ∼ 20.5–21.5 mag), may not be captured well by $I_{\mathrm{tot}}(M)$ and additional functions relating to other aspects of the SFH may be required. We discuss the measured effects of the parent stellar population on the M 31 cumulative PNLF in Sections 4.4 & 4.5.1.

4.3.4 Comparison of the shapes of the PNLFs

The differences in the PNLFs obtained for distinct regions reflect differences in their parent stellar populations (detailed in Section 4.4). We can thus establish the similarity or difference in stellar populations among substructures by statistically comparing their PNLFs, even if the color magnitude diagram for the resolved RGBs is not available for the entire region. We utilize

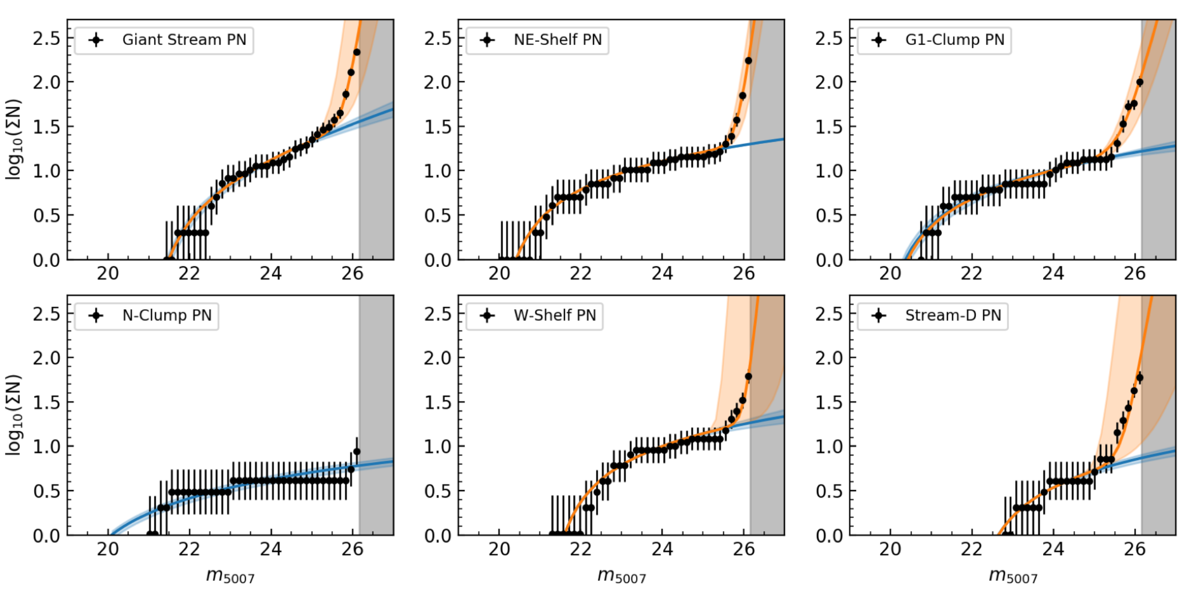

Figure 4.4: Completeness-corrected cumulative PNLF for the six different substructures are shown. The cumulative PNLF are fitted by the generalised cumulative function (in blue) for $m_{5007} \leq 25$ mag and a function which additionally includes an exponential at the faint-end (in orange; except for N-Clump). The uncertainty in the fits are shaded. The region fainter than the limiting magnitude of the shallowest field ($m_{5007} > 26.16$ mag) is shown in grey.

the two-sample Anderson-Darling test (AD-test; Scholz & Stephens 1987) to compare PNLFs of distinct PN samples. For sample sizes larger than 8 (Lewis 1961), the two-sample AD-test is a non-parametric test which checks for the null hypothesis that two samples are extracted from the same distribution. The test statistic is computed from the distance between the cumulative probability distribution of the two samples. The test statistic thus obtained is compared against the critical values[3] to derive a significance level of the two samples being drawn from the same distribution. If the significance level is less than 5%, the null hypothesis can be rejected and then the two samples are drawn from different distributions. Otherwise the two samples may or may not be drawn from the same distribution. The AD-test has high statistical power compared to other non-parametric tests like the Kolmogorov-Smirnov (KS) test, even for small sample sizes (Mohd Razali & Yap 2011). The AD-test is particularly more sensitive than the KS-test at differentiating between two distributions when the differences are most prominent near the beginning or end of the distributions. By comparing the PNLFs of distinct regions, we find which of these ones have statistically different parent stellar populations.

The cumulative probability of the completeness-corrected PNLF, computed by normalizing the PNLF between 0 and 1, is shown for the distinct substructure regions in Figure 4.5. We refrain from comparing the PNLF of the N-Clump with any other region because it has a sample

---

[3] In hypothesis testing, a critical value is a point on the test distribution that is compared to the test statistic to provide the significance level to reject the null hypothesis. For the AD-test, critical values have been defined by Scholz & Stephens (1987).

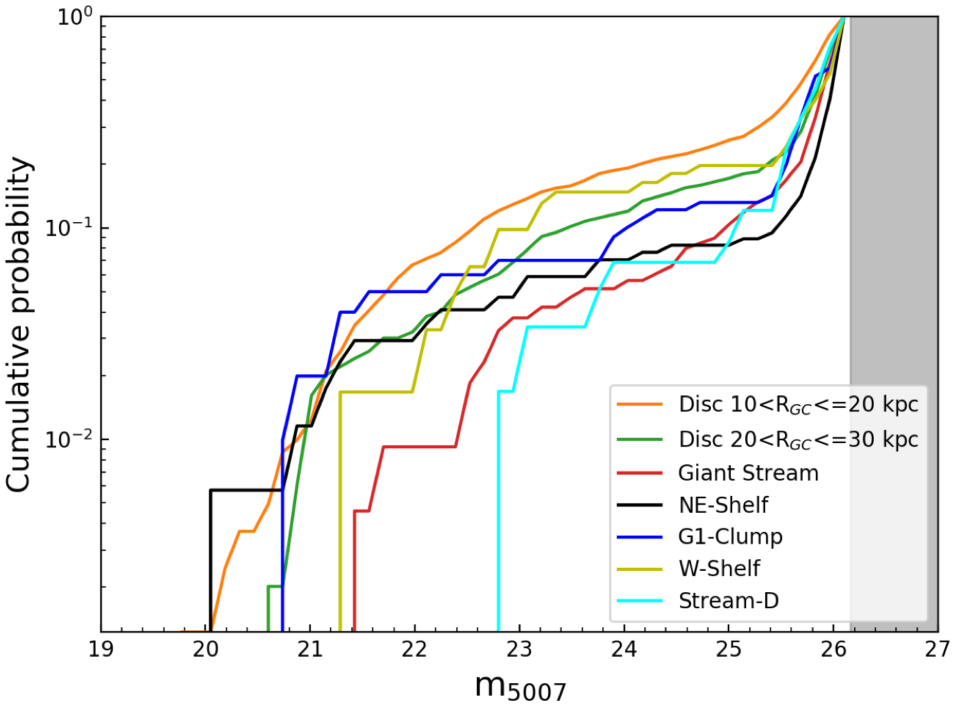

Figure 4.5: Cumulative probability of the completeness-corrected PNLF is shown, in log scale for visual clarity, for the five different substructures and the two disc regions. This diagnostic plot illustrates in which magnitude ranges the PNLFs are most different, contributing to the rejection of the null hypothesis when compared in pairs using the AD-test. Note that the AD-test utilizes the cumulative probabilities in linear scale for their comparison. The region beyond the limiting magnitude of the shallowest field (m_{5007} >26.16 mag) is shown in grey.

size which is smaller than the minimum required for the AD-test. The significance level obtained for each compared pair of regions is tabulated in Table 4.3.

We find that the PNLF of the disc regions are statistically different from each of the substructure regions. In many cases the significance level of two PNLFs being drawn from the same distribution is as low as 0.1%.We find that the two disc regions also have different PNLFs from each other, the significance level at 4.1%. We also find that the Stream-D has a PNLF, and hence a parent stellar population, different from the Giant-Stream, NE-Shelf and G1-Clump. From the AD-test results, the other substructure pairs (not marked in italics in Table 4.3) may or may not have different PNLFs, i.e. the test does not support a conclusive answer. If we recompute the AD-test on PN subsamples that are brighter than m_{5007} ≤25.9 mag, we find that the significance level of the AD-test for the two disc regions is 25% (our capped value), meaning that their stellar populations may or may not be different. This indicates that the PNe in the brighter regions of the PNLF may originate from similar parent stellar populations, while any definite difference in stellar populations is engraved in the faint-end. Recomputing the AD-tests also for the substructures with PN subsamples brighter than m_{5007} =25.9 mag, we find that all previous results are robust

Table 4.3: Comparison of PNLF shapes for regions in M 31 with the Anderson-Darling test. The null hypothesis that the two PNLF shapes come from the same distribution is rejected at a given significance level. The value is floored / capped at 0.1% / 25%. In this work, we reject the null hypothesis when the significance level less than 5%. In such cases, the region mentioned in the second column and the significance level are marked in italics in the table.

Regions compared		Significance level (%)
Disc (10<R_{GC} ≤20 kpc)	*Disc (20<R_{GC} ≤30 kpc)*	*4.1*
	Giant Stream	*0.2*
	NE-Shelf	*0.1*
	G1-Clump	*0.1*
	W-Shelf	*0.2*
	Stream-D	*0.1*
Disc (20<R_{GC} ≤30 kpc)	*Giant Stream*	*2.8*
	NE-Shelf	*0.1*
	G1-Clump	*1.0*
	W-Shelf	*0.2*
	Stream-D	*0.1*
Giant Stream	NE-Shelf	25.0
	G1-Clump	25.0
	W-Shelf	9.0
	Stream-D	*0.1*
NE-Shelf	G1-Clump	25.0
	W-Shelf	14.5
	Stream-D	*0.7*
G1-Clump	W-Shelf	25.0
	Stream-D	*4.4*
W-Shelf	Stream-D	18.1

and not solely driven by the PNe in the faintest magnitude bin in the cumulative PNLFs, with the significance level well below 5%. The exception is the comparison of the Disc (20<R_{GC} ≤30 kpc) and Giant Stream regions, where the significance level increases to 9%.

4.4 Cumulative PNLFs and stellar populations in the M31 disc and inner halo

From the deep cumulative PNLFs extracted from the regions associated with the RGB overdensities and disc annuli in M31, we can assess in which magnitude ranges the cumulative PNLFs differentiate the most (see Figure 4.5). We can then correlate the parameters in the PNLF that drive these differences with the metallicities ([M/H]) and SFH obtained from isochrone-fitting of colour-magnitude-diagrams (CMDs) of resolved stellar populations, mainly RGB stars, in these

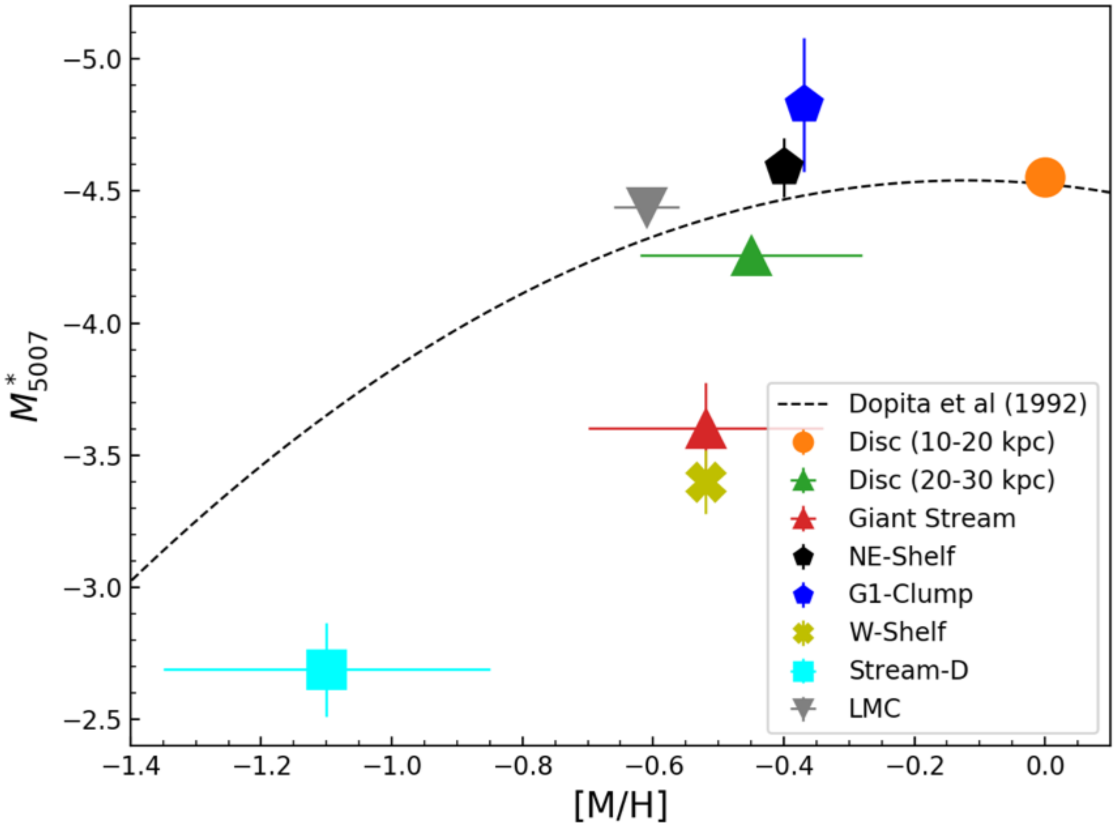

Figure 4.6: The [M/H] value for the different regions in M31 and the LMC is plotted against the M^* value obtained from fitting their PNLF. The different markers show the different references for the [M/H] measurements – circle: Williams et al. (2017); pentagon: Bernard et al. (2015); triangle: Escala et al. (2020); inverted triangle: Nidever et al. (2020); cross: Tanaka et al. (2010); square: Conn et al. (2016). The theoretical expectation from Dopita et al. (1992) is shown with the dotted line.

sub-regions and also for the LMC. We note that [M/H] measurements are also available from spectroscopy of individual RGB stars for some of the regions.

4.4.1 The absolute magnitudes of the PNLF bright cut-off and their dependency on [M/H]

The measured absolute magnitudes M^* for the PNLF bright cut off in different galaxies show that such quantities do not depend on morphology, star-formation histories and ages (Ciardullo et al. 2013), but their values depend on the metallicity of the parent stellar population (see Ciardullo et al. 2002). We examine the dependency of M^* on the [M/H] of the parent stellar population for the distinct M 31 regions and the LMC. We list the best-fitting M^* values along with the [M/H] values of the parent stellar populations from the literature, in Table 4.2.

In general, the photometrically measured [Fe/H] is taken to be equal to the [M/H] value, as [α/Fe] is assumed to be zero for the fitted isochrones (e.g. Bernard et al. 2015; Conn et al. 2016; Williams et al. 2017). The [M/H] for the $10<\mathrm{R_{GC}}\leq 20$ kpc disc region is obtained as the mean [M/H] from the PHAT photometry, covering a third of the M 31 disc at this radii, by Williams et al. (2017). The [M/H] for the the NE-Shelf and G1-Clump regions is from the pencil-beam HST photometry by Bernard et al. (2015). For Stream-D, the [M/H] measurement is from the CFHT MegaCam observations, covering this entire sub-region, by Conn et al. (2016). The [M/H] for the $20<\mathrm{R_{GC}}\leq 30$ kpc disc region and the Giant Stream [4] are obtained from the mean [Fe/H] and mean [α/Fe] values measured from individual stars in small fields observed in these regions by Escala et al. (2020). These values are converted to [M/H] using the following relation from Salaris & Cassisi (2005):

$$[\mathrm{M/H}] \sim [\mathrm{Fe/H}] + \log(0.694 \times 10^{[\alpha/\mathrm{Fe}]} + 0.306) \qquad (4.6)$$

We note that the spectroscopic [M/H] for these two regions agree within errors with that from the pencil-beam HST photometry in these regions by Bernard et al. (2015). For the LMC, we derive the median [M/H] value from the median [Fe/H] and median [α/Fe] values for APOGEE RGB stars spanning a large radial range in the LMC (Nidever et al. 2020). For the W-Shelf, Tanaka et al. (2010) construct CMDs for the resolved stellar population in the Subaru Suprime-Cam pointings. The mean [Fe/H] value is measured photometrically from isochrone-fitting to the W-Shelf CMD, assuming [α/Fe]=0.3. We use the measured [Fe/H] and assumed [α/Fe] value in Equation 4.6 to obtain the measured [M/H] for the W-Shelf. In Figure 4.6, we show the M^* values for different M 31 regions against their [M/H] values.

In Figure 4.6, we also depict the theoretical variation of M^* with [M/H]. This was computed from the variation of M^* with [O/H] obtained by Ciardullo et al. (2002) from the Dopita et al. (1992) PN evolution models. [O/H] is calibrated to [M/H] by subtracting the solar [O/H] value (=8.69; Asplund et al. 2009) as it is done for calibrating stellar and gas phase mass-metallicity relations of galaxies (e.g. Zahid et al. 2017). We find that the fitted M^* for the LMC, the two disc regions, the G1-Clump and the NE-Shelf are in agreement with the theoretical expectation from Dopita et al. (1992). However, the M^* for the PN samples in Giant Stream, W-Shelf and Stream-D areas are fainter than those predicted on the basis of the measured [M/H] of their parent stellar populations.

Given the low surface-brightness of the Stream-D and W-Shelf substructures and the short visibility lifetimes of PNe (Buzzoni et al. 2006), it is possible that the small number of detected PNe are not seen at their brightest but rather once they faded. This may possibly explain faded M^* values for the Stream-D and W-Shelf. This is not the case for the Giant Stream which is a brighter substructure with a larger number of detected PNe. In the case of the Giant Stream, the brightest PN has an absolute magnitude $M{*}_{5007} = -3.51$ with 12+ (O/H)= 8.3 dex (PN14 from

---

[4] The metallicity gradient in the Giant stream is studied by Conn et al. (2016). In their Figure 3, they show the spatial coverage of their fields and give the corresponding [Fe/H] (=[M/H] as [α/Fe]=0) values in their Table 1. With this PNe survey, we cover a spatial area in the Giant Stream corresponding to their mean metallicity range of [M/H] = −0.4 to −0.7. The [M/H] value for the Giant Stream from Escala et al. (2020) covers the metallicity range observed by Conn et al. (2016) within error and is thus an accurate [M/H] value for parent population of the PN subsample in the Giant Stream.

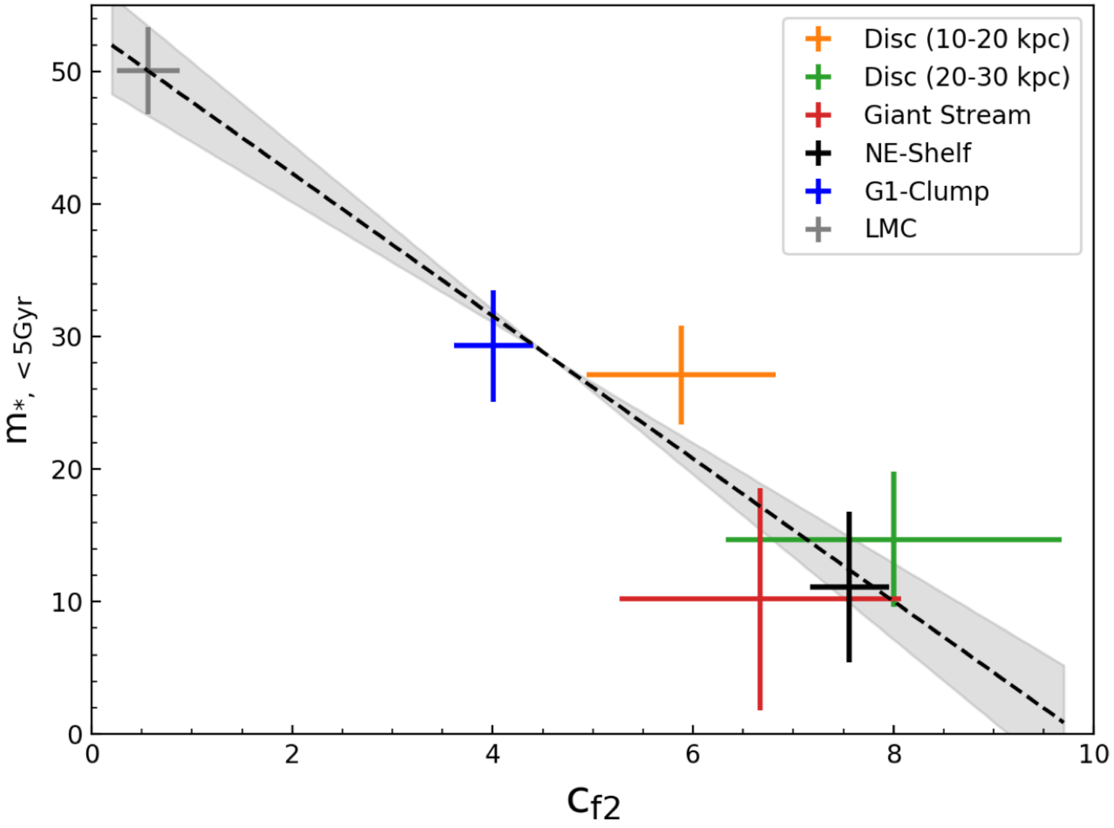

Figure 4.7: Linear relation between the slope of exponential function at the faint end of the PNLF, c_{f2}, and the percentage stellar mass formed within the last 5 Gyr, $m_{*,\ <5\ \mathrm{Gyr}}$.

Fang et al. 2018), corresponding to $[M/H] = -0.39$. Thus it is spectroscopically confirmed that the PN at the PNLF bright cut-off in the Giant Stream has a metallicity value consistent with those obtained by Escala et al. (2020) for the resolved RGBs.

To comprehend the fainter M^* for the Giant Stream, given its measured [M/H] value, metallicity and other possible effects influencing PN evolution need to be re-evaluated. This is particularly important given the significance of the absolute magnitude of the PNLF bright cut-off, M^*, as a reliable secondary distance indicator across the different Hubble galaxy types (Ciardullo et al. 2013).

4.4.2 Imprint of star-formation history on the very faint-end of the PNLFs in M 31

Bernard et al. (2015) obtained the SFHs in 14 deep HST pointings in different regions of the M 31 disc and some of the inner halo substructures. While they found that M 31 had a ubiquitous burst of star formation ~ 2 Gyr ago, they measured significant differences in the percentage of

Table 4.4: Percentage stellar mass formed within the last 5 Gyr, $m_{*,\ <5\ \mathrm{Gyr}}$, from the PNLF predicted with the pick-one-out test. The $m_{*,\ <5\ \mathrm{Gyr}}$ in the HST fields corresponding to the LMC, Disc (10-20 kpc) and all other regions are from Weisz et al. (2013), Williams et al. (2017) and Bernard et al. (2015) respectively. The $m_{*,\ <5\ \mathrm{Gyr}}$ values are predicted for each region from its c_{f2} value by fitting the relation between c_{f2} and $m_{*,\ <5\ \mathrm{Gyr}}$ for all the other regions except the selected region.

Region	$m_{*,\ <5\ \mathrm{Gyr}}$	
	HST CMD	PNLF prediction
LMC	50.1 ± 3.3	49.94 ± 11.98
Disc (10-20 kpc)	27.1 ± 3.7	20.02 ± 6.55
Disc (20-30 kpc)	14.7 ± 5.1	9.15 ± 11.02
Giant Stream	10.2 ± 8.4	18.04 ± 9.22
NE-Shelf	11.1 ± 5.7	13.49 ± 5.78
G1-Clump	29.3 ± 4.2	32.23 ± 2.77
W-Shelf	N.A.	≤ 42.19
Stream-D	N.A.	27.14 ± 9.46

stellar mass formed < 5 Gyr ago (hereafter $m_{*,\ <5\ \mathrm{Gyr}}$) in distinct HST fields aligned with different substructures. In particular, they found that HST pointings in the Giant Stream, NE-Shelf and outer disc have much smaller $m_{*,\ <5\ \mathrm{Gyr}}$ compared to the G1-Clump. Based on these SFHs, they termed the Giant Stream and NE-Shelf as *stream-like*, while the G1-Clump was termed as *disc-like*. The outer-disc field was labeled as a composite field, having a slightly larger $m_{*,\ <5\ \mathrm{Gyr}}$ value compared to the *stream-like* fields. No SFH measurements are available for the W-Shelf[5] and Stream-D. Williams et al. (2017) utilized observations from the PHAT survey (Dalcanton et al. 2012) to find that $\sim 10-20\%$ of the stellar mass within a galactocentric radius of 20 kpc is formed in a burst of star-formation ~ 2 Gyr ago with $\mathrm{m}_{*,<5Gyr} \sim 30\%$. Using their HST observations in 8 scattered fields in the LMC, Weisz et al. (2013) showed that ~ 50 % of the stellar mass in the LMC was formed in the last 5 Gyr.

Given the extended coverage of the HST fields utilised to measure the average SFH from resolved stellar populations in the LMC and the M 31 $10<\mathrm{R}_{\mathrm{GC}} \leq 20$ kpc disc region, the measured $m_{*,\ <5\ \mathrm{Gyr}}$ value is representative of the average stellar population in these regions. Since the average SFH of the parent stellar population leaves an imprint on the global PNLF of any region, the measured $m_{*,\ <5\ \mathrm{Gyr}}$ value for the aforementioned regions can be linked to their PNLF fit parameters. For the other four regions (see Figure 4.1), the SFH measured from the pencil-beam HST fields obtained by Bernard et al. (2015) may not be representative of the average one for the entire substructures (Williams et al. 2017).

However, we can assess whether the SFH values determined from the pencil-beam HST fields are representative of the average values for the entire stellar population in any substructure by checking whether the relation between the global PNLF parameters and the measured $m_{*,\ <5\ \mathrm{Gyr}}$

---

[5] The HST field linked to the W-Shelf by Bernard et al. (2015) does not overlap with the W-Shelf spatial over-density as obtained by PAndAS (McConnachie et al. 2018).

value for these regions lie on the same relation as that for the average SFH of the LMC and the M 31 10<R_{GC} ≤20 kpc disc region. Any region whose average SFH value is vastly different from that found within the tiny HST pointing would diverge significantly from any fitted relation.

We find a correlation between the percentage stellar mass from the HST fields in two age bins (see Table 4.4), younger and older than 5 Gyr following the age distinction by Bernard et al. (2015), and the exponential function fitting to the faint-end of the PNLF, c_{f2} (see Table 4.2). Figure 4.7 shows c_{f2} against $m_{*,\,<5\,\mathrm{Gyr}}$ in any HST field of a given sub-region. We find that the sub-regions whose SFH value is obtained from large spatial HST coverage lie tightly on the same relation as those regions with smaller fields. Fitting the relation between $m_{*,\,<5\,\mathrm{Gyr}}$ and c_{f2} with a linear function using a Deming regression[6] (Kummell 1879), the best fit is given by:

$$\mathrm{m}_{*,\,<5\,\mathrm{Gyr}} = -5.38\,(\pm 0.54) \times \mathrm{c}_{\mathrm{f2}} + 53.07\,(\pm 2.48) \tag{4.7}$$

Since it is not known a priori the HST field of which region would be an outlier influencing the fitted parameters of Equation 4.7, we run a “pick-one-out test” over the parameters for the six regions. The relation between c_{f2} and $m_{*,\,<5\,\mathrm{Gyr}}$ is fitted for five of the six regions and the $m_{*,\,<5\,\mathrm{Gyr}}$ value is predicted for the selected region from its c_{f2} value. This process is iterated for each of the six regions. The predicted $m_{*,\,<5\,\mathrm{Gyr}}$ values are noted for each region in Table 4.4. The predicted quantities are in good agreement with those measured from the HST fields implying that the $c_{f2} - m_{*,\,<5\,\mathrm{Gyr}}$ relation is applicable to the entire parent stellar population of the PNe in any region. We thus also use Equation 4.7 to predict the $m_{*,\,<5\,\mathrm{Gyr}}$ values for the W-Shelf and Stream-D (Table 4.4) also.

4.4.3 Stellar population dominating the very faint-end of the PNLF

Following this analysis, we infer that the c_{f2} value of the PNLF increases linearly with decreasing fraction of the stellar mass of its parent stellar population that formed in the last 5 Gyr. Hence, the rise at the faint-end of the PNLF is driven by the fraction of the stellar mass in the stellar population older than 5 Gyr. This is in agreement with the expectations from the post-AGB stellar evolution models by Marigo et al. (2004) where the faint-end of the PNLF is populated by PNe evolving from older stellar populations and powered by less-massive central stars (see their Figures 18 & 25 and associated text). However, it is in contrast to the predictions by Méndez et al. (2008) where the faint-end of the PNLF is populated by PNe from massive progenitor stars from young stellar populations which have faded rapidly while losing their envelope.

4.5 Discussion

4.5.1 Morphology of the PNLFs and stellar population parameters in the M 31 regions

Through the analysis presented in Sections 4.3 and 4.4, we linked the morphology of the deep PNLF with the metallicity and SFH of the parent stellar populations. We thus interpret the

---

[6] Regression technique where both variables are measured with error.

differences between the global PNLFs of different M 31 regions as differences in the average SFH or metallicity of their parent stellar population. To recapitulate:

- We confirmed that M^* is influenced by the metallicity (see Section 4.4.1).
- We showed that c_{f2} is linked to $m_{*,\ <5\ \mathrm{Gyr}}$, see Section 4.4.2 and Fig. 4.7.
- The c_2 parameter, i.e. the slope of the PNLF at intermediate magnitude (m_{5007}= 21–25 mag), is also influenced by the SFH of the parent stellar population. For some of the M 31 regions, we find $c_2 \approx 0$ (see Table 4.2). This occurs when there is a paucity of PNe at intermediate magnitudes and corresponds to a dip in the PNLF. Valenzuela et al. (2019) showed theoretically that such a dip is also a product of the distribution of masses of the central stars, and hence of the SFH of the parent stellar population. However, a quantitative link is yet to be established between the SFH and a dip in the PNLF, and hence its c_2 value.

For the pairs of M 31 regions that have different PNLFs (see Table 4.3), we assessed in which magnitude ranges the PNLFs differentiate the most (Figure 4.5) and presented the differences in their fitted PNLF properties (see Table 4.2). We infer the dependencies of these differences in pairs of M 31 regions on their parent stellar population parameters as follows:

- The $10< \mathrm{R}_{\mathrm{GC}} \leq 20$ kpc and $20< \mathrm{R}_{\mathrm{GC}} \leq 30$ kpc disc regions: On the basis of the spectroscopic and kinematic properties of the disc PNe (Paper II), the $10<\mathrm{R}_{\mathrm{GC}} \leq 20$ kpc disc region, which contains both young (heated) thin disc and older thicker disc stars, is found to be different from the $20<\mathrm{R}_{\mathrm{GC}} \leq 30$ kpc disc region, in that the latter has predominantly older and more metal poor disc stars, reflected in its larger c_{f2} (see Table 4.2) and fainter M^* values.
- The Giant Stream and the $10<\mathrm{R}_{\mathrm{GC}} \leq 20$ kpc disc region: The Giant Stream, with a larger c_{f2} value (see Table 4.2), has a higher percentage of older stars than the $10<\mathrm{R}_{\mathrm{GC}} \leq 20$ kpc disc region. Additionally, the PNLF of the Giant Stream has a fainter M^* (see Section 4.4.1) than the $10<\mathrm{R}_{\mathrm{GC}} \leq 20$ kpc disc, implying a more metal-poor stellar population.
- The Giant Stream and $20<\mathrm{R}_{\mathrm{GC}} \leq 30$ kpc disc region: Here the difference in the deep PNLFs stems mainly from the fainter M^* (more metal poor population; see Table 4.2) of the Giant Stream PNLF with respect to that of the outer disc region. Their stellar mass is dominated by older stars according to their PNLF c_{f2} large values.
- The NE-Shelf and $10<\mathrm{R}_{\mathrm{GC}} \leq 20$ kpc disc region: The NE-Shelf has a higher c_{f2} value (see Table 4.2), thus a higher percentage of older stars, than the $10<\mathrm{R}_{\mathrm{GC}} \leq 20$ kpc disc region. While the NE-shelf PNLF has a M^* value similar to that of the inner disc region within error, it has a $c_2 \approx 0$ value (see Table 4.2), indicating further differences in the SFH from the $10<\mathrm{R}_{\mathrm{GC}} \leq 20$ kpc disc region.
- The NE-Shelf and $20<\mathrm{R}_{\mathrm{GC}} \leq 30$ kpc disc region: The difference between the two regions originates from the slightly brighter M^* of the NE-Shelf PNLF, and also the latter having a $c_2 \approx 0$ value, implying differences the in their SFHs.

- The G1-Clump and the $10 < R_{GC} \leq 20$ kpc disc region: Both regions have similar $m_{*,\ <5\ \mathrm{Gyr}}$ (see Table 4.4) but the PNLFs have a different shape owing to the $c_2 \approx 0$ value (see Table 4.2) for the G1-Clump, thus indicating a distinct SFH from the $10 < R_{GC} \leq 20$ kpc disc region.

- The G1-Clump and the $20 < R_{GC} \leq 30$ kpc disc region: The G1-Clump has a higher $m_{*,\ <5\ \mathrm{Gyr}}$ (see Table 4.4) and lower c_{f2} value (see Table 4.2) than the $20 < R_{GC} \leq 30$ kpc disc. The difference is further aggravated due to the $c_2 \approx 0$ value of the G1-Clump PNLF, implying differences in SFHs.

- The W-Shelf and the two disc regions: We only have an upper limit of $m_{*,<5Gyr} \leq 42.19$ % for the W-Shelf. The difference with the two disc regions can still be attributed to the $c_2 \approx 0$ value of the W-Shelf PNLF (see Table 4.2) and thus a difference in SFHs. Additionally, the W-Shelf PNLF has a fainter M* (see Section 4.4.1) than the two disc regions, implying a more metal-poor stellar population.

- Stream-D: This M 31 substructure is different from both disc regions, the Giant Stream, the NE shelf and the G1-Clump because it has the faintest bright cut-off value, $M^* = -2.689 \pm 0.177$, among the PN subsamples from the M31 survey, indicating the presence of the most metal-poor population (see Section 4.4.1). Its deep PNLF also has $c_2 \approx 0$ (see Table 4.2), further implying distinct SFHs to some of the M 31 sub-regions.

In summary, the Giant Stream and the W-shelf have similarly faint M^* values (low metallicities) and large c_{f2} values, with their mass in stars dominated by > 5 Gyr old populations. The NE-shelf has an M^* value similar to the inner disc region within error but its stellar mass is dominated by a > 5 Gyr old population. Stream D has an extremely metal poor population. The G1 clump has a M^* value comparable to that of the inner disc region, with a significant contribution from a young < 5 Gyrs population.

4.5.2 The merger origin of the inner-halo substructures in M 31

Having mapped the average properties of the global stellar populations in the substructures of the M 31 inner halo, we now compare our observational results with the predictions from N-body/ hydrodynamical simulations of a merger event in M31. On one hand we have the N-body simulations of a minor merger (Fardal et al. 2013 and reference therein). This event, if it took place 1 Gyr ago, successfully reproduces the morphology of the Giant Stream, NE and W-shelves. The Giant Stream represents the trailing stream of material torn off during the progenitor's first pericentric passage, while the NE and W shelf regions contain material torn off in the second and third passages, respectively (Ferguson & Mackey 2016). The largest fraction of stellar mass in all three substructures is made up by the old stellar debris of the satellite. This is consistent with the global PNLF results for these three sub-regions of M 31: the Giant Stream, and NE shelf have large fractions of older stars, i.e. large c_{f2} values. The W-Shelf also has stellar populations different from the M 31 disc regions but the age of its stellar population is still not very well constrained. Both the Giant Stream and W-Shelf have relatively metal-poor stellar populations (see relevant discussion in Section 4.5.1). Finally, even the relatively more metal-rich NE-Shelf is consistent with this scenario as its stellar material could have been unbound from the satellite's core in later pericenter passages.

Such an evolution scenario, however, leaves out the formation of the N and G1 clumps. Following their initial discoveries (Ferguson et al. 2002; Ibata et al. 2005), these substructures had been linked to dissolution of dwarf galaxies from distinct accretion events. The G1-Clump is measured to have an absolute V-band Magnitude, $M_V = -12.6$ mag (Ferguson et al. 2002) which corresponds to a total V-band luminosity, $L_{tot} = 9.37 \times 10^6$ $M_{\odot}$. Had the G1-Clump be the result of a dissolved dwarf, following the luminosity-metallicity relation for Local Group dwarf galaxies (Kirby et al. 2011), its mean [M/H] value would be ~ -1.5. Such a value is much lower than its measured [M/H]$= -0.37$ (Table 4.2).

The last points regarding the minor merger scenario are the tensions between the timing of such an event, $\sim 1 Gyr$ ago, and the age of the burst of star formation of $\sim$ 2 Gyr in the M31 disc (Bernard et al. 2015; Williams et al. 2017), and particularly the mass of the satellite not being large enough to dynamically heat the M31 disc (Paper II).

We now examine the predictions from the major-merger scenario as simulated by Hammer et al. (2018). In these simulations, a massive gas-rich satellite was accreted with an orbit along the Giant Stream 2-3 Gyr ago. Such a massive satellite would perturb the M 31 disc and produce a thick disc from the pre-existing stars. After the merger, the replenished cold gas would lead to a burst of star-formation and the build-up of a less-extended thin disc. Within the $10<R_{GC} \leq 20$ kpc disc region, we observe in the PNLF a superposition of the stellar populations associated with both the newly-formed thin disc and the older thicker disc of M 31. This disc region thus has a larger fraction of younger stars compared to the $20<R_{GC} \leq 30$ kpc disc region where the stellar populations associated with the thicker disc stars dominate.

The simulations by Hammer et al. (2018) also predict that the stellar populations in the Giant Stream, NE-Shelf and W-Shelf are dominated by stellar debris from the infalling satellite, while the N and G1 Clumps are associated with the stellar material from the perturbed pre-existing disc. The G1 Clump has a significant fraction of stars younger than 5 Gyr just like the thin disc of M 31. While their stellar populations are statistically different, the younger stars in both the thin disc of M 31 and the G1 Clump may have formed at the same time. Having formed from the perturbed M 31 disc, the G1-Clump is expected to show a relatively metal-rich global stellar population, consistent with the observed values. Unfortunately, the stellar population of the N-Clump could not be constrained by our data. The major merger scenario thus simultaneously explains the observed global stellar population properties of the M 31 inner halo substructures, as well as the measured velocity dispersion values (Paper II) and the age of the recent burst of star-formation in the disc (Bernard et al. 2015; Williams et al. 2017).

Stream-D has a stellar population that is different from both disc regions and the other substructures: it has the faintest value for the PNLF bright cut off M^* indicating that its population is the most metal poor in the entire area surveyed around M31. This result points to an independent origin. Indeed this stream does not appear in the simulations by Hammer et al. (2018) and it could have formed in a distinct accretion event, e.g. the disruption of a low mass dwarf galaxy. Thus we find that the M 31 inner halo substructures, barring Stream-D, are consistent with having originated in a single major merger event.

4.6 Conclusions

By comparing deep PNLFs in the substructures and disc of M 31, we determine significant variations in their parent stellar populations. We confirm that metallicity influences the bright cut-off of the PNLF; the predictions by Dopita et al. (1992) may require further adjustments in the case of more metal-poor populations, as in the Giant-Stream, W-Shelf and Stream-D.

We establish a connection between the global PNLF morphology and the stellar mass of the parent stellar population in two age bins, younger and older than 5 Gyr respectively. We find that the rise in the faint-end of the PNLF is driven by the mass-fraction of stellar populations older than 5 Gyr, indicating that PNe evolving from older stars populate the faint-end of the PNLF.

This study is the first one to use the PNLFs of different regions in the same galaxy, M 31, in order to understand the origin of the galaxy's substructures. From their PNLF we find that the Giant Stream and NE-Shelf are consistent with being composed of stellar debris from an infalling satellite while the G1 Clump is linked to the pre-merger M 31 disc with younger stars having formed out of the accreted cold gas.

The constraints from the deep PNLFs on the origin of these substructures point to their formation in a single merger event in M 31. In conjunction with the age-velocity dispersion relation of the M 31 disc (Paper II), this indicates a recent single major merger in M 31, in agreement with predictions from Hammer et al. (2018). We also find that Stream-D was likely formed from a distinct accretion event, most probably from a disrupted dwarf satellite.

This work sets the stage for the spectroscopic follow-up of PNe in the outer disc and inner halo of M31, with the goal of measuring their specific metal abundances. From these discrete measurements, we will then build abundance maps for substructures and disc, leading to a better understanding of their chemical evolution.

Chapter 5

Radial metallicity gradients in the chemically distinct thin and thick discs of M 31 from PN elemental abundances

The contents of this chapter are to be submitted for publication in the Monthly Notices of the Royal Astronomical Society (MNRAS)

5.1 Introduction

Late-type galaxies can contain multi-layered disc populations that are kinematically distinct, the most typical of these are the "cold" thin disc and the "hot" thick disc, as found in the Milky Way (MW; e.g. Gilmore & Reid 1983) and nearby edge-on galaxies (Yoachim & Dalcanton 2006; Comerón et al. 2019). A major part of the MW thick disc is also found to be chemically distinct from its thin disc suggesting distinct origins for the two (see review by Bland-Hawthorn & Gerhard 2016, and references therein). Thick discs are typically thought to have formed from dynamical heating of thin discs. They may form via dynamical heating induced by secular evolution of the disc, as in the case of the MW (Sellwood 2014). Mergers with satellites can also dynamically heat discs to decrease their rotational velocity and increase velocity dispersion (Quinn & Goodman 1986), resulting in either destruction of the discs to form spheroids (Toomre 1977) or formation of thick discs (Hopkins et al. 2009).

Since galaxies are thought to evolve by hierarchical mergers with satellite galaxies (White & Rees 1978; Bullock & Johnston 2005), late-type galaxies of varying disc thickness are expected. The MW disc is thought to have evolved mainly by secular evolution (Sellwood 2014) with its most recent merger ~10 Gyr ago (Helmi et al. 2018; Belokurov et al. 2018). M 31 on the other hand is thought to have had its most recent merger ~ 2.5–4.5 Gyr ago (Bhattacharya et al. 2019b, hereafter Paper II). M31 harbours a thick disc that is about three times as dynamically hot as that of the MW (Dorman et al. 2015, Paper II). Thus, its merger history and disc thickness are both different from that of the MW. While the MW is a prime laboratory for secular evolution in discs, M 31 has the potential to be a prime laboratory for merger-effected disc evolution.

The PAndAS survey (McConnachie et al. 2009) revealed the plethora of substructures in the M 31 inner halo shedding light on its turbulent recent history. In Paper II, through velocity dispersion profiles of high- and low- extinction PNe in the M 31 disc, we found kinematically distinct dynamically colder thin and dynamically hotter thicker discs respectively. The age-velocity dispersion relation in the M 31 disc was found to be consistent with a ~1:5 major merger in M 31 ~2.5–4.5 Gyr ago. This is in agreement with the merger simulations by Hammer et al. (2018) where a gas-rich satellite was accreted on to M 31 with an orbit along the Giant Stream, perturbing the M 31 disc and producing a thick disc from the pre-existing stars. After the merger, the replenished cold gas would lead to the formation of a less-extended thin disc through a burst of star formation. The stars in the thin and thick discs of M 31 are formed in different epochs in this scenario with those in the thin disc formed from the ISM that includes contribution of accreted gas from the merging satellite. Thus, differences may arise in the chemical composition of the stars in thin disc from those in the thick disc of M 31.

The chemical evolution of discs of spiral galaxies is reflected in their radial abundance distributions, specifically through the radial abundance gradients. In an inside-out build-up scenario of a galaxy disc, negative radial metallicity gradients are expected (e.g. Sánchez-Menguiano et al. 2018). Hydrodynamical simulations have shown that the radial metallicity gradient in galaxies is modified both in case of secular evolution (e.g. Gibson et al. 2013) and also in the case of galaxy mergers (e.g. Zinchenko et al. 2015; Tissera et al. 2019). PN elemental abundances light on the ISM conditions at the time of formation of their parent stellar population. PN elemental abundances are obtained through the measurement of emission line fluxes including those that are sensitive to temperature and electron density, and using an ionisation correction factor (ICF; e.g. Delgado-Inglada et al. 2014) to convert measured ionic abundances to elemental abundances. Abundance distributions in galaxies can be mapped from PNe, thereby making them tracers of chemistry in galaxies. When PNe ages can be identified, it becomes possible to map abundance variations across different epochs of star formation in galaxies. In the MW, the radial metallicity gradient for both thin and thick disc PN formed at different epochs (Figure 1.13) have been obtained separately allowing for significant constraints on its chemical evolution (Stanghellini & Haywood 2018). In the case of M 31, elemental abundance measurements of the high- and low-extinction PNe with distinct ages can be checked to obtain separate abundance measurements of its kinematically distinct thin and thick disc.

Oxygen abundances of PNe have long been thought to reflect the ISM conditions in any galaxy at the time of their birth (e.g. Bresolin et al. 2010; Hernández-Martínez et al. 2011; Stanghellini et al. 2014). However, modification of oxygen abundances of the parent stellar population of the PN can occur in the AGB phase and has been observed in MW PNe (e.g. Delgado-Inglada et al. 2015). For PNe evolving from stars with initial mass $\geq 3M_{\odot}$, hot-bottom burning (HBB) may result in depletion of oxygen of $\sim$ 0.2 dex (e.g. Ventura et al. 2017). On the other hand, for PNe evolving from stars with initial masses of $1-2M_{\odot}$ and $Z < 0.008$, third dredge-up (TDU) effects may result in enrichment of oxygen of $\sim$ 0.3 dex (e.g. Ventura et al. 2017). Delgado-Inglada et al. (2015) found that oxygen may be enriched in PNe with Carbon-rich dust (CRDs) by $\sim$ 0.3 dex even for intermediate metallicities of 12+(O/H) = 8.2–8.7. Theoretical predictions by García-Hernández et al. (2016) are consistent with these observations when considering PNe with initial masses of $1-3M_{\odot}$. We can identify depletion or enrichment

Table 5.1: Details of MMT Hectospec observations of PNe. Brighter PNe were prioritised for observations but PNe down to m_{5007} = 26.4 mag were targeted. Some PNe were observed twice in the regions of overlap of some of the fields. Note that only the data from the first three observations were combined with the archival data from San+12 in Paper II to obtain the age-velocity dispersion relation for the M 31 disc.

Obs. date	RA [J2000] (deg)	DEC [J2000] (deg)	Exposure time (s)	No. of PN targeted	No. of PN observed
15.09.18	10.45	41.1	9000	38	19
10.10.18	10.5	41.1	9000	65	41
04.12.18	11.5	42.6	3600	202	44
23.10.19	9.62	40.48	4800	175	71
24.10.19	10.9	41.6	4800	226	174
25.10.19	9.38	40.06	6000	79	26

of oxygen in these PNe from measurement of abundances of elements that are unaffected by the aforementioned effects that modify PN surface oxygen content. Delgado-Inglada et al. (2015), observationally, and García-Hernández et al. (2016), theoretically, identified chlorine and argon as elements that are invariant in the AGB phase and thus reflect the ISM conditions at the time of birth of the PN parent stellar population.

Without separating the PN sample on the basis of extinction, the PN oxygen abundance gradient from ~ 50 observed PNe in the M 31 disc has previously been measured by San+12 who find a best-fit slope of -0.0056 ± 0.0076 dex within ~4–24 kpc, consistent also with later findings by Kwitter et al. (2012). Peña & Flores-Durán (2019) combined archival PN abundance measurements in M 31 to find a oxygen abundance gradient of -0.001 ± 0.001 dex within ~110 kpc, including both disc and halo PNe. They also computed an argon abundance gradient of -0.002 ± 0.001 dex for the same sample.

In this chapter, we obtain direct measurements of oxygen and argon abundances in M 31 disc PNe to assess whether the high- and low-extinction PNe, which form the kinematically distinct thin and thick disc of M 31, show evidence for different abundance values and gradients. Our observations and sample selection are discussed in Section 5.2. Oxygen and argon abundances are used as chemical tracers of the high- and low-extinction PNe in Section 5.3, where we obtain their radial abundance gradients. We discuss our results in Section 5.4 and conclude in Section 5.5.

5.2 Data reduction and sample selection

5.2.1 Observations

In Paper I, we identified PN candidates in a 16 sq. deg. imaging survey of M 31 with MegaCam at the CFHT, covering the disc and inner halo. Spectroscopic observations of a complete subsample of these PN candidates were carried out with the Hectospec multifibre positioner and spectrograph on the Multiple Mirror Telescope (MMT; Fabricant et al. 2005). The Hectospec

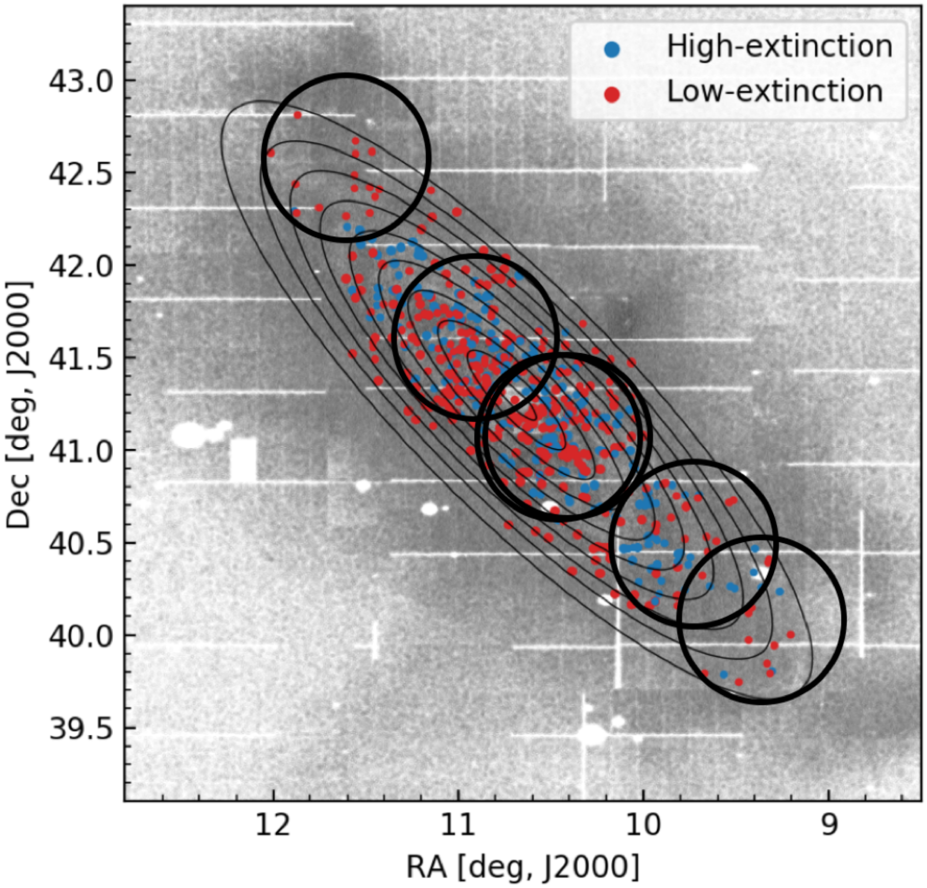

Figure 5.1: Position on sky of the PNe utilized in this work, as detailed in Section 5.2.6. The MMT pointings are marked in black. The high-extinction PNe are shown in blue while the low-extinction PNe are shown in red. The PNe are divided into elliptical bins to obtain rotation curves.

270 gpm grating was used and provided spectral coverage from 3650 to 9200 Å at a resolution of ~ 5 Å. Some spectra did not cover [O II] 3726/3729 Å because of the design of the spectrograph (alternate fibers are shifted by 30 Å) and the small blueshift of M 31. Each Hectospec fibre subtends 1.5″ on the sky and was positioned on the PN candidates in each field. Table 5.1 shows details of the fields observed in this work whose positions have been marked in Figure 5.1. 847 distinct PNe candidates were targeted with fibres in six fields in M 31.

The initial steps for the data reduction of each Hectospec spectra are similar to that described by Caldwell et al. (2009) for their observations of clusters in M 31, which was also followed by San+12 for their PN spectra. Briefly, following the de-biasing and flat-fielding of each observed field, individual spectra were extracted and wavelength calibrated, including a heliocentric correction. Standard star spectra, obtained intermittently, were used for flux calibration and instrumental response. Sky subtraction was carried out by averaging spectra from fibers placed on

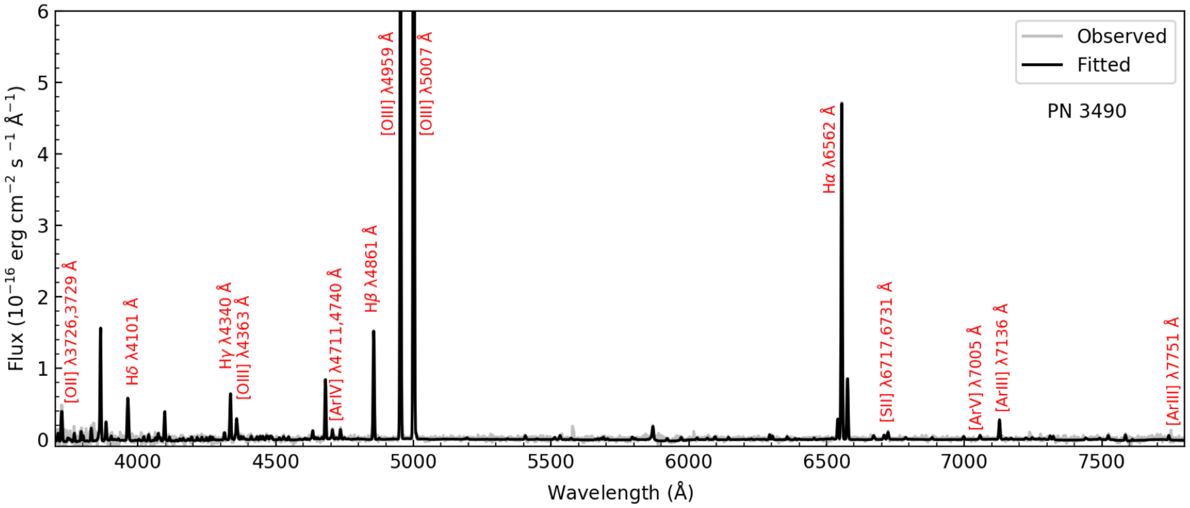

Figure 5.2: An example of the spectra observed by Hectospec for the PNe in M31. The spectra shown in grey is obtained following heliocentric correction, removal of sky-lines and flux calibration. The fitted spectra from ALFA (Wesson 2016) is shown in black. The emission lines of interest are labelled in red. Other emission lines are also observed for the brightest PNe.

blank sky from the same exposures or by offsetting the telescope by a few arcseconds (see Caldwell et al. 2009). The spectra of PN candidates that were observed multiple times (in overlapping fields) have been combined, effectively summing those integration times. Figure 5.2 shows an example of the PN spectra thus obtained.

5.2.2 Emission line fluxes and line-of-sight velocity estimation

Emission line fluxes for each PN candidate were measured using the automated line fitting algorithm, ALFA (Wesson 2016), which has been tailored for emission line sources. Following the measurement of the line-of-sight velocity (LOSV) from the strongest emission lines, with an uncertainty of 3 km s^{-1}, and after subtracting a globally-fitted continuum, ALFA derives fluxes by optimising the parameters of Gaussian fits to line profiles using a genetic algorithm. Of the 847 targeted PNe candidates, 406 had confirmed detection of the [O III] 4959/5007 Å emission lines. The [O III] 5007 Å emission line was detected in all cases with a signal-to-noise ratio higher than 8. All of them also had the Hα line present. The fraction of PNe detected as a function of magnitude is shown in Figure 5.3.

5.2.3 Extinction measurement

For each PN, the emission line fluxes thus measured are then passed to NEAT (Nebular Empirical Analysis Tool; Wesson et al. 2012), which applies an empirical scheme to calculate the extinction and elemental abundances. NEAT calculated c(Hβ) using the flux-weighted ratios of Hα/Hβ,

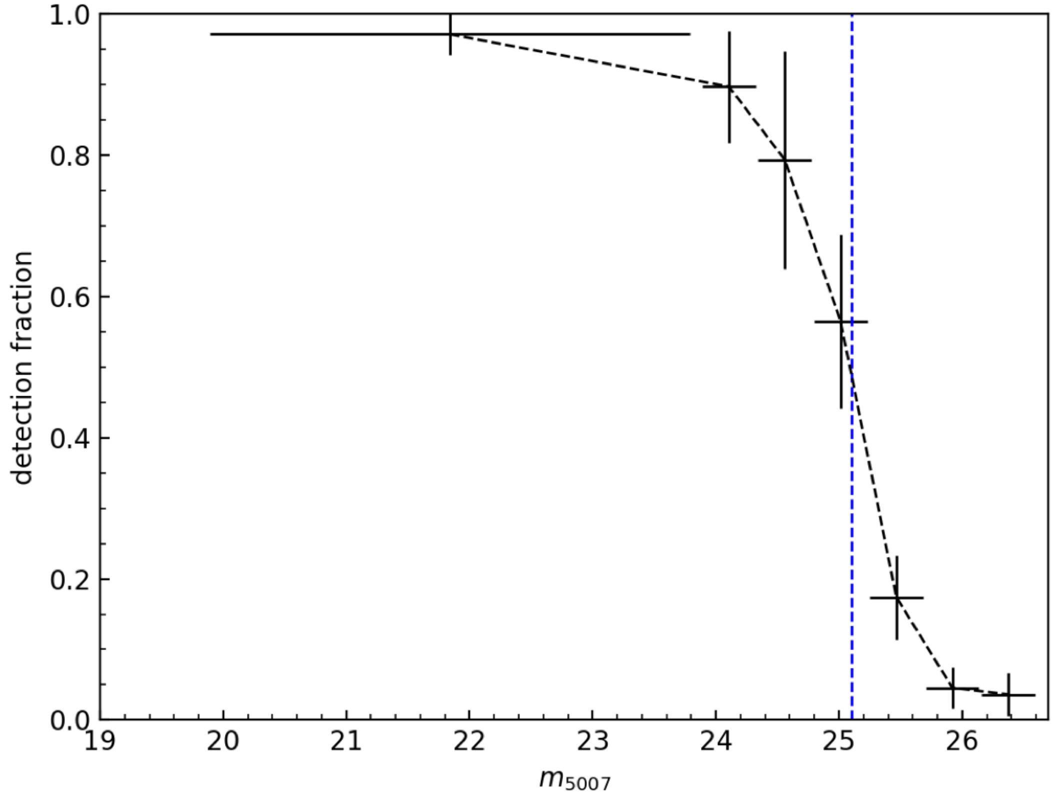

Figure 5.3: Fraction of PNe targeted with spectroscopic observations where [O III] 4959/5007 Å emission lines (the [O III] doublet) were detected. The uncertainty in detection fraction is the binomial proportion confidence-interval of observed PNe in any magnitude bin obtained using the Wilson score interval method (Wilson 1927). The blue dashed line shows the 50% detection limit of the spectroscopic follow-up.

Hγ/Hβ and Hδ/Hβ (whichever pairs are observed) and the extinction law of Cardelli et al. (1989), first assuming a nebular temperature of 10000K and an electron density of 1000 cm^{-3}, and then recalculating c(Hβ) at the measured temperature and density (whenever available). Of the 406 observed PNe, 342 showed the Hβ line and their extinctions (A_V) could be determined.

5.2.4 Position-velocity selection of M 31 disc PNe

The PNe with extinction measurements are de-projected on to the galaxy plane based on the position angle (PA = 38°) and inclination (i = 77°) of M 31 in the planer disc approximation. Those PNe beyond R_{GC} = 30 kpc are not included further in the analysis as a significant fraction of them may be associated with the prominent bright substructures, G1-Clump and Northern Spur, present at these radii. The remaining PNe within R_{GC} = 30 kpc are shown in Figure 5.4

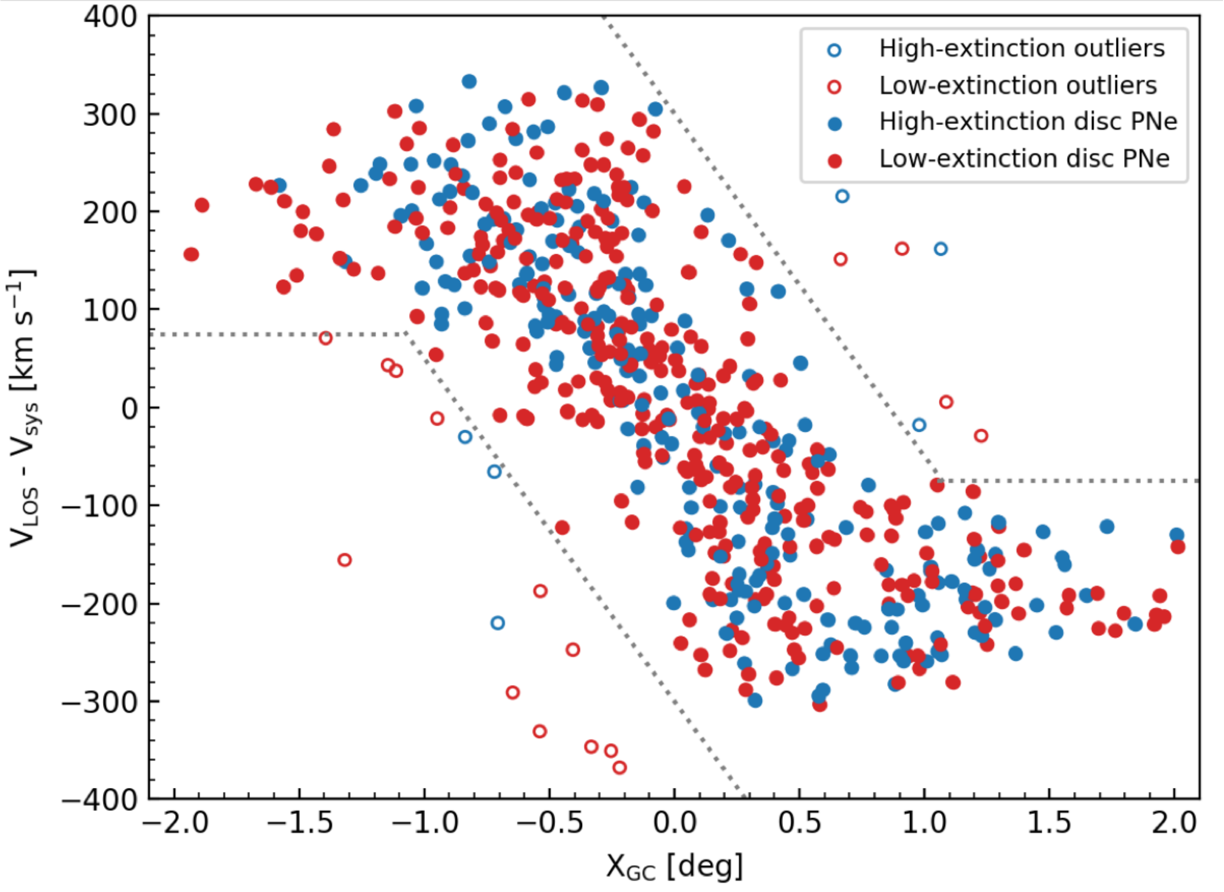

Figure 5.4: Position (X_{GC}; deprojected major-axis distance in deg; 1 deg= 13.68 kpc) vs. Velocity (LOSV – M31 systemic velocity) plot of PNe within R_{GC} = 30 kpc. The high- and low-extinction PNe are shown in blue and red respectively. The dotted lines distinguish the outliers (shown as rings) which have a non-disc angular momentum and possibly correspond to streams or halo PNe.

which plots their position, X_{GC} (de-projected major-axis distance in deg), against their LOSV – M31 systemic velocity (V_{sys} = −309 km s^{-1}; Merrett et al. 2006). While the majority of PNe in M 31 within R_{GC} = 30 kpc are associated with its bulge and disc, some PNe associated with the extension of a luminous substructure or any fainter stellar stream co-spatial with the disc may also be present.

Such non-disc PNe may present themselves as a dynamically cold component that is distinct from the disc PNe in the position-velocity plot (like the PNe associated with the extension of the Giant Stream on the disc as found by Merrett et al. 2003). The dotted lines in Figure 5.4 correspond to an offset from the the mean value of the LOSV – V_{sys} for the PNe to the maximum possible velocity dispersion of the thick disc in M 31 (160 km s^{-1} from Paper II). We identify the position-velocity outliers as those PNe whose LOSV – V_{sys} values are beyond the maximum values for the thick disc PNe in M 31. This successfully identifies as outliers those PNe on

Table 5.2: Number of PNe observed in this work and San+12 to build the total sample of disc PNe that have been included in this analysis.

	This work	San+12	Total
No. of PNe with velocity measurement	406	407	800
Those of the above with extinction measurement	342	334	663
Those of the above in the disc (within R_{GC} = 30 kpc and after PV selection)	265	306	558
Those of the above with oxygen abundance measurement	116	48	161
Those of the above with argon abundance measurement	114	–	114
No. of high extinction PNe in the disc	–	–	222
Those of the above with oxygen abundance measurement	–	–	61
Those of the above with argon abundance measurement	–	–	52
No. of low extinction PNe in the disc	–	–	336
Those of the above with oxygen abundance measurement	–	–	100
Those of the above with argon abundance measurement	–	–	63

the extension of the giant stream identified by Merrett et al. 2003 and a few other PNe. Based on these simple outlier cuts, 265 PNe with extinction measurements within R_{GC} = 30 kpc are probable M 31 disc members and have been considered for the subsequent analysis (some of these within R_{GC} = 5 kpc may also belong to the M 31 bulge). The emission line fluxes of the lines of interest for these PNe have been listed, along with their 1σ uncertainties, in Table C.1. Their measured LOSV and extinction are listed in Table C.2. A more rigorous identification of outliers on the disc plane will be presented in Arnaboldi et al. (2021).

5.2.5 Direct determination of elemental abundances for each PN

Emission lines in the spectra of each of the 265 PNe are de-reddened using the calculated c(Hβ) and then temperatures and densities are calculated using an iterative process from relevant diagnostic lines using NEAT (see Wesson et al. 2012, section 3.3). For our observations, NEAT utilizes the temperature-sensitive [O III] 4363 Å line and the density-sensitive [O II] 3726/3729 Å and [S II] 6717/6731 Å doublets to obtain temperature and electron density for each PNe, whenever the [O III] 4363 Å line is observed. Oxygen and argon ionic abundances are measured from the observed fluxes of the oxygen ([O II] 3726/3729 Å, [O III] 4363/4959/5007 Å) and argon ([Ar III] 7136/7751 Å, [Ar IV] 4711/4740 Å , [Ar V] 7005 Å) lines respectively. Elemental oxygen and argon abundances are obtained from the ionic abundances using the ionisation correction factors (ICFs) from Delgado-Inglada et al. (2014). Uncertainties are propagated through all steps of the analysis into the final values. Of the 265 PNe with extinction measurements included in this study, 116 have oxygen abundances measured, out of which 114 also have argon abundances. Table C.2 lists the oxygen and argon abundances of these PNe.

5.2.6 Final PN sample

Table 5.2 shows the number of PNe identified in each aforementioned step. As in Paper II, we combine our observed sample with those studied by San+12 in the M 31 disc. They observed

407 PNe with LOSV measurements, 334 of which had reliable extinction measurements. 306 PNe from San+12 were within R_{GC} = 30 kpc and survived the position-velocity selection of PNe belonging to the M 31 disc (see Section 5.2.4). Of these, 48 have oxygen abundances measured but no argon abundances were provided by San+12. We note that 13 PNe observed by San+12 were re-observed in this work with velocity measurements consistent within 4 km s^{-1}, three of which had oxygen abundance measurements in both the observations. The oxygen abundance measurements agreed within 0.1 dex. We consider only the measurements from the latest observations for these PNe in our work. We thus have 558 PNe with extinction measurements included in this analysis, 161 of which have oxygen abundances measured while 114 have argon abundances measured. This is the largest sample of PNe with extinction and chemical abundance measurements observed in M 31. Their spatial distribution is shown in Figure 5.1, overlaid on the PAndAS number density map of RGB stars(McConnachie et al. 2018). Table 5.2 also notes the number of San+12 PNe and total number of PNe identified in each aforementioned step.

5.2.7 Classification of planetary nebulae based on extinction measurements

The mass of PN central stars correlates with their circumstellar extinction (Ciardullo & Jacoby 1999). This is because dust production of stars in the AGB phase scales exponentially with their initial progenitor masses for the $1 \sim 2.5 M_{\odot}$ range after which it remains roughly constant (Ventura et al. 2014). Additionally, PNe with dusty high-mass progenitors evolve faster (Miller Bertolami 2016) and so their circumstellar matter has little time to disperse, while PNe with lower central star masses evolve sufficiently slowly that a larger fraction of dust is dissipated from their envelopes (Ciardullo & Jacoby 1999). In Paper II, we found that the high- and low-extinction PNe constituted the kinematically distinct thin and thicker disc of M 31 respectively. From archival CLOUDY photoionization models (Ferland et al. 1998) of a subsample of these PNe (Kwitter et al. 2012), we found ages of ~ 2.5 and ~ 4.5 Gyr for the high- and low-extinction PNe respectively. Based on the distribution of the M31 PNe extinction values (see Figure 5.5) which exhibits a sharp drop at A_V = 0.75 mag, we classify PNe with extinction values higher and lower than A_V = 0.75 mag as high- and low-extinction PNe respectively (for further details, see Section 3.1 in Paper II). Our PNe sample is then divided into 222 high- and 336 low-extinction PNe, which are expected to be associated with the thin and thicker disc stellar populations respectively. Of these, 61 high- and 100 low-extinction PNe have oxygen abundance measurements while 52 high- and 63 low-extinction PNe have argon abundance measurements. Table 5.2 summarises the number of PNe in the high- and low-extinction samples.

5.3 Abundance distribution in the M 31 disc from Planetary Nebulae

We separately explore the chemical abundance distribution of the high- and low-extinction PNe which form the kinematically distinct thin and thicker discs of M 31 (Paper II).

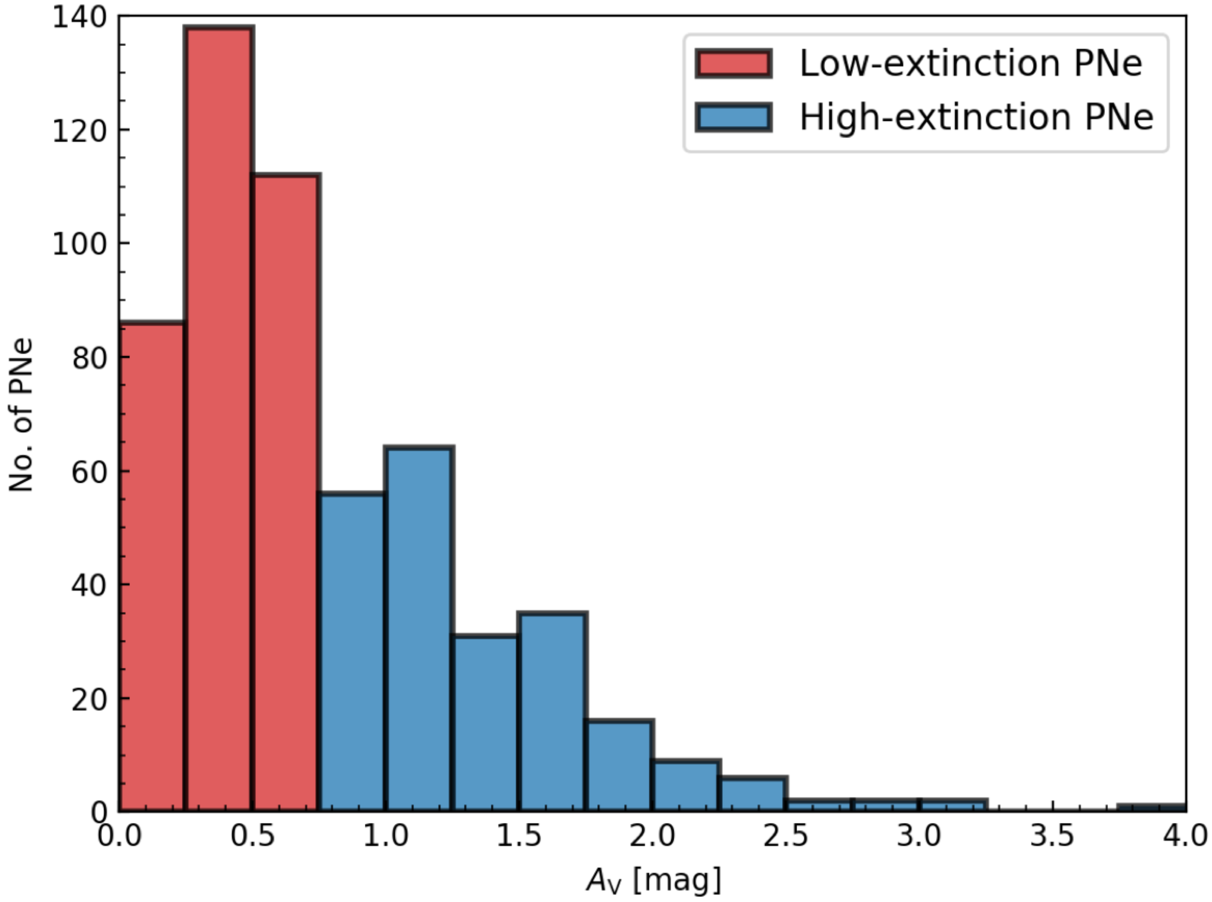

Figure 5.5: Histogram showing the distribution of extinction values of the PNe in the disc. The high- and low-extinction PNe lie in the blue and red shaded regions, respectively.

5.3.1 Oxygen and Argon as tracers of ISM conditions in M 31

While oxygen abundances in PNe have been widely used as a tracer of ISM conditions (MW - Stanghellini & Haywood 2018; M33- Magrini et al. 2009; M31- Sanders et al. 2012; Kwitter et al. 2012), modification of oxygen abundances of the parent stellar population of the PN can occur in the AGB phase and has been observed in MW PNe (e.g. Delgado-Inglada et al. 2015). We utilise our argon abundance measurements to identify evidence of the modification of surface oxygen in the M 31 PNe. Figure 5.6 shows the relation between argon and oxygen abundances in the M 31 PNe. The parameter space occupied by both the high- and low-extinction PNe in this figure is similar to that occupied by those in the MW (Milingo et al. 2010).

Figure 5.7 shows the argon-to-oxygen abundance ratio, log(Ar/O), for the PNe in M 31. The green line shows the average log(Ar/O) value (uncertainty is shaded) found by Delgado-Inglada et al. (2015) for their MW PNe with oxygen-rich dust (ORDs) which have no enrichment or depletion of oxygen, thereby representing the ISM conditions at the time of their formation. The yellow line shows the average log(Ar/O) value (uncertainty is shaded) found by Delgado-

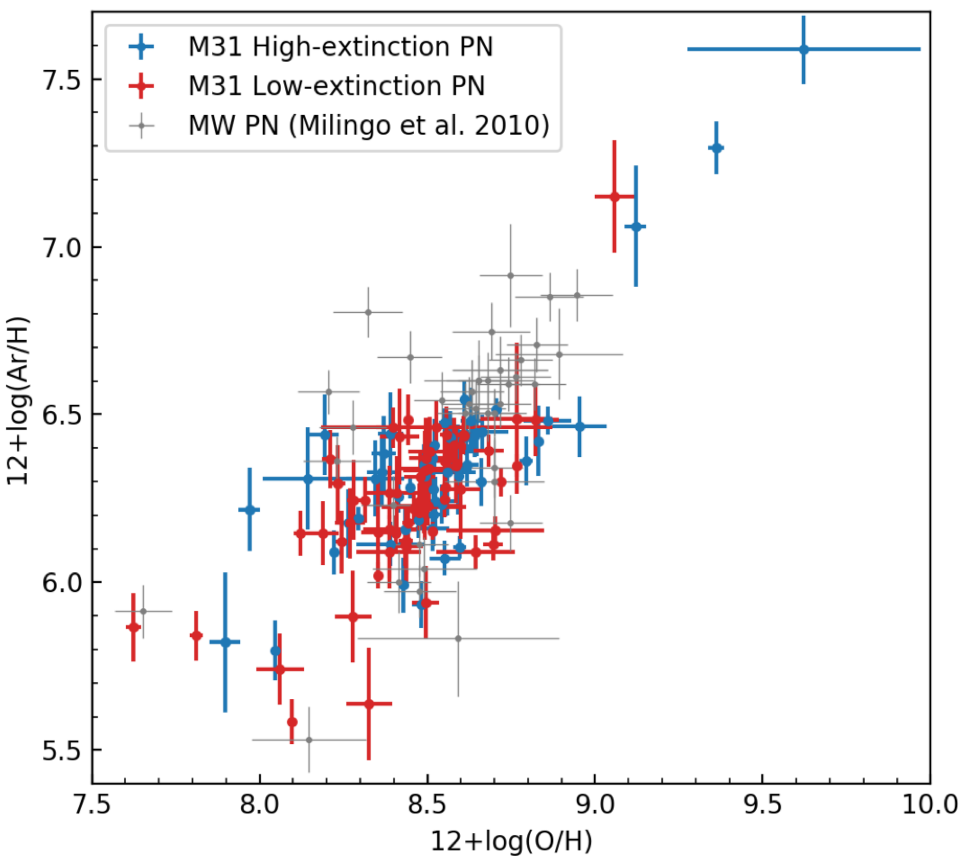

Figure 5.6: Argon abundances are plotted against oxygen abundances for the high- (blue) and low- (red) extinction PNe in M 31. The grey points show the MW PNe observed by Milingo et al. (2010).

Inglada et al. (2015) for their MW CRDs which have experience oxygen enrichment. Figure 5.7 thus illustrates that while the vast majority of M 31 PNe are consistent within errors of having no oxygen enrichment or depletion, a small fraction, coincident with the yellow shaded region, likely displays evidence of oxygen enrichment. M 31 PNe with log(Ar/O) values larger than that shown by the green shaded region have likely undergone oxygen depletion from HBB. As in the MW (Delgado-Inglada et al. 2015), we thus find that the oxygen abundances of individual PNe in M 31 may be modified during the AGB phase leading to both oxygen depletion and enrichment (Section 5.3.1). Argon abundances of PNe remain unaltered and accurately reflect the ISM conditions in the M 31 disc at the time of their birth.

Stanghellini & Haywood (2018) found that the radial abundance gradients of PNe in the MW have similar slopes within error for both Argon and Oxygen abundance gradients. The modification of surface oxygen introduces scatter in the MW PN oxygen abundance measurements but has little effect on the measured gradient given the large sample size. To facilitate comparison to previous measurements of PN oxygen abundance gradients in M 31 and in other galaxies, we continue to present the PN oxygen abundances along with the argon abundances in the following

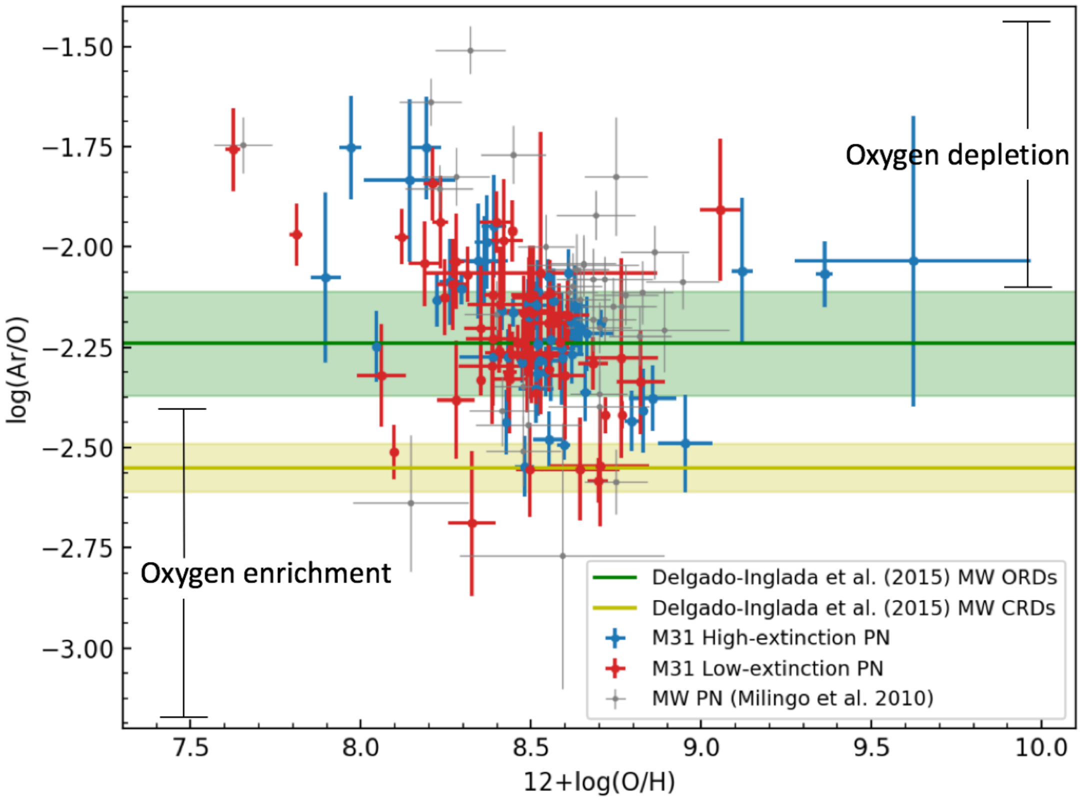

Figure 5.7: log(Ar/O) values are plotted against oxygen abundances for the high- (blue) and low- (red) extinction PNe in M 31. The grey points show the MW PNe observed by Milingo et al. (2010). The green and yellow lines show the average log(Ar/O) value found by Delgado-Inglada et al. (2015) for their MW ORDs and CRDs respectively. Their uncertainties have been shaded. PNe with log(Ar/O) values above and below the green band in this plot are oxygen depleted and enriched respectively (as marked).

analysis given the large number statistics of these measurements for the PNe in M 31.

5.3.2 Oxygen and Argon abundance distribution from PNe

Figure 5.8 shows the PN oxygen abundance distribution for the high- and low-extinction PNe in the M 31 disc within R_{GC}=30 kpc. We can establish whether the stellar populations of the two PN oxygen abundance distributions are different by statistically comparing them. We utilize the two-sample Anderson-Darling test (AD-test; Scholz & Stephens 1987) to compare the two distributions which yields a significance level of 15.8%. Since the significance level is greater than 5%, the null hypothesis that the two samples are drawn from the same distribution can not be rejected. Thus the two PN abundance distributions may or may not be drawn from the same parent stellar population, i.e, the result is inconclusive. However, the mean value of the oxygen abundance for the high-extinction PNe, $< 12 + (\mathrm{O/H}) >_{\mathrm{high-ext}} = 8.5 \pm 0.04$, is higher than

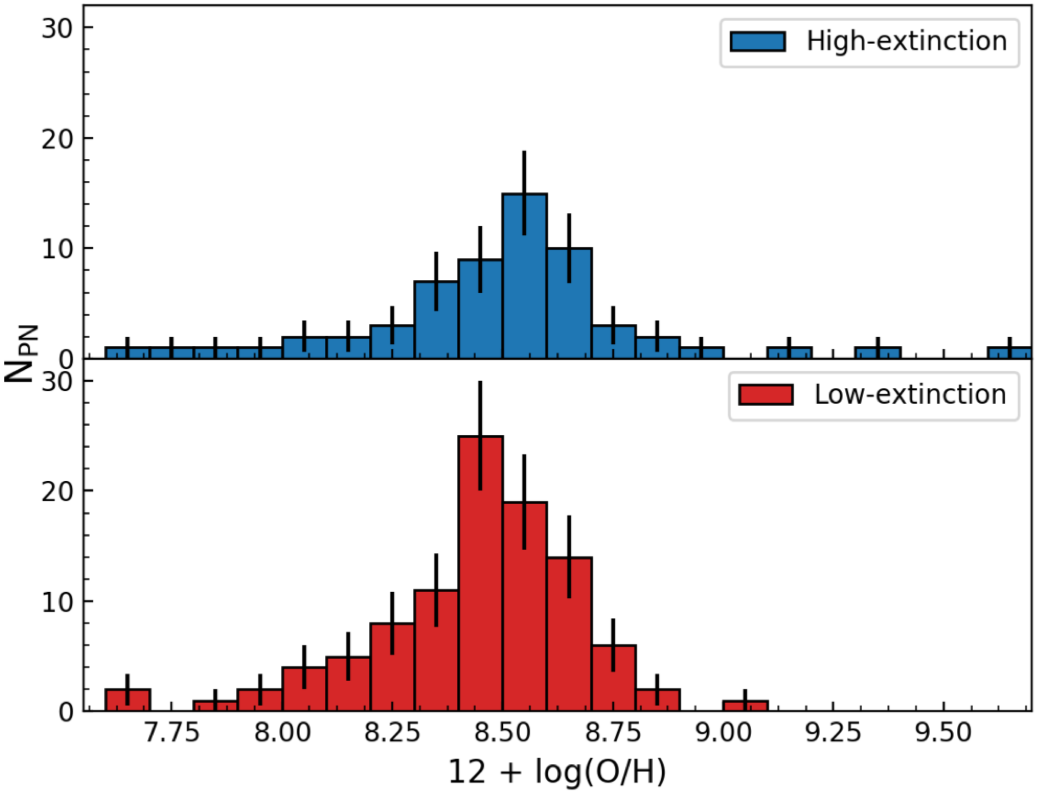

Figure 5.8: Histogram showing the distribution of oxygen abundances for the [top] high- and [bottom] low-extinction PNe. The bins are 0.1 dex wide and show the Poisonian errors as black lines.

that for the low- extinction PNe, $< 12 + (\mathrm{O/H}) >_{\mathrm{low-ext}} = 8.43 \pm 0.02$. This indicates differences between the oxygen abundances of the two PN populations with the the high-extinction PNe being more metal-rich, but there is considerable overlap in the distributions reflected in the large standard deviation of their oxygen abundance values, $\sigma(12 + (\mathrm{O/H}))_{\mathrm{high-ext}} = 0.32$ and $\sigma(12 + (\mathrm{O/H}))_{\mathrm{low-ext}} = 0.24$. The oxygen abundance values for HII regions obtained from direct measurements of nebular temperatures in M 31 (Escala et al. 2020), which show the present-day (~0.5 Gyr) ISM conditions, are $< 12 + (\mathrm{O/H}) >_{\mathrm{HII}} = 8.44 \pm 0.05$ with $\sigma(12 + (\mathrm{O/H}))_{\mathrm{HII}} = 0.16$. The mean oxygen abundance for HII regions overlaps within error with that of both the high- and low-extinction PNe. However, because of difficulties in measuring the temperature-sensitive [OIII] 4363 Å emission-line for HII regions as they have very high extinction, the HII region direct oxygen abundance measurements are only from a small sample of 12 HII regions covering a small radial range of R_{GC} =8–17 kpc. Increase in the sample size of HII regions with direct oxygen abundance measurements can give insight into any possible chemical enrichment of the ISM over time.

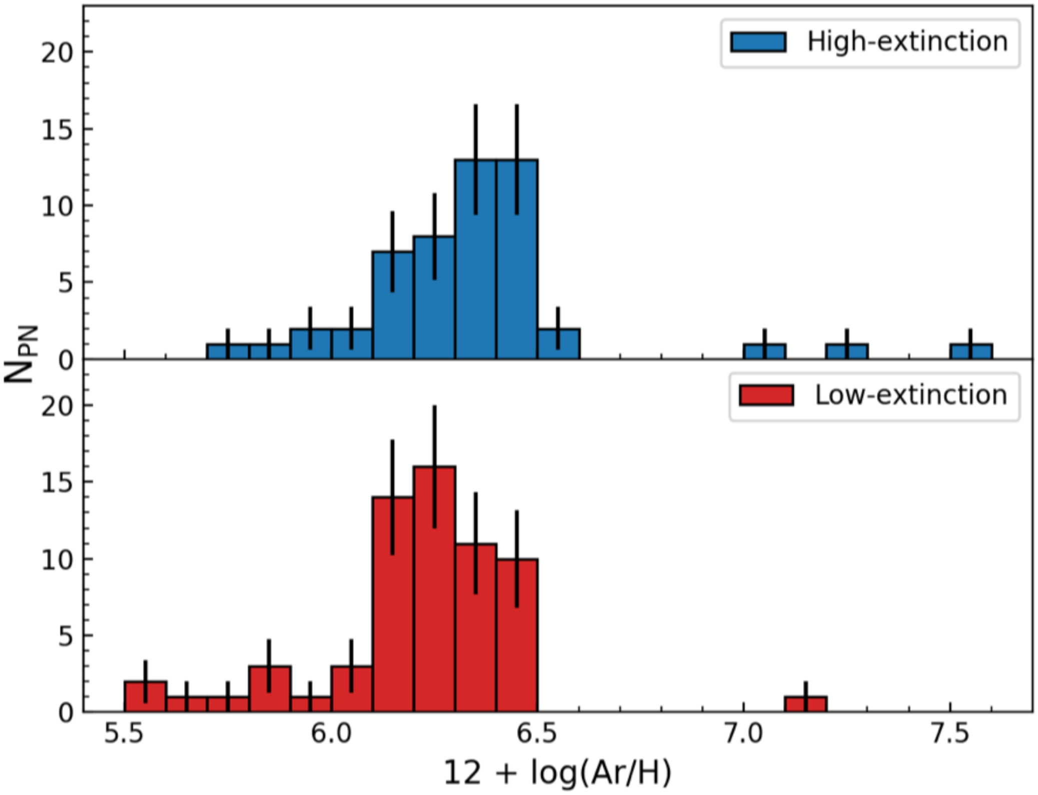

Figure 5.9: Histogram showing the distribution of argon abundances for the [top] high- and [bottom] low-extinction PNe. The bins are 0.1 dex wide and show the Poisonian errors as black lines.

Figure 5.9 shows the PN argon abundance distribution[1] for the high- and low-extinction PNe in the M 31 disc within ~30 kpc. The PN argon abundance distributions reflect the ISM conditions for the high- and low-extinction PNe. We utilize the AD-test to statistically compare the two distributions which yields a significance level of 2.4%. Since the significance level is lesser than 5%, the null hypothesis that the two samples are drawn from the same distribution is rejected. Thus the two PN argon abundance distributions are drawn from different distributions implying that the high- and low-extinction PNe were born from different ISM conditions, accurately traced with different argon elemental abundances. Their parent stellar populations, forming the thin and thicker disc of M 31, are hence both kinematically (Paper II) and chemically distinct. The latter is the result from the current analysis. The mean value of the argon abundance for

---

[1] The argon and oxygen abundances are obtained from almost the same PNe (Table 5.2) observed in this work but the oxygen abundance sample is larger due to inclusion of those PNe observed by San+12. While these authors did not present argon abundances in their paper, argon abundances can be derived from the re-analysis of their observed spectra which we will carry out in the near future.

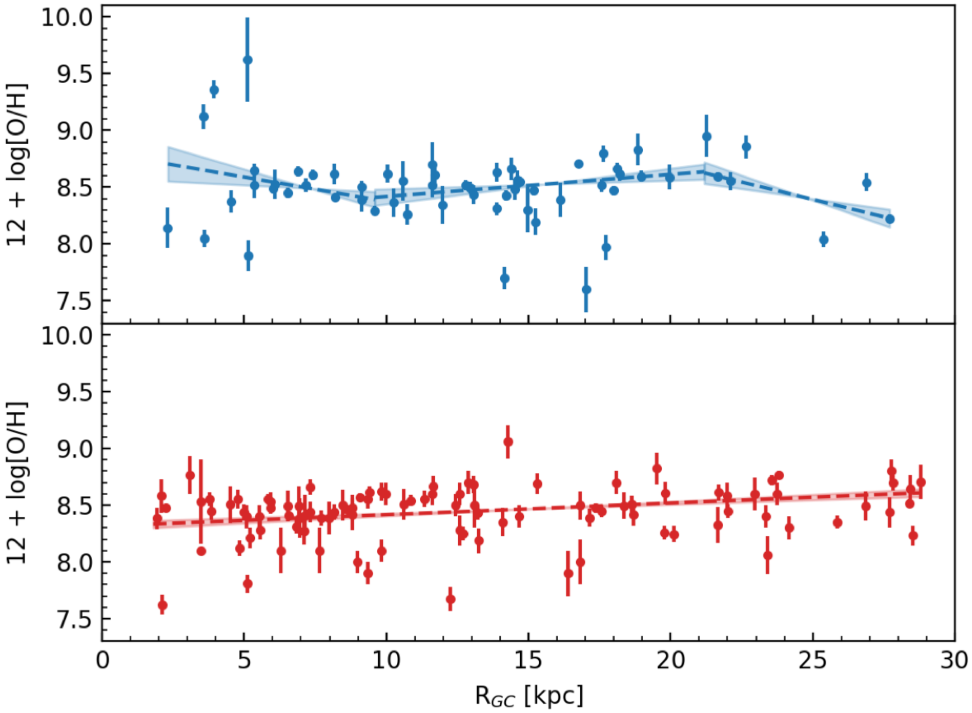

Figure 5.10: The galactocentric radial distribution of oxygen abundances for the [top] high- and [bottom] low-extinction PNe in M 31. The best-fitting piece-wise radial oxygen abundance gradient is shown for the high- (blue) and low-extinction (red) PNe. The uncertainty in the fits are shaded.

the high-extinction PNe, $< 12 + (\mathrm{Ar/H}) >_{\mathrm{high-ext}} = 6.35 \pm 0.04$, is clearly higher than that for the low- extinction PNe, $< 12 + (\mathrm{Ar/H}) >_{\mathrm{low-ext}} = 6.23 \pm 0.03$. The standard deviation of their argon abundance values, $\sigma(12 + (\mathrm{Ar/H}))_{\mathrm{high-ext}} = 0.29$ and $\sigma(12 + (\mathrm{Ar/H}))_{\mathrm{low-ext}} = 0.23$, reflects the overlap in their argon abundance distribution.

5.3.3 Oxygen abundance gradients in the M 31 discs from PNe

Figure 5.10 shows the galactocentric radial distribution of PN oxygen abundances distinctly for high- and low-extinction PNe samples. Previous authors (Sanders et al. 2012; Kwitter et al. 2012; Peña & Flores-Durán 2019) have relied on fitting the entire radial range of PN oxygen abundances with a single slope. However, for many galaxies (e.g. Sánchez-Menguiano et al. 2018), including the MW (Stanghellini & Haywood 2018), oxygen abundance gradients show different slopes at different radial distances reflecting the ISM processes that shaped their abundance distribution. From a theoretical standpoint (Mollá et al. 2019, and references therein), different ISM restructuring mechanisms, such as the presence of a bar or transient spiral arms

Table 5.3: Fitted parameters for oxygen abundance gradients in M 31.

PN sample	Segments	X_0	$\Delta X/\Delta R$ dex/kpc	Fitted range kpc
High-extinction	3	8.8 ± 0.22	-0.043 ± 0.03	2.31–9.59
		8.22 ± 0.18	0.019 ± 0.012	9.59–21.18
		9.926 ± 0.66	-0.061 ± 0.022	21.18–27.69
Low-extinction	1	8.31 ± 0.04	0.01 ± 0.002	1.94–28.78
High-extinction (median)	3	8.77 ± 0.06	-0.038 ± 0.008	2.31–9.7
		8.23 ± 0.07	0.019 ± 0.005	9.7–20.79
		9.08 ± 0.09	-0.021 ± 0.006	20.79–27.69
Low-extinction (median)	3	8.54 ± 0.06	-0.019 ± 0.01	1.94–7.86
		8 ± 0.22	0.053 ± 0.026	7.86–9.56
		8.48 ± 0.06	0.001 ± 0.003	9.56–28.78

which affect stellar radial migration, operate at different radial ranges in a galaxy disc and thus influence the radial abundance gradient differently at these radial ranges (Daniel & Wyse 2018; Ruiz-Lara et al. 2017). The ISM restructuring is further exacerbated in the case of galaxy mergers which especially lead to flat abundance gradients at large radii (Ruiz-Lara et al. 2017). Thus, galactocentric radial distribution of elemental abundances are better fit with piecewise linear fits in different radial ranges (e.g. MW- Stanghellini & Haywood 2018). Given our larger number statistics for the PNe oxygen abundance measurements in M 31, we fit both the high- and low-extinction PN samples with piecewise linear regression using PWLF (Jekel & Venter 2019).

For each PN abundance sample, we first utilise Bayesian optimization procedures[2] (see e.g. Snoek et al. 2012) using GPyOpt[3] to find the number of line segments and their break points that provide the best fit to the data. Briefly, Bayesian optimization attempts to find the global optimum in the minimum number of steps when the objective function, here a function describing the combination of line segments and break points, that describes the data is not known. We assume that the approximate objective function, termed the surrogate model, is a Gaussian process[4]. The data-set, here the PN abundance sample, is searched using an acquisition function[5] to iteratively optimise the objective function. The objective function is updated at the end of each iteration to eventually represent the best fit model, here the optimum number of line segments and their break points describing the PN abundance sample. This results in the piecewise linear regression fit to each PN abundance sample where the line segments and break points have been simultaneously fitted.

---

[2] described in brief by http://krasserm.github.io/2018/03/21/bayesian-optimization/

[3] http://github.com/SheffieldML/GPyOpt

[4] A Gaussian process is a collection of parameters such that any linear combination of them is normally distributed.

[5] The acquisition function governs the efficient sampling of the data-set. We use expected improvement (Snoek et al. 2012) as the acquisition function.

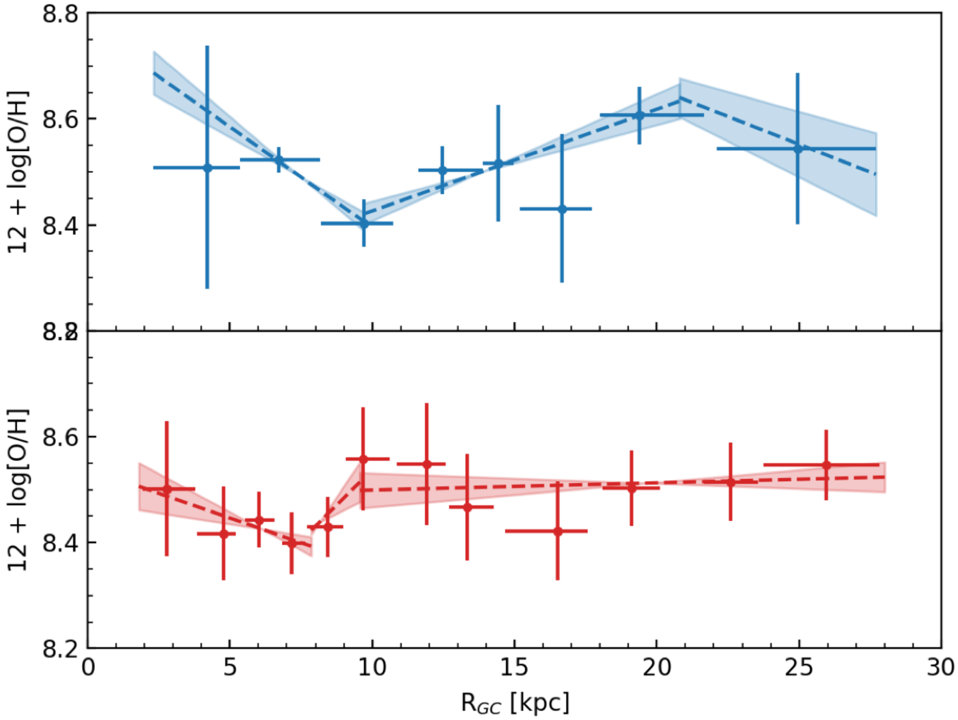

Figure 5.11: The median galactocentric radial distribution of oxygen abundances for the [top] high- and [bottom] low-extinction PNe in M 31. Each bin has eight PNe. The error on the x-axis shows the bin width. The best-fitting piece-wise radial oxygen abundance gradient is shown for the high- (blue) and low-extinction (red) PNe. The uncertainty in the fits are shaded.

Figure 5.10 shows the galactocentric radial distribution of PN oxygen abundances for high- and low-extinction PNe samples are best fit by three lines and one line respectively. Their fit parameters are noted in Table 5.3. We additionally confirm for the high-extinction PNe that three line segments are a better fit to the data than one line segment comparing the Bayesian Information Criterion[6] (BIC; Schwarz 1978) parameter in each case. A lower value of the BIC parameter indicates a better fit. For the three line-segment fit to the high-extinction PNe, BIC=−182.3 while for the one line-segment fit, BIC=−176.38 , thereby indicating that the high extinction PN sample is indeed best fit by three line segments.

---

[6] It is a criterion for model selection among a finite set of models based on bayesian statistics. Overfitting may result from adding parameters to increase the likelihood of a function. BIC introduces a penalty term for the number of parameters in the model in order to avoid overfitting.

Table 5.4: Fitted parameters for argon abundance gradients in M 31.

PN sample	Segments	X_0	ΔX/ΔR dex/kpc	Fitted range kpc
High-extinction	1	6.42 ± 0.08	-0.007 ± 0.005	2.31–27.69
Low-extinction	1	6.26 ± 0.05	-0.003 ± 0.003	1.94–28.78
High-extinction	2	6.44 ± 0.03	-0.013 ± 0.003	2.31–13.06
(median)		6.64 ± 0.06	-0.016 ± 0.003	13.89–27.69
Low-extinction	2	6.37 ± 0.08	-0.02 ± 0.012	1.94–8.61
(median)		6.45 ± 0.13	-0.009 ± 0.007	8.8–28.78

5.3.4 Median oxygen abundance gradient from PNe

For both the high- and low-extinction PNe, the scatter in the galactocentric radial distribution of their oxygen abundances is evident in Figure 5.10. This scatter can be attributed to various factors including the modification of oxygen abundances of the parent stellar population of the PNe during the AGB phase (Delgado-Inglada et al. 2015), PN evolution from multiple parent stellar populations of different ages, and effects of the vertical oxygen abundance gradient imprinted on the measured radial oxygen abundance gradient given the high-inclination of M 31 and the thickness of its disc. In order to circumvent this issue of the scatter affecting the fit to the PN radial oxygen abundance gradient, we obtain the median of the PN oxygen abundances in radial bins, having eight PNe per bin (Figure 5.11). This allows the most prominent metallicity component, stemming from the most dominant stellar population (likely in-plane), to be represented in each metallicity bin.

We also fit the median oxygen abundance gradient for both the high- and low-extinction PNe with piecewise linear regression. Figure 5.11 shows that the median galactocentric radial distribution of PN oxygen abundances for high- and low-extinction PNe samples are both best fit by three lines each. Their fit parameters are also noted in Table 5.3. For the three line-segment fit to the median oxygen abundances for the high-extinction PNe, BIC=-26.71 while for the one line-segment fit, BIC=-20.52. Similarly, for the three line-segment fit to the median oxygen abundances for the low-extinction PNe, BIC=-68.93 while for the one line-segment fit, BIC=-66.35. Thus both median PN samples are indeed best fit by three line segments.

5.3.5 Argon abundance gradient from PNe

Figure 5.12 shows the galactocentric radial distribution of PN argon abundances distinctly for high- and low-extinction PNe samples. As in Section 5.3.3, we fit both the high- and low-extinction PN samples with piecewise linear regression using PWLF (Jekel & Venter 2019). Both high- and low-extinction PNe samples are best fit by one line. Their fit parameters are noted in Table 5.4.

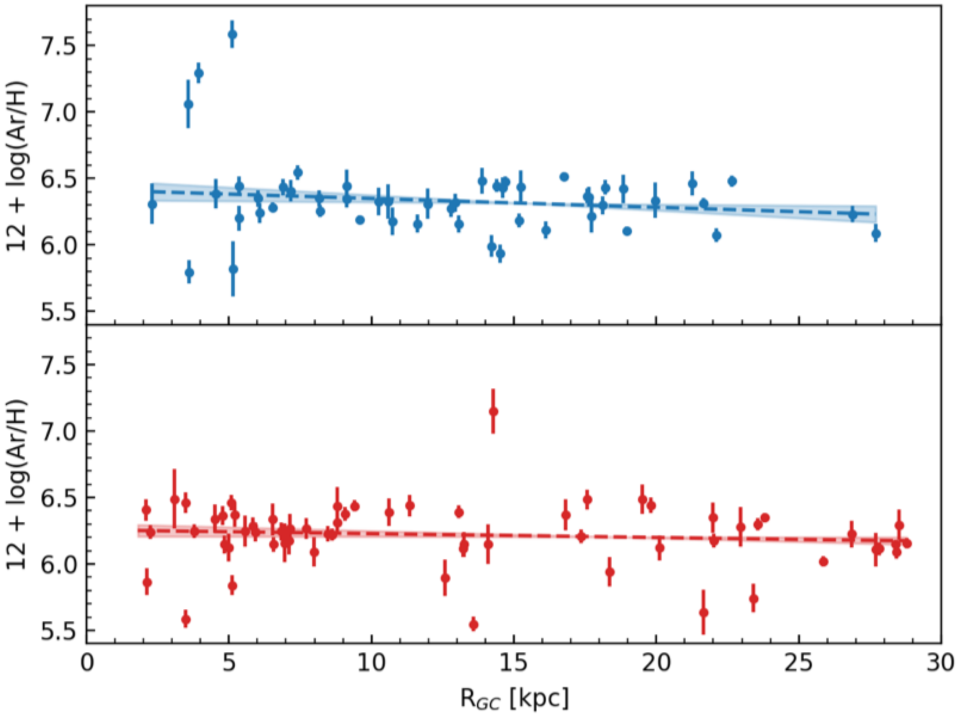

Figure 5.12: The galactocentric radial distribution of argon abundances for the [top] high- and [bottom] low-extinction PNe in M 31. The best-fitting piece-wise radial oxygen abundance gradient is shown for the high- (blue) and low-extinction (red) PNe. The uncertainty in the fits are shaded. The cyan region in the top panel highlights the galactocentric radii covered by the 10 kpc star forming ring in M 31 (Dalcanton et al. 2015). The magenta region in the bottom panel highlights the galactocentric radii at which Gregersen et al. (2015) also observe a dip in the radial metallicity gradient from RGB stars in the PHAT footprint.

5.3.6 Median argon abundance gradient from PNe

For both the high- and low-extinction PNe, the scatter in the galactocentric radial distribution of their argon abundances is evident in Figure 5.12. This scatter is more prominent for the low-extinction PNe. The scatter may be attributed to the PN evolution from multiple parent stellar populations of different ages and effects of the vertical argon abundance gradient imprinted on the measured radial argon abundance gradient given the high-inclination of M 31 and the thickness of its disc. Both these effects are more pronounced for the low-extinction PNe which cover a wider range of older parent stellar populations and are present in the thicker disc. In order to circumvent this issue of the scatter affecting the fit to the PN radial argon abundance gradient, we obtain the median of the PN argon abundances in radial bins, having seven PNe per bin (Figure 5.13). This allows the most prominent metallicity component, stemming from the most

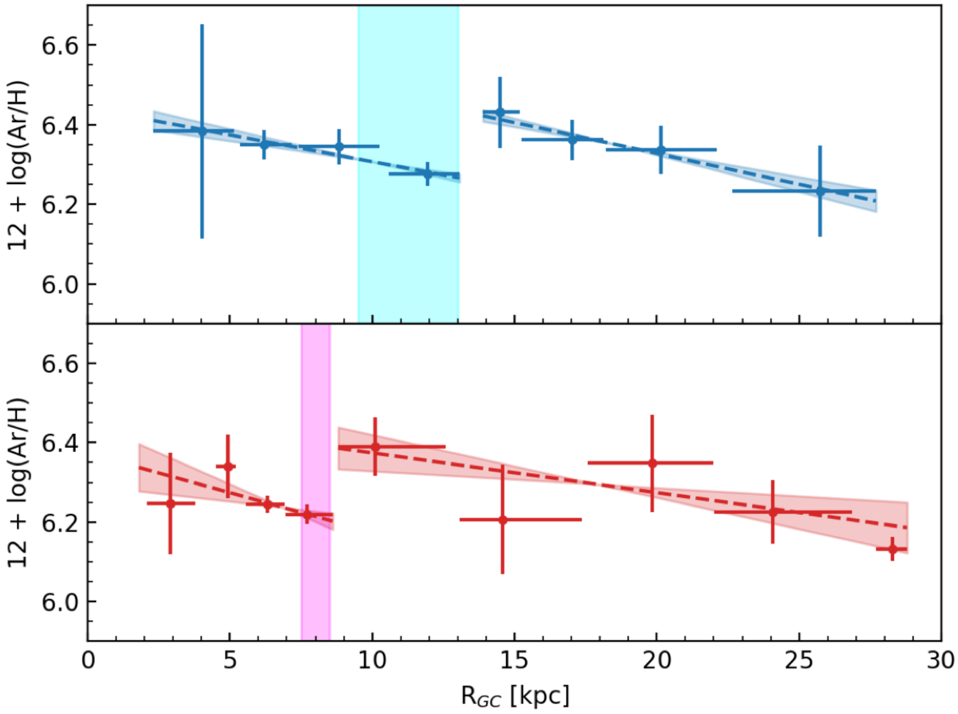

Figure 5.13: The median galactocentric radial distribution of oxygen abundances for the [top] high- and [bottom] low-extinction PNe in M 31. Each bin has eight PNe. The error on the x-axis shows the bin width. The best-fitting piece-wise radial oxygen abundance gradient is shown for the high- (blue) and low-extinction (red) PNe. The uncertainty in the fits are shaded.

dominant stellar population (likely in-plane), to be represented in each metallicity bin.

We also fit the median argon abundance gradient for both the high- and low-extinction PNe with piecewise linear regression. Figure 5.11 shows that the median galactocentric radial distribution of PN argon abundances for high- and low-extinction PNe samples are both best fit by two lines each. Their fit parameters are also noted in Table 5.4. For the two line-segment fit to the median argon abundances for the high-extinction PNe, BIC=-62.15 while for the one line-segment fit, BIC=-41.95. Similarly, for the two line-segment fit to the median argon abundances for the low-extinction PNe, BIC=-38.53 while for the one line-segment fit, BIC=-36.06. Thus both median PN samples are indeed best fit by two line segments.

5.4 Discussion

5.4.1 Interpreting the abundance gradients in M 31

We find that the high- and low-extinction PNe are both kinematically (Paper II) and chemically distinct (Section 5.3.2), forming the dynamically colder thin disc and dynamically hotter thicker disc respectively. The piece-wise fits to the radial abundance measurements in M 31 allow for the interpretation of the abundance gradients at different radial ranges. With both argon and oxygen abundance measurement, we also check for the influence of surface oxygen modification in the AGB phase on the radial abundance gradients.

For the thin disc, the radial distribution of oxygen abundances from individual PNe (Figure 5.10) and also for the median oxygen abundances (Figure 5.11) are best fitted by three line-segments showing a trough in oxygen abundances values at $R_{GC} \sim 10$ kpc and a crest at $R_{GC} \sim 21$ kpc. The trough is also seen in the radial distribution of median argon abundances values at similar radial ranges (Figure 5.13) but is not prominent enough to appear in the argon abundances from individual PNe (Figure 5.12). This trough corresponds with the 10 kpc star-forming ring in M 31 (Dalcanton et al. 2015) and indicates that the thin disc stellar population in this ring is less metal-rich than the adjacent radial regions. Williams et al. (2017) from isochrone-fitting of resolved stars in the *Hubble Space Telescope* observations in the Pan-Hubble Andromeda Treasury (PHAT- Dalcanton et al. 2012) also found in some of their isochrone fits (see their Figure 20) that the 10 kpc star-forming ring in M 31 has stars with lower metallicity than the adjacent radial regions.

The crest in the thin disc radial distribution of oxygen abundance measurements does not occur in the argon abundance distributions. There is no influence from any substructure PNe at $R_{GC} \sim 21$ kpc nor any star forming-ring. We thus check if this is an effect of surface oxygen modification in AGB stars effecting the PN oxygen abundances that influences the abundance gradients in the M 31 thin disc. The top panel of Figure 5.14 shows the galactocentric radial distribution of log(Ar/O) values for the high-extinction thin disc PNe in M 31. The oxygen-enriched PNe appear only around R_{GC}=14–23 kpc while the oxygen-depleted PNe appear intermittently at various radial distances within 18 kpc. Oxygen enrichment thus influences the fitted radial oxygen abundance gradients for the thin disc PNe. Unlike in the MW (Stanghellini & Haywood 2018), even the median oxygen abundance gradient is influenced by oxygen enrichment and thereby does not reflect the ISM conditions in the R_{GC}=14–23 kpc radial range. We thus consider the median argon abundance gradients of -0.013 ± 0.003 and -0.016 ± 0.003 in R_{GC}=2.31–13.06 kpc and R_{GC}=13.89–27.69 kpc respectively as the abundance gradients for the thin disc of M 31.

For the thick disc, the radial distribution of oxygen abundances from individual PNe (Figure 5.10) is best fit by a single line for the entire radial range with a positive slope (Table 5.3). However, the radial distribution of median oxygen abundances (Figure 5.11) are best fitted by three line-segments showing a trough in oxygen abundances values at $R_{GC} \sim 8$ kpc but with a metallicity gradient consistent with being flat (Table 5.3) in the R_{GC}=9.56–28.78 kpc radial range. For the radial distribution of argon abundances from individual PNe in the M 31 thick disc (Figure 5.12), the entire radial range is best fit by a single line but having a negative slope that is consistent with being flat (Table 5.4). However, the radial distribution of median ar-

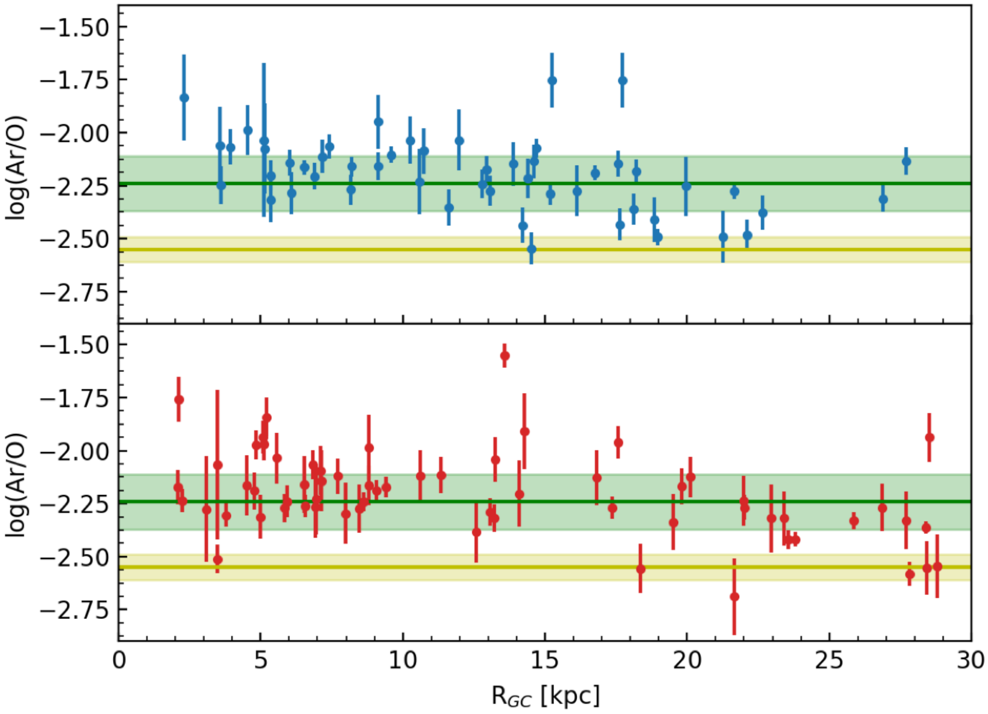

Figure 5.14: The galactocentric radial distribution of log(Ar/O) values for the [top] high- and [bottom] low-extinction PNe in M 31. The green and yellow zones are the same as in Figure 5.7. PNe with log(Ar/O) values above and below the green band in this plot are oxygen depleted and enriched respectively (as also marked in Figure 5.7).

gon abundances (Figure 5.13), similar to the median oxygen abundances, shows the trough at $R_{GC} \sim 8$ kpc and is best fitted by two linear functions. The rise in abundances from $R_{GC} \sim 8$–10 kpc, captured by the middle segment in the median oxygen abundance radial distribution, is not captured in the median argon abundances simply due to lower number of PNe with argon abundances in this radial range. A slight trough at $R_{GC} \sim 8$ kpc is also observed in the photometric metallicity ([M/H]) gradient calculated by Gregersen et al. (2015) from fitting resolved ∼ 4 Gyr old RGB stars in the PHAT footprint (see their Figure 9) but may be negligible within errors. Given its appearance in the median argon abundance distribution, this trough is a reflection of the ISM conditions at the epoch of formation of the thick disc PNe. In Section 5.4.3, we discuss the possible origin of this through with respect to the major merger scenario of M 31.

The argon abundance gradient beyond $R_{GC} \sim 9$ kpc is negative (Table 5.4) and thus differs slightly from the flat median oxygen abundance gradient. As seen in the lower panel of Figure 5.14, oxygen-enriched PNe in the thick disc appear mainly beyond R_{GC}=18 kpc while the oxygen-depleted ones appear intermittently at various radial distances. The slightly negative argon abundance gradient appears as flat in the oxygen abundance gradient since the thick disc PNe beyond R_{GC}=18 kpc have so low intrinsic abundances that their surface oxygen is enriched in the TDU process (Ventura et al. 2017). Oxygen enrichment thus influences the fitted radial oxygen abundance gradients also for the M 31 thick disc PNe and thus does not reflect the ISM conditions in the radial range beyond R_{GC}=18 kpc. We thus consider the median argon abundance gradients of -0.02 ± 0.012 and -0.009 ± 0.007 in R_{GC}=1.94–8.61 kpc and R_{GC}=8.8–28.78 kpc respectively as the abundance gradients for the thick disc of M 31. Thus, compared to previous attempts at fitting the abundance gradient in M 31 (Sanders et al. 2012; Kwitter et al. 2012; Peña & Flores-Durán 2019), where the oxygen abundance was found to be near-flat for the complete PN sample, we find a steeper abundance gradient for the outer thin disc at R_{GC}=13.89–27.69 kpc, while the near-flat abundance gradient is found for the outer thick disc at R_{GC}=8.8–28.78 kpc.

5.4.2 The radial elemental abundance distribution and the merger scenario in M 31

In a minor merger scenario in M 31 as advocated by Fardal et al. (2013), a satellite galaxy (mass ratio ~ 1:20) infalls along the giant stream on to the M 31 disc ~1 Gyr ago. Such a satellite however would not disrupt the thicker disc by the velocity dispersion measured in Paper II and would additionally not form a thin disc (Martig et al. 2014). Following the major merger scenario described by Hammer et al. (2018), however, the pre-merger disc in M 31 would be perturbed by the a massive satellite (mass ratio > 1:4.5) in a highly retrograde orbit. The first pericenter passage of the satellite takes place ~ 7 Gyr ago while the second pericenter passage occurs ~ 3 Gyr ago and the satellite then has multiple passages in the inner regions of M 31 before finally coalescing with the bulge. The thin disc is formed from the gas brought in by the satellite along with a burst of star formation.

The observed thin disc PNe are ~2.5 Gyr old (or younger; Paper II) and likely capture the thin disc during its formation while the major merger is still ongoing in the inner regions and soon after. While Hammer et al. (2018) do not analyse the radial abundance gradients in their simulations, the secular evolution of a thin disc after formation has been shown in other cosmological models (e.g. Gibson et al. 2013; Zinchenko et al. 2015) to result in a negative radial abundance gradient, consistent with the observed negative abundance gradient for the thin disc PNe.

A near-flat abundance gradient, as observed here for the M 31 thick disc, has been seen in cosmological simulations of merging galaxies with merger mass ratio ≥1:10 (Tissera et al. 2019). Zinchenko et al. (2015) studied the effect of mergers on the radial elemental abundance profiles of MW mass galaxies using N-body simulations (no new star formation). They found that the amount of flattening of the radial abundance gradient at large radii depends on the mass and inclination of the in-falling satellite, with flatter gradients observed for more massive mergers. Furthermore, chemodynamical simulations of merging galaxies (e.g. Perez et al. 2011) find that gas from the merging satellite galaxy falls into the center of the massive host galaxy during the first pericenter passage, lowering the mean-metallicity of the stars in the central regions of the host galaxy which are formed soon after. If the first pericenter passage occurred ~7 Gyr ago as predicted by Hammer et al. (2018), these lower elemental abundance stars in the central regions of M 31 would appear as the low-extinction PNe in M 31 which are older than ~4.5 Gyr, thereby lowering the central abundance measured from the low-extinction PNe and resulting in flatter abundance gradients. It is thus likely that the thick disc of M 31 exhibits the near-flat abundance gradient as a result of the recent massive merger.

It is possible that the trough observed at $R_{GC} \sim 8$ kpc results from stars from the satellite galaxy, which would be more metal poor compared to the pre-merger M 31 disc PNe following the mass-metallicity relation (e.g. Zahid et al. 2017). The elemental abundance distribution from PNe thus acts as constraints for merger simulations in M 31. While the fairly major merger simulations by Hammer et al. (2018) do predict the formation of distinct thin and thick discs as observed, predictions of the abundance gradients from such simulations must conform to the observed values.

5.4.3 Inferences on chemical evolution of galaxies

Simulations of chemical evolution in galaxies make predictions on the variation of the radial abundance gradient over time depending on the choice of physical mechanisms, particularly feedback prescriptions, that govern the enrichment of elements into the ISM (e.g. Gibson et al. 2013; Mollá et al. 2019). In secular evolution of galaxy discs, such simulations generally predict either an initial flat gradient that steepens over time or an initial steep one that flattens over time (Gibson et al. 2013). These predictions can be constrained from radial abundance gradients measurements of stars formed in different epochs in a galaxy, as carried out using the PNe in the MW by Stanghellini & Haywood (2018).

In the case of M 31, the thick disc PNe have a flatter abundance gradient than the thin disc PNe and provide two epochs of star formation where the chemical evolution of M 31 can be constrained. The present-day epoch for such comparisons is provided by the abundance gradient from direct oxygen abundance measurements in HII regions in M 31. This is found by Esteban et al. (2020) within $R_{GC} \sim 8$–18 kpc to be -0.014 ± 0.01 dex, consistent with both the thin and thick disc PN abundances. Thus constraints to chemical evolution models of M31 are subject to a more accurate measurement of the direct oxygen abundance gradient for HII regions in M 31. However, the abundance gradients from the PNe (both thin and thick disc) and HII regions are flatter than predicted by secular evolution models of galaxy evolution by Gibson et al. (2013), regardless of the enrichment prescriptions used. Since merger events typically flatten radial metallicity gradients, the flat metallicity gradient of M 31 compared to secular evolution models underscores the influence of the recent merger on the radial metallicity gradient of M 31. Further insight on the chemical evolution of M 31 may be obtained from comparison with simulations having different chemical evolution recipes for merging galaxies (e.g. Rupke et al. 2010).

5.5 Conclusions

We present the largest sample till date of PNe in the M 31 disc with extinction measurements, oxygen abundances and argon abundances. We classify our observed PNe on the basis of their measured extinction into high- and low-extinction PNe, which were found to be kinematically distinct in Paper II. Direct oxygen and argon abundance distributions and radial gradients are measured for the high- and low-extinction PNe separately in the M 31 disc. Our conclusions can be summarised as follows:

- We find that AGB evolution in PNe modifies their oxygen abundances for PNe in M 31, also affecting oxygen radial abundance gradients. This is the only galaxy outside the MW where this effect has been measured.
- Argon abundance measurements are a better indicator of the ISM conditions from PNe.
- Comparing the argon abundances in the thin and thicker disc reveals that the two discs are chemically distinct. This is the first combined evidence of kinematically and chemically distinct thin and thicker discs in M 31.
- The abundance gradients for both the thin and thick disc in M 31 are flatter than expected from secular evolution models. However, the steeper abundance gradient for the thin disc of M 31 and the near-flat abundance gradient for the thick disc of M 31 is consistent with the expectations of a major merger scenario.

Quantitative comparisons with the major merger models by Hammer et al. (2018) would require the radial metallicity distributions from their (or other) merger simulations. Given that the merger mass and orbital inclination has measurable influence on the metallicity gradient (Zinchenko et al. 2015), the observed abundance gradients provide constraints on the mass and inclination of the merging satellite in a major-merger scenario in M 31.

Chapter 6

Summary, conclusions and future prospects

Andromeda (M 31), the nearest giant spiral galaxy to the Milky Way (MW) and the largest most massive member of the Local Group, has experienced a tumultious recent merger history. This is most evident from the presence of many low-surface brightness substructures in the inner halo of M 31 (PAndAS; McConnachie et al. 2009) and a halo that is one of the most-metal rich among spiral galaxies (D'Souza & Bell 2018b). A sharp contrast to the MW, which has experienced a quiet merger history over the past ~10 Gyr, M 31 is thus a prime laboratory for the hierarchical formation of galaxies. As M 31 spans a large field-of-view over the sky with contamination from MW halo stars which overlap in velocity and colour, discrete tracers firmly in the M 31 system are required to map its physical properties over the entire spatial extent of its disc and halo. Planetary nebulae (PNe) are discrete tracers of light, kinematics and chemistry in galaxies. In this thesis, we carry out the largest survey of PNe in any galaxy covering the inner halo and disc of M 31. We explore the recent merger history of M 31 through constraints on the origin of the inner halo substructures and measurements of the kinematics and chemical abundances in the M 31 disc. Furthermore, we relate the PN population properties in M 31 with those of its parent stellar population to obtain insight on post-AGB evolution processes.

6.1 Summary of results

With the MegaCam imager at CFHT, we carry out a photometric survey of PNe in 54 sq. deg. in M 31, covering its inner halo and disc. We identify 5265 PNe, 4085 of which are newly discovered, by observing PNe down to ~6 mag below the bright cut-off of the PN luminosity function (PNLF). A complete sub-sample of these PNe in the M 31 disc are spectroscopically followed up with the Hectospec multi-object spectrograph at the MMT providing line-of-sight velocity (LOSV), extinction (A_V), and elemental abundance measurements for some of these PNe. These are combined with an archival sample of PNe with spectroscopic measurements from Sanders et al. (2012). The main results from each chapter of the thesis based on our PN survey are summarized as follows:

- Chapter 2: We survey the PN population in the inner 16 sq. deg. in M 31 with the Megacam instrument at the CFHT. PNe are identified in the disc and some of the inner halo substructures in M 31 from an automatic detection technique from narrow-band [OIII] and broad g-band images, down to $\sim$ 6 mag below the M31 PNLF bright cut-off. 4289 PNe are identified, of which only 1099 were previously known. Subsamples of the faint PNe were independently confirmed by matching with resolved HST sources from the PHAT survey (Dalcanton et al. 2012) and spectroscopic follow-up observations with Hectospec multi-object-spectrograph at the MMT. By comparing the PN number density with the surface brightness profile of M31 out to $\sim$30 kpc along the minor-axis, the stellar population in the inner halo is measured to have a α-parameter value 7 times larger than that of the disk, indicating two different stellar populations in the M 31 disc and inner halo. The PNLF shows a significant rise at the faint end, present at all radial bins covered by the survey, which is much steeper than that observed for the Magellanic clouds.

- Chapter 3: The observed PNe sample is separated based on their extinction values into high- and low-extinction PNe, which following Ciardullo & Jacoby (1999) are expected to evolve from more and less massive stars respectively. The observed velocities of our high- and low-extinction PNe are fitted in de-projected elliptical bins to obtain their rotational velocities, V_ϕ, and corresponding dispersions, σ_ϕ. Ages are assigned to the two PNe populations by comparing central-star properties of the sub-sample of PNe from Kwitter et al. (2012), having models fitted to their observed spectral features, to stellar evolution tracks by Miller Bertolami (2016). The high- and low-extinction PNe have ages of $\sim$ 2.5 Gyr and $\sim$ 4.5 Gyr respectively, with the low-extinction PN population being distinctly dynamically heated beyond a deprojected radius R_{GC} = 14 kpc. Thus the high- and low-extinction PNe are associated with the young thin and old thicker disc of M31 respectively, whose velocity dispersion values increase with age. At R_{GC}=17–20 kpc, which is the equivalent distance in disc scale lengths of the Sun in the Milky Way disc, we obtain $\sigma_{\phi,\ 2.5\ \mathrm{Gyr}} = 61 \pm 14$ km s^{-1} and $\sigma_{\phi,\ 4.5\ \mathrm{Gyr}} = 101 \pm 13$ km s^{-1}. The age-velocity dispersion relation (AVR) for the M31 disc is obtained in two radial bins, R_{GC}=14–17 and 17–20 kpc. The steep AVR in the M31 disc measured using PNe is predicted in simulated disc galaxies which have had a major-merger. The AVR in M 31 is consistent with of a single major merger that occurred 2.5 – 4.5 Gyr ago with an estimated merger mass ratio $\approx$ 1:5. Such a massive satellite would have been the third largest member of the local group.

- Chapter 4: We obtain the cumulative PNLF for six major inner-halo substructures – the Giant Stream, North East Shelf, G1-Clump, Northern Clump, Western Shelf and Stream D, in two disc annuli with galactocentric radii, R_{GC}=10–20 kpc and R_{GC}=20–30 kpc, and also in the LMC. The faint-end slope of the PNLF increases linearly with decreasing fraction of stellar mass younger than 5 Gyr across the M 31 regions and the LMC, the first independent evidence that the faint-end of the PNLF is preferentially populated by PNe evolving from older stars. While the PNLF bright cut-off, M^*, decreases with metallicity, the observed M^* value for the Giant Stream, W-Shelf and Stream-D is fainter than that expected from the theoretical metallicity variation expected by Dopita et al. (1992). The stellar populations of the Giant Stream, North East Shelf and Western Shelf are consistent with being stellar debris from a satellite with its average stellar population distinct from the M 31 discs. The G1-Clump shows an average stellar population whose higher metallicity and relatively younger age cannot be associated with the remnants of a disrupted old metal poor dwarf and so it likely formed from the perturbed M 31 disc. These substructure stellar populations are consistent with the predictions from the major merger scenario. Stream D has an unrelated, distinct, origin from a different small satellite.

- Chapter 5: Oxygen and argon abundances are measured seperately for the high- and low-extinction PNe which form the kinematically distinct discs in M 31. Argon abundances in the M 31 disc PNe are a better tracer for the initial ISM chemistry as surface oxygen is modified in the AGB stage for some PNe, affecting the derived oxygen abundance gradient measurements. Oxygen enrichment was previously observed in MW PNe (Delgado-Inglada et al. 2015) and this is its first evidence in another galaxy which affects the measurement of the abundance gradient. The argon abundance distributions in the thick and thin disc PNe are statistically different, with those PNe in the thin disc ($< 12 + (\mathrm{Ar/H}) >_{\mathrm{high-ext}} = 6.35 \pm 0.04$) having higher mean metallicity than those in the thick disc ($< 12 + (\mathrm{Ar/H}) >_{\mathrm{low-ext}} = 6.23 \pm 0.03$). This implies that the thick and thin disc in M 31 are chemically distinct, thus having independent origins. For the thin disc, the argon abundance values show a trough at the spatial region corresponding to the star-forming ring in M 31 at R_{GC} ~10 kpc, indicating the ring is composed of stars formed from more metal-poor gas. Beyond R_{GC} ~13 kpc, the radial argon abundance gradient for the thin disc shows a steep profile with a slope of −0.016 dex while for the thick disc, it is near-flat but shows a trough at R_{GC} ~8 kpc. In both cases, as well as for the abundance gradient from HII regions, the abundance gradients are flatter than those expected from secular evolution of simulated discs.

6.2 Conclusions

In this thesis, we obtain the largest sample of PNe M 31, the largest in any galaxy, with deep uniform coverage of the disc and inner halo of M 31. This has allowed for the following major conclusions:

- *The faint end of the PNLF is dominated by PNe from older stellar populations.* This is the first observational evidence of the effects of age of the stellar population on the faint-end of the PNLF. It supports the predictions of the stellar evolutionary tracks by Marigo et al. (2004). This establishes important constraints on post-AGB stellar evolution models.

- *M 31 has kinematically and chemically distinct thin and thick discs.* Through the high- and low-extinction PNe, we identify thin and thick disc of M 31. This is the first detection of the thin disc in M 31 over its 100-year old observational history of studies with other tracers. Other tracers like RGB stars (Dorman et al. 2012) were limited to a small footprint within R_{GC} =18 kpc on one side of the disc and were unable to identify the kinematically distinct discs in M 31 which only shows their differences in velocity and velocity dispersion beyond R_{GC} =14 kpc. The age resolution provided by the high-and low-extinction PNe enables the accurate identification of the distinct discs in M 31 which is hardly possible from the resolved stars with unclear age-distinction from CMDs, which were also affected by MW halo star contamination (Dorman et al. 2012). The chemical abundance measurements out to R_{GC} =30 kpc are only feasible with PNe for the current instrumentation. M 31 thus now stands with distinct thin and thick discs just like the MW but both discs are dynamically much hotter than those of the MW.

- *M 31 has experienced a recent major merger.* In addition to being dynamically hotter than expected from secular evolution, both the thin and thick disc of M 31 have radial abundance gradients which are also flatter than expected from secular evolution. The shape of the AVR in the M 31 disc and the stellar populations of the inner halo substructures both indicate a recent major merger in M 31 which disrupted its disc. The time of the merger is between 2.5–4.5 Gyr, the approximate ages of the high and low-extinction PNe. This rules out the minor merger simulations by Fardal et al. (2013) and requires a massive satellite, estimated to have a merger mass ratio of $\sim 1:5$ from comparing the AVR shape with simulations of disc disruptions from satellites. The predictions of Hammer et al. (2018) on the presence of thick and thin discs, stellar populations of substructures and estimated mass of satellite are consistent with our observations. However, further constraints are obtained from our observation on the radial metallicity gradient of the M 31 discs which must be met by present and future chemodynamical simulations of the formation of M 31. With its recent major merger, M 31 stands in sharp contrast to quiet merger history of the MW, providing us with two very different galaxies at two extremes of hierarchical formation of discs in our Local Group.

6.3 Future prospects and outlook

With the work carried out in the thesis, pathways to understanding of additional questions have been opened. Some of the possible avenues of exploration are as follows:

- *Constraints on stellar evolution models from the RGB to PNe number ratio*: Stellar evolution models of single stars (e.g. Miller Bertolami 2016) predict the timescales of evolution of stars of various metallicities and initial masses. While the stellar evolution till the AGB phase are comparatively well constrained, different rates of evolution from the AGB stars to the PN phase are predicted by different stellar evolution tracks depending on the physical processes considered. The Miller Bertolami (2016) models, for example, predict a faster rate of stellar evolution in the post-AGB phase compared to the widely used Vassiliadis & Wood (1994) models. Further complications are introduced if considering binary stellar evolution models (e.g. Izzard et al. 2009). Depending on the rate of post-AGB stellar evolution, the number ratio of PNe to RGB stars in a stellar population will be different, thus offering a constraint to post-AGB stellar evolution models.

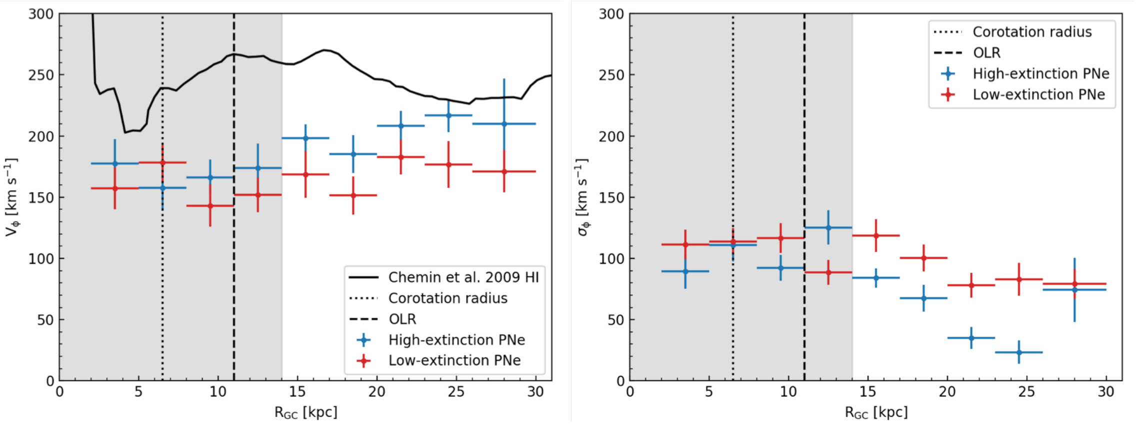

Figure 6.1: Rotational velocities [left] and Rotational velocity dispersion [right] for the high- and low-extinction PNe are shown in blue and red, respectively. The black line shows the H I rotation velocity from Chemin et al. (2009). The co-rotation radius (black dotted line) and outer Lindblad resonance (OLR; black dashed line) of the M31 bar are as found by the models of Blaña et al. (2018). The grey shaded region is possibly influenced by different dynamical heating events and is not discussed here.

The large area of our PN survey (56 sq. deg.) to uniform depth covers parent stellar populations having a range of metallicities in the substructures, halo and disc of M 31. The resolved RGB population from the photometry of the PAndAS survey (McConnachie et al. 2018), allows us to obtain the PN to RGB number ratio covering a range of metallicities as a function of magnitude down to ~6 mag below the bright cut-off. This ratio will add significant constraints on the stellar evolution models by offering insight on the yield of PNe from parent stellar populations of different metallicities.

- *Open questions on the merger in M 31*: While the results of thesis indicate that M 31 had a recent merger with a massive satellite, the exact mass and orbital inclination of this merger still need to be estimated in order to paint the picture of the galaxy that was possibly the third largest member of our Local Group. The observed radial abundance gradients on the M 31 disc already offer constraints on the mass and orbital inclination of the merging satellite which need to be reproduced by future simulations. Observations of PN LOSVs in the M 31 disc with the increased sample in Chapter 5 compared to Chapter 3, allows us to explore the PN rotational velocity and velocity dispersion with increased radial resolution (Figure 6.1). While the high- and low-extinction PNe continue to be kinematically distinct beyond R_{GC}=14 kpc, the increased radial resolution reveals a clear decrease in the radial velocity dispersion for the high-extinction PNe in the thin disc with increasing radii till R_{GC}=26 kpc. This is a possible observation evidence of the inside-out growth of the thin disc in M 31 which is almost unperturbed at large radii (R_{GC}=23–26 kpc). The radial velocity dispersion profile of the thick and thin disc of M 31 is currently under analysis but offers a further constraint for future simulations of the recent merger in M 31.

  Additionally, stars in different substructures with varied elemental abundances are stripped

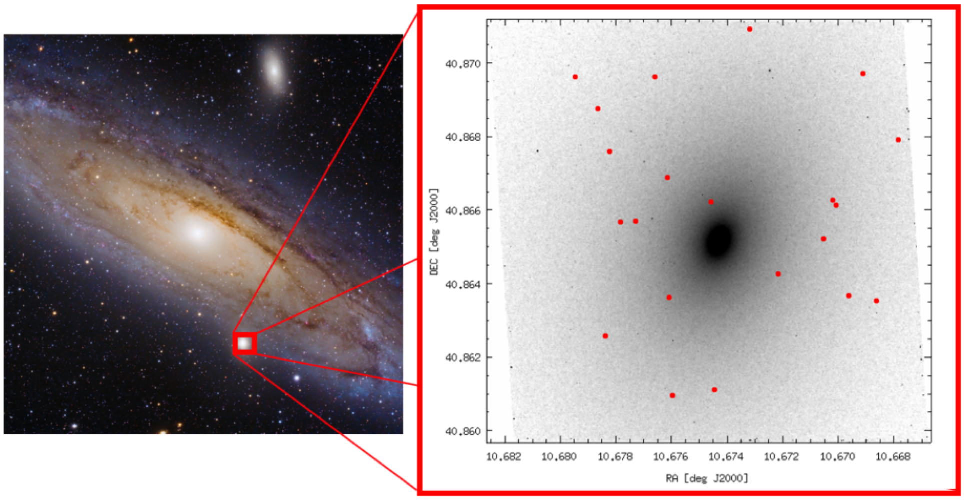

Figure 6.2: [Left] The spatial location of M 32 is shown with its proximity to M 31. [Right] An archival HST narrow-band [OIII] image of M 32. Preliminary identification of PNe in M 32 was carried out with the 21 identified PNe (14 newly identified) marked in red.

from the parent satellite in different passages, and thus the abundances of PNe associated with these substructures, along with their LOSVs, will also provide constraints on chemo-dynamical simulations of the merger event. The spectroscopic follow-up of the PNe in the substructures in M 31 will allow us to obtain LOSV and elemental abundance maps of the inner halo of M 31 with its substructures. These observations are currently scheduled at the MMT this year.

Also unknown is where the majority of the stellar mass of this merged satellite ended up in M 31. Such a massive satellite is expected to deposit a majority of its stellar mass on the luminous body of the host galaxy (Karademir et al. 2019) and Hammer et al. (2018) predict that the M 31 bulge is built-up by this satellite. However, D'Souza & Bell (2018a) find that in simulated galaxies in the Illustris cosmological simulation that have undergone a major merger like in M 31, a compact dwarf galaxy that was the core of the merging satellite is sometimes left behind after the merger. M 32 (Figure 6.2) is a compact dwarf elliptical in close proximity to the luminous disc of M 31 which D'Souza & Bell (2018a) hypothesized as being the compact remnant of the merged massive galaxy. So far no streams linking M 32 to M 31 have been detected but from our scheduled observations of M 31 PNe, streams and other structure linked with M 32 may be detected from their LOSVs even when they are co-spatial with the luminous M 31 disc. We also have further PNe identified in the central regions of M 32 (Figure 6.2) whose LOSVs and chemical abundance measurements can constrain the role of M 32 in this major merger event.

- *Dynamical models of M 31*: With its proximity to the MW, M 31 also has a long history of observational studies to characterise its bulge, bar and disc. Typically MW-like dynamical models incorporating only secular evolution processes have been utilised thus far to explain the sub-galaxy scale morphology of M 31 (e.g. Blaña et al. 2018). Some successes were achieved like describing the dynamics of its bar and the presence of a classical bulge in M 31. However, such galaxy-scale structures in the center of M 31 would be affected in a major merger event causing possible enhancement or weakening of these structures. This theses has highlighted the need for dynamical models to incorporate the merger event in their analysis of the sub-galaxy scale features in M 31. Dynamical models such as the M2M models of Blaña et al. (2018) need to account for effects from the merger, especially the distinct thin and thick disc in M 31. The dynamical interaction of the bar with the distinct discs would invariably affect the calculation of the bar-length and co-rotation radius, and would also impact the modelling of the star-forming ring in M 31. Furthermore, if the bulge of M 31 is indeed built-up from the stellar material of the satellite as predicted by Hammer et al. (2018), its dynamical model would then also need to account for such perturbations from the merger.

- *Discs in spiral galaxies*: As shown in Figure 1.5, a range of halo metallicities are measured for spiral galaxies with the MW and M 31 forming the two extremes of spiral galaxies in the accreted halo-mass vs halo-metallicity relation. In this thesis, we find that M 31 and the MW also have different disc velocity dispersions with contrasting merger histories. The beckoning question is then whether there is a range of spiral galaxy disc properties, perhaps with distinct thin and thick discs, that depend on their merger histories. (D'Souza & Bell 2018b) predict from simulated Illustris galaxies that the more metal-rich haloes of spiral galaxies are those that have had a recent major merger. Such mergers would leave an imprint on the AVR of the disc galaxies (Martig et al. 2014) and thereby their recent formation histories could be investigated.

  Furthermore, the rotational velocity profile of disc galaxies acts as constraints on the dark matter (DM) profile in the galaxy, which may either be "maximal" or "sub-maximal", having a baryon-dominated or DM-dominated central density respectively. This has been a heated debate over the past two decades (see Courteau et al. 2014, and references therein). Aniyan et al. (2018) found that NGC 628, measured to have a sub-maximal DM profile with a single rotational velocity profile for all its disc stars (Bershady et al. 2010), turned out to have a maximal baryon-dominated profile upon accounting for the presence of dynamically distinct thin and thick discs. Observations of PNe in the discs of nearby spiral galaxies thus has the potential to reveal their distinct thick and thin discs and obtain better constraints on the DM profile.

  We have scheduled observations at the CFHT for identifying PNe in M 33, the third largest galaxy in the Local Group with a metal poor low mass halo (McConnachie et al. 2009), and will attempt to unravel its recent formation history and assess if its disc structure is in line with the aforementioned expectations of a dynamically colder disc for galaxies with low halo-mass. We will then venture to observations of more distant spiral galaxies in the Local Volume.

Appendix A

Appendix: Imaging the disc and halo with MegaCam at the CFHT

The contents of this appendix chapter have been published as the appendix in Bhattacharya et al. (2019a, Astronomy & Astrophysics, 624, A132)

A.1 Catalogue extraction

A.1.1 Flux calibration for m_{5007}

The integrated flux, F_{5007}, from the [O III] 5007 Å line is related to the m_{5007} magnitude (Jacoby 1989) as

$$m_{5007} = -2.5 \log F_{5007} - 13.74 \tag{A.1}$$

where the flux is in units of erg $\mathrm{cm}^2 \mathrm{s}^-1$. The *AB* magnitude (Oke & Gunn 1983) relates to F_{5007} through the MegaCam narrow-band [O III] filter characteristics as

$$m_{\mathrm{n}} = -2.5 \log \mathrm{F}_{5007} - 2.5 \log \frac{\lambda_{\mathrm{c}}^2}{\Delta\lambda_{\mathrm{eff}} \mathrm{c}} - 48.59 \tag{A.2}$$

where $\lambda_{\mathrm{c}} = 5007$Å and $\Delta\lambda_{\mathrm{eff}} = \Delta\lambda \times T$ for the on-band with $\Delta\lambda = 102$Å and effective transmission, $T = 0.91$. The relation between the *AB* and m_{5007} magnitudes, for this narrow-band filter, is thus determined (following Arnaboldi et al. 2003) to be

$$m_{5007} = m_{\mathrm{n}} + 2.27 \tag{A.3}$$

Table A.1: Parameters for the best fitting PSF

Radius (px)	Ellipticity	β	Moffat FWHM (px)
15.2	0	5.02	5.15

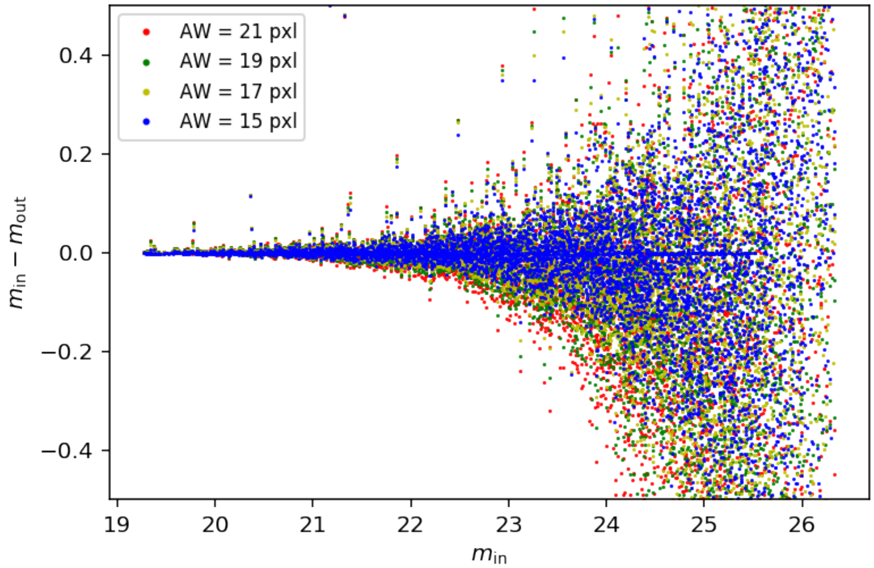

Figure A.1: Recovery of the input magnitude of simulated sources using different SExtractor aperture widths, AW, for a single field.

A.1.2 Point spread function

The point spread function (PSF) is the instrumental response to a point-like object. The degree of spreading of the PSF represents the quality of the instrument imaging. To determine the PSF, we first used the IRAF tasks *daofind*, *daophot*, and *pstsel* to respectively extract all the positions of detected sources, determine their magnitude, and select the brighter stars. We then used the IRAF task *psf*, which allowed us to select the best stars to fit the PSF, and reject bad objects (e.g. saturated or located near an another source). The confirmed stars are used to calculate the PSF. The PSF is modelled with different luminosity profiles (e.g. Gaussian, Moffat function) and the best fit is selected using χ^2 minimisation (goodness of fit). The best fit is a Moffat function (parameters in Table A.1) of the form

$$f(r,\alpha,\beta) = \frac{\beta-1}{\pi\alpha}[1+(\frac{r}{\alpha})^2]^{-\beta} \tag{A.4}$$

A.1.3 Masking of noisy regions and CCD edges

After identifying sources on the images, the image regions that were affected by dithering or saturation are masked on the on-band and off-band images. This is carried out for each field. Dithering leads to different exposure depths at the image edges. Due to the combination of the 42 MegaCam CCDs, the same effect also affects columns at the borders of the individual CCDs. Additionally, in order to mask those regions with a high background value (e.g. due to charge transfer or saturated stars) we used the rms-background map created by SExtractor and create a

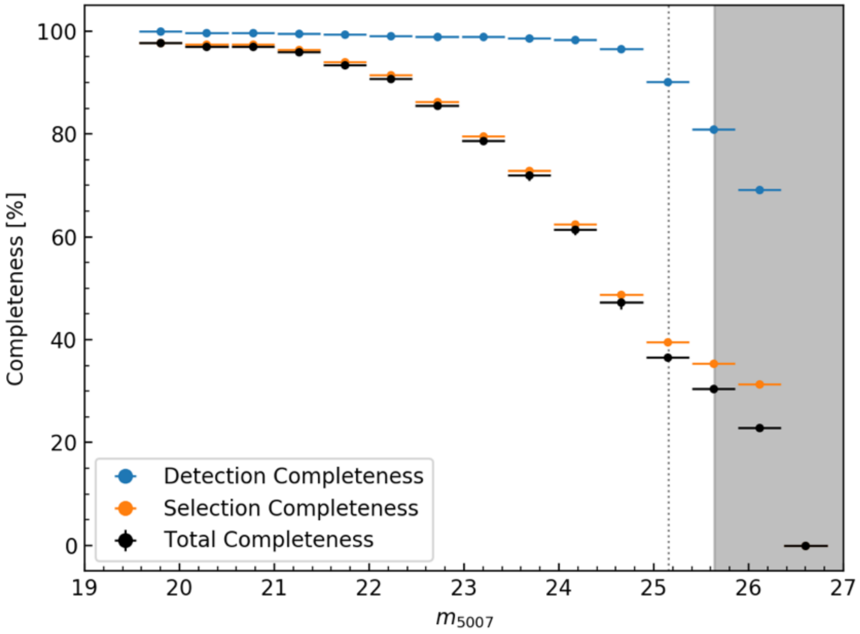

Figure A.2: For the entire survey the number of PNe in each magnitude bin (in black), and the completeness corrected number (in blue). The region beyond the limiting magnitude of the shallowest field (Field# 33_4) is shown in grey. The grey dotted line shows the 90% completeness limit of the shallowest field.

pixel-mask with all values higher than three times the median background.

A.1.4 Choice of aperture width

After simulating sources on to the on-band, we determine the magnitude aperture most suited to recovering them. Figure A.1 shows that different SExtractor aperture widths (AW) of 15, 17, 19, and 21 pixels all recover the magnitudes well but an AW of 15 pixels can recover sources most accurately even for fainter sources.

A.1.5 Completeness correction in the survey

For the entire survey, the mean percentage total completeness is shown as a function of the m_{5007} magnitude in Figure A.2 in black, while the mean percentage detection completeness and percentage selection completeness are shown in blue and orange, respectively. It is clear that the completeness correction applied is dominated by the selection completeness, correcting for the number of genuine PNe missed due to our colour and point-like selection. The percentage completeness shown is only representative in Figure A.2; the completeness varies in each field

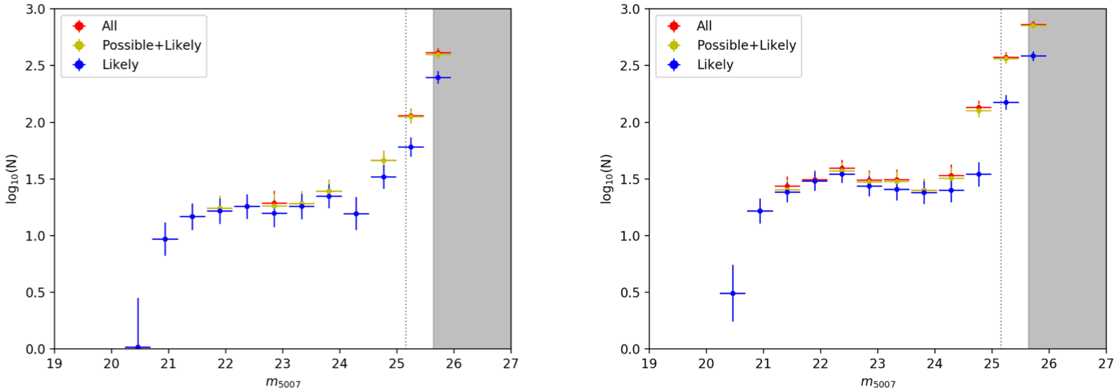

Figure A.3: Completeness-corrected PNLF for PHAT-matched PNe within (left) and outside (right) 0.3deg of the centre of M31 is shown for the 'likely' (blue), 'possible + likely' (yellow), and 'possible + likely + unlikely' (red) cases. The region beyond the limiting magnitude of the shallowest field (Field# 33_4) is shown in grey. The grey dotted line shows the 90% completeness limit of the shallowest field.

and the completeness correction is applied to PNe in each field separately.

A.1.6 Detection check on background

For each image, as a by-product of the source extraction, we obtain a background image. In order to check for spurious sources in any image, we run SExtractor on this background image with the parameters described in Section 2.3.1. The sources detected on the background image and their distribution as a function of magnitude would give us an indication of the number of spurious sources present in our PNe catalogue. However, subjecting these sources to the PNe selection criteria described in Sections 2.3.3 and 2.3.4, we find that even if these detected sources survive the colour selection, they would be rejected as PNe in the point-like selection as their half-light radius is much smaller than that expected from the simulated PNe population.

A.2 PNe counterparts in PHAT

A.2.1 The M06 PNe counterparts in PHAT

For each M06 PNe, Veyette et al. (2014) searched for counterparts within $3''$. They expected a strong relation between the M06 m_{5007} magnitude and the PHAT F475W magnitude since the majority of F475W flux is due to the [O III] 5007 Å line, and a colour excess between the PHAT F475W and F814W filters, since PNe are not expected to show a strong continuum excess. Additionally, they utilised the separation between the M06 PNe and the PHAT counterpart, and the roundness and sharpness of its PSF. Of the 711 PNe in the M06 catalogue that overlap the PHAT images, they found that only 467 had counterparts consistent with being PNe. The rest

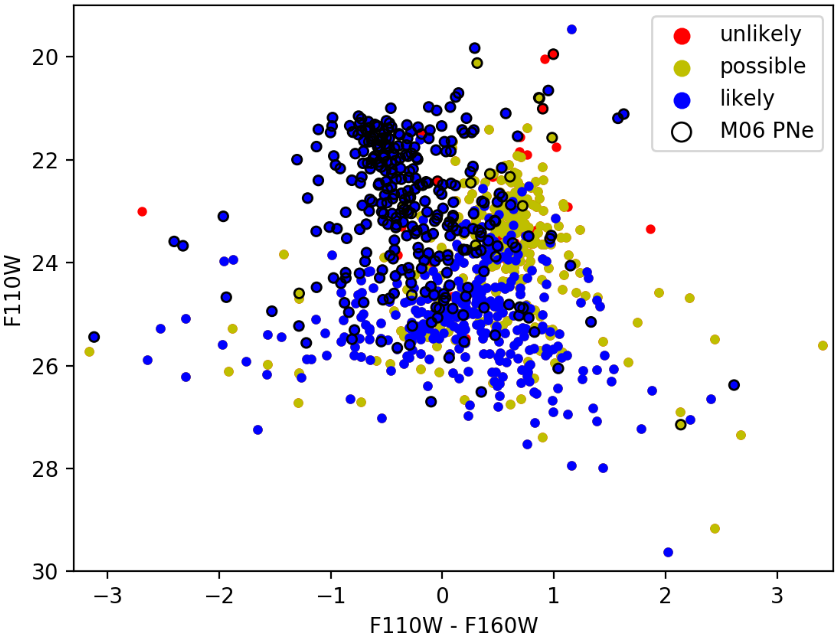

Figure A.4: F110W mag of the PHAT-matched PNe plotted against its F110W − F160W colour. The ‘likely’, ‘possible’, and ‘unlikely’ PNe are shown in blue, yellow, and red, respectively. The PNe previously found by M06 are ringed in black.

were either H II regions or possible stellar sources with no PHAT counterpart consistent with being a PNe.

A.2.2 Further characteristics of the PHAT-matched PNe

We also check the PNLF for consistency both near the crowded centre (within 0.3 deg) and in the less crowded outer disc (outside 0.3 deg) as shown in Figure A.3. The PNLF is similar in both cases, indicating again that the rise in the PNLF does not depend on crowding, but the value in the less crowded disc shows a more pronounced dip in the PNLF. This may be due to the presence of the 10kpc star-forming ring in M31 (Barmby et al. 2006), which may be populating the brightest 2.5 mag of the PNLF with PNe evolved from young massive stars. There are 954 PNe that have detections in the PHAT NIR filters. Figure A.4 shows the F110W mag of the PHAT-matched PNe plotted against its F110W − F160W colour. There are 644 PNe that have detections in the PHAT UV filters. Figure A.5 shows the F275W mag of the PHAT-matched PNe plotted against its F275W − F336W colour. The trends in the UV and the NIR are similar to those found by Veyette et al. (2014) for the M06 PNe.

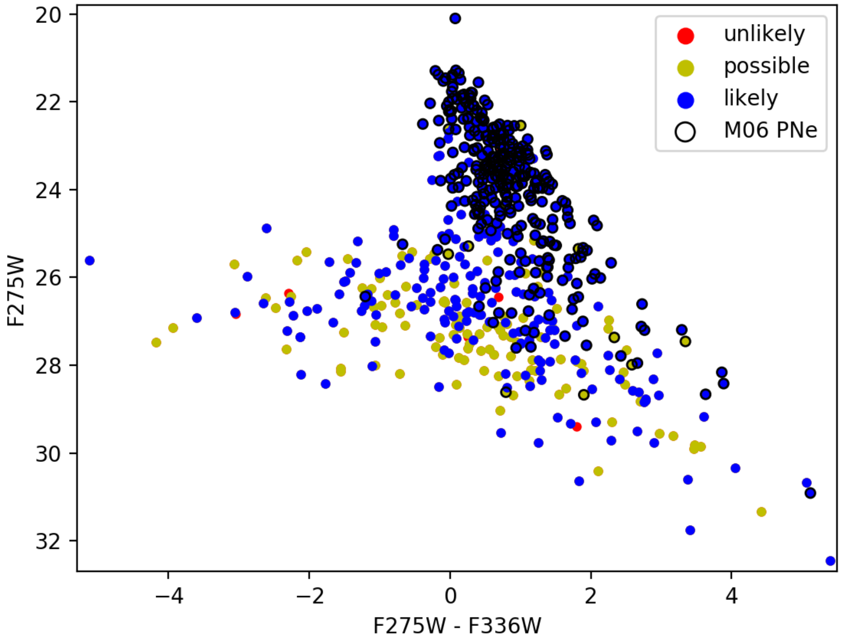

Figure A.5: F275W mag of the PHAT-matched PNe plotted against its F275W − F336W colour. The ‘likely’, ‘possible’, and ‘unlikely’ PNe are shown in blue, yellow, and red, respectively. The PNe previously found by M06 are ringed in black.

Appendix B

Appendix: Age-velocity dispersion relation in the disc from planetary nebulae

The contents of this appendix chapter have been published as the appendix in Bhattacharya et al. (2019b, Astronomy & Astrophysics, 631, A56)

B.1 Effect of line-of-sight dust attenuation in extinction-based selection of planetary nebulae

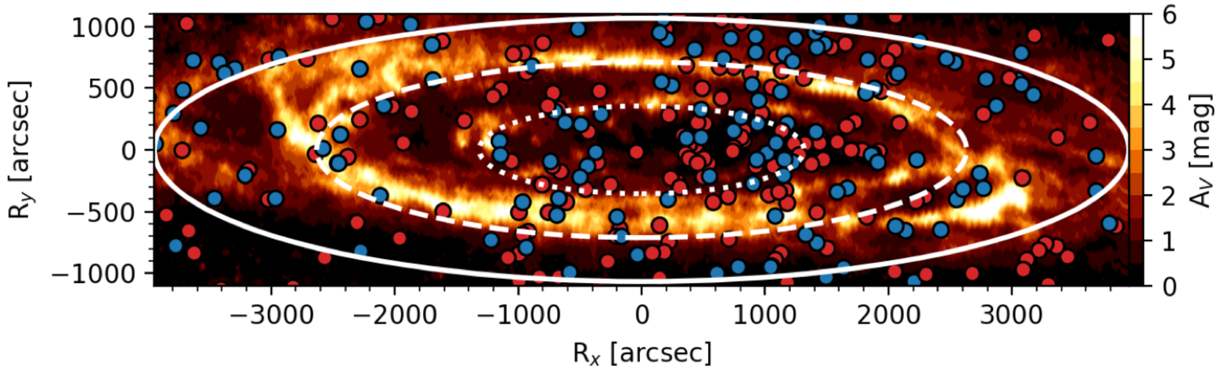

Figure B.1: High- (blue) and low- (red) extinction PNe overlaid on the de-projected LOS extinction (A_V) map of the inner region of M31 from Blaña et al. (2018). The elliptical rings show 5 (dotted), 10 (dashed), and 15 (solid) kpc de-projected distances from the centre of M31. Both the high- and low-extinction PNe are not spatially correlated with the distribution of LOS extinction in the M31 disc.

The PNe are separated into high- and low-extinction samples considering that the measured extinction values for high-extinction PNe are dominated by their circumstellar extinction, with LOS dust attenuation equally affecting both samples. Any spatial correlation between higher

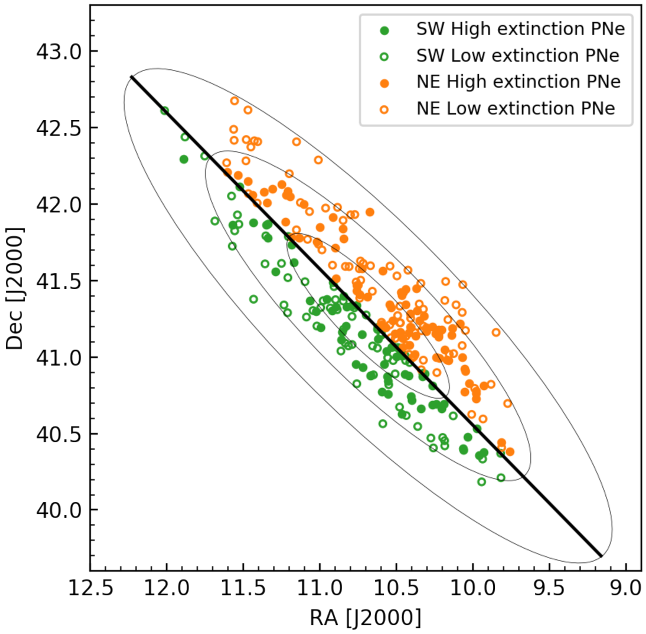

Figure B.2: Position in space of high- and low-extinction PNe marked with filled and open circles respectively. The black line indicates the major axis of M31, dividing the PNe into the northeastern (NE) and southwestern (SW) halves of the M31 disc shown in orange and green, respectively. The black ellipses show R_{GC} = 10 kpc (inner), 20 kpc (middle), and 30 kpc (outer). North is up, east is right.

LOS dust attenuation in the galaxy and the position of high-extinction PNe would result in PNe with low circumstellar extinction being misclassified. The dust in the M31 disc and IGM was mapped by Draine et al. (2014) using near-infrared data from the Spitzer Space Telescope. This was used by Blaña et al. (2018) to obtain the LOS extinction map of the inner disc of M31 shown in Figure B.1, also showing the de-projected positions of the high- (blue) and low- (red) extinction PNe. It is clear that there is no preferential selection of the high-extinction PNe at the regions of high LOS extinction in the disc. Both the high- and low-extinction PNe are not spatially correlated with the distribution of LOS extinction.

To further investigate this issue, we check whether the high-extinction PNe are preferentially found in the dustier regions of the M31 disc by taking in to account the geometry of its dust attenuation. The northeast (NE) half of the M31 disc has higher LOS dust attenuation than the southwest (SW) half (Draine et al. 2014). We thus divide the PNe sample into two halves corresponding to these two regions of the M31 disc, as shown in Figure B.2. The cumulative number of PNe is obtained along their deprojected major-axis distances (X_{PC}), with the negative values assigned to the southern side of M31, for the high-extinction PNe (solid) and all PNe (dashed), for both the NE (orange) and SW (green) halves for the M31 disc (Figure B.3). The

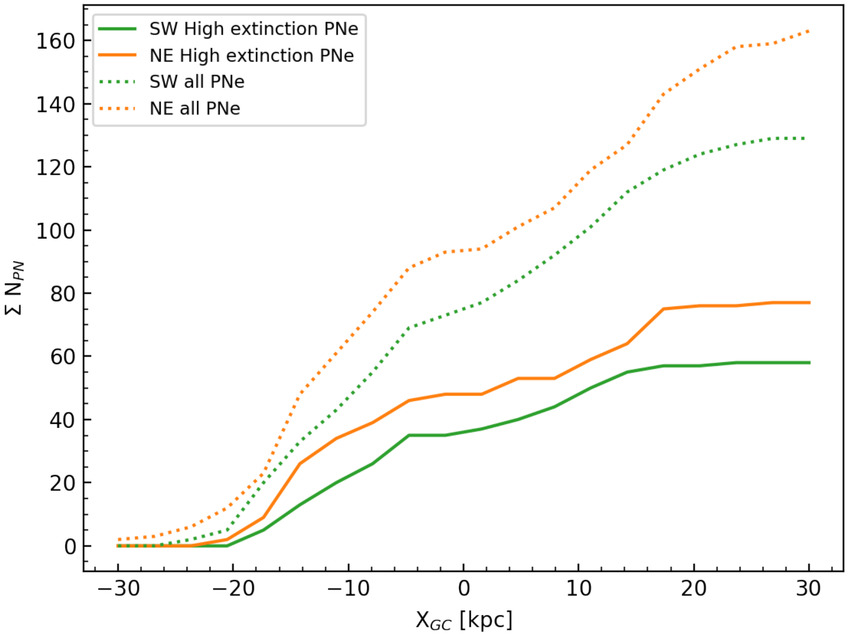

Figure B.3: Cumulative sum of high-extinction PNe (solid lines) and all PNe (dotted lines) for the NE (orange) and SW (green) along the deprojected major-axis distances, X_{GC}. Southern side of M31 is assigned negative values.

cumulative distribution of both high-extinction PNe and the entire PNe sample clearly follow a similar distribution in both halves of the M31 disc with a slightly higher number of PNe observed in the NE half. A KS test shows that the high-extinction PNe in both halves follow the same distribution with a pvalue=0.99. We classify 2% more PNe as high extinction in the SW half of M31 which is anti-correlated with the expected effects from the LOS dust attenuation. We thus conclude that the LOS dust attenuation effects do not drive the extinction-based classification of our PN populations.

B.2 Validity of the planar disc assumption for the low-extinction planetary nebulae

At the inclination of M31, deprojecting the low-extinction PNe at high z on a planer disc may result in assigned R_{GC} values which are different from the true ones. We first estimate the scale height of the low-extinction PNe ($H_{\rm Low\ ext}$). In order to establish an extinction map of M31 RGB stars found by the PHAT survey, Dalcanton et al. (2015) modelled the geometry of the M31 thicker disc to describe the distribution of RGB (~ 4 Gyr old; D15) and red clump stars in low-extinction regions. These latter authors found that this thicker disc has a ratio of vertical to horizontal exponential scale heights of $\mathrm{h_z/h_r} = 0.15$. From IRAC 3.6 μm band images of M31, Blaña et al. (2018) find that the M31 disc scale length $\mathrm{h_r} = 5.71\pm0.08$ kpc. Thus, $\mathrm{h_z} = 0.86\pm0.01$ for the M31 thicker disc. Since the RGB stars have mean age and kinematics close to that of the low-extinction PNe (see Sections 3.3.3 & 3.4.2 for details), $\mathrm{H_{Low\ ext}} = \mathrm{h_z} \approx 0.86$ kpc.

Given the inclination of M31, PNe at $z\sim$ 0.86 kpc may be deprojected with an estimated R_{GC} that is ~0.2 kpc different from its true R_{GC} value. For an exponentially decreasing stellar density (ρ) profile of the low-extinction PNe with z, $\rho \propto e^{-\frac{z}{H_{\mathrm{Low\ ext}}}}$, 1/4 of the low-extinction PNe in any bin may lie at $z\sim$ 0.86 kpc. Given the 3 kpc bin sizes used to determine $\sigma_{\phi,\mathrm{Low\ ext}}$, only $\sim$ 10% of the low-extinction PNe may be included in a different bin. The measured σ_ϕ values have $\sim$ 10% error, as in Figure 3.4. Thus the planar disc assumption for PNe does not bias the V_ϕ and σ_ϕ profiles within the estimated errors.

Appendix C

Appendix: Radial metallicity gradients in the chemically and kinematically distinct thin and thick discs of M 31 from PN elemental abundances

C.1 Catalogue of line fluxes and properties of the spectroscopically observed disc PNe in M 31

For the 265 PNe observed in the M 31 disc (within 30 kpc qualifying the position-velocity criteria) with extinction measurements, Table C.1 lists their measured line fluxes while Table C.2 lists their measured properties.

Table C.1: Measured Line Fluxes of the M31 PNe, relative to Hβ=100. Each PN should be designated as SPNA¡Sl. No.¿. E.g. PN 419 should be termed SPNA419.

Sl. No. λ (Å)	[O II] 3726	[O II] 3729	Hδ 4102	Hγ 4340	[O III] 4363	[Ar IV] 4711	[Ar IV] 4740	[O III] 4959	[O III] 5007	Hα 6562	[S II] 6717	[S II] 6731	[Ar V] 7005	[Ar III] 7136	[Ar III] 7751
419	–	–	26.6 ± 5.0	30.8 ± 5.8	–	–	–	377.0 ± 5.1	1129.4 ± 6.5	338.8 ± 4.8	–	–	–	–	–
478	17.7 ± 4.9	18.8 ± 4.8	19.3 ± 2.5	17.4 ± 1.6	15.0 ± 1.2	–	5.1 ± 1.3	581.9 ± 6.6	1753.9 ± 18.0	428.0 ± 6.2	–	–	–	28.0 ± 1.7	16.3 ± 16.3
496	36.7 ± 4.5	36.1 ± 4.6	22.7 ± 2.3	27.1 ± 1.9	17.3 ± 1.5	5.9 ± 1.4	8.1 ± 1.2	600.7 ± 7.8	1792.4 ± 21.7	331.1 ± 10.2	5.1 ± 1.1	9.2 ± 1.0	–	25.2 ± 1.4	15.1 ± 15.1
663	–	–	–	59.8 ± 13.5	–	–	–	193.9 ± 12.1	553.0 ± 9.2	429.5 ± 12.0	–	–	–	–	–
729	–	–	–	31.2 ± 8.7	–	–	–	347.9 ± 12.4	1033.7 ± 9.5	311.5 ± 9.2	–	–	–	–	–
739	–	–	21.2 ± 5.2	25.9 ± 7.0	–	–	–	375.7 ± 6.0	1125.0 ± 10.1	260.8 ± 6.3	–	–	–	–	–
740	–	–	–	62.0 ± 6.5	–	–	–	324.5 ± 8.4	984.2 ± 6.7	298.8 ± 7.4	–	–	–	–	–
749	–	–	–	79.2 ± 20.9	–	–	–	280.8 ± 24.4	905.2 ± 15.9	379.9 ± 19.2	–	–	–	–	–
764	–	–	–	34.6 ± 9.0	–	–	–	443.7 ± 8.7	1294.8 ± 14.8	301.3 ± 6.7	–	–	–	–	–
798	–	–	–	–	–	–	–	315.0 ± 31.4	889.3 ± 28.4	315.9 ± 15.5	–	–	–	–	–
820	–	–	32.5 ± 2.0	24.3 ± 0.9	–	–	–	136.8 ± 1.4	412.1 ± 5.9	227.7 ± 4.0	–	–	–	–	–
822	–	–	–	32.7 ± 8.2	–	–	–	331.1 ± 7.0	998.9 ± 14.9	241.5 ± 7.8	–	–	–	–	–
829	–	–	24.5 ± 3.5	35.0 ± 3.0	8.3 ± 2.6	–	–	305.3 ± 5.6	929.8 ± 11.1	264.1 ± 4.5	–	–	–	6.9 ± 2.3	–
831	–	–	–	–	–	–	–	260.7 ± 16.7	783.9 ± 14.7	311.1 ± 20.2	–	–	–	–	–
845	20.6 ± 6.5	25.0 ± 6.9	22.7 ± 3.2	21.9 ± 2.1	10.7 ± 3.0	6.2 ± 1.6	–	424.4 ± 3.9	1307.9 ± 14.7	165.2 ± 15.8	–	–	–	13.5 ± 1.9	–
875	86.4 ± 4.2	65.0 ± 4.2	23.7 ± 2.0	18.7 ± 0.6	2.3 ± 0.7	–	–	92.1 ± 1.4	275.7 ± 3.1	250.9 ± 5.4	–	–	–	8.5 ± 0.5	3.9 ± 3.9
937	–	–	–	36.2 ± 10.1	–	–	–	208.0 ± 15.6	534.6 ± 8.5	202.6 ± 11.8	–	–	–	–	–
942	–	–	28.1 ± 1.1	25.5 ± 0.8	8.2 ± 1.0	–	–	309.6 ± 3.9	963.3 ± 13.6	296.3 ± 3.7	–	–	–	10.5 ± 0.2	5.4 ± 5.4
945	32.1 ± 2.4	21.8 ± 2.4	–	34.8 ± 1.1	8.3 ± 0.6	–	1.5 ± 0.3	366.9 ± 3.5	1105.7 ± 13.7	277.5 ± 4.4	2.1 ± 0.2	3.2 ± 0.3	–	12.8 ± 0.4	6.9 ± 6.9
959	34.0 ± 2.0	19.8 ± 2.3	–	20.2 ± 0.8	8.5 ± 0.6	–	–	455.7 ± 5.1	1339.6 ± 13.9	311.3 ± 5.8	1.9 ± 0.3	3.9 ± 0.4	–	14.5 ± 0.4	7.3 ± 7.3
1041	–	–	–	–	–	–	–	351.0 ± 9.3	1056.2 ± 12.1	286.5 ± 14.0	–	–	–	–	–
1544	–	–	–	–	–	–	–	483.1 ± 38.8	1298.6 ± 35.7	415.9 ± 19.0	–	–	–	–	–
1596	–	–	16.4 ± 3.5	14.4 ± 1.5	–	–	–	120.4 ± 3.3	338.1 ± 4.6	303.4 ± 4.7	–	–	–	–	–
1605	–	–	84.2 ± 15.5	43.2 ± 8.7	–	–	–	448.6 ± 12.1	1262.0 ± 22.3	252.9 ± 8.6	–	–	–	–	–
1632	309.5 ± 14.4	220.8 ± 14.4	41.2 ± 4.6	24.4 ± 3.2	32.2 ± 4.3	–	–	692.7 ± 8.1	2104.3 ± 26.8	352.1 ± 5.5	49.0 ± 2.8	63.0 ± 2.2	–	55.2 ± 5.4	–
1653	–	–	–	–	–	–	–	658.2 ± 22.5	1861.3 ± 25.9	465.8 ± 13.8	–	–	–	–	–
1702	–	–	32.6 ± 3.9	13.7 ± 2.9	–	–	–	174.7 ± 4.3	546.8 ± 6.2	281.3 ± 5.6	–	–	–	–	–
1714	–	–	–	22.6 ± 1.3	5.7 ± 1.3	–	3.4 ± 0.7	419.3 ± 4.2	1308.9 ± 15.4	297.5 ± 2.5	3.6 ± 0.7	5.6 ± 0.6	–	16.3 ± 0.9	8.4 ± 8.4
1715	99.7 ± 14.4	79.6 ± 14.5	23.7 ± 4.7	25.0 ± 2.6	23.4 ± 2.9	–	–	615.1 ± 6.5	1874.9 ± 17.4	448.8 ± 5.2	31.4 ± 1.5	51.2 ± 1.8	–	58.8 ± 2.2	20.3 ± 20.3
1735	–	–	23.1 ± 3.4	31.1 ± 1.4	–	–	–	290.7 ± 5.2	864.4 ± 6.6	321.0 ± 6.3	–	–	–	–	–
1740	–	–	23.7 ± 3.9	39.4 ± 3.5	12.8 ± 3.1	–	–	375.1 ± 10.1	1083.3 ± 10.5	295.9 ± 3.5	–	–	–	29.5 ± 4.0	–
1755	–	–	36.6 ± 10.4	29.4 ± 6.4	–	–	–	348.6 ± 7.2	985.8 ± 10.3	327.3 ± 11.3	–	–	–	–	–
1798	–	–	23.2 ± 2.4	20.8 ± 1.6	–	–	–	134.8 ± 2.8	398.1 ± 1.8	253.9 ± 4.5	–	–	–	–	–
1808	–	–	–	61.1 ± 10.0	–	–	–	447.7 ± 15.5	1346.0 ± 12.7	319.1 ± 14.4	–	–	–	–	–
1820	–	–	24.9 ± 8.0	19.6 ± 2.9	–	–	–	66.7 ± 2.9	191.9 ± 4.1	362.3 ± 5.5	–	–	–	–	–
1832	–	–	–	–	–	–	–	447.7 ± 10.5	1295.2 ± 11.7	330.0 ± 13.2	–	–	–	–	–
1847	11.2 ± 3.5	11.9 ± 3.7	24.7 ± 1.8	23.2 ± 1.7	24.6 ± 1.3	–	8.0 ± 1.2	643.5 ± 6.9	1940.6 ± 17.9	379.3 ± 4.2	–	–	–	25.3 ± 1.1	7.0 ± 7.0
1853	–	–	28.9 ± 6.2	35.0 ± 4.7	29.1 ± 3.8	–	–	640.6 ± 7.9	1890.2 ± 14.5	213.3 ± 16.6	12.0 ± 3.0	13.6 ± 2.9	–	18.0 ± 4.1	26.0 ± 26.0
1859	–	–	–	–	–	–	–	215.3 ± 26.8	615.4 ± 24.6	391.5 ± 20.0	–	–	–	–	–
1862	–	–	23.0 ± 1.8	20.8 ± 1.6	–	–	–	184.8 ± 2.6	556.7 ± 4.2	276.6 ± 4.7	–	–	–	–	–
1864	–	–	17.8 ± 5.7	25.6 ± 5.2	15.5 ± 4.3	10.7 ± 3.1	8.8 ± 2.5	490.4 ± 5.6	1456.9 ± 13.4	304.0 ± 4.5	–	–	–	24.9 ± 3.8	–
1872	–	–	22.2 ± 6.7	17.2 ± 5.3	21.4 ± 4.3	–	12.9 ± 3.2	658.5 ± 9.3	1954.0 ± 15.4	490.0 ± 4.4	13.8 ± 2.8	15.8 ± 3.1	7.3 ± 2.0	32.2 ± 4.2	23.3 ± 23.3
1877	–	–	–	33.9 ± 7.1	–	–	–	323.4 ± 15.3	996.2 ± 14.3	383.4 ± 13.1	–	–	–	–	–
1882	–	–	24.6 ± 4.5	25.7 ± 2.2	6.5 ± 1.5	–	–	337.8 ± 4.6	1063.7 ± 9.7	336.0 ± 5.0	–	–	–	13.9 ± 2.1	–
1897	–	–	28.5 ± 5.7	27.5 ± 3.7	–	–	–	183.9 ± 5.5	561.0 ± 6.7	300.9 ± 7.6	–	–	–	–	–
1917	30.1 ± 2.9	18.9 ± 2.9	24.6 ± 2.2	19.8 ± 1.0	11.2 ± 1.0	4.4 ± 0.8	5.6 ± 0.9	468.7 ± 4.4	1416.4 ± 14.4	309.4 ± 3.8	4.6 ± 0.5	8.9 ± 0.6	–	27.1 ± 1.1	14.8 ± 14.8
1937	–	–	27.6 ± 2.4	19.0 ± 1.6	–	–	–	259.0 ± 5.2	767.1 ± 6.7	247.9 ± 9.0	–	–	–	–	–
1945	–	–	–	–	–	–	–	453.5 ± 18.5	1276.5 ± 15.1	315.1 ± 17.7	–	–	–	–	–
1951	38.8 ± 2.0	25.5 ± 2.2	28.7 ± 1.0	13.4 ± 1.2	6.0 ± 0.9	–	–	310.4 ± 3.4	924.9 ± 10.8	333.7 ± 4.3	2.1 ± 0.5	3.4 ± 0.5	–	20.1 ± 0.7	11.2 ± 11.2
1958	111.8 ± 6.9	81.9 ± 7.7	26.5 ± 4.0	25.3 ± 2.3	19.7 ± 2.2	–	–	445.6 ± 6.0	1330.9 ± 10.8	236.4 ± 18.0	38.7 ± 3.2	29.8 ± 1.5	–	17.4 ± 2.0	–
1960	40.1 ± 4.2	25.7 ± 4.0	27.0 ± 2.7	20.4 ± 2.7	7.3 ± 1.4	4.0 ± 1.3	–	442.2 ± 6.6	1335.9 ± 11.8	298.5 ± 6.1	4.6 ± 1.1	8.4 ± 1.0	–	18.3 ± 2.2	10.6 ± 10.6
1977	–	–	18.8 ± 2.3	17.2 ± 2.5	13.3 ± 2.9	–	–	555.7 ± 9.1	1700.9 ± 13.8	493.1 ± 5.1	–	–	–	35.5 ± 3.6	–
1981	–	–	43.5 ± 8.1	28.4 ± 8.7	–	–	–	331.8 ± 11.9	986.7 ± 13.2	324.6 ± 8.3	–	–	–	–	–
2018	–	–	29.6 ± 3.1	22.3 ± 3.8	17.2 ± 1.9	–	10.7 ± 2.2	499.2 ± 5.3	1467.7 ± 11.9	215.3 ± 13.8	9.5 ± 1.8	17.4 ± 1.3	–	27.0 ± 2.7	19.6 ± 19.6
2024	29.7 ± 5.2	21.8 ± 5.7	23.7 ± 3.6	22.6 ± 1.8	9.3 ± 1.6	–	–	489.7 ± 6.7	1483.4 ± 18.2	422.3 ± 6.5	9.4 ± 1.1	13.7 ± 1.1	–	32.9 ± 1.3	20.4 ± 20.4
2030	–	–	22.1 ± 3.8	15.5 ± 2.4	–	–	–	106.9 ± 2.6	324.1 ± 3.0	253.2 ± 5.1	–	–	–	–	–
2057	69.2 ± 8.7	45.3 ± 9.6	27.0 ± 4.2	10.5 ± 3.3	8.6 ± 2.5	–	–	316.4 ± 4.2	950.9 ± 6.7	199.3 ± 12.4	9.0 ± 1.5	13.3 ± 1.2	–	24.2 ± 1.6	–
2063	–	–	27.6 ± 1.8	26.1 ± 1.2	7.5 ± 1.5	–	–	340.7 ± 4.2	1030.3 ± 10.4	304.6 ± 4.6	3.1 ± 1.0	4.4 ± 1.2	–	16.3 ± 1.4	19.5 ± 19.5
2071	–	–	–	20.6 ± 5.5	–	–	–	281.0 ± 5.6	864.0 ± 13.7	219.9 ± 11.8	–	–	–	–	–
2110	–	–	–	90.8 ± 19.6	–	–	–	382.6 ± 25.0	1272.3 ± 28.7	312.8 ± 23.0	–	–	–	–	–

Continued on next page

Table C.1 – continued from previous page

Sl. No. λ (Å)	[O II] 3726	[O II] 3729	H δ 4102	H γ 4340	[O III] 4363	[Ar IV] 4711	[Ar IV] 4740	[O III] 4959	[O III] 5007	H α 6562	[S II] 6717	[S II] 6731	[Ar V] 7005	[Ar III] 7136	[Ar III] 7751
2113	30.6 ± 4.4	28.8 ± 4.6	25.9 ± 2.3	20.2 ± 1.9	17.6 ± 1.3	5.7 ± 1.8	7.2 ± 1.7	553.7 ± 6.0	1632.3 ± 15.9	300.1 ± 3.7	6.2 ± 1.1	9.7 ± 1.1	–	17.6 ± 3.0	–
2119	–	–	24.9 ± 4.0	14.2 ± 4.7	–	–	–	502.6 ± 8.1	1524.0 ± 16.2	328.2 ± 9.0	–	–	–	–	–
2128	–	–	–	37.2 ± 2.9	22.4 ± 2.4	–	11.2 ± 1.7	497.5 ± 8.2	1492.1 ± 13.9	322.2 ± 4.8	6.2 ± 1.7	7.6 ± 1.5	–	14.4 ± 3.7	–
2157	45.1 ± 4.4	23.9 ± 4.5	28.5 ± 2.9	30.5 ± 2.5	19.7 ± 2.1	–	8.1 ± 2.6	544.4 ± 7.7	1622.1 ± 20.3	278.4 ± 10.8	7.2 ± 1.1	12.5 ± 1.6	–	22.2 ± 1.6	16.1 ± 16.1
2169	–	–	–	–	–	–	–	551.2 ± 11.0	1632.4 ± 17.2	515.7 ± 9.7	–	–	–	–	–
2173	–	–	19.5 ± 2.2	20.6 ± 1.4	7.8 ± 1.3	–	–	323.0 ± 4.4	973.8 ± 9.6	216.8 ± 18.8	4.7 ± 1.2	6.7 ± 0.6	–	30.2 ± 1.0	–
2195	10.7 ± 3.1	16.9 ± 3.5	–	18.9 ± 1.0	15.9 ± 1.3	–	5.0 ± 0.5	471.0 ± 6.6	1385.7 ± 15.4	297.8 ± 1.9	–	–	2.0 ± 0.7	7.7 ± 1.2	–
2203	–	–	18.1 ± 3.4	7.2 ± 2.1	–	–	–	494.1 ± 5.3	1585.8 ± 24.9	458.8 ± 17.2	–	–	–	–	–
2214	–	–	39.1 ± 9.4	33.0 ± 6.6	–	–	–	438.9 ± 8.8	1306.4 ± 21.7	285.6 ± 11.3	–	–	–	–	–
2232	17.7 ± 3.3	16.6 ± 2.8	22.2 ± 2.0	13.9 ± 1.0	10.3 ± 0.9	–	1.6 ± 0.5	424.3 ± 5.7	1238.6 ± 15.2	341.3 ± 4.4	–	–	–	24.7 ± 0.6	12.1 ± 12.1
2237	37.1 ± 2.7	29.0 ± 2.6	26.1 ± 1.1	26.0 ± 0.7	14.7 ± 1.1	–	4.8 ± 0.7	476.5 ± 4.0	1423.8 ± 14.0	309.0 ± 4.8	5.7 ± 0.4	7.7 ± 0.5	–	16.7 ± 0.5	7.9 ± 7.9
2238	–	–	–	–	–	–	–	330.8 ± 15.9	884.7 ± 15.6	319.6 ± 7.0	–	–	–	–	–
2252	33.1 ± 5.7	24.1 ± 5.9	25.1 ± 1.2	30.6 ± 1.2	25.3 ± 1.5	–	3.5 ± 0.8	533.0 ± 5.7	1591.3 ± 15.7	377.7 ± 4.7	8.1 ± 0.6	15.7 ± 1.0	–	34.7 ± 1.3	15.5 ± 15.5
2273	–	–	26.9 ± 1.9	12.9 ± 1.7	–	–	–	123.2 ± 3.0	366.7 ± 3.1	264.1 ± 3.4	–	–	–	–	–
2275	28.8 ± 7.5	65.1 ± 7.3	–	23.5 ± 2.5	22.8 ± 2.9	9.5 ± 2.3	7.9 ± 2.4	472.3 ± 7.0	1405.7 ± 15.2	308.8 ± 6.6	23.7 ± 1.6	22.5 ± 1.7	–	24.9 ± 2.0	18.2 ± 18.2
2278	–	–	–	–	–	–	–	570.5 ± 37.0	1536.3 ± 21.1	471.7 ± 34.8	–	–	–	–	–
2294	–	–	–	–	–	–	–	283.9 ± 3.2	816.7 ± 4.6	350.6 ± 7.6	–	–	–	–	–
2300	–	–	30.8 ± 4.2	37.0 ± 4.9	–	–	–	368.9 ± 6.6	1100.2 ± 12.0	307.7 ± 5.1	–	–	–	–	–
2307	–	–	24.1 ± 1.5	27.7 ± 1.4	16.7 ± 2.1	–	4.9 ± 1.0	616.0 ± 6.1	1811.7 ± 16.6	324.9 ± 16.5	2.3 ± 0.5	3.5 ± 0.8	–	30.2 ± 1.1	20.1 ± 20.1
2314	–	–	22.0 ± 3.6	26.8 ± 2.1	–	–	–	249.7 ± 3.5	731.0 ± 5.6	383.5 ± 4.4	–	–	–	–	–
2315	–	–	–	41.8 ± 7.2	–	–	–	402.2 ± 8.8	1140.1 ± 8.4	367.2 ± 12.3	–	–	–	–	–
2329	–	–	–	–	–	–	–	309.6 ± 19.9	840.3 ± 16.0	418.6 ± 23.1	–	–	–	–	–
2332	–	–	–	23.2 ± 5.6	–	–	–	492.3 ± 6.9	1437.3 ± 9.4	253.2 ± 14.9	–	–	–	–	–
2333	–	–	30.2 ± 4.3	16.9 ± 4.1	16.6 ± 5.4	–	–	439.1 ± 7.5	1315.7 ± 13.9	322.6 ± 6.2	–	–	–	18.3 ± 3.3	–
2342	–	–	–	–	–	–	–	169.7 ± 14.1	516.0 ± 12.3	298.2 ± 13.6	–	–	–	–	–
2352	–	–	–	–	–	–	–	119.6 ± 13.3	361.5 ± 7.6	394.0 ± 11.8	–	–	–	–	–
2357	–	–	–	–	–	–	–	265.9 ± 11.6	752.3 ± 5.5	397.6 ± 14.1	–	–	–	–	–
2358	46.8 ± 3.9	46.1 ± 4.5	22.3 ± 2.0	23.9 ± 0.8	4.6 ± 0.9	–	–	181.1 ± 3.4	533.8 ± 5.3	181.8 ± 17.6	4.3 ± 0.5	7.5 ± 0.4	–	19.3 ± 0.6	8.0 ± 8.0
2389	101.0 ± 3.3	64.6 ± 3.3	–	21.1 ± 1.2	18.7 ± 1.8	–	13.0 ± 2.0	594.0 ± 5.7	1799.7 ± 16.1	367.7 ± 4.2	14.0 ± 0.7	18.1 ± 0.8	–	38.5 ± 1.3	20.2 ± 20.2
2404	–	–	–	–	–	–	–	371.2 ± 11.9	1074.9 ± 13.3	350.0 ± 8.8	–	–	–	–	–
2407	36.5 ± 4.2	18.8 ± 5.0	26.6 ± 4.3	19.0 ± 3.3	19.5 ± 3.2	–	–	426.2 ± 5.4	1296.2 ± 16.4	243.7 ± 6.0	–	–	–	15.4 ± 3.9	–
2432	–	–	–	–	–	–	–	313.0 ± 16.0	904.0 ± 11.8	395.8 ± 8.8	–	–	–	–	–
2435	–	–	–	–	–	–	–	209.6 ± 16.9	628.0 ± 9.4	306.3 ± 8.7	–	–	–	–	–
2450	–	–	–	–	–	–	–	389.7 ± 13.9	1131.0 ± 26.9	471.8 ± 16.0	–	–	–	–	–
2456	–	–	–	–	–	–	–	507.1 ± 14.7	1535.8 ± 11.3	431.8 ± 21.1	–	–	–	–	–
2463	–	–	–	36.4 ± 9.2	–	–	–	476.8 ± 9.9	1393.8 ± 12.9	248.2 ± 20.6	–	–	–	–	–
2469	–	–	17.8 ± 5.0	23.2 ± 1.8	–	–	–	295.7 ± 4.4	868.6 ± 6.1	412.9 ± 6.0	–	–	–	–	–
2478	–	–	–	29.1 ± 1.3	18.5 ± 1.3	–	7.6 ± 1.1	584.8 ± 6.2	1808.1 ± 24.1	349.9 ± 6.9	1.9 ± 0.6	2.7 ± 0.6	–	25.2 ± 1.1	13.2 ± 13.2
2481	–	–	–	–	–	–	–	280.7 ± 15.2	863.6 ± 29.6	407.8 ± 15.6	–	–	–	–	–
2484	–	–	–	39.3 ± 3.2	14.0 ± 3.6	–	–	392.6 ± 5.3	1132.5 ± 11.9	237.3 ± 5.4	–	–	–	15.0 ± 3.7	22.5 ± 22.5
2487	–	–	–	28.8 ± 5.5	48.0 ± 8.9	–	–	406.8 ± 9.3	1171.5 ± 10.9	243.9 ± 15.4	–	–	–	–	–
2495	21.4 ± 6.2	26.6 ± 6.0	26.6 ± 1.8	29.2 ± 1.2	18.9 ± 1.0	–	9.4 ± 1.4	541.0 ± 7.3	1619.3 ± 16.9	301.9 ± 4.7	4.8 ± 1.5	4.2 ± 1.0	–	18.5 ± 1.4	20.3 ± 20.3
2498	56.8 ± 6.8	32.8 ± 7.6	–	30.5 ± 1.5	10.7 ± 2.1	–	–	396.9 ± 5.4	1176.3 ± 18.2	264.7 ± 4.8	10.4 ± 0.8	13.4 ± 1.4	–	23.2 ± 2.8	–
2504	–	–	25.6 ± 4.8	21.4 ± 2.0	–	–	–	190.0 ± 4.0	564.0 ± 3.2	286.4 ± 5.8	–	–	–	–	–
2509	–	–	–	49.7 ± 6.0	–	–	–	370.2 ± 9.9	1094.5 ± 11.3	263.6 ± 13.7	–	–	–	–	–
2523	–	–	–	–	24.5 ± 6.5	–	–	319.4 ± 8.2	967.6 ± 6.9	338.0 ± 5.6	–	–	–	22.4 ± 7.3	–
2528	–	–	–	–	–	–	–	654.6 ± 35.4	1999.1 ± 30.5	439.3 ± 28.3	–	–	–	–	–
2534	18.9 ± 6.0	29.6 ± 6.1	22.4 ± 4.3	25.3 ± 3.9	11.4 ± 2.8	–	–	433.1 ± 6.1	1308.8 ± 11.0	470.3 ± 8.0	22.8 ± 2.6	24.2 ± 2.9	–	47.1 ± 4.4	–
2538	84.0 ± 6.5	57.9 ± 8.5	24.0 ± 4.3	23.1 ± 3.0	25.3 ± 2.6	9.1 ± 2.3	–	620.0 ± 6.4	1880.2 ± 13.0	390.6 ± 8.4	14.7 ± 1.5	19.8 ± 2.9	–	39.0 ± 3.9	–
2576	–	–	25.8 ± 3.6	15.4 ± 3.3	–	–	–	284.6 ± 5.1	817.1 ± 6.0	339.6 ± 7.6	–	–	–	–	–
2580	–	–	–	–	–	–	–	319.8 ± 10.5	985.1 ± 11.1	444.2 ± 9.1	–	–	–	–	–
2588	–	–	19.4 ± 2.8	25.2 ± 3.2	14.3 ± 3.5	7.1 ± 2.2	–	449.2 ± 6.8	1285.3 ± 11.4	303.6 ± 4.2	12.2 ± 1.5	9.8 ± 2.1	–	10.3 ± 3.0	–
2601	87.4 ± 7.2	43.3 ± 7.1	–	15.9 ± 1.6	22.1 ± 3.1	–	–	561.5 ± 4.0	1714.9 ± 15.2	431.0 ± 6.3	12.3 ± 0.7	23.9 ± 1.0	–	34.7 ± 1.3	16.0 ± 16.0
2636	–	–	–	–	22.7 ± 5.1	–	19.6 ± 5.8	415.1 ± 9.4	1232.0 ± 19.8	438.5 ± 10.4	57.0 ± 2.5	76.9 ± 2.0	–	58.2 ± 4.6	32.9 ± 32.9
2642	41.2 ± 5.7	32.6 ± 5.3	22.7 ± 2.8	27.3 ± 2.7	19.3 ± 1.3	–	8.0 ± 1.3	633.0 ± 8.3	1850.2 ± 17.2	351.8 ± 4.3	5.6 ± 1.5	7.6 ± 1.0	–	41.4 ± 1.1	13.9 ± 13.9
2644	–	–	–	23.0 ± 5.2	24.1 ± 5.4	–	–	579.9 ± 6.9	1716.6 ± 18.6	329.8 ± 6.6	11.7 ± 2.7	15.5 ± 2.8	–	37.1 ± 5.2	55.2 ± 55.2
2647	–	–	21.9 ± 2.0	11.1 ± 1.5	14.5 ± 1.2	–	3.4 ± 1.0	532.7 ± 4.4	1619.7 ± 16.4	480.9 ± 7.7	4.3 ± 0.8	5.3 ± 0.7	–	16.1 ± 0.8	13.5 ± 13.5
2651	–	–	21.4 ± 2.2	17.8 ± 2.0	10.6 ± 3.0	–	–	365.4 ± 6.4	1150.8 ± 8.4	369.7 ± 15.1	7.8 ± 1.7	10.8 ± 1.3	–	33.5 ± 1.6	11.2 ± 11.2
2660	–	–	–	–	–	–	–	81.7 ± 11.3	258.5 ± 16.0	342.9 ± 8.2	–	–	–	–	–
2661	–	–	–	–	–	–	–	708.4 ± 15.7	2175.7 ± 24.5	553.3 ± 20.0	–	–	–	–	–
2664	–	–	24.5 ± 1.6	15.7 ± 2.0	6.0 ± 2.0	–	–	376.7 ± 3.7	1171.7 ± 10.8	452.4 ± 7.4	–	–	–	29.3 ± 1.1	12.1 ± 12.1

Continued on next page

Table C.1 – continued from previous page

Sl. No. λ (Å)	[O II] 3726	[O II] 3729	Hδ 4102	Hγ 4340	[O III] 4363	[Ar IV] 4711	[Ar IV] 4740	[O III] 4959	[O III] 5007	Hα 6562	[S II] 6717	[S II] 6731	[Ar V] 7005	[Ar III] 7136	[Ar III] 7751
2673	–	–	–	–	–	–	–	576.2 ± 20.2	1625.2 ± 20.2	505.7 ± 31.1	–	–	–	–	–
2674	–	–	23.6 ± 5.0	20.2 ± 2.8	19.3 ± 3.3	7.1 ± 2.3	8.4 ± 2.7	482.7 ± 4.9	1444.5 ± 11.4	365.1 ± 5.0	–	–	–	19.0 ± 2.3	–
2692	–	–	–	–	–	–	–	506.0 ± 12.1	1448.6 ± 14.3	439.3 ± 8.5	–	–	–	–	–
2787	–	–	–	32.2 ± 8.6	–	–	–	670.8 ± 17.9	2044.3 ± 17.1	656.6 ± 11.3	–	–	–	–	–
2793	–	–	–	–	–	–	–	487.0 ± 20.4	1346.6 ± 16.9	292.5 ± 16.4	–	–	–	–	–
2814	–	–	–	–	–	–	–	763.1 ± 17.1	2206.0 ± 30.9	503.6 ± 13.3	–	–	–	–	–
2818	–	–	–	–	–	–	–	215.9 ± 24.1	597.2 ± 14.3	453.2 ± 14.8	–	–	–	–	–
2837	–	–	22.4 ± 5.1	17.2 ± 4.6	19.1 ± 3.4	–	13.8 ± 2.8	557.2 ± 7.2	1656.6 ± 8.4	460.6 ± 7.9	12.5 ± 3.3	11.5 ± 3.1	–	25.3 ± 5.3	–
2848	228.4 ± 25.1	272.6 ± 23.6	–	–	62.6 ± 13.0	–	–	572.0 ± 17.9	1675.4 ± 17.8	419.8 ± 18.2	72.6 ± 9.0	56.6 ± 7.8	–	48.6 ± 14.9	–
2872	–	–	–	–	–	–	–	291.6 ± 23.7	812.4 ± 16.2	490.8 ± 15.8	–	–	–	–	–
2874	–	–	15.9 ± 4.1	14.2 ± 2.8	33.8 ± 4.7	–	13.3 ± 3.9	562.3 ± 5.9	1604.7 ± 9.9	324.3 ± 4.3	13.2 ± 3.9	12.5 ± 2.7	–	30.1 ± 3.3	–
2878	–	–	–	–	–	–	–	760.5 ± 27.7	2066.2 ± 43.0	509.5 ± 18.8	–	–	–	–	–
2888	20.8 ± 2.3	13.2 ± 2.2	24.1 ± 1.7	21.1 ± 1.1	12.7 ± 1.7	–	–	309.7 ± 4.1	930.2 ± 6.7	308.2 ± 1.9	–	–	–	23.1 ± 2.6	6.1 ± 6.1
2957	–	–	–	–	57.5 ± 10.2	–	–	559.4 ± 15.2	1684.1 ± 15.2	397.5 ± 11.7	–	–	–	38.3 ± 11.9	–
2968	45.1 ± 5.7	47.2 ± 5.7	–	–	36.4 ± 5.2	–	–	317.0 ± 9.5	949.8 ± 10.0	332.0 ± 4.8	17.4 ± 3.7	20.6 ± 3.2	–	29.0 ± 5.2	–
2982	–	–	–	40.9 ± 6.0	–	–	–	325.8 ± 17.6	972.7 ± 15.0	371.7 ± 9.8	–	–	–	–	–
2983	–	–	30.8 ± 8.4	38.3 ± 3.2	25.3 ± 4.4	–	–	499.3 ± 9.1	1431.6 ± 14.6	315.4 ± 7.8	–	–	–	40.7 ± 5.2	–
2993	–	–	–	–	–	–	–	559.9 ± 9.2	1749.0 ± 26.4	493.9 ± 12.4	–	–	–	–	–
2994	–	–	–	–	24.8 ± 4.5	–	–	579.3 ± 9.2	1736.7 ± 18.9	330.1 ± 6.7	–	–	–	–	–
3001	44.7 ± 3.5	20.0 ± 4.2	25.4 ± 1.6	29.2 ± 2.1	11.9 ± 1.1	–	7.1 ± 2.3	403.6 ± 5.5	1215.8 ± 15.3	324.6 ± 4.6	6.4 ± 1.5	13.7 ± 1.3	–	27.3 ± 3.2	–
3011	–	–	–	–	–	–	–	405.7 ± 25.4	1238.7 ± 20.8	355.8 ± 15.5	–	–	–	–	–
3018	31.2 ± 4.3	30.7 ± 4.4	26.6 ± 3.2	14.8 ± 2.4	22.8 ± 1.5	–	–	627.4 ± 7.4	1842.5 ± 8.7	316.5 ± 3.0	–	–	–	25.7 ± 2.6	–
3031	–	–	–	–	–	–	–	361.0 ± 12.7	1123.0 ± 11.2	380.5 ± 6.3	–	–	–	–	–
3032	–	–	32.7 ± 4.6	15.2 ± 3.5	–	–	–	242.0 ± 4.1	709.6 ± 5.5	417.4 ± 2.7	–	–	–	–	–
3047	–	–	–	–	–	–	–	208.4 ± 11.2	607.5 ± 9.9	330.9 ± 6.6	–	–	–	–	–
3048	–	–	–	–	–	–	–	381.6 ± 19.8	1183.9 ± 26.2	408.4 ± 20.3	–	–	–	–	–
3064	–	–	23.4 ± 3.3	12.6 ± 1.3	–	–	–	324.8 ± 3.9	990.2 ± 4.6	464.8 ± 3.9	–	–	–	–	–
3072	–	–	15.0 ± 4.2	18.8 ± 2.1	58.7 ± 2.4	–	–	186.6 ± 4.2	565.7 ± 4.2	291.1 ± 7.0	8.5 ± 2.4	10.5 ± 1.7	8.5 ± 2.2	20.2 ± 2.3	–
3075	18.4 ± 4.3	18.2 ± 3.9	26.8 ± 1.9	23.8 ± 2.1	13.7 ± 2.1	–	–	233.9 ± 2.4	702.1 ± 6.7	329.4 ± 3.1	–	–	–	16.5 ± 1.8	9.3 ± 9.3
3085	–	–	–	–	58.9 ± 2.4	–	–	718.5 ± 10.9	2118.1 ± 11.0	334.3 ± 5.3	–	–	–	18.4 ± 2.6	–
3102	22.4 ± 3.9	19.3 ± 3.8	28.4 ± 2.1	18.6 ± 1.3	33.2 ± 2.0	–	–	133.6 ± 2.5	408.0 ± 4.6	615.2 ± 6.8	7.5 ± 0.6	10.1 ± 0.5	–	9.1 ± 0.5	–
3146	93.6 ± 6.4	44.8 ± 6.4	26.6 ± 3.5	22.8 ± 2.1	31.0 ± 2.1	–	9.7 ± 2.5	641.4 ± 7.2	1952.3 ± 26.0	295.8 ± 11.7	–	–	–	21.4 ± 2.0	10.2 ± 10.2
3147	–	–	28.7 ± 3.1	32.2 ± 3.9	18.3 ± 2.8	–	10.0 ± 3.2	402.0 ± 5.2	1195.8 ± 11.7	310.8 ± 5.6	–	–	–	16.1 ± 3.8	–
3162	–	–	33.2 ± 8.7	50.7 ± 5.2	39.6 ± 4.6	–	23.5 ± 5.1	688.4 ± 10.3	2045.5 ± 23.0	409.1 ± 7.3	20.0 ± 6.4	30.2 ± 5.4	–	39.5 ± 9.1	–
3163	–	–	25.1 ± 2.0	14.0 ± 1.5	11.2 ± 2.0	–	–	475.6 ± 6.8	1450.3 ± 21.6	401.8 ± 6.8	5.1 ± 0.9	8.9 ± 0.9	–	27.4 ± 2.0	–
3173	–	–	29.8 ± 3.8	29.1 ± 1.1	–	–	–	354.7 ± 6.4	1048.5 ± 11.1	333.5 ± 3.5	–	–	–	–	–
3180	–	–	–	–	–	–	–	610.6 ± 9.8	1910.2 ± 14.7	527.9 ± 16.5	–	–	–	–	–
3188	–	–	26.6 ± 3.9	21.1 ± 4.8	–	–	–	273.0 ± 5.5	832.3 ± 11.8	303.6 ± 4.3	–	–	–	–	–
3197	–	–	–	–	–	–	–	225.4 ± 5.1	695.6 ± 6.9	437.4 ± 13.2	–	–	–	–	–
3203	–	–	20.0 ± 3.2	30.7 ± 2.1	19.0 ± 2.7	8.0 ± 2.1	8.4 ± 1.9	443.3 ± 4.9	1321.9 ± 12.3	303.3 ± 3.9	–	–	–	9.0 ± 2.7	–
3214	–	–	20.6 ± 3.0	6.7 ± 2.2	17.2 ± 2.5	–	–	347.7 ± 5.5	1052.8 ± 8.8	384.8 ± 3.8	–	–	–	18.2 ± 2.9	–
3225	–	–	–	–	–	–	–	374.2 ± 17.6	1093.1 ± 9.5	333.7 ± 15.0	–	–	–	–	–
3228	–	–	–	–	–	–	–	335.7 ± 5.1	985.7 ± 15.5	402.0 ± 9.8	–	–	–	–	–
3235	40.5 ± 1.5	21.1 ± 1.4	27.5 ± 0.8	23.6 ± 0.8	8.0 ± 0.5	2.4 ± 0.5	2.6 ± 0.3	501.8 ± 5.7	1500.1 ± 18.4	318.2 ± 6.2	2.2 ± 0.2	3.7 ± 0.2	–	17.7 ± 0.7	4.6 ± 4.6
3239	60.9 ± 6.8	33.9 ± 8.0	29.2 ± 3.7	9.0 ± 2.8	17.0 ± 4.0	–	–	532.9 ± 8.6	1554.5 ± 18.6	317.0 ± 5.9	–	–	–	32.6 ± 4.9	–
3242	–	–	–	–	–	–	–	238.5 ± 15.1	726.2 ± 14.1	353.2 ± 8.3	–	–	–	–	–
3256	80.1 ± 19.4	101.6 ± 19.1	–	–	65.7 ± 6.8	–	–	757.0 ± 23.6	2207.8 ± 19.8	362.7 ± 19.5	27.9 ± 7.0	46.1 ± 6.9	21.2 ± 7.0	73.1 ± 14.0	–
3260	46.2 ± 3.7	22.6 ± 3.3	–	32.5 ± 1.2	12.5 ± 1.4	–	–	419.5 ± 4.9	1263.8 ± 15.0	302.7 ± 3.4	6.6 ± 0.6	9.3 ± 0.7	–	18.9 ± 1.4	–
3262	–	–	–	–	–	–	–	631.6 ± 21.0	1874.9 ± 22.7	300.4 ± 17.9	–	–	–	–	–
3273	–	–	18.3 ± 5.7	21.3 ± 4.9	–	–	–	347.5 ± 10.2	1027.5 ± 14.9	327.7 ± 7.8	–	–	–	–	–
3337	–	–	–	–	–	–	–	272.7 ± 22.4	891.0 ± 20.4	316.0 ± 18.1	–	–	–	–	–
3367	–	–	22.7 ± 5.0	18.6 ± 3.9	–	–	–	321.6 ± 6.4	934.0 ± 11.4	395.0 ± 4.0	–	–	–	–	–
3373	–	–	–	–	53.8 ± 10.8	–	–	692.3 ± 12.2	2009.4 ± 26.4	480.7 ± 13.9	–	–	34.8 ± 9.4	76.7 ± 11.7	–
3397	18.4 ± 2.9	13.8 ± 3.5	25.3 ± 2.6	16.2 ± 1.4	15.8 ± 1.8	–	7.4 ± 1.5	638.2 ± 11.8	1919.9 ± 18.8	352.0 ± 4.5	–	–	–	26.0 ± 0.8	14.1 ± 14.1
3406	15.4 ± 3.3	21.3 ± 3.0	–	24.7 ± 1.3	8.3 ± 1.0	–	–	392.8 ± 3.6	1188.4 ± 12.6	300.9 ± 5.6	3.7 ± 0.5	6.0 ± 0.6	–	16.7 ± 1.1	13.0 ± 13.0
3410	–	–	–	51.2 ± 9.8	–	–	–	316.2 ± 8.0	981.1 ± 10.5	296.1 ± 14.0	–	–	–	–	–
3419	–	–	33.2 ± 9.2	30.7 ± 5.0	–	–	–	182.2 ± 5.5	529.0 ± 6.7	260.3 ± 6.8	–	–	–	–	–
3420	–	–	40.1 ± 12.7	43.3 ± 5.6	–	–	–	363.8 ± 8.5	1035.6 ± 10.9	269.8 ± 5.3	–	–	–	–	–
3425	–	–	30.8 ± 2.7	29.8 ± 2.2	9.5 ± 2.6	–	–	408.7 ± 6.8	1207.5 ± 13.6	316.8 ± 5.3	–	–	–	20.9 ± 2.9	–
3428	–	–	24.4 ± 3.0	17.8 ± 1.9	18.9 ± 1.7	–	7.8 ± 1.6	612.2 ± 7.2	1855.6 ± 16.6	405.5 ± 6.3	–	–	–	31.2 ± 1.7	12.9 ± 12.9
3429	65.2 ± 4.0	48.0 ± 4.9	–	15.6 ± 1.4	16.6 ± 1.5	–	7.8 ± 1.7	599.7 ± 8.7	1815.5 ± 17.3	362.2 ± 3.7	10.6 ± 1.3	14.8 ± 1.0	–	31.0 ± 1.3	15.3 ± 15.3

Continued on next page

Table C.1 – continued from previous page

Sl. No. λ (Å)	[O II] 3726	[O II] 3729	Hδ 4102	Hγ 4340	[O III] 4363	[Ar IV] 4711	[Ar IV] 4740	[O III] 4959	[O III] 5007	Hα 6562	[S II] 6717	[S II] 6731	[Ar V] 7005	[Ar III] 7136	[Ar III] 7751
3431	–	–	–	–	–	–	–	694.0 ± 24.5	2176.8 ± 25.7	807.5 ± 12.1	–	–	–	–	–
3436	–	–	21.2 ± 5.7	14.3 ± 2.4	–	–	–	364.3 ± 5.2	1063.5 ± 12.0	365.7 ± 3.4	–	–	–	–	–
3439	–	–	–	–	–	–	–	309.1 ± 18.6	952.2 ± 24.0	467.9 ± 15.2	–	–	–	–	–
3444	–	–	–	–	–	–	–	508.7 ± 23.7	1546.1 ± 23.4	313.1 ± 15.4	–	–	–	–	–
3447	–	–	44.1 ± 8.7	31.9 ± 3.9	–	–	–	383.8 ± 8.1	1155.2 ± 13.7	279.2 ± 8.6	–	–	–	–	–
3449	–	–	–	55.5 ± 17.7	–	–	–	471.7 ± 24.1	1420.5 ± 31.3	485.6 ± 20.5	–	–	–	–	–
3451	–	–	24.4 ± 5.2	14.1 ± 2.7	–	–	–	293.6 ± 5.4	853.0 ± 9.9	334.9 ± 6.0	–	–	–	–	–
3455	–	–	25.7 ± 3.2	19.1 ± 2.1	–	–	–	131.1 ± 3.8	402.3 ± 4.1	354.0 ± 4.0	–	–	–	–	–
3456	–	–	–	–	–	–	–	597.3 ± 25.7	1786.5 ± 30.0	613.4 ± 28.5	–	–	–	–	–
3472	–	–	23.8 ± 3.2	13.7 ± 1.9	6.5 ± 1.6	4.8 ± 0.8	–	333.1 ± 4.0	1008.2 ± 12.0	333.7 ± 3.2	10.2 ± 1.6	11.6 ± 1.8	–	20.4 ± 1.7	–
3473	–	–	–	38.3 ± 8.5	–	–	–	352.0 ± 11.2	1028.8 ± 23.6	451.2 ± 12.8	–	–	–	–	–
3474	–	–	30.4 ± 4.8	22.3 ± 2.0	–	–	–	336.4 ± 4.4	1035.8 ± 10.7	377.5 ± 4.6	–	–	–	–	–
3477	25.6 ± 1.8	8.2 ± 2.2	24.5 ± 1.4	22.8 ± 0.7	6.7 ± 0.5	2.7 ± 0.4	2.7 ± 0.4	503.4 ± 6.4	1499.9 ± 17.2	372.4 ± 8.8	2.1 ± 0.4	4.4 ± 0.5	–	28.2 ± 0.7	11.4 ± 11.4
3480	–	–	16.0 ± 4.1	8.7 ± 2.7	15.7 ± 1.7	11.8 ± 2.9	10.8 ± 3.5	505.2 ± 7.0	1490.2 ± 12.4	289.6 ± 8.8	5.9 ± 1.8	5.5 ± 1.5	–	24.3 ± 1.7	13.7 ± 13.7
3490	16.2 ± 5.2	20.8 ± 5.1	29.2 ± 3.2	16.7 ± 1.9	17.3 ± 1.8	8.8 ± 1.4	9.2 ± 1.7	574.4 ± 7.2	1713.1 ± 16.5	364.0 ± 3.6	5.7 ± 0.9	9.6 ± 1.3	4.5 ± 0.8	23.3 ± 1.2	–
3499	–	–	–	–	–	–	–	363.7 ± 6.9	1030.6 ± 8.6	293.5 ± 3.5	–	–	–	–	–
3660	–	–	27.8 ± 2.2	21.7 ± 0.9	–	–	–	162.3 ± 1.9	483.3 ± 4.0	275.1 ± 2.8	–	–	–	–	–
3664	–	–	–	–	–	–	–	246.8 ± 10.9	740.0 ± 13.5	290.2 ± 13.5	–	–	–	–	–
3671	23.5 ± 1.6	7.8 ± 1.7	16.7 ± 1.0	14.7 ± 0.5	2.3 ± 0.5	–	–	256.6 ± 3.8	818.0 ± 10.4	363.4 ± 4.3	1.6 ± 0.3	3.6 ± 0.4	–	20.9 ± 0.4	6.2 ± 6.2
3688	–	–	20.2 ± 2.3	14.4 ± 1.9	9.6 ± 2.3	–	4.5 ± 1.4	474.9 ± 3.6	1481.6 ± 15.6	362.0 ± 2.6	–	–	–	18.3 ± 1.7	11.2 ± 11.2
3697	–	–	14.4 ± 1.3	16.2 ± 0.8	10.2 ± 0.9	–	–	516.3 ± 6.1	1653.1 ± 19.1	470.1 ± 4.3	3.2 ± 0.6	5.1 ± 0.5	–	20.9 ± 0.7	8.0 ± 8.0
3700	16.0 ± 1.4	6.4 ± 1.4	23.7 ± 1.2	17.7 ± 0.6	10.8 ± 0.8	1.5 ± 0.4	1.7 ± 0.5	453.7 ± 3.1	1388.9 ± 14.7	357.6 ± 2.8	1.4 ± 0.3	3.1 ± 0.3	–	15.8 ± 0.5	5.4 ± 5.4
3702	–	–	–	–	–	–	–	213.5 ± 8.4	613.5 ± 9.6	405.2 ± 6.5	–	–	–	–	–
3708	–	–	17.8 ± 2.6	13.7 ± 1.4	–	–	–	382.4 ± 3.5	1163.0 ± 8.9	392.2 ± 2.3	–	–	–	–	–
3710	–	–	23.5 ± 1.9	13.0 ± 1.2	18.9 ± 0.9	8.2 ± 1.1	7.9 ± 1.0	537.6 ± 6.7	1672.4 ± 16.9	362.4 ± 3.8	5.3 ± 1.0	6.1 ± 1.4	4.1 ± 0.7	19.2 ± 1.2	–
3716	–	–	–	–	–	–	–	304.0 ± 20.8	844.4 ± 22.0	365.1 ± 24.5	–	–	–	–	–
3717	–	–	16.8 ± 1.9	13.0 ± 1.2	9.0 ± 0.9	–	4.3 ± 0.8	495.8 ± 3.7	1528.2 ± 13.6	377.2 ± 4.4	2.5 ± 0.6	3.3 ± 0.5	–	14.9 ± 0.7	6.0 ± 6.0
3721	–	–	27.9 ± 8.9	23.0 ± 7.4	–	–	–	448.6 ± 6.1	1337.7 ± 14.5	301.0 ± 5.1	–	–	–	–	–
3742	–	–	14.2 ± 2.1	15.8 ± 1.3	9.3 ± 1.0	–	4.0 ± 1.0	533.9 ± 4.2	1642.3 ± 15.5	504.1 ± 4.2	2.1 ± 0.6	6.2 ± 0.6	–	30.3 ± 0.7	–
3751	–	–	–	–	–	–	–	480.5 ± 22.3	1646.9 ± 33.0	578.3 ± 13.2	–	–	–	–	–
3759	–	–	–	–	–	–	–	332.5 ± 6.2	1059.7 ± 19.0	683.6 ± 5.8	–	–	–	–	–
3762	–	–	16.4 ± 1.6	11.3 ± 1.1	–	–	–	378.8 ± 6.4	1132.5 ± 10.0	406.9 ± 2.4	–	–	–	–	–
3770	13.4 ± 2.2	11.8 ± 2.3	17.1 ± 1.0	16.3 ± 0.9	13.8 ± 0.9	–	7.9 ± 0.6	608.3 ± 5.8	1857.3 ± 16.6	382.8 ± 3.3	7.1 ± 0.7	12.6 ± 0.5	3.4 ± 0.7	30.1 ± 0.8	8.1 ± 8.1
3773	–	–	–	–	–	–	–	334.9 ± 12.4	977.5 ± 7.8	347.8 ± 10.5	–	–	–	–	–
3780	–	–	20.8 ± 2.1	17.4 ± 1.0	12.5 ± 1.1	4.7 ± 0.7	4.6 ± 0.9	473.1 ± 3.5	1486.4 ± 8.9	363.0 ± 2.9	5.0 ± 0.8	8.3 ± 0.9	–	15.4 ± 1.1	–
3782	–	–	16.8 ± 0.7	14.5 ± 0.4	6.3 ± 1.0	–	–	378.9 ± 4.9	1136.1 ± 11.2	373.3 ± 2.5	–	–	–	18.1 ± 0.5	5.9 ± 5.9
3784	–	–	–	–	–	–	–	503.1 ± 14.9	1393.7 ± 14.4	369.3 ± 18.1	–	–	–	–	–
3793	–	–	9.2 ± 1.0	17.6 ± 0.9	6.2 ± 1.2	–	–	363.9 ± 3.6	1165.4 ± 10.0	472.2 ± 3.4	6.1 ± 0.6	6.3 ± 0.9	–	22.2 ± 0.8	–
3795	–	–	–	–	–	–	–	485.7 ± 14.8	1592.2 ± 23.6	590.2 ± 11.0	–	–	–	–	–
3802	–	–	–	28.0 ± 2.6	–	–	–	465.8 ± 4.7	1394.9 ± 14.2	268.0 ± 2.8	–	–	–	–	–
3805	–	–	13.0 ± 1.8	13.2 ± 2.0	8.8 ± 1.4	–	4.4 ± 1.2	478.3 ± 4.3	1479.6 ± 13.5	470.4 ± 4.8	23.2 ± 1.0	36.2 ± 0.9	–	43.2 ± 1.4	11.7 ± 11.7
3811	–	–	13.7 ± 3.5	20.1 ± 1.7	–	–	–	129.4 ± 2.5	386.9 ± 2.9	237.5 ± 2.6	–	–	–	–	–
3814	23.3 ± 2.5	11.1 ± 3.1	15.9 ± 1.3	16.0 ± 1.2	14.9 ± 1.3	–	7.3 ± 1.2	610.3 ± 5.3	1862.2 ± 18.6	444.3 ± 3.0	11.2 ± 0.9	17.1 ± 0.9	3.6 ± 0.7	38.2 ± 0.9	14.8 ± 14.8
3818	–	–	–	–	–	–	–	243.8 ± 10.0	736.6 ± 15.9	323.8 ± 10.6	–	–	–	–	–
3833	–	–	–	–	–	–	–	507.4 ± 11.2	1542.7 ± 17.0	359.0 ± 9.4	–	–	–	–	–
3844	–	–	–	–	–	–	–	131.7 ± 38.6	253.3 ± 42.3	382.8 ± 25.9	–	–	–	–	–
3854	–	–	–	28.7 ± 4.1	–	–	–	251.8 ± 6.0	755.5 ± 4.0	168.0 ± 6.2	–	–	–	–	–
3864	–	–	21.6 ± 1.4	19.3 ± 1.4	12.5 ± 1.8	–	6.0 ± 1.4	519.3 ± 9.7	1522.3 ± 16.6	331.9 ± 3.6	7.3 ± 1.1	7.9 ± 0.7	–	27.6 ± 1.4	–
3876	–	–	17.8 ± 5.6	16.1 ± 4.8	–	–	–	319.6 ± 5.4	1005.3 ± 6.7	355.5 ± 6.1	–	–	–	–	–
3881	–	–	–	46.9 ± 14.6	–	–	–	438.3 ± 31.5	1161.7 ± 30.3	451.2 ± 28.7	–	–	–	–	–
3885	32.2 ± 6.2	39.6 ± 6.5	26.1 ± 3.2	9.0 ± 2.2	25.6 ± 4.1	–	–	653.2 ± 5.3	2003.9 ± 13.1	461.0 ± 5.2	–	–	–	35.1 ± 2.7	–
3892	–	–	–	–	–	–	–	348.3 ± 9.9	1044.5 ± 9.2	399.8 ± 6.4	–	–	–	–	–
3897	–	–	–	–	–	–	–	538.1 ± 14.9	1576.6 ± 14.6	402.9 ± 11.5	–	–	–	–	–
3902	–	–	–	31.7 ± 7.1	–	–	–	363.3 ± 12.1	1071.5 ± 9.4	381.6 ± 10.4	–	–	–	–	–
3907	–	–	–	–	–	–	–	362.2 ± 7.0	1074.5 ± 6.7	325.4 ± 5.1	–	–	–	–	–
3914	–	–	23.8 ± 1.2	17.1 ± 0.8	–	–	–	220.0 ± 1.8	663.8 ± 4.6	320.1 ± 2.2	–	–	–	–	–
3923	–	–	26.0 ± 2.3	22.2 ± 1.1	5.9 ± 1.4	3.3 ± 0.9	–	348.0 ± 3.3	1099.4 ± 12.0	314.1 ± 2.3	–	–	–	17.0 ± 1.4	–
3925	–	–	–	–	–	–	–	320.4 ± 33.3	937.5 ± 23.1	472.8 ± 23.6	–	–	–	–	–
3939	–	–	–	36.8 ± 3.5	–	–	–	322.3 ± 4.8	975.9 ± 6.0	302.7 ± 4.5	–	–	–	–	–
3941	–	–	–	–	–	–	–	415.4 ± 6.5	1307.6 ± 15.8	367.4 ± 4.6	–	–	–	–	–
3942	–	–	–	–	–	–	–	193.4 ± 19.1	589.1 ± 21.1	394.6 ± 20.2	–	–	–	–	–

Continued on next page

Table C.1 – continued from previous page

Sl. No. λ (Å)	[O II] 3726	[O II] 3729	H δ 4102	H γ 4340	[O III] 4363	[Ar IV] 4711	[Ar IV] 4740	[O III] 4959	[O III] 5007	H α 6562	[S II] 6717	[S II] 6731	[Ar V] 7005	[Ar III] 7136	[Ar III] 7751
3945	–	–	22.3 ± 2.0	13.5 ± 1.4	–	–	–	357.9 ± 2.4	1149.9 ± 12.2	355.4 ± 2.9	–	–	–	–	–
3952	–	–	18.4 ± 3.5	29.4 ± 2.0	13.1 ± 2.0	–	7.1 ± 2.3	660.4 ± 4.4	2005.9 ± 10.7	522.5 ± 5.6	4.5 ± 1.1	5.9 ± 1.2	–	46.7 ± 1.6	16.0 ± 16.0
3979	–	–	–	–	–	–	–	204.1 ± 12.8	625.4 ± 10.1	333.2 ± 17.9	–	–	–	–	–
4002	–	–	13.8 ± 1.7	16.9 ± 1.3	7.9 ± 1.5	–	3.5 ± 1.1	527.1 ± 5.9	1610.8 ± 13.4	448.5 ± 3.9	2.7 ± 0.9	6.4 ± 1.1	–	29.3 ± 0.7	10.5 ± 10.5
4008	55.5 ± 7.0	29.2 ± 7.9	20.1 ± 3.6	14.3 ± 2.5	19.9 ± 3.2	–	–	603.5 ± 7.8	1727.0 ± 11.0	584.9 ± 6.3	11.8 ± 1.5	20.3 ± 1.9	–	55.2 ± 1.6	–
4015	–	–	–	12.1 ± 2.3	22.8 ± 1.7	7.6 ± 1.5	8.9 ± 1.5	550.1 ± 5.0	1667.0 ± 15.8	252.4 ± 2.2	4.0 ± 0.8	4.7 ± 1.1	–	12.7 ± 1.9	–
4016	–	–	24.7 ± 2.0	10.2 ± 1.9	–	–	–	212.6 ± 4.7	616.5 ± 5.8	277.1 ± 2.2	–	–	–	–	–
4025	–	–	28.4 ± 4.0	19.0 ± 2.3	–	–	–	219.4 ± 3.5	644.1 ± 7.7	377.8 ± 4.5	–	–	–	–	–
4031	–	–	29.0 ± 2.6	23.2 ± 1.8	8.4 ± 2.2	–	–	394.8 ± 5.4	1158.5 ± 6.5	344.6 ± 3.1	–	–	–	19.6 ± 1.0	–
4046	–	–	–	31.9 ± 4.9	–	–	–	440.0 ± 5.7	1257.2 ± 7.3	315.6 ± 7.6	–	–	–	–	–
4053	33.4 ± 1.6	15.0 ± 2.0	30.7 ± 1.7	18.0 ± 1.1	12.5 ± 1.2	–	–	541.4 ± 4.0	1617.6 ± 13.1	298.5 ± 3.5	–	–	–	12.6 ± 0.9	5.7 ± 5.7
4068	19.9 ± 1.9	13.4 ± 1.9	–	25.0 ± 1.0	10.6 ± 0.9	4.0 ± 0.7	4.2 ± 0.6	506.6 ± 4.9	1545.0 ± 15.8	244.7 ± 2.7	2.1 ± 0.4	3.5 ± 0.4	–	12.4 ± 0.7	–
4094	–	–	19.3 ± 2.0	13.2 ± 1.3	16.6 ± 1.3	–	4.4 ± 1.3	431.9 ± 4.2	1323.5 ± 7.6	372.5 ± 3.2	–	–	–	22.4 ± 1.0	8.4 ± 8.4
4107	–	–	–	–	–	–	–	229.4 ± 26.4	725.4 ± 30.8	393.7 ± 23.5	–	–	–	–	–
4118	–	–	–	–	–	–	–	322.6 ± 24.3	885.1 ± 28.6	299.8 ± 12.0	–	–	–	–	–
4121	45.2 ± 1.9	20.7 ± 1.9	28.8 ± 1.3	20.6 ± 0.5	9.2 ± 0.7	–	–	437.2 ± 2.0	1301.7 ± 6.7	334.7 ± 2.8	3.8 ± 0.5	7.0 ± 0.4	–	14.7 ± 0.4	3.8 ± 3.8
4259	–	–	26.6 ± 5.0	41.7 ± 3.3	21.1 ± 3.5	11.3 ± 3.2	12.2 ± 3.9	453.5 ± 5.7	1386.2 ± 11.5	329.5 ± 3.4	–	–	–	18.5 ± 5.4	–
4263	–	–	–	–	–	–	–	563.7 ± 18.1	1643.9 ± 20.3	398.7 ± 17.9	–	–	–	–	–
4266	–	–	–	26.5 ± 7.2	–	–	–	337.5 ± 7.5	979.8 ± 13.7	300.2 ± 11.0	–	–	–	–	–
4391	–	–	35.2 ± 5.2	37.5 ± 4.9	19.1 ± 4.9	–	–	552.1 ± 7.0	1649.7 ± 13.9	318.1 ± 4.8	–	–	–	27.4 ± 5.1	–
4412	–	–	–	–	–	–	–	513.0 ± 16.5	1451.5 ± 9.7	383.4 ± 12.4	–	–	–	–	–
4416	–	–	–	–	–	–	–	398.3 ± 4.3	1172.1 ± 10.7	260.9 ± 10.1	–	–	–	–	–

Table C.2: Measured properties of the M31 PNe. Each PN should be designated as SPNA<Sl. No.>. E.g. PN 419 should be termed SPNA419.

Sl. No.	RA [J2000] (deg)	DEC [J2000] (deg)	LOSV (km s^{-1})	c(Hβ) (mag)	A$_V$ (mag)	12+log(O/H)	12+log(Ar/H)
419	11.049986	41.9030782	-150.4	0.31	0.65	–	–
478	11.3247088	41.9470492	-223.5	0.68	1.44	8.52 ± 0.01	6.28 ± 0.07
496	11.2640144	41.9713806	-125.7	0.32	0.69	8.68 ± 0.02	6.39 ± 0.05
663	11.6066227	42.2105318	-159.6	0.53	1.12	–	–
729	11.6095294	42.2697161	-25.0	0.26	0.54	–	–
739	11.4832604	42.2826013	-167.9	0.17	0.35	–	–
740	11.8784122	42.2830969	-98.2	0.06	0.12	–	–
749	11.8917535	42.2967133	-82.1	0.39	0.82	–	–
764	11.7527169	42.3140414	-128.6	0.2	0.41	–	–
798	11.4508905	42.3729803	-96.7	0.14	0.3	–	–
820	11.1524821	42.4071436	-75.3	0.16	0.33	–	–
822	11.4281158	42.4136772	-156.4	0.12	0.26	–	–
829	11.5605146	42.4165725	-131.6	0.1	0.21	8.33 ± 0.03	5.64 ± 0.17
831	11.4813787	42.4213275	-62.4	0.12	0.26	–	–
845	11.8816823	42.4384344	-81.0	0.25	0.52	8.6 ± 0.03	6.28 ± 0.15
875	11.5634224	42.488415	-109.1	0.18	0.37	8.06 ± 0.04	5.74 ± 0.11
937	11.5584717	42.6025591	-185.7	0.11	0.23	–	–
942	12.0147552	42.610521	-102.0	0.18	0.37	8.35 ± 0.01	6.02 ± 0.04
945	11.4699967	42.6147482	-174.0	0.09	0.18	8.52 ± 0.01	6.15 ± 0.03
959	11.5577759	42.6747226	-83.8	0.24	0.51	8.7 ± 0.07	6.16 ± 0.04
1041	11.8687874	42.8154351	-152.7	0.0	0.0	–	–
1544	10.8623832	41.0392293	-370.4	0.35	0.74	–	–
1596	10.8335923	41.0902162	-431.8	0.24	0.5	–	–
1605	11.139103	41.1333003	-239.6	0.04	0.09	–	–
1632	10.7606995	41.145227	-291.5	0.39	0.82	8.52 ± 0.0	6.41 ± 0.08
1653	10.8634661	41.1639183	-339.0	0.71	1.49	–	–
1702	11.0391466	41.2183018	-404.2	0.18	0.37	–	–
1714	11.1824381	41.2411017	-316.7	0.17	0.36	8.82 ± 0.04	6.49 ± 0.11
1715	10.9055741	41.2416942	-253.6	0.72	1.52	8.5 ± 0.01	6.34 ± 0.06
1735	10.9996452	41.2598133	-254.4	0.26	0.54	–	–
1740	10.8691402	41.2626319	-355.4	0.13	0.27	8.27 ± 0.02	6.18 ± 0.1
1755	11.1169641	41.2785925	-278.5	0.31	0.65	–	–
1798	10.9679418	41.3141913	-71.0	0.18	0.37	–	–
1808	10.9402807	41.3219796	-293.7	0.14	0.29	–	–
1820	11.1309293	41.3360703	-231.2	0.44	0.92	–	–

Continued on next page

Table C.2 – continued from previous page

Sl. No.	RA [J2000] (deg)	DEC [J2000] (deg)	LOSV (km s^{-1})	c(Hβ) (mag)	A_V (mag)	12+log(O/H)	12+log(Ar/H)
1832	11.0510623	41.3444136	-189.8	0.21	0.43	–	–
1847	10.9842386	41.3705292	-211.0	0.5	1.07	8.41 ± 0.0	6.26 ± 0.05
1853	10.8974998	41.3750905	-84.1	0.11	0.23	8.44 ± 0.01	6.12 ± 0.1
1859	11.2662983	41.380426	-139.0	0.46	0.96	–	–
1862	10.961537	41.3781536	-34.8	0.17	0.35	–	–
1864	11.0090652	41.3808176	-235.4	0.25	0.52	8.42 ± 0.03	6.43 ± 0.14
1872	11.0216923	41.3861244	-217.8	0.85	1.8	8.39 ± 0.02	6.44 ± 0.12
1877	11.2332612	41.3900987	-257.6	0.51	1.08	–	–
1882	11.2778688	41.3932575	-199.4	0.33	0.69	8.5 ± 0.02	5.94 ± 0.11
1897	10.9057644	41.3984839	-136.9	0.18	0.38	–	–
1917	11.0432714	41.4050039	-223.2	0.25	0.53	8.61 ± 0.01	6.44 ± 0.04
1937	11.0558738	41.4183776	-321.6	0.16	0.34	–	–
1945	11.2806851	41.4246141	-191.9	0.19	0.4	–	–
1951	11.0306794	41.4256324	-154.5	0.32	0.69	8.5 ± 0.05	6.23 ± 0.06
1958	11.1651875	41.4280979	-137.8	0.16	0.34	8.43 ± 0.0	6.11 ± 0.07
1960	10.7947476	41.4276811	-96.6	0.19	0.4	8.77 ± 0.05	6.49 ± 0.22
1977	10.7049578	41.4319019	-305.8	0.87	1.83	8.52 ± 0.02	6.2 ± 0.1
1981	10.8857749	41.4378687	-175.8	0.24	0.51	–	–
2018	10.8170892	41.450968	-92.0	0.17	0.37	8.53 ± 0.17	6.46 ± 0.08
2024	11.0402918	41.4534196	-124.7	0.63	1.32	8.62 ± 0.02	6.35 ± 0.06
2030	10.9303735	41.4583543	0.5	0.18	0.39	–	–
2057	10.6873982	41.4653915	-14.6	0.19	0.39	8.41 ± 0.05	6.27 ± 0.11
2063	11.0108582	41.4676458	-45.8	0.2	0.42	8.49 ± 0.06	6.23 ± 0.08
2071	10.6582028	41.4711724	-51.5	0.19	0.4	–	–
2110	11.4510557	41.4930474	-316.7	0.13	0.27	–	–
2113	10.7626204	41.4904456	-223.1	0.22	0.46	8.55 ± 0.01	6.28 ± 0.07
2119	10.8591658	41.4936219	-60.9	0.31	0.66	–	–
2128	11.0550987	41.5026998	-312.6	0.23	0.49	8.39 ± 0.01	6.27 ± 0.08
2157	10.9312989	41.5158059	-118.7	0.12	0.25	8.55 ± 0.03	6.36 ± 0.07
2169	11.0340905	41.5219465	-193.2	0.81	1.7	–	–
2173	10.9507823	41.5239525	4.5	0.22	0.47	8.4 ± 0.02	6.46 ± 0.06
2195	11.0268337	41.5341917	-313.4	0.21	0.43	8.41 ± 0.0	6.15 ± 0.05
2203	11.0398367	41.5374168	12.7	0.75	1.58	–	–
2214	10.961269	41.5476773	-130.3	0.12	0.25	–	–
2232	10.8182846	41.5499013	18.0	0.38	0.81	8.45 ± 0.0	6.28 ± 0.03
2237	11.1095631	41.5541434	-115.8	0.23	0.49	8.46 ± 0.0	6.22 ± 0.04
2238	11.4647891	41.5594643	-101.0	0.16	0.34	–	–
2252	11.143913	41.5581427	-162.4	0.48	1.01	8.29 ± 0.01	6.19 ± 0.03
2273	11.2981024	41.5732953	-24.8	0.15	0.32	–	–

Continued on next page

Table C.2 – continued from previous page

Sl. No.	RA [J2000] (deg)	DEC [J2000] (deg)	LOSV (km s^{-1})	c(Hβ) (mag)	A_V (mag)	12+log(O/H)	12+log(Ar/H)
2275	11.0468256	41.573437	-96.3	0.24	0.51	8.31 ± 0.0	6.25 ± 0.07
2278	10.9294464	41.5753876	-103.2	0.8	1.69	–	–
2294	10.9779358	41.5840582	-75.4	0.31	0.65	–	–
2300	11.2251452	41.5858427	-244.2	0.15	0.32	–	–
2307	11.4628542	41.5883246	-134.7	0.29	0.61	8.61 ± 0.03	6.44 ± 0.06
2314	11.0777639	41.5922701	-22.2	0.49	1.04	–	–
2315	10.9554457	41.592182	-143.9	0.41	0.87	–	–
2329	10.825946	41.6348424	-220.6	0.56	1.17	–	–
2332	10.9854205	41.6360404	-159.6	0.17	0.35	–	–
2333	10.9569119	41.6355284	-76.7	0.3	0.64	8.39 ± 0.04	6.16 ± 0.15
2342	10.9301853	41.6421599	-186.9	0.06	0.14	–	–
2352	10.8997143	41.6488178	-85.8	0.46	0.96	–	–
2357	11.1228878	41.6501043	-76.2	0.54	1.13	–	–
2358	11.3101307	41.6509145	-110.1	0.22	0.47	8.19 ± 0.02	6.15 ± 0.09
2389	11.0392289	41.6665478	-105.7	0.45	0.95	8.61 ± 0.0	6.55 ± 0.06
2404	11.2583102	41.6772304	-117.6	0.35	0.73	–	–
2407	11.0984502	41.6802696	5.9	0.17	0.35	8.39 ± 0.05	6.09 ± 0.11
2432	10.8006179	41.6960284	-150.6	0.48	1.01	–	–
2435	11.0817075	41.699589	-112.4	0.1	0.21	–	–
2450	10.9902447	41.7058517	-187.1	0.73	1.53	–	–
2456	11.0396084	41.7098083	-27.3	0.6	1.26	–	–
2463	11.2227717	41.7177917	-74.3	0.1	0.21	–	–
2469	11.4231437	41.7183825	-208.0	0.66	1.4	–	–
2478	11.4833929	41.721185	-183.6	0.36	0.77	8.52 ± 0.02	6.37 ± 0.05
2481	10.9337653	41.7276836	-214.0	0.57	1.21	–	–
2484	10.8261019	41.7263806	-227.1	0.06	0.13	8.28 ± 0.03	5.9 ± 0.14
2487	11.3120292	41.7294924	-142.1	0.15	0.31	7.67 ± 0.02	–
2495	11.0013958	41.7323594	-116.8	0.19	0.41	8.57 ± 0.0	6.38 ± 0.05
2498	11.0518592	41.7386336	-157.0	0.11	0.24	8.48 ± 0.02	6.31 ± 0.08
2504	11.1152667	41.7412968	-136.5	0.18	0.39	–	–
2509	11.4763287	41.7482662	-104.8	0.01	0.03	–	–
2523	10.8065478	41.7583443	-99.1	0.26	0.56	9.06 ± 0.03	7.15 ± 0.17
2528	11.1221883	41.7614508	-140.4	0.62	1.31	–	–
2534	10.9786909	41.7608276	-225.3	0.77	1.62	8.36 ± 0.02	6.33 ± 0.1
2538	10.8589331	41.7614586	-265.1	0.55	1.15	8.49 ± 0.0	6.32 ± 0.07
2576	11.440781	41.7848392	-88.3	0.38	0.8	–	–
2580	11.0056013	41.7855632	-173.2	0.64	1.35	–	–
2588	11.4034796	41.7889718	-70.5	0.25	0.52	8.35 ± 0.02	6.15 ± 0.15
2601	11.3020296	41.7958139	-89.4	0.67	1.42	8.51 ± 0.03	6.16 ± 0.07

Continued on next page

Table C.2 – continued from previous page

Sl. No.	RA [J2000] (deg)	DEC [J2000] (deg)	LOSV (km s^{-1})	c(Hβ) (mag)	A_V (mag)	12+log(O/H)	12+log(Ar/H)
2636	10.8605861	41.8265177	-204.8	0.66	1.4	8.19 ± 0.02	6.44 ± 0.12
2642	11.4411008	41.829041	-213.5	0.4	0.84	8.55 ± 0.01	6.48 ± 0.04
2644	11.2196758	41.8290874	-185.5	0.31	0.66	8.51 ± 0.03	6.39 ± 0.1
2647	10.9023922	41.8286002	-231.0	0.83	1.75	8.43 ± 0.0	5.99 ± 0.08
2651	11.321112	41.831711	-72.2	0.49	1.03	8.34 ± 0.04	6.31 ± 0.11
2660	10.9879364	41.8401793	-190.7	0.26	0.56	–	–
2661	10.8298883	41.8381438	-222.0	0.96	2.03	–	–
2664	11.1603378	41.8388482	-18.9	0.72	1.51	8.56 ± 0.04	6.33 ± 0.13
2673	11.1799961	41.8470524	-121.7	0.84	1.77	–	–
2674	11.1566107	41.8456148	-160.3	0.47	1.0	8.26 ± 0.02	6.18 ± 0.1
2692	10.5606555	40.8725913	-468.6	0.53	1.13	–	–
2787	10.1577355	40.9792212	-603.4	1.22	2.58	–	–
2793	10.5354773	40.9847293	-390.8	0.08	0.18	–	–
2814	10.5005475	41.0018823	-511.1	0.87	1.84	–	–
2818	10.4657488	41.0091756	-480.5	0.77	1.62	–	–
2837	10.4740205	41.0254486	-607.7	0.77	1.63	8.37 ± 0.02	6.38 ± 0.11
2848	10.5626706	41.0377143	-489.1	0.62	1.31	7.9 ± 0.02	5.82 ± 0.21
2872	10.4911486	41.06398	-496.9	0.99	2.1	–	–
2874	10.529392	41.0623585	-495.7	0.38	0.8	9.36 ± 0.01	7.29 ± 0.08
2878	10.5175981	41.0698018	-479.1	0.88	1.86	–	–
2888	10.4328191	41.0767465	-413.4	0.26	0.55	8.12 ± 0.01	6.15 ± 0.07
2957	10.5091996	41.153178	-539.2	0.54	1.13	9.12 ± 0.02	7.06 ± 0.18
2968	10.5988549	41.156626	-436.2	0.28	0.6	7.62 ± 0.01	5.87 ± 0.1
2982	10.4739792	41.162937	-505.2	0.71	1.5	–	–
2983	10.7201702	41.1606764	-303.7	0.21	0.44	8.21 ± 0.01	6.37 ± 0.09
2993	10.3032602	41.167833	-328.9	0.62	1.31	–	–
2994	10.5905234	41.1653024	-339.5	0.23	0.48	8.39 ± 0.01	–
3001	10.6181175	41.1657129	-322.1	0.28	0.58	8.58 ± 0.0	6.41 ± 0.08
3011	10.0482316	41.1735576	-424.3	0.31	0.66	–	–
3018	10.6358655	41.1707339	-561.6	0.29	0.61	8.48 ± 0.0	6.24 ± 0.05
3031	10.222042	41.1778257	-457.8	0.49	1.04	–	–
3032	10.2047002	41.1801486	-422.4	0.58	1.23	–	–
3047	10.569183	41.1852766	-499.5	0.29	0.61	–	–
3048	10.1338149	41.1884775	-352.4	0.5	1.06	–	–
3064	10.4057661	41.1957358	-523.7	0.85	1.8	–	–
3072	10.262792	41.1994271	-464.4	0.27	0.57	7.1 ± 0.0	5.55 ± 0.06
3075	10.4943323	41.201215	-504.3	0.33	0.7	7.81 ± 0.01	5.84 ± 0.07
3085	10.7159954	41.2041082	-549.7	0.32	0.67	8.1 ± 0.0	5.59 ± 0.07
3102	10.0819926	41.2200601	-342.9	1.17	2.46	7.11 ± 0.01	4.85 ± 0.03

Continued on next page

Table C.2 – continued from previous page

Sl. No.	RA [J2000] (deg)	DEC [J2000] (deg)	LOSV (km s^{-1})	c(Hβ) (mag)	A$_V$ (mag)	12+log(O/H)	12+log(Ar/H)
3146	10.8293256	41.2526803	-107.8	0.21	0.44	8.48 ± 0.01	6.24 ± 0.07
3147	10.8200647	41.254007	-27.1	0.22	0.46	8.28 ± 0.01	6.25 ± 0.12
3162	10.5480599	41.2698115	-314.1	0.56	1.17	9.62 ± 0.17	7.59 ± 0.1
3163	10.5217269	41.2693607	-328.6	0.58	1.22	8.53 ± 0.03	6.24 ± 0.07
3173	10.42889	41.2768965	-332.5	0.28	0.59	–	–
3180	10.409876	41.2838572	-460.4	1.18	2.49	–	–
3188	10.0694187	41.2917681	-358.7	0.22	0.47	–	–
3197	10.3639789	41.3032362	-335.4	0.88	1.85	–	–
3203	10.1822502	41.3111779	-378.3	0.22	0.47	8.25 ± 0.01	6.12 ± 0.09
3214	10.6361605	41.321325	-508.6	0.55	1.15	8.05 ± 0.0	5.8 ± 0.09
3225	10.786926	41.3334441	-364.0	0.26	0.56	–	–
3228	10.6007977	41.336091	-248.1	0.49	1.04	–	–
3235	10.1093167	41.3409845	-349.2	0.26	0.54	8.77 ± 0.0	6.35 ± 0.03
3239	10.8611465	41.3408089	-226.5	0.27	0.57	8.51 ± 0.04	6.34 ± 0.11
3242	10.3502541	41.3466451	-365.1	0.29	0.61	–	–
3256	10.8025234	41.3546212	-132.8	0.4	0.85	8.14 ± 0.07	6.31 ± 0.15
3260	10.1830581	41.3697419	-309.7	0.17	0.36	8.44 ± 0.01	6.18 ± 0.05
3262	10.8524504	41.3677389	-196.7	0.13	0.28	–	–
3273	10.5717313	41.3768411	-260.4	0.33	0.69	–	–
3337	10.4098169	41.4237883	-438.6	0.04	0.07	–	–
3367	10.5523036	41.4380953	-320.4	0.55	1.15	–	–
3373	10.3699112	41.446503	-275.6	0.81	1.7	7.97 ± 0.02	6.22 ± 0.12
3397	10.7445624	41.4631969	-196.7	0.41	0.86	8.65 ± 0.01	6.45 ± 0.07
3406	10.8622041	41.4723637	-144.3	0.19	0.41	8.55 ± 0.01	6.25 ± 0.05
3410	10.3398743	41.4815345	-301.8	0.2	0.43	–	–
3419	10.5283461	41.4916559	-248.0	0.12	0.26	–	–
3420	10.1777585	41.4939555	-276.3	0.15	0.31	–	–
3425	10.7532999	41.5031274	-301.6	0.23	0.49	8.49 ± 0.03	6.33 ± 0.12
3428	10.7758112	41.5053462	-233.0	0.6	1.26	8.49 ± 0.0	6.35 ± 0.06
3429	10.7471311	41.5081283	-259.1	0.43	0.92	8.64 ± 0.0	6.44 ± 0.06
3431	10.6384239	41.5095965	-172.5	1.52	3.2	–	–
3436	10.609369	41.5168601	-347.7	0.46	0.97	–	–
3439	10.592487	41.5232822	-184.1	0.77	1.63	–	–
3444	10.4961312	41.5302328	-271.1	0.14	0.29	–	–
3447	10.2574671	41.5395826	-246.4	0.05	0.11	–	–
3449	10.7187637	41.5488145	-182.2	0.76	1.6	–	–
3451	10.5518682	41.551668	-239.0	0.34	0.72	–	–
3455	10.8010336	41.5543722	-98.3	0.41	0.86	–	–
3456	10.5992212	41.5598848	-390.0	1.12	2.36	–	–

Continued on next page

Table C.2 – continued from previous page

Sl. No.	RA [J2000] (deg)	DEC [J2000] (deg)	LOSV (km s^{-1})	c(Hβ) (mag)	A$_V$ (mag)	12+log(O/H)	12+log(Ar/H)
3472	10.5413612	41.5943667	-330.7	0.34	0.72	8.5 ± 0.03	6.37 ± 0.12
3473	10.665413	41.5942058	-302.0	0.66	1.39	–	–
3474	10.8036376	41.5914072	-192.1	0.46	0.98	–	–
3477	10.4209291	41.6374848	-4.3	0.46	0.96	8.86 ± 0.04	6.48 ± 0.04
3480	10.5708199	41.6428633	-43.8	0.21	0.43	8.44 ± 0.0	6.48 ± 0.08
3490	10.5630273	41.6527436	-330.6	0.45	0.95	8.62 ± 0.01	6.43 ± 0.06
3499	10.3322717	41.6860064	-357.8	0.04	0.08	–	–
3660	9.4166837	40.1476529	-498.5	0.15	0.31	–	–
3664	9.8194243	40.1621922	-454.6	0.02	0.04	–	–
3671	9.9424013	40.1840678	-426.1	0.46	0.97	8.95 ± 0.04	6.46 ± 0.09
3688	9.9182428	40.2235053	-458.5	0.46	0.97	8.59 ± 0.02	6.34 ± 0.13
3697	9.7775575	40.2499615	-560.0	0.82	1.72	8.6 ± 0.01	6.1 ± 0.03
3700	9.5094188	40.2525583	-462.1	0.44	0.92	8.55 ± 0.02	6.07 ± 0.05
3702	9.3654581	40.259104	-500.7	0.51	1.07	–	–
3708	9.6419536	40.2656855	-510.9	0.62	1.31	–	–
3710	9.5321447	40.263699	-538.4	0.46	0.98	8.59 ± 0.0	6.32 ± 0.03
3716	10.0260225	40.2911886	-495.1	0.36	0.76	–	–
3717	9.9027979	40.2975378	-512.7	0.53	1.11	8.66 ± 0.01	6.3 ± 0.07
3721	9.6837885	40.3262157	-519.4	0.2	0.42	–	–
3742	9.7605584	40.380635	-525.3	0.9	1.91	8.8 ± -0.01	6.36 ± 0.07
3751	9.8169925	40.3999352	-542.4	1.02	2.15	–	–
3759	9.7474262	40.4246766	-473.3	1.33	2.8	–	–
3762	9.8198847	40.4376357	-463.7	0.62	1.3	–	–
3770	9.798285	40.4446673	-454.2	0.55	1.16	8.7 ± 0.0	6.51 ± 0.03
3773	9.6539862	40.4500222	-506.8	0.28	0.6	–	–
3780	10.0868701	40.469069	-510.4	0.47	0.99	8.47 ± 0.0	6.18 ± 0.05
3782	9.4008457	40.4672397	-435.6	0.51	1.08	8.54 ± 0.01	6.23 ± 0.06
3784	10.0552325	40.4746362	-568.2	0.37	0.79	–	–
3793	9.974131	40.4928321	-557.7	0.83	1.75	8.48 ± 0.01	5.93 ± 0.07
3795	9.8905295	40.4969385	-486.3	0.99	2.09	–	–
3802	9.6108538	40.5122516	-465.2	0.14	0.28	–	–
3805	9.9312591	40.5133834	-561.0	0.82	1.74	8.57 ± 0.01	6.43 ± 0.08
3811	9.776381	40.5188924	-512.5	0.23	0.49	–	–
3814	9.9391574	40.5284861	-543.7	0.75	1.58	8.66 ± 0.04	6.45 ± 0.05
3818	9.6617663	40.5345836	-531.8	0.18	0.38	–	–
3833	9.9368072	40.5643302	-476.1	0.35	0.74	–	–
3844	10.4352568	40.6172979	-443.9	0.21	0.44	–	–
3854	9.8557968	40.6404836	-487.1	0.2	0.41	–	–
3864	10.2066804	40.6628447	-415.3	0.35	0.74	8.56 ± 0.01	6.44 ± 0.08

Continued on next page

Table C.2 – continued from previous page

Sl. No.	RA [J2000] (deg)	DEC [J2000] (deg)	LOSV (km s^{-1})	c(Hβ) (mag)	A$_V$ (mag)	12+log(O/H)	12+log(Ar/H)
3876	10.2656028	40.6869321	-574.7	0.44	0.93	–	–
3881	10.2396822	40.6940349	-529.3	0.8	1.68	–	–
3885	9.9932988	40.6996647	-515.3	0.76	1.61	8.43 ± 0.01	6.16 ± 0.07
3892	9.971516	40.7082416	-562.5	0.46	0.97	–	–
3897	9.9316859	40.7124144	-549.2	0.5	1.06	–	–
3902	10.3977902	40.7189793	-597.3	0.45	0.96	–	–
3907	9.536849	40.7197905	-443.3	0.17	0.35	–	–
3914	9.5179781	40.7287152	-499.6	0.31	0.65	–	–
3923	9.7063105	40.7403683	-550.3	0.25	0.52	8.59 ± 0.02	6.35 ± 0.11
3925	10.4060083	40.7425433	-363.3	0.81	1.7	–	–
3939	9.8216325	40.7535695	-562.3	0.14	0.3	–	–
3941	9.7015565	40.7587971	-427.3	0.37	0.77	–	–
3942	10.5551037	40.7596958	-438.5	0.47	0.99	–	–
3945	9.7759626	40.757653	-436.1	0.43	0.9	–	–
3952	9.9793703	40.7644089	-514.5	0.9	1.91	8.63 ± 0.01	6.48 ± 0.1
3979	9.9880621	40.7950027	-469.2	0.22	0.47	–	–
4002	9.8447539	40.8123215	-567.7	0.75	1.58	8.83 ± 0.01	6.42 ± 0.1
4008	9.9292168	40.8143389	-514.2	1.11	2.34	8.39 ± 0.05	6.11 ± 0.07
4015	9.8938176	40.8201111	-413.3	0.15	0.32	8.48 ± 0.0	6.21 ± 0.05
4016	9.8809426	40.8215601	-421.7	0.15	0.31	–	–
4025	10.0258875	40.8302985	-387.9	0.49	1.03	–	–
4031	9.3380766	39.8473296	-522.4	0.3	0.62	8.49 ± 0.03	6.23 ± 0.1
4046	9.2941791	39.9478383	-530.5	0.22	0.47	–	–
4053	9.2054541	40.0037235	-501.3	0.2	0.42	8.7 ± 0.01	6.11 ± 0.05
4068	9.4357764	40.1193703	-534.5	0.15	0.31	8.72 ± 0.0	6.3 ± 0.04
4094	9.2683848	40.2372087	-430.4	0.52	1.1	8.22 ± 0.0	6.09 ± 0.07
4107	9.4070438	40.3392368	-469.0	0.47	0.99	–	–
4118	9.328285	40.3916823	-500.5	0.08	0.16	–	–
4121	9.3220664	40.4104646	-513.3	0.33	0.7	8.64 ± 0.06	6.09 ± 0.05
4259	9.4872608	39.7457804	-520.7	0.24	0.51	8.23 ± 0.01	6.29 ± 0.11
4263	9.567648	39.7870102	-529.9	0.48	1.02	–	–
4266	9.6720787	39.7946121	-537.0	0.19	0.39	–	–
4391	9.3170891	39.7920578	-450.9	0.2	0.43	8.44 ± 0.03	6.11 ± 0.13
4412	9.3077834	39.807575	-438.8	0.43	0.91	–	–
4416	9.4366892	39.9761627	-518.8	0.24	0.51	–	–

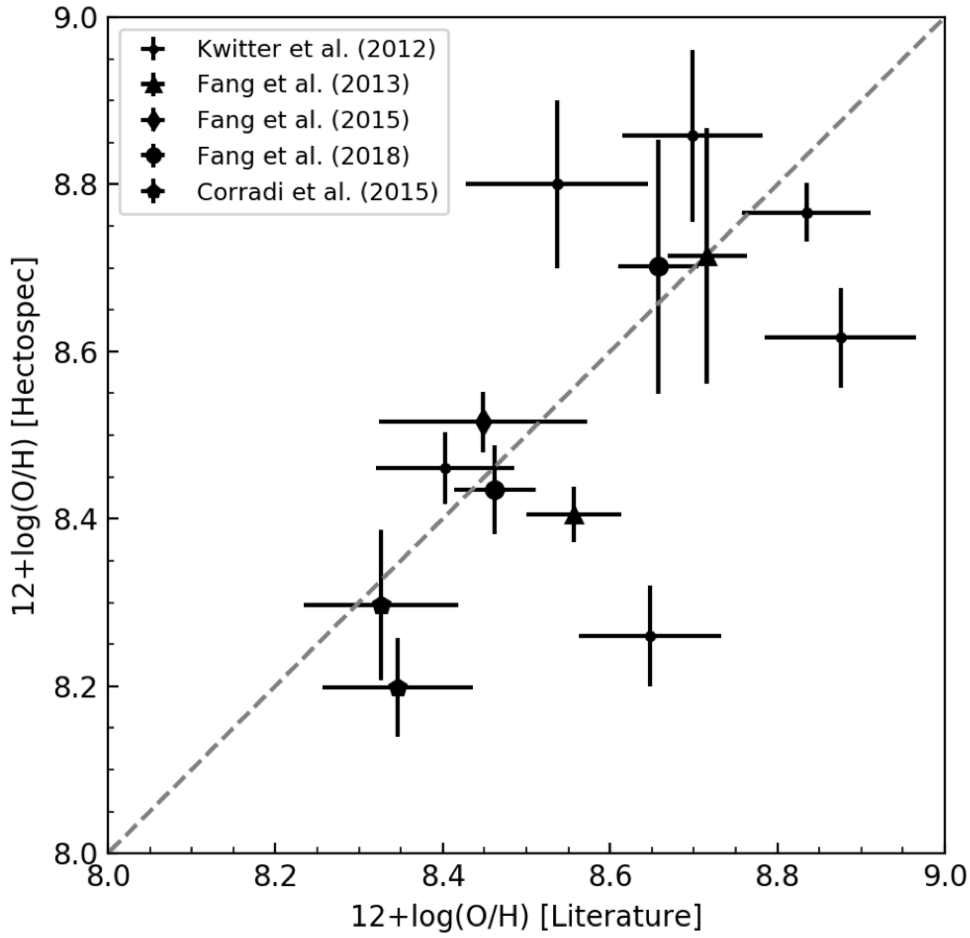

Figure C.1: Comparison of the oxygen abundances measured with Hectospec (in this work and San+12) with those measured in the literature for the PNe in common. The PNe studied by different authors are marked with different symbols. The dotted line shows the 1:1 line.

C.2 Comparison with Literature

Figure C.1 compares the oxygen abundances measured for PNe observed in this work which have oxygen abundances measurements in the literature (Kwitter et al. 2012; Corradi et al. 2015; Fang et al. 2013, 2015, 2018). While most of the oxygen abundances values agree with each other, scatter is particularly evident for the PNe in common with Kwitter et al. (2012). This likely stems from the use of the different ICFs employed to measure the abundances. The ICFs by Delgado-Inglada et al. (2014), used in this work, have been shown to be an improvement over previous ICF determinations over a large sample of observed MW PNe.

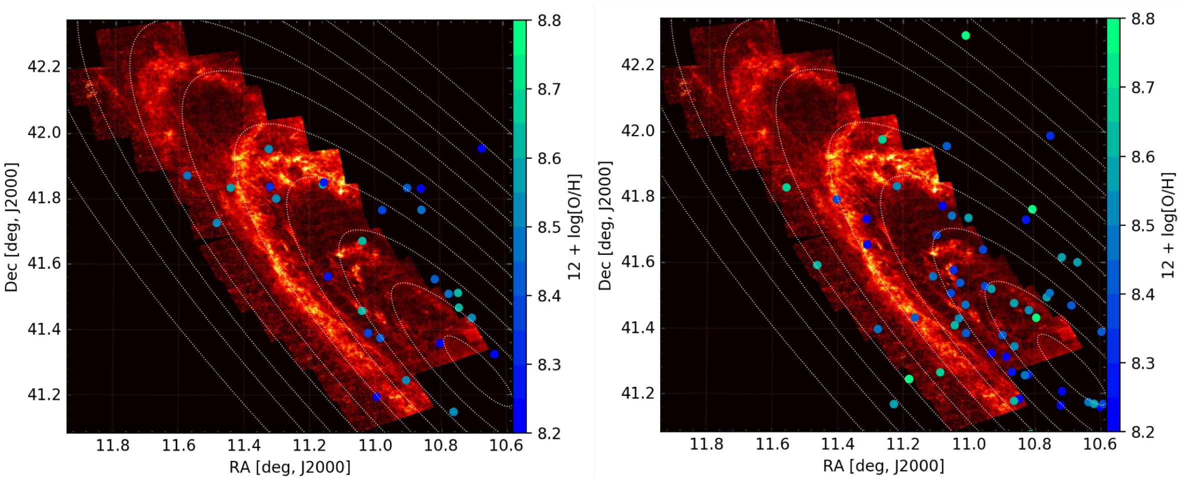

Figure C.2: The high- [left] and low- [right] extinction PNe are overplotted, coloured by their oxygen abundance, on the extinction map of the PHAT data derived by Dalcanton et al. (2015). The region in black is outside the PHAT footprint.

C.3 Effect of dust attenuation on measured abundances

Figure C.2 shows the extinction map in the M 31 PHAT footprint derived by Dalcanton et al. (2015, see their Fig 21). The extinction varies between A_V=0 (light red) to A_V=4 (yellow). We find that there are very few PNe with oxygen abundances measured for the most extincted regions in the PHAT footprint. The measured oxygen abundance values also show no obvious spatial correlation with insterstellar extinction in M 31. In Paper II, we also noted that the dust in M 31 is unrelated to the extinction classification of the PNe.

Bibliography

Acker, A., Marcout, J., Ochsenbein, F., et al. 1992, The Strasbourg-ESO Catalogue of Galactic Planetary Nebulae. Parts I, II.

Aller, L. H. 1942, ApJ, 95, 52

Aniyan, S., Freeman, K. C., Arnaboldi, M., et al. 2018, MNRAS, 476, 1909

Aniyan, S., Freeman, K. C., Gerhard, O. E., Arnaboldi, M., & Flynn, C. 2016, MNRAS, 456, 1484

Antoja, T., Helmi, A., Romero-Gómez, M., et al. 2018, Nature, 561, 360

Arnaboldi, M., Aguerri, J. A. L., Napolitano, N. R., et al. 2002, AJ, 123, 760

Arnaboldi, M., Freeman, K. C., Gerhard, O., et al. 1998, ApJ, 507, 759

Arnaboldi, M., Freeman, K. C., Mendez, R. H., et al. 1996, ApJ, 472, 145

Arnaboldi, M., Freeman, K. C., Okamura, S., et al. 2003, AJ, 125, 514

Arp, H. 1964, ApJ, 139, 1045

Asplund, M., Grevesse, N., Sauval, A. J., & Scott, P. 2009, ARA&A, 47, 481

Barmby, P., Ashby, M. L. N., Bianchi, L., et al. 2006, ApJ, 650, L45

Beckwith, S. V. W., Stiavelli, M., Koekemoer, A. M., et al. 2006, AJ, 132, 1729

Belokurov, V., Erkal, D., Evans, N. W., Koposov, S. E., & Deason, A. J. 2018, MNRAS, 478, 611

Berendzen, R. & Hoskin, M. 1971, Leaflet of the Astronomical Society of the Pacific, 10, 425

Bernard, E. J., Ferguson, A. M. N., Richardson, J. C., et al. 2015, MNRAS, 446, 2789

Bershady, M. A., Verheijen, M. A. W., Westfall, K. B., et al. 2010, ApJ, 716, 234

Bertin, E. & Arnouts, S. 1996, Astronomy and Astrophysics Supplement Series, 117, 393

Bertin, E., Mellier, Y., Radovich, M., et al. 2002, in Astronomical Data Analysis Software and Systems XI, ed. D. A. Bohlender, D. Durand, & T. H. Handley, Vol. 281, 228

Bhattacharya, S., Arnaboldi, M., Hartke, J., et al. 2019a, A&A, 624, A132

Bhattacharya, S., Arnaboldi, M., Caldwell, N., et al. 2019b, A&A, 631, A56

Bílek, M., Duc, P.-A., Cuilland re, J.-C., et al. 2020, MNRAS[[arXiv]2007.13772]

Blaña, M., Gerhard, O., Wegg, C., et al. 2018, MNRAS, 481, 3210

Bland-Hawthorn, J. & Gerhard, O. 2016, Annual Review of Astronomy and Astrophysics, 54, 529

Bond, J. R., Kofman, L., & Pogosyan, D. 1996, Nature, 380, 603

Bonnarel, F., Fernique, P., Bienaymé, O., et al. 2000, Astronomy and Astrophysics Supplement Series, 143, 33

Boulade, O., Charlot, X., Abbon, P., et al. 2003, in Instrument Design and Performance for Optical/Infrared Ground-based Telescopes, ed. M. Iye & A. F. M. Moorwood, Vol. 4841, 72–81

Bovy, J., Rix, H.-W., & Hogg, D. W. 2012, ApJ, 751, 131

Braun, R., Oosterloo, T. A., Morganti, R., Klein, U., & Beck, R. 2007, A&A, 461, 455

Bresolin, F., Stasińska, G., Vílchez, J. M., Simon, J. D., & Rosolowsky, E. 2010, MNRAS, 404, 1679

Brooks, A. & Christensen, C. 2016, Astrophysics and Space Science Library, Vol. 418, Bulge Formation via Mergers in Cosmological Simulations, ed. E. Laurikainen, R. Peletier, & D. Gadotti, 317

Bullock, J. S. & Johnston, K. V. 2005, ApJ, 635, 931

Buzzoni, A., Arnaboldi, M., & Corradi, R. L. M. 2006, MNRAS, 368, 877

Caldwell, N., Harding, P., Morrison, H., et al. 2009, AJ, 137, 94

Cardelli, J. A., Clayton, G. C., & Mathis, J. S. 1989, ApJ, 345, 245

Casagrande, L., Schönrich, R., Asplund, M., et al. 2011, A&A, 530, A138

Chemin, L., Carignan, C., & Foster, T. 2009, ApJ, 705, 1395

Ciardullo, R. 2010, Publications of the Astronomical Society of Australia, 27, 149

Ciardullo, R., Durrell, P. R., Laychak, M. B., et al. 2004, ApJ, 614, 167

Ciardullo, R., Feldmeier, J. J., Jacoby, G. H., et al. 2002, ApJ, 577, 31

Ciardullo, R., Gronwall, C., Adams, J. J., et al. 2013, ApJ, 769, 83

Ciardullo, R. & Jacoby, G. H. 1992, ApJ, 388, 268

Ciardullo, R. & Jacoby, G. H. 1999, ApJ, 515, 191

Ciardullo, R., Jacoby, G. H., Ford, H. C., & Neill, J. D. 1989, ApJ, 339, 53

Ciardullo, R., Sigurdsson, S., Feldmeier, J. J., & Jacoby, G. H. 2005, ApJ, 629, 499

Coccato, L., Gerhard, O., Arnaboldi, M., et al. 2009, MNRAS, 394, 1249

Cole, S., Percival, W. J., Peacock, J. A., et al. 2005, MNRAS, 362, 505

Colless, M., Ellis, R. S., Taylor, K., & Hook, R. N. 1990, MNRAS, 244, 408

Comerón, S., Salo, H., Knapen, J. H., & Peletier, R. F. 2019, A&A, 623, A89

Conn, A. R., McMonigal, B., Bate, N. F., et al. 2016, MNRAS, 458, 3282

Corradi, R. L. M., Kwitter, K. B., Balick, B., Henry, R. B. C., & Hensley, K. 2015, ApJ, 807, 181

Cortesi, A., Arnaboldi, M., Coccato, L., et al. 2013, A&A, 549, A115

Courteau, S., Cappellari, M., de Jong, R. S., et al. 2014, Reviews of Modern Physics, 86, 47

Courteau, S., Widrow, L. M., McDonald, M., et al. 2011, ApJ, 739, 20

Crnojević, D., Sand, D. J., Spekkens, K., et al. 2016, ApJ, 823, 19

Dalcanton, J. J., Fouesneau, M., Hogg, D. W., et al. 2015, ApJ, 814, 3

Dalcanton, J. J., Williams, B. F., Lang, D., et al. 2012, The Astrophysical Journal Supplement Series, 200, 18

Daniel, K. J. & Wyse, R. F. G. 2018, MNRAS, 476, 1561

Davis, B. D., Ciardullo, R., Jacoby, G. H., Feldmeier, J. J., & Indahl, B. L. 2018, ApJ, 863, 189

De Lucia, G., Springel, V., White, S. D. M., Croton, D., & Kauffmann, G. 2006, MNRAS, 366, 499

Delgado-Inglada, G., Morisset, C., & Stasińska, G. 2014, MNRAS, 440, 536

Delgado-Inglada, G., Rodríguez, M., Peimbert, M., Stasińska, G., & Morisset, C. 2015, MNRAS, 449, 1797

Delhaye, J. 1965, Solar Motion and Velocity Distribution of Common Stars (University of Chicago Press, Chicago, ILL USA), 61

Dopita, M. A., Jacoby, G. H., & Vassiliadis, E. 1992, ApJ, 389, 27

Dorman, C. E., Guhathakurta, P., Fardal, M. A., et al. 2012, ApJ, 752, 147

Dorman, C. E., Guhathakurta, P., Seth, A. C., et al. 2015, ApJ, 803, 24

Douglas, N. G., Arnaboldi, M., Freeman, K. C., et al. 2002, Publications of the Astronomical Society of the Pacific, 114, 1234

Draine, B. T., Aniano, G., Krause, O., et al. 2014, ApJ, 780, 172

D'Souza, R. & Bell, E. F. 2018a, Nature Astronomy, 2, 737

D'Souza, R. & Bell, E. F. 2018b, MNRAS, 474, 5300

Dubois, Y., Peirani, S., Pichon, C., et al. 2016, MNRAS, 463, 3948

Eisenstein, D. J., Zehavi, I., Hogg, D. W., et al. 2005, ApJ, 633, 560

Escala, I., Gilbert, K. M., Kirby, E. N., et al. 2020, ApJ, 889, 177

Esteban, C., Bresolin, F., García-Rojas, J., & Toribio San Cipriano, L. 2020, MNRAS, 491, 2137

Fabricant, D., Fata, R., Roll, J., et al. 2005, Publications of the Astronomical Society of the Pacific, 117, 1411

Fang, X., García-Benito, R., Guerrero, M. A., et al. 2015, ApJ, 815, 69

Fang, X., García-Benito, R., Guerrero, M. A., et al. 2018, ApJ, 853, 50

Fang, X., Zhang, Y., García-Benito, R., Liu, X. W., & Yuan, H. B. 2013, ApJ, 774, 138

Fardal, M. A., Babul, A., Geehan, J. J., & Guhathakurta, P. 2006, MNRAS, 366, 1012

Fardal, M. A., Guhathakurta, P., Babul, A., & McConnachie, A. W. 2007, MNRAS, 380, 15

Fardal, M. A., Weinberg, M. D., Babul, A., et al. 2013, MNRAS, 434, 2779

Ferguson, A. M. N., Irwin, M. J., Ibata, R. A., Lewis, G. F., & Tanvir, N. R. 2002, AJ, 124, 1452

Ferguson, A. M. N. & Mackey, A. D. 2016, in Tidal Streams in the Local Group and Beyond, ed. H. J. Newberg & J. L. Carlin, Vol. 420, 191

Ferland, G. J., Korista, K. T., Verner, D. A., et al. 1998, Publications of the Astronomical Society of the Pacific, 110, 761

Firmani, C. & Avila-Reese, V. 2000, MNRAS, 315, 457

Fragkoudi, F., Grand, R. J. J., Pakmor, R., et al. 2020, MNRAS, 494, 5936

Frew, D. J., Bojičić, I. S., & Parker, Q. A. 2013, MNRAS, 431, 2

Gaia Collaboration, Brown, A. G. A., Vallenari, A., et al. 2018, A&A, 616, A1

García-Hernández, D. A., Ventura, P., Delgado-Inglada, G., et al. 2016, MNRAS, 458, L118

Geha, M., Wechsler, R. H., Mao, Y.-Y., et al. 2017, ApJ, 847, 4

Gesicki, K., Zijlstra, A. A., & Miller Bertolami, M. M. 2018, Nature Astronomy, 2, 580

Gibson, B. K., Pilkington, K., Brook, C. B., Stinson, G. S., & Bailin, J. 2013, A&A, 554, A47

Gilmore, G. & Reid, N. 1983, MNRAS, 202, 1025

Gonçalves, D. R. 2019, in IAU Symposium, Vol. 344, Dwarf Galaxies: From the Deep Universe to the Present, ed. K. B. W. McQuinn & S. Stierwalt, 161–177

Grand, R. J. J., Gómez, F. A., Marinacci, F., et al. 2017, MNRAS, 467, 179

Grand, R. J. J., Kawata, D., Belokurov, V., et al. 2020, MNRAS[[arXiv]2001.06009]

Gregersen, D., Seth, A. C., Williams, B. F., et al. 2015, AJ, 150, 189

Guhathakurta, P., Ostheimer, J. C., Gilbert, K. M., et al. 2005, arXiv e-prints [astro-ph/0502366]

Guhathakurta, P., Rich, R. M., Reitzel, D. B., et al. 2006, AJ, 131, 2497

Hammer, F., Flores, H., Lilly, S. J., et al. 1997, ApJ, 481, 49

Hammer, F., Yang, Y. B., Wang, J. L., et al. 2018, MNRAS, 475, 2754

Harmsen, B., Monachesi, A., Bell, E. F., et al. 2017, MNRAS, 466, 1491

Hartke, J., Arnaboldi, M., Gerhard, O., et al. 2018, A&A, 616, A123

Hartke, J., Arnaboldi, M., Longobardi, A., et al. 2017, A&A, 603, A104

Helmi, A., Babusiaux, C., Koppelman, H. H., et al. 2018, Nature, 563, 85

Henize, K. G. & Westerlund, B. E. 1963, ApJ, 137, 747

Hernández-Martínez, L., Carigi, L., Peña, M., & Peimbert, M. 2011, A&A, 535, A118

Hernández-Martínez, L. & Peña, M. 2009, A&A, 495, 447

Herrmann, K. A., Ciardullo, R., Feldmeier, J. J., & Vinciguerra, M. 2008, ApJ, 683, 630

Herwig, F. 2005, ARA&A, 43, 435

Hogg, D. W., Cohen, J. G., Blandford, R., & Pahre, M. A. 1998, ApJ, 504, 622

Hopkins, P. F., Cox, T. J., Younger, J. D., & Hernquist, L. 2009, ApJ, 691, 1168

Hopkins, P. F., Hernquist, L., Cox, T. J., Younger, J. D., & Besla, G. 2008, ApJ, 688, 757

House, E. L., Brook, C. B., Gibson, B. K., et al. 2011, MNRAS, 415, 2652

Hubble, E. P. 1926, ApJ, 64, 321

Hubble, E. P. 1929, ApJ, 69, 103

Hubble, E. P. 1936, Realm of the Nebulae

Hui, X., Ford, H. C., Freeman, K. C., & Dopita, M. A. 1995, ApJ, 449, 592

Huxor, A. P., Mackey, A. D., Ferguson, A. M. N., et al. 2014, MNRAS, 442, 2165

Ibata, R., Chapman, S., Ferguson, A. M. N., et al. 2005, ApJ, 634, 287

Ibata, R., Irwin, M., Lewis, G., Ferguson, A. M. N., & Tanvir, N. 2001, Nature, 412, 49

Ibata, R. A., Gilmore, G., & Irwin, M. J. 1994, Nature, 370, 194

Ibata, R. A., Lewis, G. F., McConnachie, A. W., et al. 2014, ApJ, 780, 128

Irwin, M. J., Ferguson, A. M. N., Ibata, R. A., Lewis, G. F., & Tanvir, N. R. 2005, ApJ, 628, L105

Izzard, R. G., Glebbeek, E., Stancliffe, R. J., & Pols, O. R. 2009, A&A, 508, 1359

Jacoby, G. H. 1980, The Astrophysical Journal Supplement Series, 42, 1

Jacoby, G. H. 1989, ApJ, 339, 39

Jacoby, G. H., Ciardullo, R., De Marco, O., et al. 2013, ApJ, 769, 10

Jacoby, G. H. & De Marco, O. 2002, AJ, 123, 269

Jacoby, G. H., De Marco, O., Davies, J., et al. 2017, ApJ, 836, 93

Jekel, C. F. & Venter, G. 2019, pwlf: A Python Library for Fitting 1D Continuous Piecewise Linear Functions

Johnston, K. V., Bullock, J. S., Sharma, S., et al. 2008, ApJ, 689, 936

Jones, D. & Boffin, H. M. J. 2017, Nature Astronomy, 1, 0117

Kam, S. Z., Carignan, C., Chemin, L., et al. 2017, AJ, 154, 41

Karademir, G. S., Remus, R.-S., Burkert, A., et al. 2019, MNRAS, 487, 318

Kennicutt, R. C., Calzetti, D., Aniano, G., et al. 2011, PASP, 123, 1347

Kirby, E. N., Lanfranchi, G. A., Simon, J. D., Cohen, J. G., & Guhathakurta, P. 2011, ApJ, 727, 78

Kovacevic, A. V., Parker, Q. A., Jacoby, G. H., et al. 2011, MNRAS, 414, 860

Kummell, C. H. 1879, The Analyst, 6, 97

Kwitter, K. B., Lehman, E. M. M., Balick, B., & Henry, R. B. C. 2012, ApJ, 753, 12

Leavitt, H. S. 1908, Annals of Harvard College Observatory, 60, 87

Lewis, P. A. W. 1961, Ann. Math. Statist., 32, 1118

Li, A., Li, Z., Dong, H., Fang, X., & Xu, X. 2018, ArXiv e-prints, arXiv:1805.12092

Lindblad, P. A. B., Lindblad, P. O., & Athanassoula, E. 1996, A&A, 313, 65

Longobardi, A., Arnaboldi, M., Gerhard, O., et al. 2013, A&A, 558, A42

Longobardi, A., Arnaboldi, M., Gerhard, O., & Hanuschik, R. 2015, A&A, 579, A135

Mackey, A. D., Huxor, A. P., Ferguson, A. M. N., et al. 2010, ApJ, 717, L11

Magnier, E. A. & Cuillandre, J. C. 2004, Publications of the Astronomical Society of the Pacific, 116, 449

Magrini, L., Coccato, L., Stanghellini, L., Casasola, V., & Galli, D. 2016, A&A, 588, A91

Magrini, L., Stanghellini, L., & Villaver, E. 2009, ApJ, 696, 729

Majaess, D. 2010, Acta Astron., 60, 55

Mancillas, B., Duc, P.-A., Combes, F., et al. 2019, A&A, 632, A122

Marigo, P., Girardi, L., Weiss, A., Groenewegen, M. A. T., & Chiosi, C. 2004, A&A, 423, 995

Marmo, C. & Bertin, E. 2008, in Astronomical Data Analysis Software and Systems XVII, ed. R. W. Argyle, P. S. Bunclark, & J. R. Lewis, Vol. 394, 619

Martig, M., Minchev, I., & Flynn, C. 2014, MNRAS, 443, 2452

Martin, T. B., Drissen, L., & Melchior, A.-L. 2018, MNRAS, 473, 4130

Martínez-Delgado, D., Gabany, R. J., Crawford, K., et al. 2010, AJ, 140, 962

McConnachie, A. W., Ibata, R., Martin, N., et al. 2018, ApJ, 868, 55

McConnachie, A. W., Irwin, M. J., Ibata, R. A., et al. 2009, Nature, 461, 66

Méndez, R. H., Riffeser, A., Kudritzki, R. P., et al. 2001, ApJ, 563, 135

Méndez, R. H., Teodorescu, A. M., Schönberner, D., Jacob, R., & Steffen, M. 2008, ApJ, 681, 325

Merrett, H. R., Kuijken, K., Merrifield, M. R., et al. 2003, MNRAS, 346, L62

Merrett, H. R., Merrifield, M. R., Douglas, N. G., et al. 2006, MNRAS, 369, 120

Mestel, L. 1963, MNRAS, 126, 553

Mihos, J. C., Harding, P., Feldmeier, J., & Morrison, H. 2005, ApJ, 631, L41

Mikołajewska, J., Caldwell, N., & Shara, M. M. 2014, MNRAS, 444, 586

Milingo, J. B., Kwitter, K. B., Henry, R. B. C., & Souza, S. P. 2010, ApJ, 711, 619

Miller Bertolami, M. M. 2016, A&A, 588, A25

Mohd Razali, N. & Yap, B. 2011, J. Stat. Model. Analytics, 2

Mollá, M., Díaz, Á. I., Cavichia, O., et al. 2019, MNRAS, 482, 3071

Monachesi, A., Bell, E. F., Radburn-Smith, D. J., et al. 2016, MNRAS, 457, 1419

Naidu, R. P., Conroy, C., Bonaca, A., et al. 2020, arXiv e-prints, arXiv:2006.08625

Newville, M., Stensitzki, T., Allen, D. B., & Ingargiola, A. 2014, LMFIT: Non-Linear Least-Square Minimization and Curve-Fitting for Python

Nidever, D. L., Hasselquist, S., Hayes, C. R., et al. 2020, ApJ, 895, 88

Nomoto, K., Kobayashi, C., & Tominaga, N. 2013, ARA&A, 51, 457

Nordström, B., Mayor, M., Andersen, J., et al. 2004, A&A, 418, 989

Oke, J. B. & Gunn, J. E. 1983, ApJ, 266, 713

Oser, L., Ostriker, J. P., Naab, T., Johansson, P. H., & Burkert, A. 2010, ApJ, 725, 2312

Osterbrock, D. E. & Ferland, G. J. 2006, Astrophysics of gaseous nebulae and active galactic nuclei

Ostriker, J. P. & Peebles, P. J. E. 1973, ApJ, 186, 467

Pagel, B. E. J. & Edmunds, M. G. 1981, ARA&A, 19, 77

Pastorello, N., Sarzi, M., Cappellari, M., et al. 2013, MNRAS, 430, 1219

Peña, M. & Flores-Durán, S. N. 2019, Rev. Mexicana Astron. Astrofis., 55, 255

Peña, M., Richer, M. G., & Stasińska, G. 2007, A&A, 466, 75

Peebles, P. J. E. & Yu, J. T. 1970, ApJ, 162, 815

Perez, J., Michel-Dansac, L., & Tissera, P. B. 2011, MNRAS, 417, 580

Pfeffer, J., Kruijssen, J. M. D., Crain, R. A., & Bastian, N. 2018, MNRAS, 475, 4309

Pillepich, A., Springel, V., Nelson, D., et al. 2018, MNRAS, 473, 4077

Planck Collaboration, Ade, P. A. R., Aghanim, N., et al. 2014, A&A, 571, A1

Planck Collaboration, Aghanim, N., Akrami, Y., et al. 2018, arXiv e-prints, arXiv:1807.06209

Pulsoni, C., Gerhard, O., Arnaboldi, M., et al. 2018, A&A, 618, A94

Quinn, P. J. & Goodman, J. 1986, ApJ, 309, 472

Quirk, A., Guhathakurta, P., Chemin, L., et al. 2019, ApJ, 871, 11

Reid, W. A. & Parker, Q. A. 2010, MNRAS, 405, 1349

Rich, R. M., Mosenkov, A., Lee-Saunders, H., et al. 2019, MNRAS, 490, 1539

Richardson, J. C., Ferguson, A. M. N., Johnson, R. A., et al. 2008, AJ, 135, 1998

Roberts, M. S. 1966, ApJ, 144, 639

Rodríguez-González, A., Hernández-Martínez, L., Esquivel, A., et al. 2015, A&A, 575, A1

Rubin, V. C. & Ford, W. Kent, J. 1970, ApJ, 159, 379

Ruiz-Lara, T., Few, C. G., Florido, E., et al. 2017, A&A, 608, A126

Rupke, D. S. N., Kewley, L. J., & Barnes, J. E. 2010, ApJ, 710, L156

Saglia, R. P., Opitsch, M., Fabricius, M. H., et al. 2018, A&A, 618, A156

Salaris, M. & Cassisi, S. 2005, Evolution of Stars and Stellar Populations

Sánchez, S. F. 2020, ARA&A, 58, annurev

Sánchez-Menguiano, L., Sánchez, S. F., Pérez, I., et al. 2018, A&A, 609, A119

Sanders, N. E., Caldwell, N., McDowell, J., & Harding, P. 2012, ApJ, 758, 133

Scannapieco, C., Wadepuhl, M., Parry, O. H., et al. 2012, MNRAS, 423, 1726

Schaye, J., Crain, R. A., Bower, R. G., et al. 2015, MNRAS, 446, 521

Schlegel, D. J., Finkbeiner, D. P., & Davis, M. 1998, ApJ, 500, 525

Scholz, F. W. & Stephens, M. A. 1987, Journal of the American Statistical Association, 82, 918

Schwarz, G. 1978, The Annals of Statistics, 6, 461

Sellwood, J. A. 2014, Reviews of Modern Physics, 86, 1

Seo, H.-J. & Eisenstein, D. J. 2003, ApJ, 598, 720

Silk, J. 1977, ApJ, 211, 638

Snoek, J., Larochelle, H., & Adams, R. P. 2012, arXiv e-prints, arXiv:1206.2944

Stanghellini, L. & Haywood, M. 2018, ApJ, 862, 45

Stanghellini, L., Magrini, L., Casasola, V., & Villaver, E. 2014, A&A, 567, A88

Straughn, A. N., Cohen, S. H., Ryan, R. E., et al. 2006, ApJ, 639, 724

Strömberg, G. 1925, ApJ, 61, 363

Strömberg, G. 1946, ApJ, 104, 12

Tanaka, M., Chiba, M., Komiyama, Y., et al. 2010, ApJ, 708, 1168

Teklu, A. F., Remus, R.-S., Dolag, K., et al. 2015, ApJ, 812, 29

Tempel, E., Tamm, A., & Tenjes, P. 2010, A&A, 509, A91

Teplitz, H. I., Malkan, M. A., Steidel, C. C., et al. 2000, ApJ, 542, 18

Tissera, P. B., Rosas-Guevara, Y., Bower, R. G., et al. 2019, MNRAS, 482, 2208

Toomre, A. 1977, in Evolution of Galaxies and Stellar Populations, ed. B. M. Tinsley & D. C. Larson, Richard B. Gehret, 401

Trimble, V. 1995, PASP, 107, 1133

Valenzuela, L. M., Méndez, R. H., & Miller Bertolami, M. M. 2019, ApJ, 887, 65

Vasiliev, E. & Belokurov, V. 2020, arXiv e-prints, arXiv:2006.02929

Vassiliadis, E. & Wood, P. R. 1994, The Astrophysical Journal Supplement Series, 92, 125

Veljanoski, J., Mackey, A. D., Ferguson, A. M. N., et al. 2014a, MNRAS, 442, 2929

Veljanoski, J., Mackey, A. D., Ferguson, A. M. N., et al. 2014b, MNRAS, 442, 2929

Ventura, P., Dell'Agli, F., Schneider, R., et al. 2014, MNRAS, 439, 977

Ventura, P., Stanghellini, L., Dell'Agli, F., & García-Hernández, D. A. 2017, MNRAS, 471, 4648

Veyette, M. J., Williams, B. F., Dalcanton, J. J., et al. 2014, ApJ, 792, 121

Vogelsberger, M., Genel, S., Springel, V., et al. 2014, MNRAS, 444, 1518

Walsh, D., Carswell, R. F., & Weymann, R. J. 1979, Nature, 279, 381

Walterbos, R. A. M. & Kennicutt, R. C., J. 1988, A&A, 198, 61

Weisz, D. R., Dolphin, A. E., Skillman, E. D., et al. 2013, MNRAS, 431, 364

Wenger, S., Ament, M., Steffen, W., et al. 2012, Computing in Science and Engineering, 14, 78

Wesson, R. 2016, MNRAS, 456, 3774

Wesson, R., Stock, D. J., & Scicluna, P. 2012, MNRAS, 422, 3516

White, S. D. M. & Rees, M. J. 1978, MNRAS, 183, 341

Wielen, R. 1977, A&A, 60, 263

Wilkinson, D. M., Maraston, C., Thomas, D., et al. 2015, MNRAS, 449, 328

Williams, B. F., Dolphin, A. E., Dalcanton, J. J., et al. 2017, ApJ, 846, 145

Williams, B. F., Lang, D., Dalcanton, J. J., et al. 2014, The Astrophysical Journal Supplement Series, 215, 9

Wilson, E. B. 1927, Journal of the American Statistical Association, 22, 209

Wyse, A. B. & Mayall, N. U. 1942, ApJ, 95, 24

Yin, J., Hou, J. L., Prantzos, N., et al. 2009, A&A, 505, 497

Yoachim, P. & Dalcanton, J. J. 2006, AJ, 131, 226

Zahid, H. J., Kudritzki, R.-P., Conroy, C., Andrews, B., & Ho, I. T. 2017, ApJ, 847, 18

Zinchenko, I. A., Berczik, P., Grebel, E. K., Pilyugin, L. S., & Just, A. 2015, ApJ, 806, 267

Acknowledgements

This work could not have been completed without the support of many individuals, some of whom I thank here.

I thank my supervisors, Magda Arnaboldi and Ortwin Gerhard, for providing me with the opportunity to carry out my PhD in this interesting topic and for the support and guidance. I would especially thank Magda for her patience with me and support both professionally and at a personal level. It was a pleasure working with you both and will hopefully continue to be so in future collaborations.

I thank my scientific collaborators – Nelson Caldwell, Ken Freeman, Alan McConnachie, Puragra Guhathakurta, Johanna Hartke, Matias Blana, Claudia Pulsoni and Valentin Comte, whose feedback helped shape the scientific results of this thesis. Special thanks to Nelson for the time and effort required to carry out the observation and reduction of the PN spectra. Shout out to Ken and the RSAA/ANU for hosting me during my visit and the DAAD for financing it. Thanks also to the observing teams at CFHT and MMT who made this PhD possible. Also thank developers of various software utilized in this thesis.

I thank the administration at ESO, particularly the Office for Science – Nelma, Stella, Giacomo, Paola and Eric, for making the PhD a smooth experience, providing a great working climate and financial support. Thanks to Remco for being my fellow mentor and Henri for his inputs during thesis committee meetings. I also thank the IMPRS office for their support.

I would also like to thank members of the Dynamics group at MPE for scientific exchanges and cordial banter. A shout out to the friends I made through IMPRS for making my time in Munich a memorable experience. Special thanks to Mou for her continued tolerance. A big thank you to my parents for everything. Whatever I do, I owe it to them.

Finally, I thank all creators of fiction, past and present, for the stories told in various forms in print and visual media, which were a source of continued comfort during the PhD and life in general.